# Application du groupe de renormalisation dans l'étude des propriétés de transport métalliques et de l'état supraconducteur sous champ magnétique dans les conducteurs organiques

# Application of the Renormalization Group in the study of the metallic transport properties and the superconducting state under magnetic field in organic conductors


par

Maryam Shahbazi


thèse présentée au département de physique

en vue l'obtention du grade de docteur ès sciences (Ph.D.)


FACULTÉ des SCIENCES, DÉPARTEMENT de PHYSIQUE

UNIVERSITÉ de SHERBROOKE


Sherbrooke, Québec, Canada

3 mars 2017

Le 31 janvier 2017

*le jury a accepté la thèse de M. Shahbazi dans sa version finale.*

Professeur René Côté
Président-rapporteur
Département de physique, Université de Sherbrooke

Professeur Kamran Behnia
examinateur externe
École supérieure de Physique et Chimie Industrielle de Paris

Professeur Denis Morris
Évaluateur interne
Département de physique, Université de Sherbrooke

Professeur Claude Bourbonnais
Directeur de recherche
Département de physique, Université de Sherbrooke

To my parents

# Abstract

This thesis tackles the problem of the possible phase transitions in the presence of a magnetic field, and of the transport properties of quasi-one-dimensional (quasi-1D) superconductors like Bechgaard salts. In the framework of the quasi-1D electron-gas model, the renormalization group (RG) method is used for studying the effect of Zeeman coupling to a magnetic field on the structure of the phase diagram of the quasi-1D electron gas model. For the transport theory, a combination of linearized Boltzmann equation and renormalization group method is used to investigate the electrical resistivity and the Seebeck coefficient of quasi-1D correlated organic metals like the Bechgaard salts near their quantum critical point that joins antiferromagnetism and superconductivity.

The thesis is organized in four chapters. In the first chapter, an introduction to the Bechgaard and Fabre salts is given and properties of their generic temperature-pressure phase diagram are explained. These compounds are considered as the reference systems for the comparison between theory and experiments on the nature and symmetry of the superconducting phase in a magnetic field and the anomalous transport properties in the normal phase.

The problem of the observed anomalously high value of the upper critical field of Bechgaard salts is the main issue of chapter two. We approach this problem with the aid of the weak coupling renormalization group technique in the presence of Zeeman coupling, for an extended quasi-1D electron-gas model, which includes inter-chain hopping, nesting deviations along with both intra-chain and inter-chain repulsive interactions. This allows us to study the effect of quasi-1D spin fluctuations originating from constructive interference between unconventional superconductivity (SC) and density-wave instabilities on the magnetic field *vs* temperature phase diagram of these quasi-1D superconductors. Our results support the existence of a crossover from $d$-wave to an inhomogeneous $d$-wave FFLO superconducting state under field.

In the third chapter, we introduce the semi-classical Boltzmann equation for transport in its linearized form. The Boltzmann theory is coupled to the RG method for the calculation of the renormalized umklapp scattering amplitude for the anisotropic scattering time. We then study the temperature and pressure variation of the electrical resistivity and the Seebeck coefficient of the

Bechgaard salts quasi-one-dimensional organic superconductors in the quantum critical domain of their normal phase. We demonstrate that momentum and temperature dependence of umklapp scattering strongly affects the temperature behavior of transport in the metallic state, as a function of nesting deviations that simulate the influence of pressure in the actual phase diagram. This defines a characteristic quantum critical region where significant deviations from the Fermi-liquid behavior are seen, either as an anomalous power law of electrical resistivity or sign reversal of the Seebeck coefficient.

# Sommaire

Cette thèse aborde le problème des transitions de phase possibles, en présence d'un champ magnétique, et des propriétés de transport dans des supraconducteurs quasi-unidimensionnels (quasi-1D) comme les sels de Bechgaard. Dans le cadre du modèle d'un gaz d'électrons quasi-1D, on utilise la méthode du groupe de renormalisation (GR) pour étudier l'effet du couplage Zeeman sur le diagramme de phase ce système. Pour la théorie du transport, une combinaison de l'équation de Boltzmann linéarisée et de la méthode de groupe de renormalisation est utilisée pour étudier la résistivité électrique et le coefficient de Seebeck de métaux organiques comme les sels de Bechgaard au voisinage de leur point critique quantique joignant l'antiferromagnétisme et la supraconductivité.

La thèse est organisée en quatre chapitres. Dans le chapitre un, une introduction aux sels de Bechgaard et de Fabre est donnée et les propriétés de leur diagramme de phase générique en température-pression sont expliquées. Ces composés sont considérés comme des systèmes de référence pour la comparaison entre la théorie et les expériences sur la nature et la symétrie de la phase supraconductrice sous un champ magnétique et les propriétés anormales de transport dans la phase normale.

Le problème de la valeur anormalement élevée du champ critique supérieur observée dans les sels de Bechgaard est la question principale traitée au chapitre deux. Nous abordons ce problème à l'aide de la technique de couplage faible du groupe de renormalisation, pour le modèle du gaz d'électrons quasi-1D étendu, qui contient le saut inter-chaînes, les déviations par rapport à l'emboitement parfait, ainsi que les interactions intra-chaînes et inter-chaînes répulsives. Ceci nous permet d'étudier l'effet des fluctuations de spin quasi-1D provenant d'une interférence constructive entre la supraconductivité non conventionnelle (SC) et les instabilités d'onde de densité sur le diagramme de phase en champ magnétique et en température de ces supraconducteurs quasi-1D. Grâce à notre approche, nous examinons les instabilités possibles dans la partie basse température/champ élevé du diagramme de phase.

Dans le troisième chapitre, nous introduisons l'équation semi-classique de Boltzmann pour le transport dans sa forme linéarisée. La théorie de Boltzmann est couplée à la méthode du GR pour

le calcul de l'amplitude de diffusion umklapp renormalisée entrant dans l'évaluation du temps de diffusion anisotrope. Nous étudions ensuite la variation en température et en pression de la résistivité électrique et le coefficient de Seebeck pour les supraconducteurs organiques quasi-1D, les sels de Bechgaard, dans le domaine critique quantique de leur phase métallique. Nous démontrons que la variation en quantité du mouvement et en température de la diffusion umklapp sur la surface de Fermi affecte fortement le comportement thermique du transport dans l'état métallique, en fonction des déviations à l'emboîtement parfait. Dans notre modèle, ces déviations simulent l'influence de la pression dans le diagramme de phase réel. Ceci définit une région critique quantique caractéristique où des écarts significatifs par rapport au comportement du liquide de Fermi sont observés, soit comme une loi de puissance anormale de la résistivité électrique, soit comme un changement de signe du coefficient de Seebeck.

# Acknowledgments

I would like to express my sincere gratitude to my supervisor, Professor *Claude Bourbonnais*, for his generous support of my work, his exceptional knowledge of the field that he shared with me, and his genuine passion for research, supervision, and mentoring. I truthfully appreciate his availability, his patience, and his encouragement during my entire PhD studies.

I would like to thank Professor *René Côté* for agreeing to be the chair of my thesis examination committee, and also for his advice and support during the advisory committee meetings. I do appreciate the time he devoted to read my thesis despite his busy schedule as the director of graduate studies in the department.

I would like to thank Professor *Denis Morris* for agreeing to be the member of my thesis examination committee although a theoretical thesis is not always easy for an experimenter to follow. I thank him again for his advice and support along the thesis committee meetings.

I thank the external member of my thesis examination committee, Professor *Kamran Behnia*, for accepting this hard work and for his availability. I am very grateful to him, and it has been my honor to receive his comments.

I am deeply thankful to Dr. *Hassan Bakrim* who has generously helped me in conducting the first programming part of this thesis. I would also like to thank *HuiZhong Lu*, high-performance computation analyst in the scientific computer center of the university, for his assistance in facilitating parallel computations.

I thank Dr. *Abdelouahab Sedeki* for his constructive comments helped to progress the first part of the project.

Last but not least, I would like to thank all my friends and the staff in the Department of Physics for their friendly supports in difficult situations of my academic life for the last five years.

# Contents

**Abstract** ii

**Introduction** 1

**1 Organic conductors: Bechgaard salts** 4
- 1.1 Organic charge transfer salts . . . 4
  - 1.1.1 $(TMTTF)_2PF_6$ under pressure . . . 6
- 1.2 Bechgaard salts . . . 8
  - 1.2.1 Crystal structure . . . 8
  - 1.2.2 Electronic band structure . . . 8
  - 1.2.3 Phase diagram . . . 11

**2 Renormalization group approach to the electron gas model in the presence of magnetic field** 27
- 2.1 Main instabilities of the electron gas . . . 27
- 2.2 Quasi-one-dimensional electron gas model . . . 28
  - 2.2.1 Partition function . . . 30
- 2.3 Renormalization group method . . . 32
  - 2.3.1 Renormalization of the coupling constants . . . 34
  - 2.3.2 Response functions . . . 37
- 2.4 One-Loop contributions to the RG equations . . . 43

**3 Boltzmann equation and transport** 58
- 3.1 Transport in strongly correlated systems . . . 58
- 3.2 Boltzmann equation . . . 59
  - 3.2.1 Linearization of the collision integral . . . 61
- 3.3 Transport properties . . . 63
  - 3.3.1 Currents and response functions . . . 64

**4 Complement to the theory of the Seebeck coefficient of chapter 3** **101**
4.1 Seebeck coefficient at low temperatures . . . . . 101
4.2 Self-energy in the presence of antiferromagnetic fluctuations . . . . . 102
4.3 Density of states . . . . . 104
4.4 Results and discussion . . . . . 108

**Conclusion** **109**

**Bibliography** **110**

# List of Tables

2.1 Possible superconducting form factors (order parameters) in a quasi-1D geometry. . 39

# List of Figures


1.1 (a) Generic phase diagram of $(TM)_2X$ salts first suggested by Jérome [39]. The ambient pressure value for different compounds is indicated. The various ground states are colored. $T_\rho$ and $T^*$ illustrate the onset temperatures of one-dimensional charge localization and one-dimensional to two-dimensional crossover, respectively [40]. (b) DC resistivity versus temperature for several $(TM)_2X$ salts [4]. . . . . 6

1.2 Crystal structure of Bechgaard salts. Left: the view along the $b$-axis. The $\pi$ orbitals of the atoms within TMTSF molecule are shown. Right: the view along the $a$-axis. Bottom: unit cell with a dimer of TMTSF molecules. . . . . 9

1.3 Electronic structure of Bechgaard salts . . . . . 10

1.4 Spin-susceptibility of $(TMTSF)_2AsF_6$ as deduced from static measurements with magnetic field along the respective crystal axes. The magnetic field 3 kG, is lower than critical spin-flip field [38]. . . . . 11

1.5 Schematic SC gap symmetries for a quasi-1D Fermi surface. The dashed lines illustrate the nodes of the gap whose $k_b$ dependence is omitted for simplicity. $\pm$ show the sign of the gap function. . . . . 13

1.6 (a) $P-T$ phase diagram of $(TMTSF)_2PF_6$ [20]. (b) Low temperature part of $P-T$ phase diagram of $(TMTSF)_2PF_6$. The data for the coexistence regime below the critical pressure ($=$ 9.4 kbar) are obtained through the resistivity measurements along the $a$ crystallographic axis (downward triangles), along the $b$-axis (squares), and along the $c$-axis (hexagons). The full symbols are for SC transition temperature and the empty symbols for the SDW transition temperature [70, 71]. The data above 9.4 kbar are captured by the longitudinal ($a$-axis) resistivity measurements from reference [20] (red circles), and from reference [72] (green triangles). (c) Phase diagram of $(TMTSF)_2ClO_4$ deduced by longitudinal resistivity measurements from [20] (red circles) and from [73] (green triangles). . . . . 15

1.7 (a) Specific heat versus temperature in $(TMTSF)_2ClO_4$ for two different single crystals presented by sample #1 : 0.257 mg and by sample #2 : 0.364 mg. The dashed curves represent the fittings with the Sommerfeld-Debye formula ($c_p/T = \gamma_e + \beta_p T^2$) to the normal state data above 1.3 K. (b) Electronic specific heat [7]. . . . . 16
1.8 Anisotropy of the upper critical field obtained from resistivity measurements. The magnetic field is applied parallel to the conducting $a - b'$ planes and perpendicular to the planes ($c^*$-direction). The orbital destroying effect is weakest when the magnetic field is aligned the $b'$-direction. . . . . 16
1.9 $^{77}$Se NMR study of $(TMTSF)_2ClO_4$ . . . . . 17
1.10 $H - T$ phase diagram obtained through specific heat measurements (solid symbols) and from resistivity measurements (open symbols), as well as the one obtained by determining the temperature at which the resistance along the $c^*$-direction is zero (crosses) [92]. . . . . 18
1.11 Field-angle ($\phi$) dependence of superconducting onset temperature $T_c^{\text{onset}}$. Every polar plot is for a given value of magnetic field and each point represents the direction of magnetic field from the $a$-axis ($\phi = 0$) and the value of $T_c^{\text{onset}}$ as the distance from the origin [90]. . . . . 19
1.12 FFLO pairing ($\boldsymbol{q} \neq 0$) possibility in different dimensions. The dashed lines represents the zero field Fermi surface and the full colored lines represent the Zeeman split Fermi surfaces for spin-down and spin-up electrons. For a spherical isotropic Fermi surface, the electron of $-\boldsymbol{k}'$ cannot locate on the spin-down Fermi surface through the transfer of $\boldsymbol{q}$ vector and thus the pair of $(\uparrow \boldsymbol{k}', \downarrow -\boldsymbol{k}' + \boldsymbol{q})$ cannot be formed. In 2D, the Fermi surface is nested in parts and therefore some pairs like $(\uparrow \boldsymbol{k}', \downarrow -\boldsymbol{k}' + \boldsymbol{q})$ can be formed but others like $(\uparrow \boldsymbol{k}'', \downarrow -\boldsymbol{k}'' + \boldsymbol{q})$ cannot. On a quasi-1D Fermi surface almost all pairs can locate on the split Fermi surface [18]. . 20
1.13 Intricate phase diagram of $(TMTSF)_2PF_6$ obtained from resistivity measurements in the coexistence regime [71]. . . . . 22
1.14 (a) $^{77}$Se NMR spin lattice relaxation rate versus temperature, for applied pressures greater than and less than the critical pressure $P_c = 0.6$ GPa [121]. (b) $P$-$T$ phase diagram of $(TMTSF)_2PF_6$ to which added the variation of Curie-Weiss scale $\Theta$ with pressure obtained from the NMR data in (a) [19]. . . . . 23
1.15 (a) Longitudinal electrical resistivity of $(TMTSF)_2PF_6$ as a function of temperature at various pressures greater and smaller than the critical pressure $P_c \sim 11.8$ Kbar. (b) The log-log plot of the inelastic part of the data $\Delta\rho_a(T) = \rho_a(T) - \rho_0$ [19]. . . . . 24
1.16 The variation of resistivity exponent $\alpha$ with pressure and temperature. . . . . 24
1.17 Ambient pressure longitudinal Seebeck coefficient versus temperature [21]. . . . . 25

2.1 Decomposition of two-electron interactions on a quasi-1D Fermi surface according to the $g$-ology model. . . . . 30
2.2 Diagrams of possible scattering processes of the quasi-1D electron gas model: backward scattering between electrons of spins opposite (parallel) $g_{1\perp(\parallel)}$, forward scattering $g_{2\perp}$ with anti-parallel spins, and umklapp scattering for opposite spins $g_{3\perp}$. The continuous (dashed) lines refer to $p = +(-)$ electrons. The open (full) red square represents the generic vertex part for the normal (backward and forward) and umklapp scattering amplitudes. . . . . 31
2.3 Diagrammatic representation of the renormalization of the coupling constants at the one-loop level. . . . . 35
2.4 Diagrammatic representation of flow equations for the pair vertex functions as the shaded circles. . . . . 38

3.1 The Fermi surface of the quasi-1D electron-gas model. . . . . 65

4.1 The Lee-Rice-Anderson approximation to the electron self-energy in the absence of vertex corrections. . . . . 102
4.2 (a) The bare density of states for a slightly dimerized quasi-1D tight-binding band. (b) The density of states as given by equation (4.19) at a given value of temperature showing a reduction of density of states at the Fermi level ($\omega/t = 0$) after the introduction of antiferromagnetic fluctuations. . . . . 105
4.4 The band part of the Seebeck coefficient versus temperature obtained from the perturbed density of states (red dotted line) and compared with the one from the bare spectrum (dashed balck line) . . . . . 107

# Introduction

In strictly one-dimensional (1D) electronic systems any long-range order is avoided at finite temperature by the effect of fluctuations [1]. The low-energy spin and charge excitations behave as collective modes which propagate at different velocities and characterize the metallic state in one dimension known as the Tomonaga-Luttinger liquid (TLL). However, in real crystalline materials consisting of one-dimensional chains, the coupling to the lattice and/or the inter-chain interactions establish finite-$T$ phase transitions, and long-range ordered states. This is the case of quasi-one-dimensional (quasi-1D) systems which exhibit broken symmetry states where electronic charge, spin, and even lattice degrees of freedom tend to develop ordered structures.

$TM_2X$ compounds, named the Bechgaard and the Fabre salts, are well-known examples of quasi-1D electron systems, where TM represents the planar TMTSF or TMTTF organic molecules forming 1D stacks separated by different monovalent anions X. A three-quarter-filled HOMO (highest occupied molecular orbital) conduction band of TM molecules is then realized which is split by a slight dimerization along the stacking direction, turning it into an effective half-filled band with the possibility of umklapp scattering for carriers close to the Fermi level. Being nearly confined along the stacking direction by strong anisotropy, the $\pi$ electrons in these charge transfer salts form a relatively simple Fermi surface of only two slightly warped sheets in which novel electronic phenomena can take place.

The union of the above mentioned characteristics, as well as the large crystal compressiblity and thermal expansion coefficient makes a plethora of phase transitions possible by variation of the temperature and some tuning parameter such as pressure, magnetic field, or anion substitution [2, 3, 4, 5]. At high enough temperatures, the curvature of the Fermi surface, due to inter-chain electron hopping, is blurred by thermal fluctuations. This allows us to visualize the signatures of one-dimensional physics and the Luttinger-liquid effects. This is where the electronic correlations are magnified by one-dimensionality, and where dimerization leads to 1D Mott localization. This is found experimentally in the Fabre $(TMTTF)_2X$ salts. Decreasing temperature, the localized electron spins undergo an antiferromagnetic transition or a non magnetic spin-Peierls order depending on

the pressure or the choice of anion X. On the other hand, by applying pressure, the transverse hopping is enhanced and the carriers are no more confined along the 1D chains. In these conditions, the Mott behavior is suppressed and the system shows a two-dimensional, though highly anisotropic, correlated metal. In these pressure conditions, the $(TMTTF)_2X$ become similar to the $(TMTSF)_2X$. There, the nesting of the quasi-1D Fermi surface triggers a weak itinerant antiferromagnetic ordered state at low temperatures, the spin-density-wave (SDW) like the one found in $(TMTSF)_2X$ at low pressure.

The salient feature of the phase diagram of $(TMTSF)_2X$ is the emergence of superconductivity (SC) after the suppression of the SDW phase at the critical pressure $P_c$ (see figure 1.1a) [6, 7]. Besides the proximity between SDW and SC phases, the existence of spin fluctuations in the low temperature part of the metallic phase down to the superconducting transition temperature ($T_c$) supports a picture where superconducting pairing is mediated by antiferromagnetic spin fluctuations linked to the quantum critical point around $P_c$ (QCP) at the junction of SDW and SC along the pressure axis. The quantum criticality is affected by the interplay between different instabilities. This is confirmed, on the theoretical grounds, by the weak coupling renormalization group (RG) where the electron-electron and electron-hole scattering channels at the microscopic level are taken into account on equal footing. The SDW and SC instabilities are thus intimately connected by quantum interference [8, 9, 10, 11]. The proximity of a SC state to a magnetically ordered insulating state is a common feature of other strongly correlated electron systems. Members of heavy fermion compounds [12, 13], layered high-$T_c$ copper oxide [14, 15, 16], and pnictide [17, 12] superconductors are celebrated examples where magnetic quantum fluctuations are typically associated to unusual precursor metallic properties. Thanks to their reduced dimension and to their simple electronic structure, the quasi-1D organic superconductors could be simpler to modelize providing us key physics which might be helpful in understanding similar phenomena in other unconventional superconductors.

The work reported in this thesis covers still-open problems mentioned in previous paragraphs. In the first chapter, we give an overview of the content of the generic phase diagram of $TM_2X$ salts with key experimental features about magnetism and transport in the metallic phase of Bechgaard salts which are the principal compounds our model is based on.

Although several experimental works in quasi-1D organic conductors like Bechgaard salts support the existence of a nodal $d$-wave symmetry for the superconducting gap [6, 7], the survival of superconductivity for magnetic fields greater than the Pauli limiting field of $2 - 2.5$ T is still under debate as to how the superconducting order parameter transforms under high magnetic field. With the aid of the weak coupling renormalization group approach in the presence of a magnetic field, which includes stack dimerization through electron-electron umklapp scattering processes, we study the possible symmetries of the SC order parameter under magnetic field. We explore whether a

triplet or a singlet pairing symmetry would be realized in the low temperature and high field part of the phase diagram. Recently, RG calculations of Fuseya et al. [18], supported the formation of an inhomogeneous fluctuating SC state, the so-called Fulde–Ferrell–Larkin–Ovchinnikov or FFLO state. The FFLO state has in the present case a $d$-wave symmetry. It favors the persistence of superconductivity at high magnetic fields, namely beyond the Pauli limiting field. We generalize the study by including the effect of umklapp and a small Coulomb repulsion term coupling between electrons of nearest-neighbor chains. Chapter two of the thesis is devoted to the description of the RG method on the basis of a quasi-1D electron gas model and to our calculations of vertices and response functions in the presence of Zeeman coupling to a magnetic field. The chapter is followed by a related paper in which the results are detailed. There, we will show how at the low temperature there is a crossover from the $d$-wave homogeneous SC to a $d$-wave FFLO state at high magnetic field. Furthermore, at certain intermediate value of inter-chain interaction, an exotic FFLO state for triplet pairing of total spin $S_z = 0$ follows after the $d$-wave non-FFLO instability in the quantum critical region of the phase diagram. However, no transition from the singlet to triplet superconductivity is found.

The second part of this work contains the study of transport coefficients such as resistivity and Seebeck coefficient. As a function of a control parameter these observables can shed light into the microscopic structure of the normal phase that precedes the competing ordering SDW and SC states. It corresponds to the puzzling non-Fermi-liquid transport and magnetic properties of the normal phase above the quantum critical point [19, 20]. In Bechgaard salts, the measured low temperature longitudinal resistivity is found to follow a linear temperature dependence as $\rho(T) = \rho_0 + AT$ being strongly correlated to the temperature distance from the QCP and indirectly linked to the amplitude of SDW fluctuations [19, 20]. The measured Seebeck coefficient in these materials has also exhibited deviations from simple linear temperature band term and even sign reversal in the low temperature interval in the absence of any phase transition that would reconstruct the Fermi surface [21].

In chapter three, we study the effect of quantum fluctuations on transport properties. We linearize the semi-classical Boltzmann equation and feed it with the umklapp vertex function, as calculated by the RG [22]. This gives the possibility to determine microscopically the low energy variation of the electron-electron relaxation time over the Fermi surface and its influence on the temperature behavior of the resistivity and the Seebeck coefficient. The corresponding papers are joined at the end of the chapter. As an unpublished complement to this chapter, we include a calculation of fluctuation effects on the density of states entering in the Seebeck coefficient.

Chapter 1

# Organic conductors: Bechgaard salts

## 1.1 Organic charge transfer salts

Organic materials are made up of a combination of Carbon with Hydrogen, Oxygen, Nitrogen, and a plethora of other elements. They are generally regarded as electrical insulators like plastics, nylon, and other polymers. However, the efforts to find conductive organic crystals lead to the synthesis of the first stable organic metal, the two-chain charge transfer salt TTF-TCNQ, in 1973 [23]. It is formed of a good electron acceptor, the TCNQ molecule, synthesized in 1960 [24], and the electron donner TTF synthesized in 1970 [25]. It exhibits a high conductivity parallel to the stacking direction of the molecules, which is about $500(\Omega.cm)^{-1}$ at ambient temperature, reaching a value of $10^4 \cdots 10^5(\Omega.cm)^{-1}$ down to 59 K where a sharp metal-insulator transition occurs [26, 23, 27]. Indeed, it turned out that many quasi-one-dimensional (quasi-1D) organic metals share this common feature, i.e., the low temperature gap at the Fermi level. In 1955, Peierls showed that a one dimensional (1D) metal at zero temperature is unstable towards the formation of a coupled electron-lattice superstructure and the opening of a gap at the Fermi level [28]. The Peierls transition is a consequence of the nesting of the one-dimensional Fermi surface. When the lattice vibrations couple to the electron density response, nesting induces an instability of the metallic state against the formation of a superstructure, the so-called charge-density-wave (CDW) or Peierls state, at finite temperature.

The relevance of electron-phonon interaction gave rise to the quest for superconductivity in these materials, as for ordinary superconductors in three dimensions (3D). H. Fröhlich, before the Bardeen-Cooper-Schrieffer (BCS) theory of superconductivity [29], proposed a model in which an incommensurate CDW can slide in a 1D chain without dissipation, leading to a superconducting state. In 1964, W. A. Little suggested the possibility of high temperature superconductivity in a 1D polymeric

chain on which a series of highly polarizable lateral chains were attached. The charge oscillations in the side chains could induce an attractive interaction between delocalized electrons moving along the polymeric backbone [30]. Even if this prediction was never realized and an insulating CDW state was almost systematically observed, it induced intense research in the field of organic superconductivity. Following almost unfruitful efforts to observe superconductivity, the physicists and the chemists came to the conclusion that the Peierls instability at low temperatures is a dominant obstacle preventing superconducting transition in the low-dimensional organic conductors. The key solution was to find a way to weaken the underlying driving force of this structural instability, i.e. nesting, for the electron-hole symmetry and logarithmic singularity of the electron system. Introduction of transverse molecular overlap or in other words of a finite single-electron hopping between nearest-neighbor chains deteriorates the perfect nesting [31]. The combination of application of hydrostatic pressure and replacement of new synthesized molecules with higher transverse molecular overlap paved the way to success.

On the chemistry side, the two-chain compound TMTSF-DMTCNQ was synthesized at the end of seventies as the first stable organic metal at $T \to 0$ [32, 33]. It is composed of the donor molecule TMTSF [34] born from the TTF molecule by substituting sulfur (S) with selenium (Se), and replacing each corner hydrogen (H) with the methyl group ($CH_3$); and of DMTCNQ from TCNQ by substituting two H with $CH_3$ on each side of the carbon ring at the center. The Peierls insulating state was entirely suppressed under the pressure of 13 kbar [35].

The great breakthrough was the synthesis of one-chain cation radical salts, the $(TMTSF)_2X$ [36], where the organic chains are separated with small inorganic ions $X = PF_6^-, AsF_6^-, NO_3^-, \cdots$. This family of isostructural compounds are known as the Bechgaard salts. The $(TMTSF)_2PF_6$ compound was the first to show superconductivity at 0.9 K under 9 kbar of hydrostatic pressure [2]. The insulating state, at 12.1 K in the absence of applied pressure, was found to be magnetic in character, namely a spin-density-wave (SDW) state [37, 38], another interesting low-dimensional phenomenon which will be discussed more in the following sections.

The Bechgaard salts are isostructural with another family of salts, the Fabre $(TMTTF)_2X$ salts [41]. The (TMTTF) comprises the sulfur atom instead of selenium. With $(TMTSF)_2X$ they form a common class of materials of general formula $(TM)_2X$ [39]. Their generic phase diagram through varying the pressure and substituting the cation or anion is given in figure 1.1a. The $(TMTTF)_2PF_6$ is the most insulating compound of the phase diagram and is at the origin of the pressure scale. It becomes a superconductor at low temperatures under the pressure of 45 kbar. Moving from the left side to the right side of the generic phase diagram, a sequence of ground states from a one-dimensional Mott insulator to superconductivity is observed depending on the choice of anion or cation in the member series placed according to their ambient pressure properties. $(TMTSF)_2ClO_4$ was found to

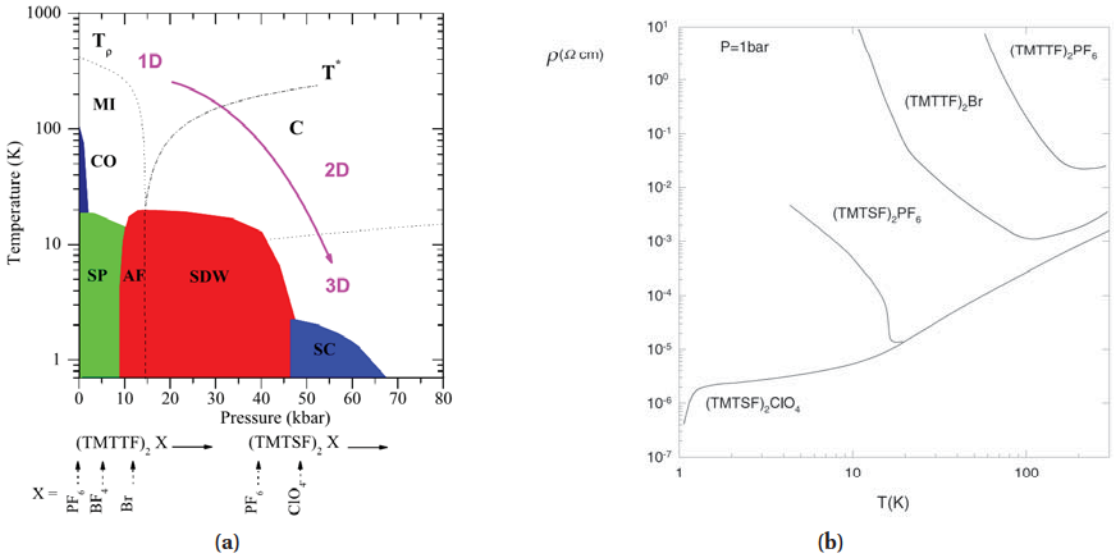


**Figure 1.1** (a) Generic phase diagram of $(TM)_2X$ salts first suggested by Jérome [39]. The ambient pressure value for different compounds is indicated. The various ground states are colored. $T_\rho$ and $T^*$ illustrate the onset temperatures of one-dimensional charge localization and one-dimensional to two-dimensional crossover, respectively [40]. (b) DC resistivity versus temperature for several $(TM)_2X$ salts [4].

exhibit superconductivity (under proper cooling conditions) at 1.2 K at ambient pressure. In the generic phase diagram of figure 1.1a, it is located at 47 kbar along the pressure axis [42].

### 1.1.1 $(TMTTF)_2PF_6$ under pressure

In the $(TM)_2X$ family, the $(TMTTF)_2PF_6$ Fabre salt spans the broadest variety of phase transitions with changing pressure and temperature (see figure 1.1a). The compound has a stoechiometry 2:1 due to a charge transfer of one electron per two TMTTF molecule towards the anion leading to a three-quarter band filling (in terms of holes) commensurate with the underlying 1D lattice. However, because of the periodicity of the anion packing being twice the periodicity of the molecular packing, the inter-molecular overlap is dimerized. This opens a gap in the middle of the three-quarter-filled band making the system effectively half-filled (one hole per dimer) [43]. This weak but important dimerization induces $4k_F$ umklapp scattering terms between electrons [44]. The dimerization depends on the geometry of the anion X. It is larger in Fabre salts than in Bechgaard salts and diminishes at low temperature and high pressure values [45].

In $(TMTTF)_2PF_6$, the emergence of each phase depends on the strength of on-site and inter-site coulomb repulsions and the electron-phonon coupling. At ambient pressure, the dimerization of

transfer integral along the chains creates favorable condition for charge localization. The on-site coulomb repulsion induces a bond order charge localization with a periodicity twice the period of the main lattice. This is the so called Mott-Hubbard state consisting of one hole per dimer. This is confirmed by the observation of an activated electrical resistivity at the temperature $T_\rho$, around $\sim 250$ K for the $(TMTTF)_2PF_6$ compound, whose value depends significantly on the anion X (figure 1.1b) [44, 41, 46, 47]. The one-dimensional character of the Mott insulator is confirmed by a charge gap size $\Delta_\rho \sim 2T_\rho$, which is much larger than the highest transverse transfer integral $t_\perp$[41, 44, 46]. As illustrated in figure 1.1a, with decreasing temperature the insulating state is characterized by a charge disproportion. It corresponds to a charge modulated insulating state (CO) with localized spins located on the charge rich sites. The dielectric measurements in the radio-frequency range gave the first indications of a CO state whereas NMR spectroscopy results support the absence of the spin anomalies and structural modifications [48, 49, 50] at the CO transition. Upon further cooling, the spin-lattice coupling gives rise to a spin-Peierls (SP) instability around 18 K where the spins are localized on the neighboring dimer pairs and form spin singlets with a periodicity four times the period of the main lattice which corresponds to a tetramerization. This has been detected through elastic neutron scattering in $(TMTTF)_2PF_6$ [51]. By applying pressure the CO and the SP states are suppressed and the SP ground sate evolves towards an antiferromagnetic insulating state (AF) due to strong electron correlations. This corresponds to a staggered pattern of the localized spin moments with $(2k_F)^{-1}$ periodicity [52]. This is the same ground state as $(TMTTF)_2Br$ salt at ambient pressure. Moving along the pressure axis the onset temperature of charge localization ($T_\rho$) decreases uniformly ( figure 1.1a), as a result of inter-chain coupling enhancement and decrease of dimerization of the stacks. It carries over until the Mott-Hubbard localized state becomes in turn suppressed and a $2k_F$ spin-density-wave (SDW) replaces the localized antiferromagnetism (figure 1.1a). The SDW is a modulated spin state and results from a nesting type of mechanism. It has been studied by transport [36], spin susceptibility [37], and NMR measurements [53].

The merging point of the Mott state with SDW state sets the threshold pressure (about 15 kbar) under which the one-dimensional confinement of electrons ceases and a quasi-one-dimensional Fermi surface becomes coherent in the transverse direction [47, 4, 54] (see figure 1.1a). Consequently, the properties of Fabre salts and those of the Bechgaard salts at low pressure become similar. In figure 1.1a, the characteristic temperature scale $T^*$ marks the temperature at which the transverse resistivity along the least conducting direction switches from an insulating to a metallic temperature dependence at a given pressure [54, 55]. The high temperature region separated by $T^*$ could be considered as a 1D region where the physics of a Tomonaga-luttinger liquid is relevant. As a result, $T^*$ could be associated to a crossover from one-dimensional to two-dimensional regions.

Finally, under the pressure of 52-54 kbar, $(TMTTF)_2PF_6$ displays superconductivity at $T_c = 1.4 - 1.8$ K. In the phase diagram of figure 1.1a, this corresponds to the $(TMTSF)_2PF_6$ of the

Bechgaard salts series at 12 kbar or so. It also corresponds to the case of $(TMTSF)_2ClO_4$ at $P = 1$ bar, which is already a superconductor at $T_c \approxeq 1.2$ K at ambient pressure.

## 1.2 Bechgaard salts

### 1.2.1 Crystal structure

If one now considers specifically the Bechgaard salts $(TMTSF)_2X$, these were synthesized in Denmark by the team of K. Bechgaard [36]. The organic Tetramethyltetraselenfulvalen (TMTSF) molecule contains 4 selenium, 10 carbon, and 12 hydrogen atoms. X is the inorganic anion of various symmetries e.g., $PF_6$, $SbF_6$, ..., and $ClO_4$. According to figure 1.2, the planar TMTSF molecules stack in a zig-zag fashion forming chains along the crystal $a$-axis. Along the $b$-axis direction (the short direction of molecule), the stacks are shifted from each other forming donor layers on the $a$-$b$ plane. The X anions fill the methyl group cavities of the neighboring stacks along the $c$-axis (the long direction of molecule). The crystal structure is triclinic [56], and each unit cell contains two TMTSF molecules and one anion (see figure 1.2). The orthorhombic is often taken as the approximate unit cell structure which explains most physical features. The ambient temperature lattice parameters for $(TMTSF)_2PF_6$ are $a = 7.297\mathring{A}$, $b = 7.711\mathring{A}$, $c = 13.522\mathring{A}$, $\alpha = 83.39°$, $\beta = 86.27°$, $\gamma = 71.01°$ [57, 58]. The $b'$ and $c^*$-axis are mostly used in literature as shown in figure 1.2. The $b'$-axis is the projection of $b$-axis onto the plane perpendicular to the $a$-axis, and $c^*$ is taken as the direction perpendicular to the $a$-$b$ plane. The alternating distances between adjacent molecules, indicated by $d_1$ and $d_2$ in the figure 1.2, reflect a weak dimerization that occurs along the $a$-direction; It is characterized by an amplitude of $2(d_1 - d_2)/a$ [59].

### 1.2.2 Electronic band structure

The physics of Bechgaard salts are well characterized by quasi-1D models justified by the high anisotropy in conductivity. This is because of their large inter-chain and inter-plane distances, which permit the electrons to move most easily along the chain direction. The transfer integral $t_i$, is the largest along the stacking direction, $a$-direction, and much smaller along $b$-direction. The hopping integral $t_c$ is very small due to the presence of closed shell anions between TMTSF molecules. The transfer integrals for $(TMTSF)_2X$ materials at room temperature, were calculated from semi-empirical molecular-orbital calculations to be $(4t_a : 4t_b) \approx (0.5eV : 0.05eV)$ [60], within the tight binding approximation to be $(t_a : t_b : t_c) \approx (0.2eV : 0.02eV : < 0.001eV)$ [61], and from room temperature measurements of plasma frequency to be $4t_a : 4t_b : 4t_c = 1 : 0.1 : 0.003eV$ [62]. The conductivity

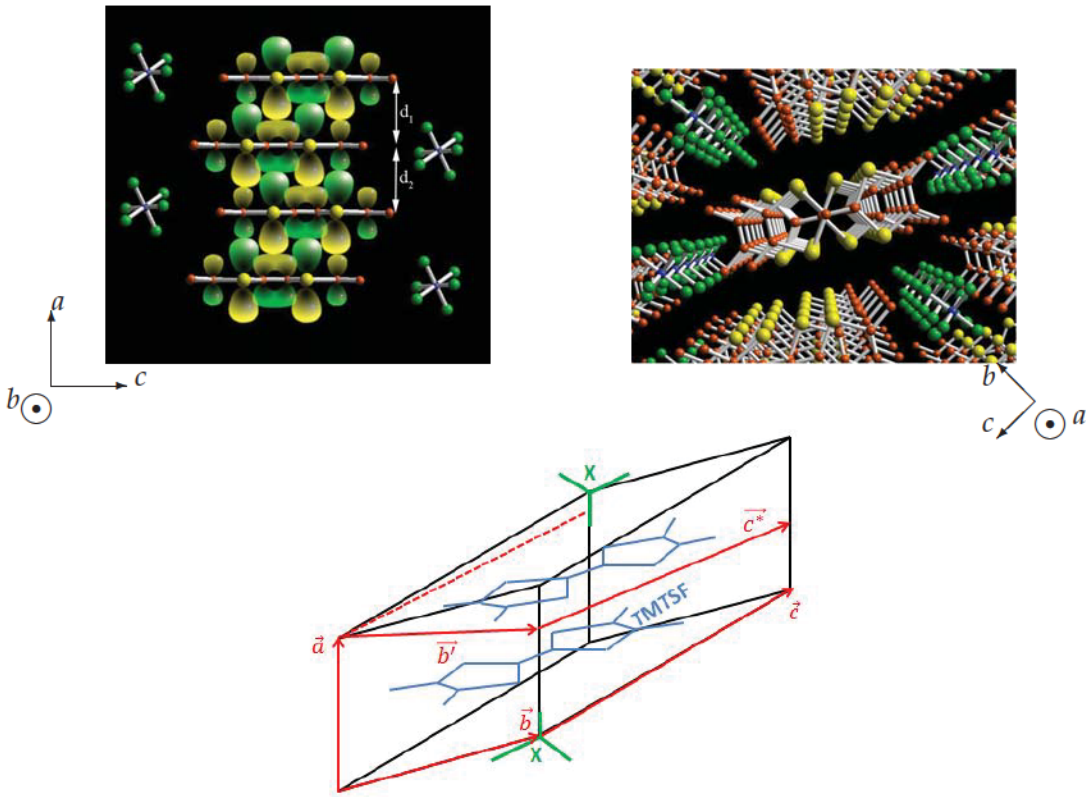


**Figure 1.2** Crystal structure of Bechgaard salts. Left: the view along the $b$-axis. The $\pi$ orbitals of the atoms within TMTSF molecule are shown. Right: the view along the $a$-axis. Bottom: unit cell with a dimer of TMTSF molecules.

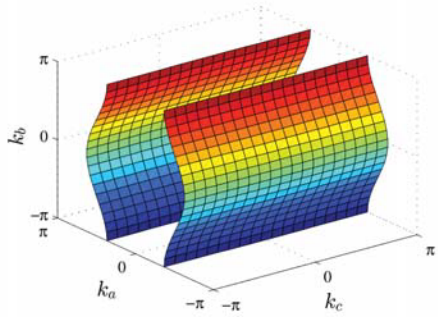


(a) Typical open quasi-1D Fermi surface

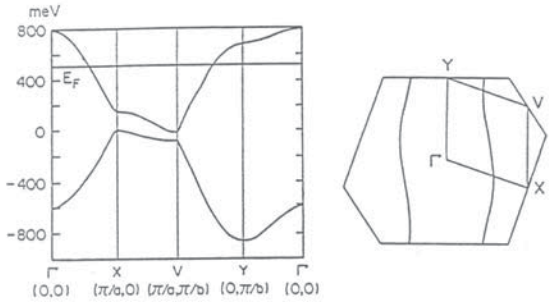


(b) Left: Band strucutre of $(TMTSF)_2ASF_6$. Right: The corresponding 2D Fermi surface [60, 61]

**Figure 1.3** Electronic structure of Bechgaard salts

ratio at room temperature is given by $\sigma_a : \sigma_b : \sigma_c = 1 : 10^{-2} : 10^{-5}(\Omega.cm)^{-1}$. In fact, the electronic structure anisotropy reflects room temperature conductivity anisotropy, and the relationship $\sigma_i \sim t_i^2$ seems to hold.

Because of the charge transfer from the organic molecules to the counter-ions, the electronic bands are only partially filled. Here a full charge transfer of one electron per two TMTSF molecules causes the band to be a three-quarter-filled hole band leading to the metallic properties. However, the above-mentioned weak dimerization along the chains alters the band, which becomes effectively half-filled (one hole per dimer) by opening a gap $\Delta_D$ at $\pm 2k_F$, called the dimerization gap in the middle of the three-quarter-filled band. The band formation is due to the largest intra-chain overlap between the anti-bonding out of plane $\pi$ molecular orbitals from the neighboring TMTSF molecules. The electronic band structure is calculated in a tight-binding approximation assuming that the close Se-Se contact causes the strongest overlap [60, 61]. Thus energy-dispersion relation describing the electron band structure takes the following form [3]

$$\varepsilon(\boldsymbol{k}) = -2t_a \cos(k_a a) - 2t_b \cos(k_b b) - 2t_a \cos(k_c c). \tag{1.1}$$

The resulting open Fermi surface for a small $c$-axis overlap is shown in figure 1.3a. It is formed of two warped opposing sheets characterized by a weak modulation along the $b$-axis due to $t_b$, and a negligible one along the $c$-axis. The calculated band structure from the extended Huckel approach of reference [61] is shown in figure 1.3b.

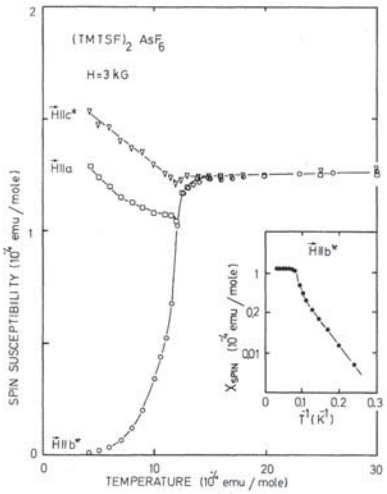


**Figure 1.4** Spin-susceptibility of $(TMTSF)_2AsF_6$ as deduced from static measurements with magnetic field along the respective crystal axes. The magnetic field 3 kG, is lower than critical spin-flip field [38].

### 1.2.3 Phase diagram

#### Spin-density-wave phase transition

In quasi-1D organics at low temperatures, the coupling of the electronic charge density to the underlying lattice can cause a charge modulation and a gap opening at the Fermi surface. The insulating state then is a charge-density-wave (CDW) state. In Bechgaard salts, however, CDW was not observed. In $(TMTSF)_2PF_6$ the sharp metal-insulator transition corresponds to a spin-density-wave (SDW) ground state at $T_{SDW} = 12$ K (figure 1.1b) [36]. The low field susceptibility of the SDW phase behaves very much like the susceptibility of a regular antiferromagnet as displayed in figure 1.4. The results for the $(TMTSF)_2AsF_6$ compound show that the easy axis is aligned along the $b'$ direction and that a spin flip transition arises around 5 kOe [38].

The magnetic nature of the ground state has also been confirmed by the observation of antiferromagnetic (AF) resonance and the measurement of a local field by nuclear magnetic resonance (NMR) and $\mu^1$SR [63, 64]. A sinusoidal SDW modulation of wave vector $\boldsymbol{Q}_{SDW} = (0.5, 0.24 \pm 0.03, -0.06 \pm 0.2)$ in units of $2\pi/a$, $2\pi/b$, and $2\pi/c$, with an amplitude of 8% $\mu_B$/molecule was suggested by two independent proton NMR experiments [65, 53].

The transition to the SDW phase is driven by a specific nesting property of the hole Fermi surface of $(TMTSF)_2PF_6$ and of some other materials from the family which have centrosymmetric anions. Indeed, the characteristic vector of the spin modulation is defined by this Fermi surface property. In Bechgaard salts, the two opposing Fermi surface sheets for a spectrum like in (1.1) fit one

onto another under a translation in the reciprocal space by the nesting vector $\boldsymbol{Q} = (2k_F, \pi/b, \pi/c)$. This vector links the occupied states close to one Fermi surface sheet to the unoccupied states close to the other Fermi surface sheet by the electron-hole symmetry $\varepsilon(\boldsymbol{k}) = -\varepsilon(\boldsymbol{k}+\boldsymbol{Q})$. This symmetry leads to a logarithmic divergence in the bare spin susceptibility function $\chi_0(\boldsymbol{q} \approx \boldsymbol{Q})$ of the free electron gas as $T \to 0$, and eventually to a SDW state when interactions are present. A spatial modulation in spin density is characterized by the $\boldsymbol{Q}$ wave vector. The difference between the density of electron spins polarized upward and downward is modulated in space according to:

$$\rho(x) = \rho(x)_\uparrow - \rho(x)_\downarrow = \rho_0 \cos(\boldsymbol{Q}\cdot\mathbf{x} + \varphi(x)) = \rho_0 \cos(2k_F x + \varphi(x)). \tag{1.2}$$

This $2k_F$ SDW was observed experimentally, as already mentioned above [65, 53]. The development of SDW opens a gap $2\Delta$ at the Fermi surface, giving rise to the metal to insulator transition [66]. In the SDW phase, the resistance shows the activated behavior, $R = R_0 \exp(\Delta/T)$ [67]. For high quality samples $\Delta \approx 21$ K , and the mean field BCS relation $2\Delta = 3.52 T_{\mathrm{SDW}}$ is well satisfied for $(TMTSF)_2PF_6$ and $(TMTSF)_2AsF_6$ materials [68].

In a non-interacting electron gas featuring the dispersion $\varepsilon(\boldsymbol{k})$, a perturbation by a small periodic potential $V$ leads to a small modulation of the electronic distribution, as $\Delta_\rho(\boldsymbol{q}) = \chi_0(\boldsymbol{q})V(\boldsymbol{q})$ in the linear response theory. The bare magnetic susceptibility $\chi_0$ is given by Lindhard response function

$$\chi_0(\boldsymbol{q}) \propto \sum_{\boldsymbol{k}} \frac{f_{\boldsymbol{k}} - f_{\boldsymbol{k}+\boldsymbol{q}}}{\varepsilon(\boldsymbol{k}+\boldsymbol{q}) - \varepsilon(\boldsymbol{k})}, \tag{1.3}$$

where $f_{\boldsymbol{k}} = \dfrac{1}{e^{(\varepsilon(\boldsymbol{k})-\mu)}+1}$ is the Fermi-Dirac distribution function. the summation in (1.3) for perfect nesting leads to logarithmic divergence, $\chi_0(\boldsymbol{Q}, T) \propto \log(E_F/T)$, of the bare susceptibility, with $E_F$ as the Fermi energy. Introducing repulsive electron-electron and/or electron-phonon interactions into this non-interacting electron gas, the generalized susceptibility, obtained using the random phase approximation (RPA), takes the form

$$\chi(\boldsymbol{Q}, T) = \frac{\chi_0(\boldsymbol{Q})}{1 - X(\boldsymbol{Q})\chi_0(\boldsymbol{Q})}, \tag{1.4}$$

where $X(\boldsymbol{Q})$ represents the interaction. With this simple RPA expression, we can understand qualitatively that in the Bechgaard salts the condition $1 \equiv X(\boldsymbol{Q})\chi_0(\boldsymbol{Q})$ is easily realized. In other words, when the Stoner criterion $X\chi_0(\boldsymbol{Q}, T) = 1$ is fulfilled, the SDW ground state is expected below an ordering temperature [1] $T_{\mathrm{SDW}} \propto E_F \exp(-\frac{1}{N(E_F)X})$. Here $N(E_F)$ is the density of states at the Fermi level.

[1] It should be stressed that within the more rigorous RG approach (see Chapter 2), which fully takes into account two scattering channels, namely the electron-hole (Peierls) and electron-electron (Cooper) channels, the transition towards a SDW state occurs as well, but at lower temperature than RPA prediction.

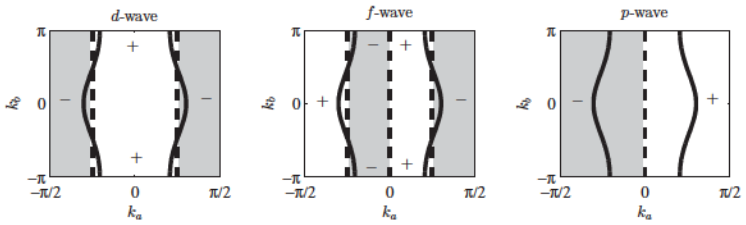


**Figure 1.5** Schematic SC gap symmetries for a quasi-1D Fermi surface. The dashed lines illustrate the nodes of the gap whose $k_b$ dependence is omitted for simplicity. $\pm$ show the sign of the gap function.

### The superconducting (SC) state and the pairing symmetry

In order to consider the origin of superconductivity in the Bechgaard salts, one can ask how the SDW state can be suppressed upon applying pressure. In a compound like $(TMTSF)_2PF_6$, one can think that nesting is to a certain degree imperfect. In order to introduce nesting deviations in the model, we consider the tight-binding spectrum

$$\varepsilon(\boldsymbol{k}) = -2t_a\cos(k_a a) - 2t_b\cos(k_b b) - 2t_c\cos(k_c c). \tag{1.5}$$

Close to the 1D Fermi points at $k = \pm k_F$, the first longitudinal term of this dispersion can be linearized without significant modifications in the physical properties of the model. Neglecting in addition the dispersion along $c$-direction ($t_c << t_b$), we arrive at the following spectrum of free electrons in 2D

$$\varepsilon(\boldsymbol{k}) = 2t_a a\sin(k_F a)(|k_a| - k_F) - 2t_b\cos(k_b b). \tag{1.6}$$

We introduce a next-to-nearest neighbor hopping term of amplitude $t'_{\perp b} \ll t_{\perp b}$ along the transverse $b$-direction, which is small but important. It corrects the electron spectrum following

$$\varepsilon(\boldsymbol{k}) = v_F(|k_a| - k_F) - 2t_\perp\cos(k_b) - 2t'_{\perp b}\cos(2k_b). \tag{1.7}$$

Here the Fermi velocity $v_F$ is equal to $2at_a sin(k_F a)$, and for a half-filled band of dimerized chains, $k_F = \pi/2a$. $t'_\perp$ causes the deviations from perfect nesting and leads to the formation of the unnested pockets of Fermi surface for which the energy relation $\varepsilon(\boldsymbol{k}) = -\varepsilon(\boldsymbol{k} + \boldsymbol{Q})$ does not hold. Since the pressure is considered to increase the overlap between the $\pi$-orbitals, and the respective transfer integrals, the $t'_\perp$ grows in importance and thus the nesting property deteriorates. According to the simple model (1.4) $\chi_0(\boldsymbol{Q})$ decreases and this causes a drop of SDW ordering temperature, $T_{SDW}$ ,so that above a critical value of $t'^*_\perp$ the $T_{SDW}$ is totally suppressed [31].

In an isobaric experiment on $(TMTSF)_2PF_6$ in the pressure range above $p_c \approx 9 - 10$ kbar, decreasing temperature leads to the observation of a metal-to-SC transition below $T_c = 1.2$ K [2].

The observation of the Meissner flux expulsion and of specific heat anomaly are consistent with bulk superconductivity [69]. The generic temperature-pressure phase diagram is illustrated in figure 1.6.

Substituting anion $PF_6$ with non-centrosymmetric anion $ClO_4$, led to the first organic superconductor $(TMTSF)_2ClO_4$, at ambient pressure which can be regarded as a chemical pressure effect [42]. The symmetry of the superconducting order parameter in these materials is still a controversial issue. The strong suppression of $T_c$ due to nonmagnetic impurities in studies made in the 1980s [74, 75, 41, 76] and more recently [77, 78] could point toward the existence of non $s$-wave unconventional SC pairing with a gap that changes sign over the Fermi surface. However, a singlet $d(g)$-wave symmetry or a triplet $f(p)$-wave symmetry (see figure 1.5) are as many possible order parameters compatible with these observations. The absence of a Hebel-Slichter coherence peak and the power-law behavior in the temperature dependent proton spin-lattice relaxation rate ($1/T_1 \propto T^3$) [79] from $T_c$ down to $\sim T_c/2$ were argued for some nodal structure on the Fermi surface indicative of non s-wave symmetry. The calculations of NMR relaxation rate also indicated that the power law is congruent with the presence of lines of zeroes for the gap [80]. On the contrary, the exponentially vanishing electric thermal conductivity below $T_c$ in $(TMTSF)_2ClO_4$ [81] indicated a finite gap on the Fermi surface. Recent measurements of the specific heat versus temperature in zero magnetic field on the $(TMTSF)_2ClO_4$ compound [7], show a jump at $T_c = 1.2$ K and an electronic specific heat coefficient of value $\gamma_e = 10.6 - 10.8$ mJ/K$^2$mol, obtained by fitting the Sommerfeld-Debye formula to the data, consistent with the earlier work [82] (See figure 1.7). The specific heat jump $\Delta c$ at $T_c$ is found to be near $\gamma_e T_c$, which is smaller than the prediction of BCS theory ($\Delta c/\gamma_e T_c \simeq 1.43$) for $s$-wave superconductivity. This is rather compatible with what is expected from an anisotropic SC gap [59]. Furthermore, as we see in figure 1.7, below $T \sim 0.7$ K, $c_{el}/T$ is essentially linear in a wide temperature interval supporting a nodal structure.

All of the aforementioned experiments involve the orbital symmetry of the pair function and they give no direct information on the spin parity. In 1986, Lebed predicted an induced dimensional crossover in the electron motion from three to two dimensions, upon an applied in-plane ($a$-$b$ plane) magnetic field. For this orientation, the orbital pair breaking for superconductivity is largely suppressed, leading to a divergent upper critical field specifically if it is triplet superconducting [85]. This paved the way towards an extensive study of the superconductivity under the magnetic field. The resistivity measurements by Lee and co-workers, showed that in $(TMTSF)_2PF_6$ superconductivity persists up to four times the so-called Pauli-Clogston limiting field ($\parallel b$-axis) for the suppression of singlet $s$-wave superconductivity [86, 87], $\mu_0 H_p \sim 2$ T (see figure 1.8a). They also illustrated that the low temperature upper critical field increases significantly as the critical pressure is approached from high pressures [83, 88]. The survival of superconductivity beyond 5 T was also observed in $ClO_4$ salt from resistivity and magnetic torque measurements [89, 84, 90] (see figure 1.8b).

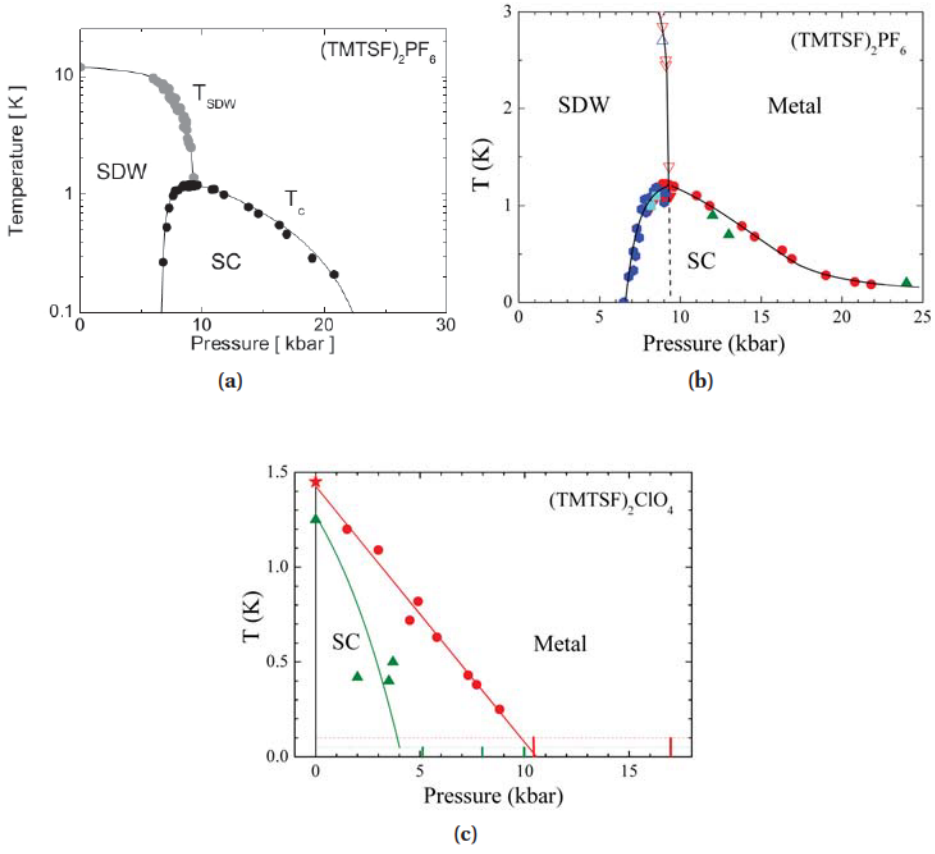


**Figure 1.6** (a) $P-T$ phase diagram of $(TMTSF)_2PF_6$ [20]. (b) Low temperature part of $P-T$ phase diagram of $(TMTSF)_2PF_6$. The data for the coexistence regime below the critical pressure (= 9.4 kbar) are obtained through the resistivity measurements along the *a* crystallographic axis (downward triangles), along the *b*-axis (squares), and along the *c*-axis (hexagons). The full symbols are for SC transition temperature and the empty symbols for the SDW transition temperature [70, 71]. The data above 9.4 kbar are captured by the longitudinal (*a*-axis) resistivity measurements from reference [20] (red circles), and from reference [72] (green triangles). (c) Phase diagram of $(TMTSF)_2ClO_4$ deduced by longitudinal resistivity measurements from [20] (red circles) and from [73] (green triangles).

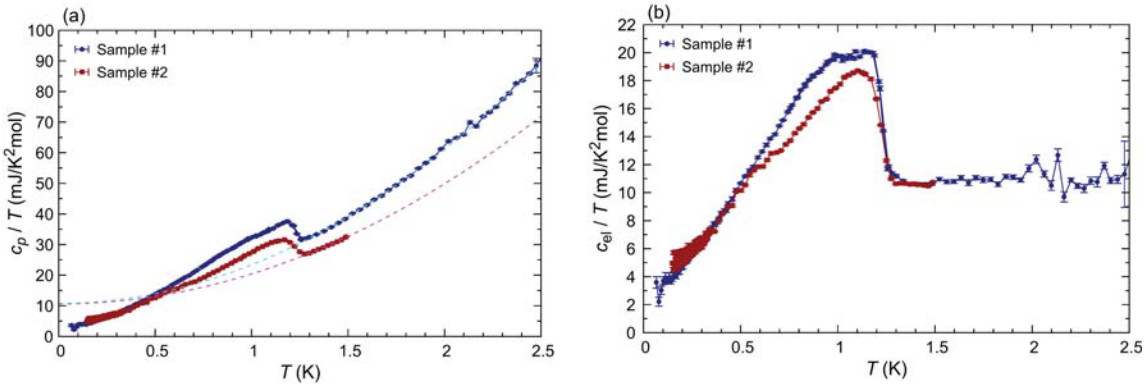


**Figure 1.7** (a) Specific heat versus temperature in $(TMTSF)_2ClO_4$ for two different single crystals presented by sample #1 : 0.257 mg and by sample #2 : 0.364 mg. The dashed curves represent the fittings with the Sommerfeld-Debye formula ($c_p/T = \gamma_e + \beta_p T^2$) to the normal state data above 1.3 K. (b) Electronic specific heat [7].

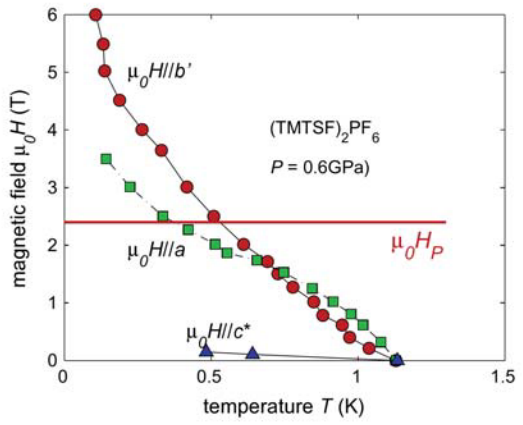


**(a)** Field-tempertaure phase diagram for $(TMTSF)_2PF_6$ [83].

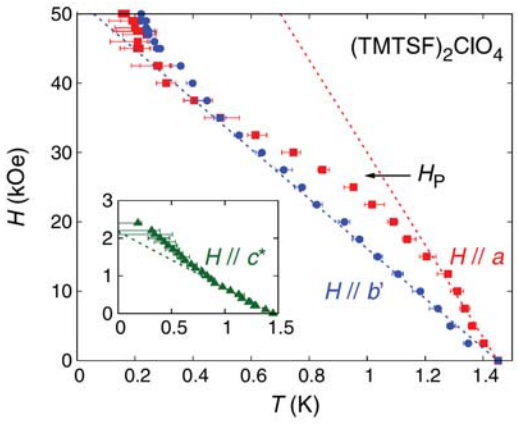


**(b)** Field-tempertaure phase diagram for $(TMTSF)_2ClO_4$ [84]. The dashed lines indicate the zero field slopes of the curves.

**Figure 1.8** Anisotropy of the upper critical field obtained from resistivity measurements. The magnetic field is applied parallel to the conducting $a - b'$ planes and perpendicular to the planes ($c^*$-direction). The orbital destroying effect is weakest when the magnetic field is aligned the $b'$-direction.

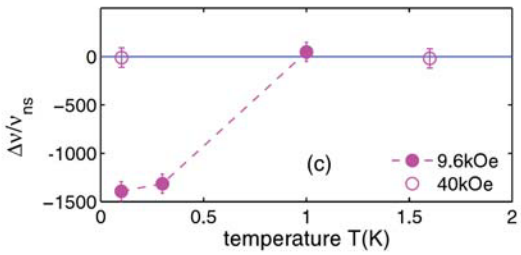


(a) $^{77}$Se NMR Knight shift of $(TMTSF)_2ClO_4$ for magnetic fields parallel to the most conducting $a$-axis [91].

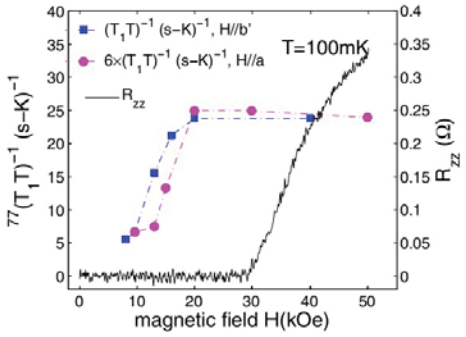


(b) $^{77}$Se relaxation rate of $(TMTSF)_2ClO_4$ versus magnetic field along $a$ and $b'$-directions at $T = 100$ mK. Added, for comparison, the field dependence of inter-plane resistance $R_{zz}$ on the right hand side axis [91].

**Figure 1.9** $^{77}$Se NMR study of $(TMTSF)_2ClO_4$

In $^{77}$Se NMR Knight shift measurements on $(TMTSF)_2ClO_4$ [91], the spin susceptibility was observed to decrease when entering the SC state in low magnetic fields. According to figure 1.9a, in a field value of 0.96 T along the $a$-axis, the relative $^{77}$Se shift decreases upon entering the superconducting sate at $T_c = 1.4$ K, while it does not deviate from the normal state shift at higher magnetic field of 4 T. This invalidates the hypothesis of triplet superconductivity at least in low fields. As illustrated in figure 1.9b, the relaxation rate in the superconducting state of $ClO_4$ salt increases sharply around a field of 2 T and reaches its normal state value [91]. This occurs while the inter-layer resistance shows a non-zero value only above 3 T [91]. It seems that we are dealing with two regimes of magnetic field in the superconducting state: a low-field regime under about $1-2$ T and a high-field regime above this value.

In figure 1.10, the $H(\|\ a)$-$T$ phase diagram for $ClO_4$ compound, established through specific heat measurements, is compared with the one given by resistivity measurements [84, 92]. The zero temperature upper critical field $H_{c2}^{\text{thm}}$ for the thermodynamic measurements is smaller than that of resistivity measurements, $H_{c2}^{\text{resis}}$. It is rather close to the Pauli limit $\mu_0 H_p \sim 2.3-2.6$ T [90], indicating a singlet pairing state at low fields. This is consistent with the decrease in the spin susceptibility mentioned above. This also shows that there is a high-field interval between $H_{c2}^{\text{thm}}$ and $H_{c2}^{\text{resis}}$ where the superconductivity is incomplete or probably fluctuating.

As we have mentioned previously, the extensive study concerning the effect of impurities on superconductivity [93, 78] and zero-field NMR relaxation rate [79] support the change of sign over the Fermi surface and presence of nodes. The possibility of a $d$-wave symmetry pairing mediated by inter-chain antiferromagnetic spin fluctuations has been predicted to occur long-ago from

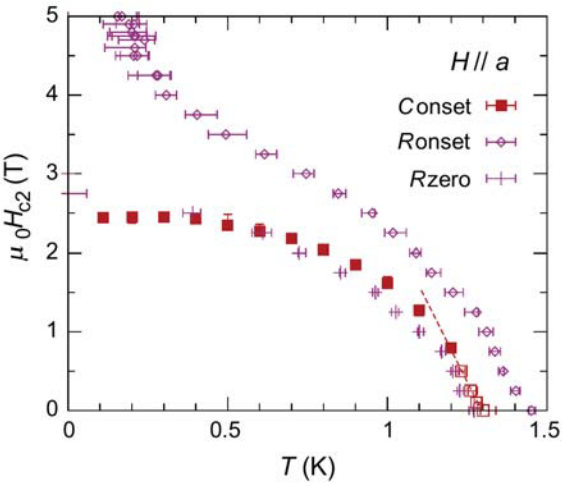


**Figure 1.10** $H-T$ phase diagram obtained through specific heat measurements (solid symbols) and from resistivity measurements (open symbols), as well as the one obtained by determining the temperature at which the resistance along the $c^*$-direction is zero (crosses) [92].

renormalization group calculations in zero field [10, 11]. However, superconductivity and its pairing symmetry in high fields is still under debate. A possible scenario proposed by several theoreticians is a crossover or even a first-order phase transition from a singlet spin $d$-wave symmetry at low fields to an inhomogeneous spin singlet superconducting state, the so-called FFLO state, at high fields [94, 95, 96, 18]. In this superconducting state, the Pauli upper critical field can be pushed to higher values due to the existence of finite momentum Cooper pairs [97, 98]. In another scenario, some have argued a transition from a singlet $d$-wave state to a triplet superconducting state in strong magnetic fields [99, 100, 101, 102].

On the experimental side, to explore more precisely the superconducting pairing symmetry, Yonezawa et al. studied in detail through resistivity measurements the variation of the superconducting onset temperature with the amplitude as well as the direction of in-plane magnetic field [84, 90]. The $H-T$ phase diagrams for field along $a$ and $b'$ directions in figure 1.8b are obtained by additional application of a small magnetic field of $0.05-1$ T along the $c^*$-axis, in order to suppress superconductivity and find the onset temperature. Taking a quick glance at the low-field region of figure 1.8b, we realize that for the field along the three principal axes, the onset curve is linear in temperature. It is consistent with a Ginzburg-Landau model for a type-II superconductor, where only the orbital pair breaking effect is considered. In this case, it is showed that orbital limiting effect is dominant at low fields in all three directions [90]. In figure 1.11 we show the field-angle dependence of the superconducting onset temperature for field oriented in the conducting $a$-$b'$ plane. The magnetic field rotates with the azimuthal angle $\phi$ measured from the $a$-axis. The superconducting onset temperature at low fields is found to have a sharp maximum along the $a$-axis and a broad minimum along the $b$-axis. Increasing the magnetic field, the onset temperature begins decreasing

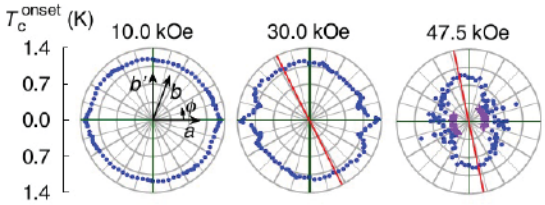


**Figure 1.11** Field-angle ($\phi$) dependence of superconducting onset temperature $T_c^{onset}$. Every polar plot is for a given value of magnetic field and each point represents the direction of magnetic field from the $a$-axis ($\phi = 0$) and the value of $T_c^{onset}$ as the distance from the origin [90].

until around the value of 3 T where it shows dips around $\phi = \pm 17°$. The emerging of the dips is explained as a result of the competition between the field-induced dimensional crossover (FIDC) and the orbital pair breaking effect. On the one hand, moving away from the $a$-axis, the orbital pair breaking effect tries to reduce $T_c$. On the other hand, approaching the $b'$-axis, the FIDC from three to two dimensions causes the quasiparticles to become confined in the conducting plane and as $\phi$ increases, it is detected at the angle where the resistivity along the least conducting $c^*$-axis turns out to be non-metallic in the normal state and therefore $T_c$ begins to increase due to the decrease of super-current flow in the $c^*$-direction. At high magnetic fields, the maximum onset temperature is observed to be along the red color axis $X$ as shown in the figure 1.11. The emergence of another principal axis $X$ in high magnetic fields with $|\phi| > 17°$ indicates an additional spatial symmetry breaking of the superconducting state. An FFLO superconducting state is a plausible explanation for this behavior. In this state, the cooper pairs have a finite momentum ($q_{FFLO}$) due to the nesting of split spin-up and spin-down quasi-1D Fermi surface sheets in the magnetic field. Therefore, there is an additional spatial symmetry breaking and the superconducting order parameter has an oscillating component with the wave vector $q_{FFLO}$ whose direction depends on the field strength. For the high magnetic field values with $|\phi| < 17°$, the principal axis is $a$- axis.

The measurements of the onset temperature versus field on two samples with different scattering relaxation times, have shown that the upturn in the onset curve for fields along the $a$-direction is just observed in the sample with larger relaxation time. It is then speculated that the upturn is due to appearance of a superconducting state in high fields which is very sensitive to impurity scattering but which is robust against the Pauli pair breaking effects. Predicted to be easily suppressed by impurity scattering [103], the existence of a superconducting FFLO state is once more conceivable.

### FFLO state

In a type-II superconductor, the application of a magnetic field can quench superconductivity through two mechanisms. Increasing the magnetic field, the regular array of flux tubes in the from of the Abrikosov vortex lattice begin to overlap and eventually destroy the superconductivity at the upper

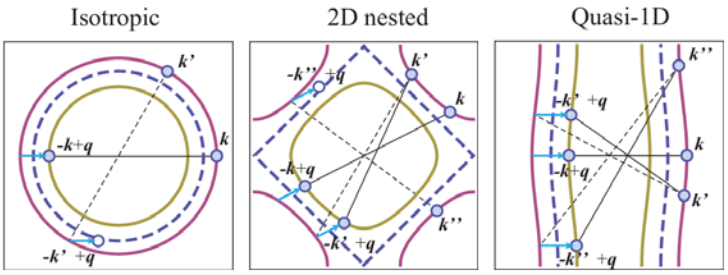


**Figure 1.12** FFLO pairing ($q \neq 0$) possibility in different dimensions. The dashed lines represents the zero field Fermi surface and the full colored lines represent the Zeeman split Fermi surfaces for spin-down and spin-up electrons. For a spherical isotropic Fermi surface, the electron of $-k'$ cannot locate on the spin-down Fermi surface through the transfer of $q$ vector and thus the pair of $(\uparrow k', \downarrow -k' + q)$ cannot be formed. In 2D, the Fermi surface is nested in parts and therefore some pairs like $(\uparrow k', \downarrow -k' + q)$ can be formed but others like $(\uparrow k'', \downarrow -k'' + q)$ cannot. On a quasi-1D Fermi surface almost all pairs can locate on the split Fermi surface [18].

critical field value of $H_{c_2}^{orb} = \Phi_0/2\pi\xi^2$, where $\Phi_0 = h/(2e)$ is the magnetic flux quantum and $\xi$ is the superconducting correlation length [104]. This is the orbital pair breaking effect. The magnetic field can also destroy superconductivity through its interaction with spin degrees of freedom of the conduction electrons, the so-called Zeeman effect. A sufficiently large magnetic field can break the spin-singlet Cooper pairs by flipping one spin of the pair and then polarize the condensed conduction electrons. The superconductivity is then destroyed when the Pauli paramagnetic energy becomes equal to the superconducting condensation energy. The Pauli limiting upper critical field is given by the Clogston-Chandrasekhar limit

$$H_{c_2}^{p} = \sqrt{2}\Delta/g\mu_B, \tag{1.8}$$

where $\Delta$ is the superconducting gap, $g$ is the spectroscopic g-factor, and $\mu_B$ is the Bohr magneton [86, 105]. This mechanism is the Pauli paramagnetic pair breaking effect.

The relative ratio between the two upper critical fields is given by the Maki parameter as $\alpha = \sqrt{2}H_{c_2}^{orb}/H_{c_2}^{p}$ [106]. According to the above expressions for the critical fields and since $\xi \propto E_F/\Delta$, the Maki parameter is proportional to $\Delta/E_F$ where $E_F$ is the Fermi energy. For most superconductors $E_F \gg \Delta$, the Maki parameter is much smaller than unity, and thus the orbital effects are responsible for the destruction of superconductivity. However, the Pauli limited superconductors with large Maki parameter can be realized in materials with heavy electron mass such as heavy fermions or in layered systems like the Bechgaard salts where for field parallel to the layers, the orbital effects can be considerably reduced.

Fulde and Ferrell [97], and Larkin and Ovchinnikov [98] in independent studies suggested that the Pauli upper critical field can exceed its theoretical limit *via* the formation of a novel kind of

pairs where the electrons are formed from the Zeeman split spin-up and spin-down parts of the Fermi surface. In such a case, the electrons pair with a finite total momentum $(\uparrow \boldsymbol{k}, \downarrow -\boldsymbol{k}+\boldsymbol{q})$ where $q \sim 2\mu_B H/\hbar v_F$; this is in contrast with the conventional Cooper pairs $(\uparrow \boldsymbol{k}, \downarrow -\boldsymbol{k})$ of the BCS prediction. The new superconducting state, named the FFLO state, has a lower condensation energy than its BCS counterpart stabilized by the reduction of paramagnetic energy. The FFLO superconducting order parameter develops an oscillatory component in real space. The simplest form of the order parameter proposed by Fulde and Ferrell varying as $\Delta(\mathbf{r}) = \left[\Delta e^{i\boldsymbol{q}\cdot\mathbf{r}} + \Delta^* e^{-i\boldsymbol{q}\cdot\mathbf{r}}\right]$ with a homogeneous amplitude describes the essence of the FFLO state.

In a real type-II superconductor, on one hand, the orbital effects try to organize a vortex lattice and on the other hand, the paramagnetic effects favor a periodic FFLO structure. The survival of a FFLO phase in this competition depends on the characteristics of the system under study, such as gap symmetry, its dimensionality, and the specific experimental conditions [107]. The FFLO sate is more stable when a large part of the split Fermi surfaces of spin up and spin down are connected by the $\boldsymbol{q}$ vector. This is the reminiscent of the nesting effect of CDW and SDW transitions. As shown in figure 1.12 for a 3D system with spherical Fermi surface, for many pairs of points $(\uparrow \boldsymbol{k}', \downarrow -\boldsymbol{k}'+\boldsymbol{q})$, both the electrons of the pair cannot be located on the split Fermi surfaces. In other words, the spin-up and spin-down Fermi surfaces touch only at one point by a transfer of $\boldsymbol{q}$ [107, 108]. In a 2D system, the two cylindrical Fermi surfaces touch on a line by a single shift of $\boldsymbol{q}$ vector and therefore more pairs can locate on the split Fermi surface. In the case of a quasi-1D Fermi surface, almost all the pairs of finite momentum $\boldsymbol{q}$ can locate on the Fermi surface and the Fermi surfaces touch on more lines by the $\boldsymbol{q}$ transformation, see figure 1.12. Moreover, it has been pointed out in the case of an anisotropic SC gap function, the FFLO sate is more robust compared to an isotropic $s$-wave gap through optimization of the $\boldsymbol{q}$ vector [107]. The stability of the FFLO state can further be compromised in superconductors in the clean limit where the electron mean free path is much larger than the SC coherence length, and this is because the FFLO state is strongly unstable against nonmagnetic impurities [109, 107].

To sum up, it seems that FFLO state is more likely to occur in clean unconventional superconductors. In spite of the fact that FFLO state was predicted nearly fifty years ago, its experimental realization remains still evasive. Nonetheless, several materials have been discovered in recent years that fulfill the extreme conditions for the formation of the FFLO state. Heavy fermions [110, 111, 112] and layered organic superconductor [113, 114, 115] are considered as possible candidates which meet the expectations due to their large Maki parameters, very large mean free paths, and unconventional pairing symmetries.

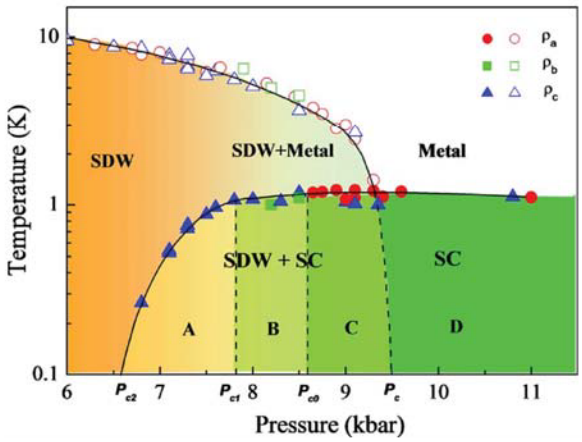


**Figure 1.13** Intricate phase diagram of $(TMTSF)_2PF_6$ obtained from resistivity measurements in the coexistence regime [71].

### SC-SDW boundary region of the phase diagram

One of the intriguing features of the phase diagram 1.6 which is not the main concern of the present work, but which is worth noting, is the meeting of SDW and superconductivity. The first experimental investigations of superconductivity under pressure in $(TMTSF)_2PF_6$ have noticed a metal to SDW and SDW to SC transition in a narrow pressure interval around the SDW-SC boundary [116]. Same phase diagram investigation of analogous compound $(TMTSF)_2AsF_6$ has led to similar observations [117]. Such a coexistence is also observed in $(TMTSF)_2ClO_4$, when $ClO_4$ anion disorder is tuned by the cooling rate [118].

Simultaneous NMR and resistivity measurements in this pressure interval suggest a second-order metal to SDW phase transition line and a first-order SDW to SC phase transition line merging at a tricritical point below which there is a coexistence of spatially separated regions of SDW and metal(SC) order [119]. The phase diagram of figure 1.13 shows this SDW/SC (metal) coexistence region between $6.6 - 9.4$ kbar which is derived from resistivity measurements along the three crystallographic axes. In the part of the phase diagram marked as A, only the resistivity along the $c^*$-axis shows a partial superconducting drop at about 1 K while along the two other directions the resistivity stays insulating [120]. In part B, both $b$ and $c^*$-axis resistivities show a superconducting transition with the resistivity drop along $b$-axis that is milder than for $c^*$, and this is while the $a$-axis resistivity is still insulating. In phase C, both $b$ and $c^*$-axis resistivities sharply decrease at $T_c$. The longitudinal resistivity now shows a similar drop as the $b$-axis resistivity behavior in Part B. Finally, above 9.4 kbar we have an homogeneous superconductor. This confirms the existence of 2D domains of metal in the SDW region which develop perpendicular to the most conducting $a$-axis [71]. More Recently, the simulations measurement of magnetoresistance and thermometric power along the three crystal axis of $(TMTSF)_2PF_6$ confirmed the existence of macroscopic domains of metallic

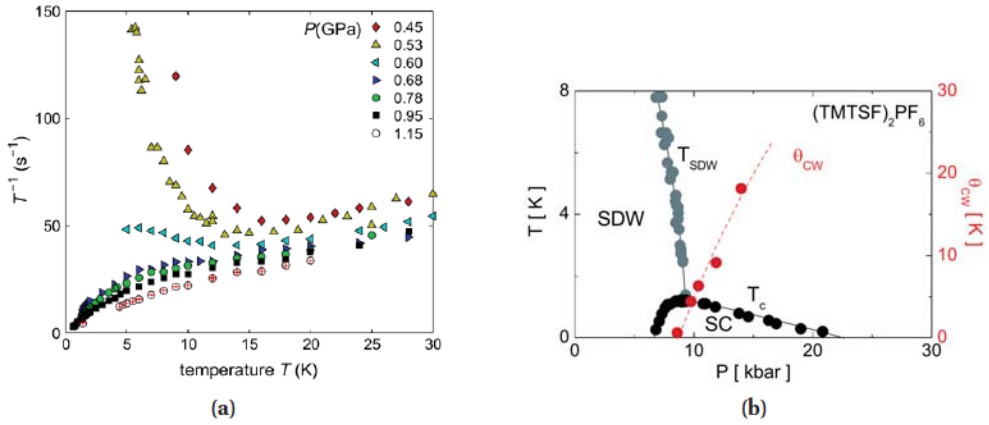


**Figure 1.14** (a) $^{77}$Se NMR spin lattice relaxation rate versus temperature, for applied pressures greater than and less than the critical pressure $P_c = 0.6$ GPa [121]. (b) $P$-$T$ phase diagram of $(TMTSF)_2PF_6$ to which added the variation of Curie-Weiss scale $\Theta$ with pressure obtained from the NMR data in (a) [19].

and SDW phase. Furthermore, it is suggested that the metallic domains in the coexistence regime and those of the high pressure metallic phase have the same properties [120].

### The normal state: AF fluctuations, quantum criticality, and transport

The study of the normal state at low temperature, in the vicinity of phase transitions has revealed key information for the description of unconventional nature of the superconducting state. Of special interest are the results of the $^{77}$Se nuclear spin lattice relaxation rate of $(TMTSF)_2PF_6$ [121, 122]. Figure 1.14a shows the temperature dependence of $T_1^{-1}$ versus $T$ for a range of pressures. At low pressures upon approaching the SDW ordering temperature, $T_1^{-1}$ diverges due to the long-range SDW correlations. Near the critical pressure $P_c = 0.6$ GPa [2], there is no divergence yet the relaxation rate is enhanced compared to the expectation based on the Korringa law $T_1^{-1} \propto T$, that normally holds for a normal Fermi liquid. More interestingly, the Korringa relation is re-established at sufficiently high pressures where $T_c \to 0$ and $[T_1T]^{-1} \to$ constant [123]. The temperature profile of relaxation data at pressures close to $P_c$ is turned out to be well described by the Curie-Weiss (CW) relation $T_1T \sim T + \Theta$ with $\Theta$ as the Curie-Weiss energy scale for SDW spin fluctuations. $\Theta$ shows a quantum critical behavior near $P_c$, namely $\Theta \sim (P - P_c)^{\eta}, \eta = 1$ [124, 91]. The low energy spin fluctuations are regarded as the underlying source of scattering and the abnormal behavior in the relaxation rate which are well captured by $[T_1T]^{-1} \sim \chi(Q)$ at the SDW wave vector $Q$ with $\chi(Q)^{-1} \sim T + \Theta$ [125, 126, 10].

Through comprehensive study of longitudinal resistivity [19, 20], a $T$-linear temperature depen-

[2] The value of critical pressure is different in different experimental groups depending on the probe used.

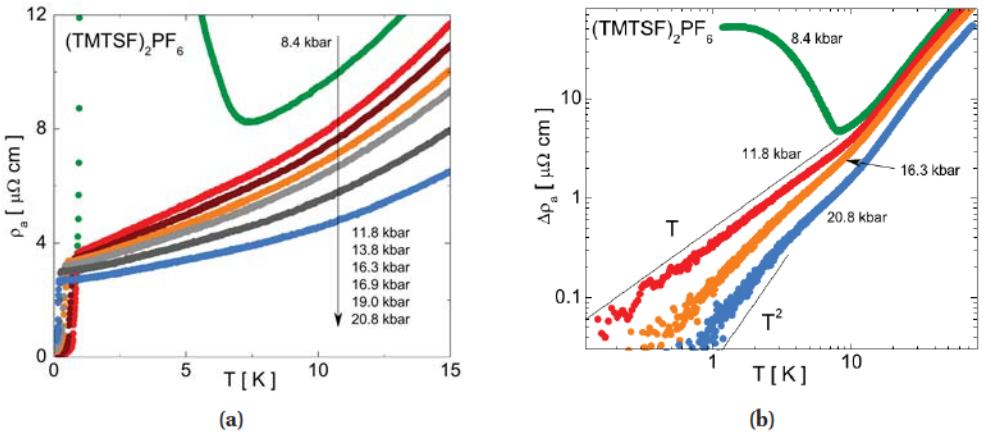


**Figure 1.15** (a) Longitudinal electrical resistivity of $(TMTSF)_2PF_6$ as a function of temperature at various pressures greater and smaller than the critical pressure $P_c \sim 11.8$ Kbar. (b) The log-log plot of the inelastic part of the data $\Delta\rho_a(T) = \rho_a(T) - \rho_0$ [19].

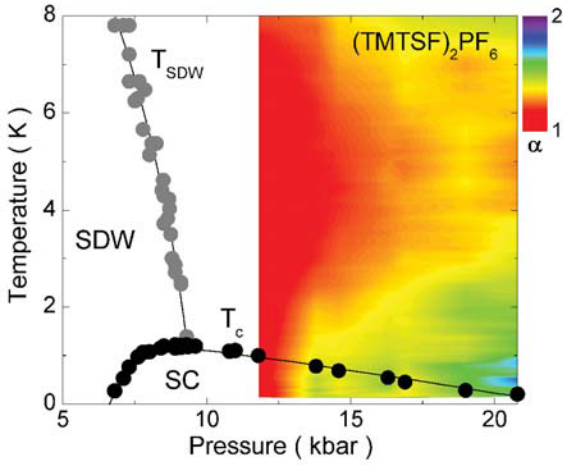


**Figure 1.16** The variation of resistivity exponent $\alpha$ with pressure and temperature.

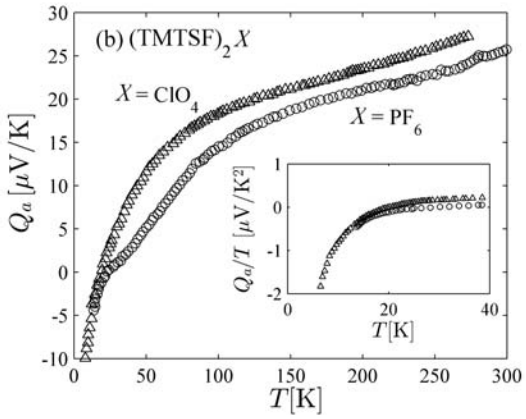


**Figure 1.17** Ambient pressure longitudinal Seebeck coefficient versus temperature [21].

dent resistivity of the form $\rho(T) = \rho_0 + AT$ was found near the critical pressure (11.8 kbar) down to $T_c$. $\rho_0$ is the residual resistivity and $A > 0$ (see figure 1.15). At very high pressures, the resistivity shows a certain curvature compatible with the polynomial of the form $\rho(T) = \rho_0 + AT + BT^2$. The linear-$T$ coefficient $A$ is found to be strongly correlated with the size of the superconducting transition temperature $T_c$ whereas the Fermi-liquid coefficient $B$ first grows with pressure and finally decreases monotonically. Another way to illustrate the change of regime in the resistivity data is to express resistivity in a form of a power law temperature dependence as $\Delta\rho(T) = \rho(T) - \rho_0 \sim T^\alpha$. Figure 1.16 shows the temperature and pressure dependence of the resistivity exponent $\alpha$ which captures an extended quantum criticality in which the resistivity is linear around critical pressure following an unconventional area where the exponent is between 1 and 2. The Fermi-liquid temperature behavior appears only at sufficiently high value of pressure and low value of $T_c$. These observations go hand in hand with those of relaxation rate. Therefore, superconducting pairing is associated with antiferromagnetic spin fluctuations.

Another probe that can be sensitive to fluctuations near quantum critical part is the thermoelectric power or the Seebeck coefficient ($Q$). In ordinary metals, it is expected to display a linear temperature-dependence for temperature low compared to the Fermi temperature, with a magnitude much smaller than the fundamental unit of Seebeck coefficient: $\frac{k_B}{|e|} \approx 86\mu$V/K [127, 128, 129]. Furthermore, the sign of $Q$ in ordinary metals is expected to reflect the nature of carriers (electrons or holes). However, experiments probing the thermoelectric response in correlated systems where Coulomb interactions plays a dominant role, may display a highly non-monotonic temperature dependence for reasonably low temperatures. Values of $Q$ may be significantly larger than $k_B/|e|$, and one can observe sign reversal whose origin is unclear [129].

The temperature dependence of the Seebeck coefficient in Bechgaard salts and their sulfur

base analogues, Fabre salts, can be used as a probe of deviations from the Fermi-liquid picture. Figure 1.17 shows the most recent experiments on the ambient pressure temperature dependence of the longitudinal thermoelectric response ($Q_a$) of $(TMTSF)_2X$ (X = $PF_6$ and $ClO_4$) from room temperature down to low temperature [21]. It is clear that the high temperature dependence of the two salts deviates from the perfect linearity expected for a free electron system. This indicates some enhancement suggesting possible corrections to the linear band or thermodynamic term. A positive Seebeck coefficient at high temperature is consistent with hole carriers. Below $T = 100 - 140$ K the Seebeck coefficient decreases more rapidly with $T$ and changes sign at $T_0 = 18.5$K for $ClO_4$ and $T_0 = 25$ K for $PF_6$. The $T_0$ value for the sign reversal is observed to vary for different authors in the case of $PF_6$ and $ClO_4$ compound [130]. The deviations from the Fermi-liquid behavior, and in particular the sign reversal have not been examined from a theoretical point of view so far.

Chapter 2

# Renormalization group approach to the electron gas model in the presence of magnetic field

In this chapter we introduce the renormalization group method for the quasi-one-dimensional electron gas model. The method is developed to study possible unconventional phases of the model when a magnetic field is Zeeman coupled to the spin degrees of freedom.

## 2.1 Main instabilities of the electron gas

In this section we will outline the main ideas underlying the renormalization group method utility for one-dimensional electron gas systems. In 1D systems, strong fluctuations prevent any long range order at finite temperature. Let us consider a 1D non-interacting electron gas at low enough energy so that the energy spectrum can be linearized with respect to the Fermi points at $\pm k_F$, as

$$\varepsilon_p(k) = v_F(pk - k_F). \tag{2.1}$$

Here $p = \pm 1$ refers to the right $(+)$ and the left $(-)$ going electrons and $v_F$ is the Fermi velocity. The model shows up two infrared singularities in pair susceptibilities $\chi^0$ in response to either an

electron-hole field (Peierls) at the wave vector $2k_F$ or to a electron-electron (Cooper) field at zero momentum. In the static limit and at low temperatures, these are of the form [4]

$$\left.\begin{matrix}\chi^0(q=2k_F,T)\\ \chi^0(q=0,T)\end{matrix}\right\} = 2N(E_F)\int_T^{E_F}\frac{dE}{\varepsilon_+(k)-m\varepsilon_-(mk-q)} = N(E_F)\ln(\frac{E_F}{T}). \tag{2.2}$$

Both susceptibilities then present a logarithmic singularity as the temperature $T$ ($k_B=1$) goes to zero. The similar and simultaneous logarithmic singularities are a peculiarity of a 1D electron gas. For the same electron states, the singularities result from the symmetry properties of the energy spectrum, namely the time inversion symmetry ($\varepsilon_+(k)=\varepsilon_-(-k)$) with $m=-1$ in the evaluation of Cooper susceptibility at $q=0$ and the particle-hole symmetry ($\varepsilon_+(k)=-\varepsilon_-(k-2k_F)$) -called nesting- with $m=1$ in the evaluation of Peierls response function at $q=2k_F$. Since each part of the integral (2.2) inside the energy interval between $T$ and $E_F$ for the two pair correlations gives similar logarithmic contributions as $\ln\frac{E_F}{T}=\ln(\frac{E_F}{E_1}\frac{E_1}{E_2}\cdots\frac{E_n}{T})=\ln\frac{E_F}{E_1}+\ln\frac{E_1}{E_2}+\cdots+\ln\frac{E_n}{T}$, there is the lack of characteristic energy scale in this energy interval, and this indicates the existence of scaling, an essential ingredient behind renormalization.

In the presence of non-negligible interactions between electrons in one spatial dimension, the logarithmic singularity of both pair correlations and the absence of energy scale will carry over up to the highest energy, namely the cut-off, $E_F$ at the band edge. As a result, the perturbation theory faces with a problem of infinite coupled energy scales. The renormalization group theory, as a perturbation method, allows us to tackle this problem by the successive summation, order by order, of the logarithmic contributions.

## 2.2 Quasi-one-dimensional electron gas model

We now consider an electron gas on a linear array of $N_P$ weakly coupling chains of length $L$ with the chain lattice constant $a$ and the inter-chain distance $d_\perp$, which are both put equal to unity in this chapter. As it was explained in the previous chapter, equation (1.7), in the simplest form of tight-binding approximation, the energy-dispersion relationship takes the following form

$$\varepsilon_p(k)=\hbar v_F(pk-k_F)-2t_\perp\cos(k_\perp)-2t'_\perp\cos(2k_\perp), \tag{2.3}$$

where we have replaced for simplicity $k_a=k$, $k_{\perp b}=k_\perp$, and $t_{\perp b}=t_\perp$. As in the purely 1D case, $p=\pm1$ refers to right (+) and left (−) going electrons. The Bechgaard salt compounds have the following anisotropic sequence of hopping integrals $t_a\gg t_b\gg t_c$ along the $a$-, $b$-, and $c$-axis. As a consequence of this anisotropy, when a magnetic field is applied in the $a$-$b$ conducting plane of the

systems like $(TMTSF)_2X$, the orbital movement of the screening currents which by the Meissner effect excludes the external field, is negligible along the $c$-axis. In this way, the coupling to the magnetic field reduces to the Zeeman term. Thus, in this case the relevant electron spectrum becomes

$$\varepsilon_{p,\sigma}(\boldsymbol{k}) = v_F(pk - k_F) - 2t_\perp \cos(k_\perp) - 2t'_\perp \cos(2k_\perp) - \mu_B \sigma H, \tag{2.4}$$

where $\mu_B$ is the Bohr magneton. In what follows, we use $\mu_B H = h$. The non-interacting Hamiltonian $H_0$ in second quantification is written as

$$H_0 = \sum_{k,\sigma} \varepsilon_{p,\sigma}(\boldsymbol{k}) a^\dagger_{pk\sigma} a_{pk\sigma}, \tag{2.5}$$

where $a^{(\dagger)}_{pk\sigma}$ is the annihilation (creation) operator of a particle of spin $\sigma$ in the momentum state $\boldsymbol{k}$ on the left ($p = -$) or on the right ($p = +$) Fermi sheet.

**Interactions**

In the weak coupling limit, the interactions between electrons on the opposite sheets of the Fermi surface $\boldsymbol{k}_F^P(k_\perp) = (k_F^P(k_\perp), k_\perp)$ (parametrized by $k_\perp$ through the condition $\varepsilon_p(\boldsymbol{k}_F^P) = 0$) are added as a perturbation to the non-interacting quasi-1D gas. These interactions are expressed in terms of two-particle coupling constants in the $g$-ology model. Therefore, the interacting part of the Hamiltonian can be written as the following

$$\begin{aligned} H_I = \frac{1}{LN_P} \sum_{\{k,\sigma\}} \Big\{ & g_{\{\sigma\}}(\boldsymbol{k}^+_{F,1}, \boldsymbol{k}^-_{F,2}, \boldsymbol{k}^+_{F,3}) a_{+k_1\sigma_1} a_{-k_2\sigma_2} a^\dagger_{+k_3\sigma_3} a^\dagger_{-k_4\sigma_4} \delta_{k_1+k_2,k_3+k_4} \\ & + \Big[\frac{1}{2} g_{3\perp}(\boldsymbol{k}^+_{F,1}, \boldsymbol{k}^+_{F,2}, \boldsymbol{k}^-_{F,3}) a_{+k_1\sigma_1} a_{+k_2\sigma_2} a^\dagger_{-k_4\sigma_4} a^\dagger_{-k_3\sigma_3} \\ & \times \delta_{k_1+k_2,k_3+k_4+G} \delta_{\sigma_1,\sigma_4} \delta_{\sigma_2,\sigma_3} \delta_{\sigma_1,-\sigma_2} + \text{c.c} \Big] \Big\}, \end{aligned} \tag{2.6}$$

with

$$g_{\{\sigma\}} = \big[(g_{1\parallel}\delta_{\sigma_1,\sigma_4}\delta_{\sigma_2,\sigma_3} - g_{2\parallel}\delta_{\sigma_2,\sigma_4}\delta_{\sigma_1,\sigma_3})\delta_{\sigma_1,\sigma_2} + (g_{1\perp}\delta_{\sigma_1,\sigma_4}\delta_{\sigma_2,\sigma_3} - g_{2\perp}\delta_{\sigma_2,\sigma_4}\delta_{\sigma_1,\sigma_3})\delta_{\sigma_1,-\sigma_2}\big],$$

as the normal bare interactions. Here, the $\parallel$ ($\perp$) subscripts refer to the scattering processes between the electrons with spins parallel and opposite, respectively; thus become distinguishable in the presence of Zeeman magnetic field. As for the normal bare interactions, $g_1$ is the backward scattering for which the electrons on different parts of the Fermi surface are scattered and exchange their places so that every electron transfer a momentum of the order of $2k_F$, while the total transferred momentum is zero; $g_2$ is the forward scattering in which each electron remains on the same side of the Fermi surface after the scattering and therefore the transferred momentum is small. $g_3$ is

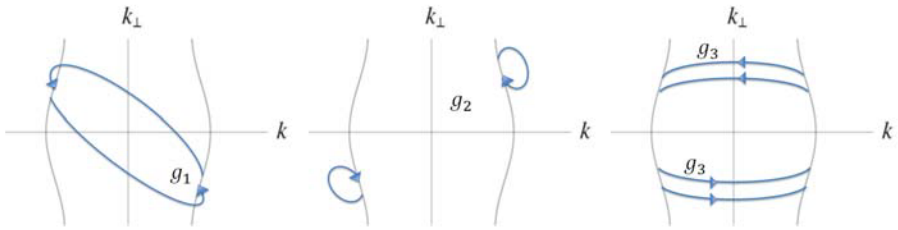


**Figure 2.1** Decomposition of two-electron interactions on a quasi-1D Fermi surface according to the $g$-ology model.

the umklapp scattering which is present due to a small dimerization gap in the band structure of $(TMTSF)_2X$ that makes the conduction band effectively half-filled. This scattering amplitude contains the total momentum transfer of $G = 4k_F$, which is equal to a vector of the reciprocal lattice in the case of half-filling. The different types of scattering on the quasi-1D Fermi surface are shown in figure 2.1.

It should be noted that because of the Pauli exclusion principle, the umklapp scattering can just couple the electrons of opposite spins. Moreover, at first glance, we realize that the $g_{1\perp}$ process transfers a net spin since it permutes two electrons of opposite spin from one side of the Fermi surface to the other side while the $g_{3\perp}$ transfers a net charge due to the transfer of two electrons of opposite spins together.

### 2.2.1 Partition function

The thermodynamic properties of a system of weakly interacting electrons with $H = H_0 + H_I$ can be obtained from the partition function $z$. In the grand canonical ensemble, it can be expressed as a functional integral over the anticommuting Grassman variables $\psi$'s [131]

$$Z = Tr(e^{-\beta\hat{H}}) = \int\int \mathfrak{D}\psi^*\mathfrak{D}\psi \; e^{S_0[\psi^*,\psi]+S_I[\psi^*,\psi]}, \tag{2.7}$$

where $\mathfrak{D}\psi^*\mathfrak{D}\psi = \prod_{p,\sigma,\bar{k}} d\psi^*_{p,\sigma}(\bar{k})d\psi_{p,\sigma}(\bar{k})$, $\bar{k} = (k, \omega_m)$, $k = (k, k_\perp)$, and $\omega_m = (2n+1)\pi T = \pm\pi T, \pm 3\pi T, \cdots$ are the fermion Matsubara frequencies. The Grassmann variables $\psi$'s are the eigenvalues of the fermion operators $a$'s acting on coherent states of fermions. The action $S$ contains a non-interacting ($S_0$) and an interacting ($S_I$) parts. The former is given by

$$S_0[\psi^*, \psi] = \sum_{p,\bar{k},\sigma} \psi^*_{p,\sigma}(\bar{k})[G^0_p(\bar{k})]^{-1}\psi_{p,\sigma}(\bar{k}), \tag{2.8}$$

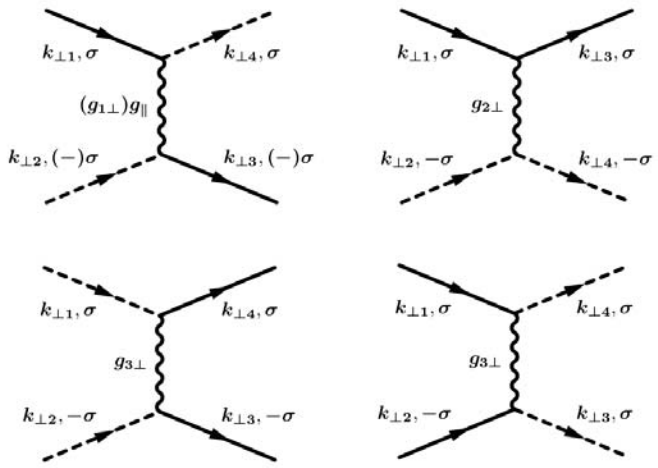


**Figure 2.2** Diagrams of possible scattering processes of the quasi-1D electron gas model: backward scattering between electrons of spins opposite (parallel) $g_{1\perp(\parallel)}$, forward scattering $g_{2\perp}$ with anti-parallel spins, and umklapp scattering for opposite spins $g_{3\perp}$. The continuous (dashed) lines refer to $p = +(-)$ electrons. The open (full) red square represents the generic vertex part for the normal (backward and forward) and umklapp scattering amplitudes.

where

$$G_p^0(\bar{k}) = [i\omega_m - \varepsilon_{p,\sigma}(k)]^{-1}, \tag{2.9}$$

is the free fermion propagator in the Fourier-Matsubara space.

The interacting part of the action in the presence of magnetic field takes the following form

$$\begin{aligned}
S_I[\psi,\psi^*] = {} & \pi v_F \frac{T}{LN_P}\sum_{\bar{k},\sigma} g_{\parallel}(k_{\perp 1},k_{\perp 2},k_{\perp 3})\psi_{+,\sigma}(\bar{k}_1)\psi_{-,\sigma}(\bar{k}_2)\psi^*_{+,\sigma}(\bar{k}_3)\psi^*_{-,\sigma}(\bar{k}_4)\delta_{\bar{k}_1+\bar{k}_2,\bar{k}_3+\bar{k}_4} \\
& + \pi v_F \frac{T}{LN_P}\sum_{\bar{k},\sigma} g_{1\perp}(k_{\perp 1},k_{\perp 2},k_{\perp 3})\psi_{+,\sigma}(\bar{k}_1)\psi_{-,-\sigma}(\bar{k}_2)\psi^*_{+,-\sigma}(\bar{k}_3)\psi^*_{-,\sigma}(\bar{k}_4)\delta_{\bar{k}_1+\bar{k}_2,\bar{k}_3+\bar{k}_4} \\
& + \pi v_F \frac{T}{LN_P}\sum_{\bar{k},\sigma} g_{2\perp}(k_{\perp 1},k_{\perp 2},k_{\perp 3})\psi_{+,\sigma}(\bar{k}_1)\psi_{-,-\sigma}(\bar{k}_2)\psi^*_{-,-\sigma}(\bar{k}_4)\psi^*_{+,\sigma}(\bar{k}_3)\delta_{\bar{k}_1+\bar{k}_2,\bar{k}_3+\bar{k}_4} \\
& + \pi v_F \frac{T}{2LN_P}\sum_{\bar{k},\sigma} g_{3\perp}(k_{\perp 1},k_{\perp 2},k_{\perp 3})\big[\psi_{+,\sigma}(\bar{k}_1)\psi_{+,-\sigma}(\bar{k}_2)\psi^*_{-,\sigma}(\bar{k}_4)\psi^*_{-,-\sigma}(\bar{k}_3) \\
& \times \delta_{\bar{k}_1+\bar{k}_2,\bar{k}_3+\bar{k}_4+\bar{G}} + \text{c.c}\big].
\end{aligned} \tag{2.10}$$

Here, all the four interaction amplitudes are dimensionless and normalized by $\hbar\pi v_F$. For simplicity, the coupling constants are represented by three transverse momentum variables. The fourth variable is determined by the momentum conservation $k_{\perp 4} = k_{\perp 1} + k_{\perp 2} - k_{\perp 3}$. $\bar{G} = (4k_F, 0, 0)$

is the longitudinal reciprocal lattice vector. In addition, $g_{\parallel} = g_{1\parallel} - g_{2\parallel}$ since the two $g_{1\parallel}$ and $g_{2\parallel}$ processes are the same by the permutation of a fermion line. The scattering processes are illustrated diagrammatically in figure 2.2. It is important noting that the scattering amplitudes are independent of momentum at the bare level but they will develop momentum dependence through the RG transformation. For our calculations their bare range of values can be determined from experiments and band calculations. Since the backward scattering coupling ($g_{\parallel(1\perp)}$) governs the spin degrees of freedom [132], we refer to the experiments on Bechgaard salts showing an enhancement of the static spin susceptibility from its non-interacting band value at low temperature [133, 134, 135]. This delimits the values in the interval $g_1 \simeq [0.3, 0.5]$. The forward scattering bare amplitude $g_2$ can be set by the values for which the SDW transition temperature falls in the range of observed values $10 - 20$ K leading to the values in the interval $[0.5, 0.7]$. In the case of weakly dimerized chains due to the modulation of the electron transfer integral along the chains, the umklapp scattering is proportional to the small dimerization gap $\Delta_D$ through $g_3 \approx g_1 \frac{\Delta_D}{E_F}$ [44, 136]. The estimated values of $g_3$ umklapp scattering falls within the interval $[0.02, 0.04]$.

## 2.3 Renormalization group method

The renormalization group transformation consists in carrying out successive partial traces of high energy electronic degrees of freedom in the partition function $z$ in (2.7). In the transformation, it is essential to fix an initial energy cut-off, $\Lambda_0 = \hbar v_F k_F$, above and below the quasi-1D Fermi sheets, which fixes the range of $k$ in $\varepsilon_p(k)$ with a bandwidth of $2\Lambda_0$. The calculation of partial trace is carried out by taking infinitesimal steps at energy distance $\Lambda$ from the Fermi surface, which is determined by the continuous RG flow parameter $\ell$, defined as $\Lambda \equiv \Lambda(\ell) = \Lambda_0 e^{-\ell}$. This is done in such a way that the degrees of freedom in the outer high energy shells of thickness $\Lambda d\ell$ are integrated successively. The repetitive partial trace leads to the transformation or renormalization of the action from its bare expression $S_{\Lambda_0}$, defined at the initial energy cut-off $\Lambda_0$, to $S_\Lambda$ at step $\Lambda(\ell)$.

Explicitly, in the expression (2.10), all summations over momentum are decomposed into outer $\{k\}'$ and inner $\{k\}_<$ shell variables

$$\sum_{\{k\}} = \sum_{\{k\}_<} + \sum_{\{k\}'}.$$

This allows us to write

$$S[\psi^*, \psi]_\ell = S[\psi^*_<, \psi_<]_\ell + S[\psi^*_<, \psi_<, \bar{\psi}^*, \bar{\psi}],$$

where $S[\psi^*_<, \psi_<]_\ell$ refers to the action containing all $\psi$'s in the inner shell at the step $\ell$, and $S[\psi^*_<, \psi_<, \bar{\psi}^*, \bar{\psi}]$ is the action with all possible combinations of $\bar{\psi}$'s in the outer shell.

In the Kadanoff-Wilson (KW) RG scheme, the transformation of the action from $\ell$ to $\ell + d\ell$ keeps the partition function invariant so that the partial trace integration over the $\psi$'s leads to

$$\begin{aligned} Z &= e^{A(\ell)} \int\int_< \mathfrak{D}\psi^* \mathfrak{D}\psi e^{S[\psi_<, \psi^*_<]_\ell} \int\int \mathfrak{D}\bar{\psi}^* \mathfrak{D}\bar{\psi} e^{S[\psi^*_<, \psi_<, \bar{\psi}^*, \bar{\psi}]} \\ &= e^{A(\ell+d\ell)} \int\int_< \mathfrak{D}\psi^* \mathfrak{D}\psi e^{S[\psi_<, \psi^*_<]_{\ell+d\ell}}, \end{aligned} \tag{2.11}$$

where $S[\psi_<, \psi^*_<]_{\ell+d\ell}$ is the renormalized action at the step $\ell + d\ell$. This reduced partition function describes the same low-energy physics as the original partition function. Here $A(\ell)$ corresponds to the free energy density at step $\ell$.

More explicitly, the partial trace of $\bar{\psi}$'s in the energy shell $\Lambda(\ell)d\ell$ proceeds from the decomposition of $S[\psi^*_<, \psi_<, \bar{\psi}^*, \bar{\psi}]$, which can be written as

$$S[\psi^*_<, \psi_<, \bar{\psi}^*, \bar{\psi}] = S_0[\bar{\psi}^*, \bar{\psi}] + \sum_{i=1}^{4} S_{I,i}[\psi^*_<, \psi_<, \bar{\psi}^*, \bar{\psi}]. \tag{2.12}$$

It consists a free part with both $\bar{\psi}$'s in the outer shell and an interacting part having $i$ fields $\bar{\psi}$'s in the outer momentum shell. Making use of the linked cluster theorem [132], the outer shell integration becomes

$$\begin{aligned} Z &= e^{A(\ell)} \int\int_< \mathfrak{D}\psi^* \mathfrak{D}\psi e^{S[\psi, \psi^*]_<} \int\int \mathfrak{D}\psi^* \mathfrak{D}\psi e^{S_0[\bar{\psi}^*, \bar{\psi}]} \exp\Big\{ \sum_{i=1}^{4} S_{I,i}[\psi^*_<, \psi_<, \bar{\psi}^*, \bar{\psi}] \Big\} \\ &= e^{A(\ell) + \ln z_{o,d\ell}} \int\int \mathfrak{D}\bar{\psi}^* \mathfrak{D}\bar{\psi} \exp\Big\{ S[\psi, \psi^*]_< + \sum_{n=1}^{\infty} 1/n! \langle \Big( \sum_i S_{I,i}[\psi^*_<, \psi_<, \bar{\psi}^*, \bar{\psi}] \Big)^n \rangle_{\bar{o},c} \Big\}, \end{aligned} \tag{2.13}$$

where the non-interacting averages in the outer shell are

$$\langle \cdots \rangle_{\bar{o},c} = z_{\bar{o}}^{-1} \int\int \mathfrak{D}\bar{\psi}^* \mathfrak{D}\bar{\psi} (\cdots) e^{S_0[\bar{\psi}^*, \bar{\psi}]}, \tag{2.14}$$

and the outer shell free partition function is

$$z_{\bar{0}} = \int\int \mathfrak{D}\bar{\psi}^* \mathfrak{D}\bar{\psi} e^{S_0[\bar{\psi}^*, \bar{\psi}]}. \tag{2.15}$$

### 2.3.1 Renormalization of the coupling constants

The partial integration can be most easily performed with the aid of diagrams. The renormalization of backward, forward, and umklapp scattering amplitudes as the two-particle interactions at the one-loop level comes from the $n = 2$ outer shell averages $\frac{1}{2}\langle (S_{I,2})^2 \rangle$ in (2.13). In $S_{I,2}$ there are three terms corresponding to putting two particles or two holes in the outer momentum shell (the Cooper channel), one particle and one hole on opposite branches (the Peierls channel), and putting a particle and a hole on the same branch (the Landau channel). There is a delicate point that must be taken into consideration in calculating these diagrams. In fact, in presence of a quasi-one-dimensional Fermi surface, there are many two-particle interaction processes for which only one fermion line belongs to the outer energy shell while the other refers to previous contraction steps at higher energy. As a result, a large number of processes can be included in the outer shell integration through the contractions arising from three-particle interactions, noted, $S_I^{(3)}$. Note that although this term is absent in the bare action, it is generated at each step $\ell$ of renormalization group transformation from the contraction $\frac{1}{2}\langle (S_{I,1})^2 \rangle_{\bar{o},c}$. The recursion relation for the interacting part of the action at the one-loop level is

$$s_I[\psi,\psi^*]_{\ell+d\ell} = S_I[\psi,\psi^*]_\ell + \frac{1}{2}\langle (S_{I,1})^2 \rangle_{\bar{o},c} + \langle S_I^{(3)} \rangle_{\bar{o},c}. \tag{2.16}$$

In the limit $d\ell \to 0$, this gives rise to the renormalization or the flow equation of the scattering amplitudes shown diagrammatically in figure 2.3 and which read

$$\begin{aligned}\partial_\ell g_{1\perp}(k_{\perp 1},k_{\perp 2},k_{\perp 3}) = -\frac{1}{2}\sum_{k_\perp}\Big\{ & g_\parallel(\xi_{\perp 1})g_{1\perp}(\xi_{\perp 2})\left[\mathcal{I}_P^{4h}(k_\perp,k_{\perp 2}-k_{\perp 3})+\mathcal{I}_{P\ell}^{0}(k_\perp,k_{\perp 4}-k_{\perp 1})\right] \\ & + g_\parallel(\xi_{\perp 2})g_{1\perp}(\xi_{\perp 1})\left[\mathcal{I}_{P\ell}^{0}(k_\perp,k_{\perp 2}-k_{\perp 3})+\mathcal{I}_{P\ell}^{4h}(k_\perp,k_{\perp 4}-k_{\perp 1})\right] \\ & + g_{2\perp}(\beta_{\perp 1})g_{1\perp}(\beta_{\perp 2})\left[\mathcal{I}_{C\ell}^{0}(k_\perp,k_{\perp 1}+k_{\perp 2})+\mathcal{I}_{C\ell}^{4h}(k_\perp,k_{\perp 3}+k_{\perp 4})\right] \\ & + g_{2\perp}(\beta_{\perp 2})g_{1\perp}(\beta_{\perp 1})\left[\mathcal{I}_{C\ell}^{4h}(k_\perp,k_{\perp 1}+k_{\perp 2})+\mathcal{I}_{C\ell}^{0}(k_\perp,k_{\perp 3}+k_{\perp 4})\right]\Big\},\end{aligned} \tag{2.17}$$

$$\begin{aligned}\partial_\ell g_{2\perp}(k_{\perp 1},k_{\perp 2},k_{\perp 3}) = -\frac{1}{2}\sum_{k_\perp}\Big\{ & g_{1\perp}(\beta_{\perp 1})g_{1\perp}(\beta_{\perp 2})\left[\mathcal{I}_{C\ell}^{4h}(k_\perp,k_{\perp 1}+k_{\perp 2})+\mathcal{I}_{C\ell}^{4h}(k_\perp,k_{\perp 3}+k_{\perp 4})\right] \\ & + g_{2\perp}(\beta_{\perp 1})g_{2\perp}(\beta_{\perp 2})\left[\mathcal{I}_{C\ell}^{0}(k_\perp,k_{\perp 1}+k_{\perp 2})+\mathcal{I}_{C\ell}^{0}(k_\perp,k_{\perp 3}+k_{\perp 4})\right] \\ & - g_{2\perp}(\xi_{\perp 1})g_{2\perp}(\xi_{\perp 2})\left[\mathcal{I}_{P\ell}^{0}(k_\perp,k_{\perp 2}-k_{\perp 3})+\mathcal{I}_{P\ell}^{0}(k_\perp,k_{\perp 4}-k_{\perp 1})\right] \\ & - g_{3\perp}(\xi_{\perp 3})g_{3\perp}(\xi_{\perp 4})\left[\mathcal{I}_{P\ell}^{0}(k_\perp,k_{\perp 1}-k_{\perp 4})+\mathcal{I}_{P\ell}^{0}(k_\perp,k_{\perp 3}-k_{\perp 2})\right]\Big\},\end{aligned} \tag{2.18}$$

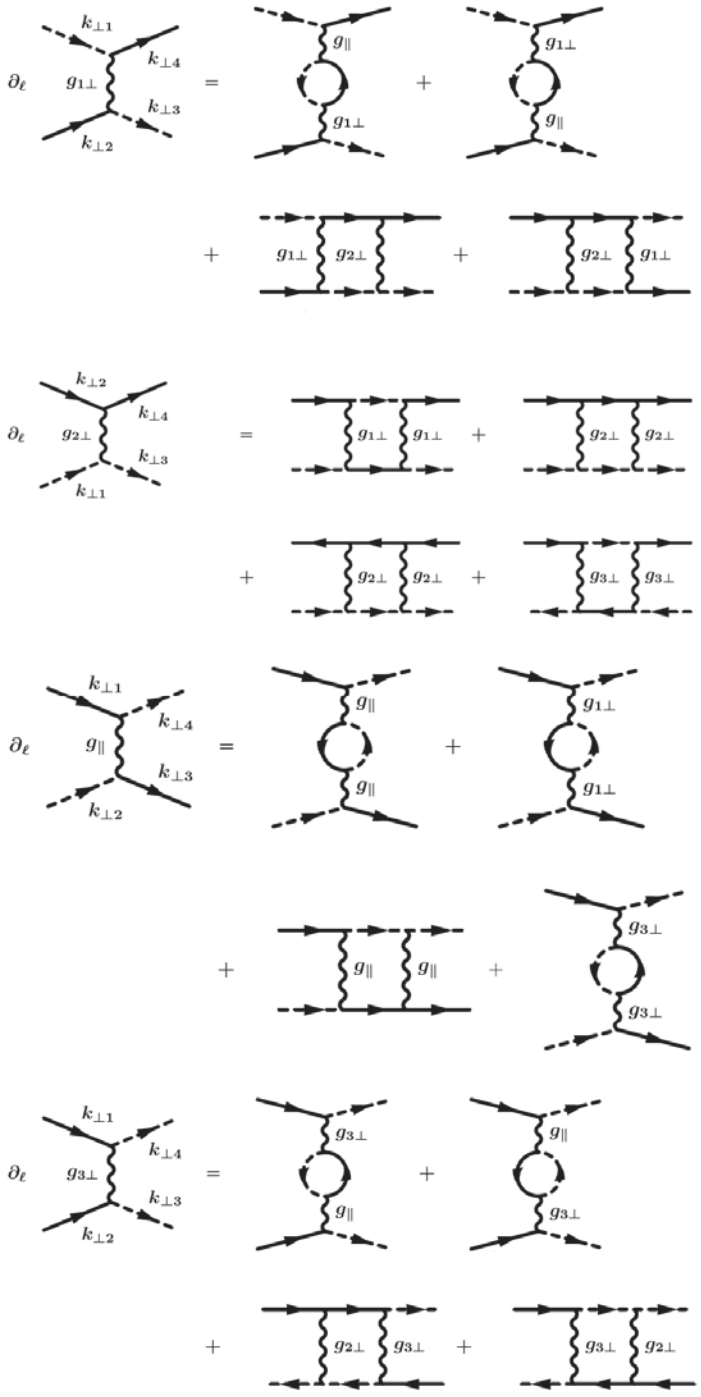


**Figure 2.3** Diagrammatic representation of the renormalization of the coupling constants at the one-loop level.

$$\partial_\ell g_{3\perp}(k_{\perp 1},k_{\perp 2},k_{\perp 3}) = -\frac{1}{2}\sum_{k_\perp}\Big\{ g_\parallel(\xi_{\perp 1})g_{3\perp}(\xi_{\perp 2})\left[\mathcal{I}^0_{P\ell}(k_\perp,k_{\perp 1}-k_{\perp 4})+\mathcal{I}^{4h}_{P\ell}(k_\perp,k_{\perp 3}-k_{\perp 2})\right] + g_\parallel(\xi_{\perp 2})g_{3\perp}(\xi_{\perp 1})\left[\mathcal{I}^{4h}_{P\ell}(k_\perp,k_{\perp 4}-k_{\perp 1})+\mathcal{I}^0_{P\ell}(k_\perp,k_{\perp 2}-k_{\perp 3})\right] - g_{2\perp}(\xi_{\perp 5})g_{3\perp}(\xi_{\perp 6})\left[\mathcal{I}^0_{P\ell}(k_\perp,k_{\perp 4}-k_{\perp 2})+\mathcal{I}^0_{P\ell}(k_\perp,k_{\perp 1}-k_{\perp 3})\right] - g_{2\perp}(\xi_{\perp 5})g_{3\perp}(\xi_{\perp 6})\left[\mathcal{I}^0_{P\ell}(k_\perp,k_{\perp 2}-k_{\perp 4})+\mathcal{I}^0_{P\ell}(k_\perp,k_{\perp 3}-k_{\perp 1})\right]\Big\}, \tag{2.19}$$

$$\partial_\ell g_\parallel(k_{\perp 1},k_{\perp 2},k_{\perp 3}) = -\frac{1}{2}\sum_{k_\perp}\Big\{ g_\parallel(\xi_{\perp 1})g_\parallel(\xi_{\perp 2})\left[\mathcal{I}^0_{P\ell}(k_\perp,k_{\perp 1}-k_{\perp 4})+\mathcal{I}^0_{P\ell}(k_\perp,k_{\perp 3}-k_{\perp 2})\right] + g_{1\perp}(\xi_{\perp 1})g_{1\perp}(\xi_{\perp 1})\left[\mathcal{I}^{4h}_{P\ell}(k_\perp,k_{\perp 1}-k_{\perp 4})+\mathcal{I}^{4h}_{P\ell}(k_\perp,k_{\perp 3}-k_{\perp 2})\right] - g_\parallel(\beta_{\perp 2})g_\parallel(\beta_{\perp 1})\left[\mathcal{I}^0_{C\ell}(k_\perp,k_{\perp 1}+k_{\perp 2})+\mathcal{I}^0_{C\ell}(k_\perp,k_{\perp 3}+k_{\perp 4})\right] + g_{3\perp}(\xi_{\perp 1})g_{3\perp}(\xi_{\perp 2})\left[\mathcal{I}^{4h}_{P\ell}(k_\perp,k_{\perp 4}-k_{\perp 1})+\mathcal{I}^{4h}_{P\ell}(k_\perp,k_{\perp 2}-k_{\perp 3})\right]\Big\}. \tag{2.20}$$

Here we have used the contracted notations:

$$\begin{aligned}
\xi_{\perp 1} &= (k_\perp,k_{\perp 4},k_{\perp 1}),\\
\xi_{\perp 2} &= (k_\perp,k_{\perp 2},k_{\perp 3}),\\
\beta_{\perp 1} &= (k_{\perp 1},k_{\perp 2},k_\perp),\\
\beta_{\perp 2} &= (k_{\perp 3},k_{\perp 4},k_\perp),\\
\xi_{\perp 3} &= (k_{\perp 1},k_\perp,k_{\perp 4}),\\
\xi_{\perp 4} &= (k_{\perp 3},k_\perp,k_{\perp 2}),\\
\xi_{\perp 5} &= (k_\perp,k_{\perp 4},k_{\perp 2}),\\
\xi_{\perp 6} &= (k_{\perp 1},k_\perp,k_{\perp 3}).
\end{aligned} \tag{2.21}$$

The expressions for the bubbles $\mathcal{I}^{0(4)}_{P\ell}$ and $\mathcal{I}^{0(4)}_{C\ell}$ are given in section 2.4. The integration of these equations for the above mentioned specified bare values of $g_i$ up to $\ell \to \infty$, namely down to zero energy at the Fermi surface, leads to the momentum and temperature dependent values of the scattering amplitudes.

### 2.3.2 Response functions

We now proceed to the calculation of the spin-density-wave and superconducting susceptibilities, which give information on the possible instabilities of the electron gas. To do so, we add a set of linear couplings to pair correlation fields in the Peierls and Cooper channel through an infinitesimal source field $\{h_\mu(\bar{q})\}$ in the interacting part of the action at $\ell = 0$. We write

$$S_I[\psi^*, \psi, h^*, h] = S_I[\psi^*, \psi] + S_h[\psi^*, \psi]. \tag{2.22}$$

The source field term reads

$$S_h[\psi^*, \psi] = \sum_{\bar{q}} \Big[ \sum_{\mu_P, M} h^{M*}_{\mu_P}(\bar{q}) \mathcal{O}^M_{\mu_P}(\bar{q}) + \sum_{\mu_C} h^*_{\mu_C}(\bar{q}) \mathcal{O}_{\mu_C}(\bar{q}) + \text{c.c} \Big], \tag{2.23}$$

where $\bar{q} = (q, \omega_m)$. The first term describes the linear coupling of charge- or spin-density-wave correlations located either on site ($M = +1$) or on bond ($M = -1$) due to the presence of umklapp scattering. The second term is related to the linear coupling to electron-electron pairing correlations.

The corresponding composite fields in the Peierls channel $\mu_P$ are:

$$\begin{aligned}
\mathcal{O}^M_{\mu_P}(\bar{q}) &= \frac{1}{2}[O_{\mu_P}(\bar{q}) + M O^*_{\mu_P}(\bar{q})], \\
O_{\mu_P}(\bar{q}) &= \sum_{\bar{k}} z_{\mu_P}(\bar{k}, \bar{k} + \bar{q}) o_{\mu_P}(\bar{k}, \bar{q}), \\
o_{\mu_P}(\bar{k}, \bar{q}) &= \sqrt{\frac{T}{L N_p}} \sum_{\alpha,\beta} \psi^*_{-,\alpha}(\bar{k}) \sigma^{\alpha\beta}_{\mu_P} \psi_{+,\beta}(\bar{k} + \bar{q}),
\end{aligned} \tag{2.24}$$

where ($\mu_P = 0$ , $\sigma_0 = \mathbf{1}$) is attributed to the charge-density-wave ($M = +1$) and bond-order-wave ($M = -1$) correlations, CDW and BOW respectively, while ($\mu_P \neq 0$, $\sigma_{1,2,3} = \sigma_{x,y,z}$) is attributed to the spin-density-wave correlations (SDW and BSDW). Here $\sigma_{\mu_P=1,2,3}$ are the Pauli matrices.

The particle-particle fields in the Cooper channel are

$$\begin{aligned}
\mathcal{O}_{\mu_C}(\bar{q}) &= \sum_{\bar{k}} z_{\mu_C}(\bar{k}, \bar{q} - \bar{k}) \Delta(k_\perp) o_{\mu_C}(\bar{k}, \bar{q}), \\
o_{\mu_C=0}(\bar{k}, \bar{q}) &= \sqrt{\frac{T}{L N_p}} \sum_{\alpha} \alpha \psi_{-,-\alpha}(\bar{k}) \psi_{+,\alpha}(\bar{q} - \bar{k}), \\
o_{\mu_C\neq 0}(\bar{k}, \bar{q}) &= \sqrt{\frac{T}{L N_p}} \sum_{\alpha\beta} \alpha \psi_{-,-\alpha}(\bar{k}) \sigma^{\alpha\beta}_{\mu_C} \psi_{+,\beta}(\bar{q} - \bar{k}),
\end{aligned} \tag{2.25}$$

where $\mu_C = 0$ corresponds to singlet superconducting channel (SS) and $\mu_C \neq 0$ is for the triplet

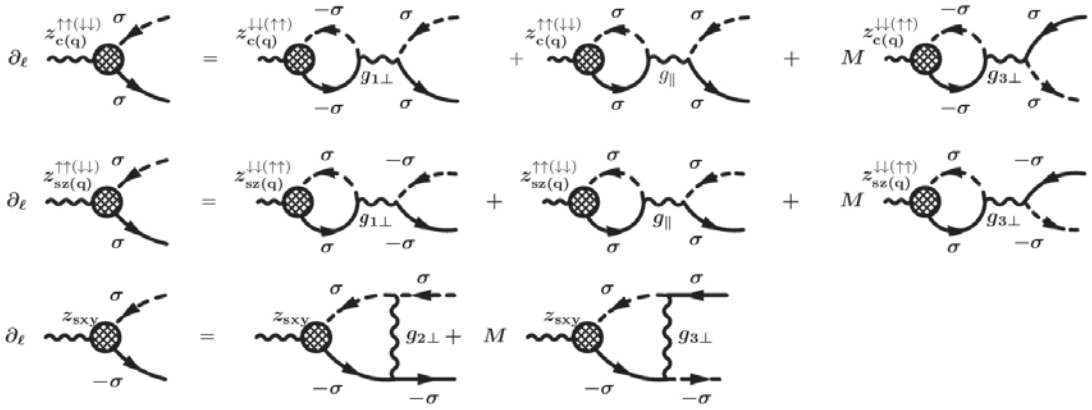

(a) density-wave (DW)

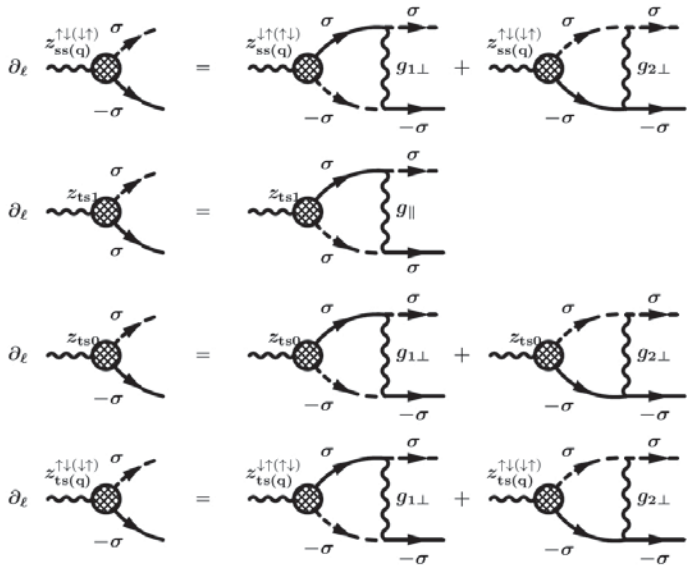

(b) superconducting (SC)

**Figure 2.4** Diagrammatic representation of flow equations for the pair vertex functions as the shaded circles.

| name | spin pairing | $\Delta(k_\perp)$ |
|---|---|---|
| $s$ | singlet | 1 |
| $p_x$ | triplet | 1 |
| $p_y$ | | $\sin(k_\perp)$ |
| $d_{x^2-y^2}$ | singlet | $\cos(k_\perp)$ |
| $d_{xy}$ | | $\sin(k_\perp)$ |
| $f$ | triplet | $\cos(k_\perp)$ |
| | | $\sin(2k_\perp)$ |
| $g$ | singlet | $\cos(2k_\perp)$ |
| | | $\sin(2k_\perp)$ |
| $h$ | triplet | $\cos(2k_\perp)$ |
| $i$ | singlet | $\sin(3k_\perp)$ |

**Table 2.1** Possible superconducting form factors (order parameters) in a quasi-1D geometry.

superconducting channel (TS). $\Delta(k_\perp)$ is the form factor of the response function. These are listed in table 2.1.

The coefficient $z_{\mu_{C(P)}}$ is the renormalization factor for the pair vertex part in the channel $\mu$. In the limit $h_{\mu_{C(P)}} \to 0$, the partial trace at the one-loop level generates the corrections to the renormalization factors and to the susceptibilities at each step $\ell$. These are obtained from the recursion relation that corrects $S_h$:

$$S_h[\psi^*, \psi]_{\ell+d\ell} = S_h[\psi^*, \psi]_\ell + \langle S_h S_I \rangle_{\bar{o},c} + \frac{1}{2}\langle {S_h}^2 \rangle_{\bar{o},c}, \tag{2.26}$$

where the second term on the right side is of the order of source field $h_\mu^{M(*)}$ and then leads to the flow equations for $z_\mu$. The last term on the right side is proportional to $h_\mu^{(M)} h_\mu^{*(M)}$ and generates the contributions correcting the different electronic susceptibilities $\chi$ at step $\ell$:

$$\tilde{\chi}^M_{\mu_{P(C)}}(\bar{q}) = \frac{\partial^2 S_h[\psi, \psi^*]_\ell}{\partial h^*_{\mu_{P(C)}} \partial h_{\mu_{P(C)}}}\bigg|_{h_{\mu_{P(C)}} \to 0} = 2\int_\ell \frac{1}{N_P} \sum_{\bar{k}} |z^M_{\mu_{P(C)}}(\bar{k}, (-)\bar{k} + \bar{q})|^2 \mathcal{I}_{P(C)} {\ell}^2 d\ell, \tag{2.27}$$

where $\tilde{\chi} = \hbar \pi v_F \chi$.

The RG equations for the different pair vertex functions are shown diagrammatically in figure

2.4 and read as follow:

a) For density-wave with $\tilde{\boldsymbol{q}}_P = (2k_F, q_{\perp P} = \pi, \omega_m = 0)$; the subscript $P$ refers to the Peierls channel, c to the charge-density-wave, and s to the spin-density-wave:

$$\begin{aligned}\partial_\ell z_{\rm c}(k_\perp, k_\perp + q_{\perp P}) = -\frac{1}{2}\sum_{k'_\perp}\Big\{ &\big[g_{\perp 1}(k'_\perp + q_{\perp P}, k_\perp, k_\perp + q_{\perp P}) + g_\parallel(k'_\perp + q_{\perp P}, k_\perp, k_\perp + q_{\perp P}) \\ &+ M g_{3\perp}(k'_\perp + q_{\perp P}, k_\perp + q_{\perp P}, k_\perp)\big] \\ &\times z_c(k'_\perp, k'_\perp + q_{\perp P})\mathcal{I}^{2h}_{P\ell}(k'_\perp, q_{\perp P})\Big\},\end{aligned} \tag{2.28}$$

$$\begin{aligned}\partial_\ell z_{sz}(k_\perp, k_\perp + q_{\perp P}) = \frac{1}{2}\sum_{k'_\perp}\Big\{ &\big[g_{\perp 1}(k'_\perp + q_{\perp P}, k_\perp, k_\perp + q_{\perp P}) - g_\parallel(k'_\perp + q_{\perp P}, k_\perp, k_\perp + q_{\perp P}) \\ &+ M g_{3\perp}(k'_\perp + q_{\perp P}, k_\perp + q_{\perp P}, k_\perp)\big] \\ &\times z_{sz}(k'_\perp, k'_\perp + q_{\perp P})\mathcal{I}^{2h}_{P\ell}(K'_\perp, q_{\perp P})\Big\},\end{aligned} \tag{2.29}$$

$$\begin{aligned}\partial_\ell z_{sxy}(k_\perp, k_\perp + q_{\perp P}) = \frac{1}{2}\sum_{k'_\perp}\Big\{ &\big[g_{2\perp}(k'_\perp + q_{\perp P}, k_\perp, k_\perp + q_{\perp P}) \\ &+ M g_{3\perp}(k'_\perp + q_{\perp P}, k_\perp + q_{\perp P}, k'_\perp)\big] \\ &\times z_{sxy}(k'_\perp, k'_\perp + q_{\perp P})\mathcal{I}^{2h}_{P\ell}(K'_\perp, q_{\perp P})\Big\},\end{aligned} \tag{2.30}$$

where $z$ and $xy$ refer to the components of the spin-density-wave perpendicular and parallel to the applied field along the conducting planes.

b) For density wave with $\tilde{\boldsymbol{q}}_P = (2h/v_F + 2k_F, q_{\perp P} = 0, \omega_m = 0)$. $2h/v_F = k_{F\downarrow} - k_{F\uparrow}$ is the

distance between the spin up and spin down Fermi surfaces in the presence of a magnetic field.

$$\begin{aligned}\partial_\ell z_{cq}^{\downarrow\downarrow(\uparrow\uparrow)}(k_\perp, k_\perp + q_{\perp P}) = -\frac{1}{2}\sum_{k'_\perp}\Big\{ & [g_{1\perp}(k'_\perp + q_{\perp P}, k_\perp, k_\perp + q_{\perp P}) \\ & + M g_{3\perp}(k'_\perp + q_{\perp P}, k_\perp + q_{\perp P}, k_\perp)] \\ & \times z_{cq}^{\uparrow\uparrow(\downarrow\downarrow)}(k'_\perp, k'_\perp + q_{\perp P}) \mathcal{I}_{P\ell}^{0(4h)}(K'_\perp, q_{\perp P}) \\ & + g_\parallel(k'_\perp + q_{\perp P}, k_\perp, k_\perp + q_{\perp P}) \\ & z_{cq}^{\downarrow\downarrow(\uparrow\uparrow)}(k'_\perp, k'_\perp + q_{\perp P}) \mathcal{I}_{P\ell}^{4h(0)}(K'_\perp, q_{\perp P})\Big\}, \end{aligned} \tag{2.31}$$

$$\begin{aligned}\partial_\ell z_{szq}^{\downarrow\downarrow(\uparrow\uparrow)}(k_\perp, k_\perp + q_{\perp P}) = \frac{1}{2}\sum_{k'_\perp}\Big\{ & [g_{1\perp}(k'_\perp + q_{\perp P}, k_\perp, k_\perp + q_{\perp P}) \\ & + M g_{3\perp}(k'_\perp + q_{\perp P}, k_\perp + q_{\perp P}, k_\perp)] \\ & \times z_{szq}^{\uparrow\uparrow(\downarrow\downarrow)}(k'_\perp, k'_\perp + q_{\perp P}) \mathcal{I}_{P\ell}^{0(4h)}(K'_\perp, q_{\perp P}) \\ & - g_\parallel(k'_\perp + q_{\perp P}, k_\perp, k_\perp + q_{\perp P}) \\ & z_{szq}^{\downarrow\downarrow(\uparrow\uparrow)}(k'_\perp, k'_\perp + q_{\perp P}) \mathcal{I}_{P\ell}^{4h(0)}(K'_\perp, q_{\perp P})\Big\}. \end{aligned} \tag{2.32}$$

c) For superconductivity with $\tilde{\boldsymbol{q}}_C = (0, q_{\perp C} = 0, \omega_m = 0)$. The subscript $C$ refers to the Cooper channel:

$$\begin{aligned}\partial_\ell z_{\rm ss}(k_\perp, q_{\perp C} - k_\perp) = -\frac{1}{2}\sum_{k'_\perp}[g_{1\perp}(q_{\perp C} - k'_\perp, k'_\perp, q_{\perp C} - k_\perp) + g_{2\perp}(q_{\perp C} - k'_\perp, k'_\perp, q_{\perp C} - k_\perp)] \\ \times z_{\rm ss}(k'_\perp, q_{\perp C} - k'_\perp) \mathcal{I}_{C\ell}^{2h}(k'_\perp, q_{\perp C}),\end{aligned} \tag{2.33}$$

$$\partial_\ell z_{\rm ts1}(k_\perp, q_{\perp C} - k_\perp) = \frac{1}{2}\sum_{k'_\perp} g_\parallel(q_{\perp C} - k'_\perp, k'_\perp, q_{\perp C} - k_\perp) z_{\rm ts1}(k'_\perp, q_{\perp C} - k'_\perp) \mathcal{I}_{C\ell}^{0}(k'_\perp, q_{\perp C}), \tag{2.34}$$

$$\partial_\ell z_{\mathrm{ts0}}(k_\perp, q_{\perp C}-k_\perp) = \frac{1}{2}\sum_{k'_\perp}[g_{1\perp}(q_{\perp C}-k'_\perp, k'_\perp, q_{\perp C}-k_\perp) - g_{2\perp}(q_{\perp C}-k'_\perp, k'_\perp, q_{\perp C}-k_\perp)] \times z_{\mathrm{ts0}}(k'_\perp, q_{\perp C}-k'_\perp)\mathcal{I}^{2h}_{C\ell}(k'_\perp, q_{\perp C}), \tag{2.35}$$

where the ss abbreviation is for singlet superconductivity and ts for triplet superconductivity. For triplet superconductivity, the $S_z$ component of the total spin are distinguished by ts1 for $S_z = \pm 1$ and by ts0 for $S_z = 0$.

d) For an inhomogeneous FFLO superconducting state in which the electrons pair with a finite total momentum $\tilde{\boldsymbol{q}}_C = (2h/v_F, q_{\perp C} = 0, \omega_m = 0)$:

$$\partial_\ell z^{\uparrow\downarrow(\downarrow\uparrow)}_{\mathrm{ss}q}(k_\perp, q_{\perp C}-k_\perp) = -\frac{1}{2}\sum_{k'_\perp}[g_{1\perp}(q_{\perp C}-k'_\perp, k'_\perp, q_{\perp C}-k_\perp) z^{\downarrow\uparrow(\uparrow\downarrow)}_{\mathrm{ss}q}(k'_\perp, q_{\perp C}-k'_\perp) \times \mathcal{I}^{0(4h)}_{C\ell}(k'_\perp, q_{\perp C}) + g_{2\perp}(q_{\perp C}-k'_\perp, k'_\perp, q_{\perp C}-k_\perp) \times z^{\uparrow\downarrow(\downarrow\uparrow)}_{\mathrm{ss}q}(k'_\perp, q_{\perp C}-k'_\perp)\mathcal{I}^{4h(0)}_{C\ell}(k'_\perp, q_{\perp C})], \tag{2.36}$$

$$\partial_\ell z^{\uparrow\downarrow(\downarrow\uparrow)}_{\mathrm{ts}q}(k_\perp, q_{\perp C}-k_\perp) = \frac{1}{2}\sum_{k'_\perp}[g_{1\perp}(q_{\perp C}-k'_\perp, k'_\perp, q_{\perp C}-k_\perp) z^{\downarrow\uparrow(\uparrow\downarrow)}_{\mathrm{ts}q}(k'_\perp, q_{\perp C}-k'_\perp) \times \mathcal{I}^{4h(0)}_{C\ell}(k'_\perp, q_{\perp C}) - g_{2\perp}(q_{\perp C}-k'_\perp, k'_\perp, q_{\perp C}-k_\perp) \times z^{\uparrow\downarrow(\downarrow\uparrow)}_{\mathrm{ts}q}(k'_\perp, q_{\perp C}-k'_\perp)\mathcal{I}^{0(4h)}_{C\ell}(k'_\perp, q_{\perp C})]. \tag{2.37}$$

For all the above $z$'s, the initial condition is $z = 1$ at $\ell = 0$. Recall that $z_{\mu_C}$ describes the orbital symmetry of the superconducting form factor (order parameter) $\Delta(k_\perp)$ whose list is given in table 2.1.

The electronic susceptibilities $\bar{\chi}_\mu = \hbar\pi v_F \chi_\mu$ at temperature $T$ are computed with the aid of the above pair vertex functions:

$$\bar{\chi}_c(T) = 2\int_0^\infty (z_c)^2 \mathcal{I}^{2h}_{P\ell} d\ell, \tag{2.38}$$

$$\bar{\chi}_{cq}(T) = \int_0^\infty [(z^{\uparrow\uparrow}_{cq})^2 \mathcal{I}^{0}_{P\ell} + (z^{\uparrow\uparrow}_{cq})^2 \mathcal{I}^{4h}_{P\ell}] d\ell, \tag{2.39}$$

$$\bar{\chi}_{\mathrm{sz}}(T) = 2\int_0^\infty (z_{\mathrm{sz}})^2 \mathcal{I}^{2h}_{P\ell} d\ell, \tag{2.40}$$

$$\bar{\chi}_{\mathrm{s}q}(T) = \int_0^\infty \left[(z^{\uparrow\uparrow}_{\mathrm{sz}q})^2 \mathcal{I}^{0}_{P\ell} + (z^{\uparrow\uparrow}_{\mathrm{sz}q})^2 \mathcal{I}^{4h}_{P\ell}\right] d\ell, \tag{2.41}$$

$$\bar{\chi}_{\mathrm{s}xy}(T) = 2\int_0^\infty (z_{\mathrm{s}xy})^2 \mathcal{I}^{0}_{P\ell} d\ell, \tag{2.42}$$

$$\bar{\chi}_{\mathrm{ss}}(T) = 2\int_0^\infty (z_{\mathrm{ss}})^2 \mathcal{I}^{2h}_{C\ell} d\ell, \tag{2.43}$$

$$\bar{\chi}_{\mathrm{ts}0}(T) = 2\int_0^\infty (z_{\mathrm{ts}0})^2 \mathcal{I}^{2h}_{C\ell} d\ell, \tag{2.44}$$

$$\bar{\chi}_{\mathrm{ts}1}(T) = 2\int_0^\infty (z_{\mathrm{ts}1})^2 \mathcal{I}^{0}_{C\ell} d\ell, \tag{2.45}$$

$$\bar{\chi}_{\mathrm{ss}q}(T) = \int_0^\infty \left[(z^{\uparrow\downarrow}_{\mathrm{ss}q})^2 \mathcal{I}^{0}_{C\ell} + (z^{\downarrow\uparrow}_{\mathrm{ss}q})^2 \mathcal{I}^{4h}_{P\ell}\right] d\ell, \tag{2.46}$$

$$\bar{\chi}_{\mathrm{ts}q}(T) = \int_0^\infty \left[(z^{\uparrow\downarrow}_{\mathrm{ts}q})^2 \mathcal{I}^{0}_{C\ell} + (z^{\downarrow\uparrow}_{\mathrm{ts}q})^2 \mathcal{I}^{4h}_{P\ell}\right] d\ell. \tag{2.47}$$

## 2.4 One-Loop contributions to the RG equations

To solve the RG flow equations at the one-loop level, we need to calculate the value of different bubbles $\mathcal{I}_{P(C)\ell}$ entering in these equations.

$$\begin{aligned}\mathcal{I}_{\nu\ell}(k_\perp, q^{(\prime)}_{\perp\nu}) d\ell = -\eta_\nu \frac{\pi v_F T}{L N_p} \sum_{k}\sum_{\omega_n} \Big\{ & 2\mathcal{H}\big(|E_-(k)| - \Lambda(\ell)\big)\mathcal{H}_\ell\big(E_+(\mathbf{q}^{(\prime)}_\nu + \eta_\nu k)\big) \\ & + \mathcal{H}_\ell\big(E_+(\mathbf{q}^{(\prime)}_\nu + \eta_\nu k)\big)\mathcal{H}_\ell\big(E_-(k)\big)\Big\} G_0^-(\bar{k}) G_0^+(\eta_\nu \bar{k} + \bar{\mathbf{q}}^{(\prime)}_\nu),\end{aligned} \tag{2.48}$$

where $\nu = P, C$ and $\eta_P = +1$, $\eta_C = -1$. $\mathbf{q}^{(\prime)}_P = k_3 - k_2 = k_1 - k_4 (k_3 - k_1 = k_2 - k_4)$ and $\mathbf{q}_C = k_1 + k_2 = k_3 + k_4$. The condition $\mathcal{H}_\ell(E) = 1$ considers the fermion line within the outer energy shell at step $\ell$ for which $\Lambda(\ell+1) < |E| \leqslant \Lambda(\ell)$ and $\mathcal{H}(|E| - \Lambda(\ell)) = 1$ takes

into account the fermion line contribution from the preceding renormalization step for which $\Lambda(\ell) < |E| \leqslant \Lambda_0$. Dividing the outer energy shell into $N_p$ patches each determined by a discrete transverse momentum $k_{\perp,i}$, the above summation over momentum can be written as

$$\begin{aligned}\frac{1}{LN_p}\sum_{k} &= \frac{1}{N_p}\sum_{k_\perp}\int_{o.s}\frac{dE}{2\pi v_F} \\ &= \frac{1}{2\pi}\sum_{k_{\perp,i}}\int_{k_{\perp,i}-\pi/N_p}^{k_{\perp,i}+\pi/N_p} dk_\perp \frac{dE}{2\pi v_F}.\end{aligned} \tag{2.49}$$

After carrying out the summation on frequency and performing the integration on energy, we arrive at the following expression

$$\begin{aligned}\mathcal{I}_{v\ell}^{\alpha h}(k_\perp, q_{\perp v}^{(\prime)}) = \frac{\Lambda(\ell)}{2}\sum_{\mu=\pm 1}\int_{k_\perp-\frac{\pi}{N_p}}^{k_\perp+\frac{\pi}{N_p}}\frac{dk_\perp}{2\pi}\times\frac{\theta(|\Lambda(\ell)+\mu A_v^{\alpha h}|-\Lambda(\ell))}{2\Lambda(\ell)+\mu A_v^{\alpha h}} \\ \times\Big[\tanh[\beta\Lambda(\ell)/2]+\tanh[\beta(\Lambda(\ell)/2+\mu A_v/2)]\Big].\end{aligned} \tag{2.50}$$

For the bubble diagrams in the flow equations of the coupling constants, we have:

$$\begin{aligned}A_v^{\alpha h}(k_\perp, q_{\perp v}^{(\prime)}) = &-\epsilon_\perp(k_\perp)-\eta_v\epsilon_\perp(\eta_v k_\perp + q_{\perp v}^{(\prime)}) \\ &+\eta_v\epsilon_\perp(\eta_v k_{\perp 2(4)}+q_{\perp v}^{(\prime)})+\epsilon_\perp(k_{\perp 2(4)})+\alpha h,\end{aligned} \tag{2.51}$$

where $\alpha = -\sigma_{k_{\perp 2(4)}} - \eta_v\sigma_{\eta_v k_{\perp 2(4)}+q_{\perp v}^{(\prime)}} + \sigma_{k_\perp} + \eta_v\sigma_{k_\perp+q_{\perp P}^{(\prime)}}$, and $\epsilon_\perp(k_\perp) = -2t_\perp\cos(k_\perp) - 2t'_\perp\cos(2k_\perp)$.

For the bubble diagrams in the flow equations of the pair vertex functions with $q_P = 2k_F + (2h/v_F)$ and $q_C = 0$, we have:

$$A_v^{\alpha h}(k_\perp, q_{\perp v}) = -\epsilon_\perp(k_\perp) - \eta_v\epsilon_\perp(\eta_v k_\perp + q_{\perp v}^{(\prime)}) + \alpha h, \tag{2.52}$$

where $\alpha = \sigma_{k_\perp} + \eta_v\sigma_{\eta_v k_\perp + q_{\perp v}} + (-\eta_v 2)$. Here by the notation $\sigma_{k_\perp}$ we mean the spin on the fermion line with the transverse momentum $k_\perp$.

The following paper contains the detailed results obtained by the numerical integration of the renorlmalization group flow equations 2.17-2.20 and 2.28-2.37 up to $\ell \to \infty (\ell = \ln\frac{\Lambda_0}{T})$. This yields the most singular scattering amplitudes and consequently the most singular response functions at temperature $T$. With the variation of the anti-nesting parameter $t'_\perp$, and in the presence of both intra-chain and inter-chain electron-electron interactions, we have been able to capture the detailed phase diagram of a quasi-one-dimensional electron gas with spins coupled to a magnetic field. The crossover to an inhomogeneous d-wave FFLO in the limit of purely intra-chain repulsive interactions and the possible transitions toward triplet superconductivity under filed by switching the inter-chain

repulsive interactions are examined.

## Publication

- **Superconducting and density-wave instabilities of low dimensional conductors with a Zeeman coupling to a magnetic field**

**M. Shahbazi**, Y. Fuseya, H. Bakrim, A. Sedeki, and C. Bourbonnais, **arXiv:1702.04201v1 (2017)**, submitted in **Phys. Rev. B**

I have derived the Renormalization Group flow equations for an extended quasi-1D electron gas model in the presence of Zeeman coupling of spins to the magnetic field. I have modified and optimized the fortran program that was originally developed by A. Sedeki and H. Bakrim to perform the numerical solution of these equations. I have produced all the figures and have written all the manuscript. The co-authors have participated to the correction of the manuscript for publication.

# Superconducting and density-wave instabilities of low dimensional conductors with a Zeeman coupling to a magnetic field

M. Shahbazi,[1] Y. Fuseya,[2] H. Bakrim,[1] A. Sedeki,[1] and C. Bourbonnais[1]

[1] *Regroupement Québecois sur les Matériaux de Pointe, Département de physique, Université de Sherbrooke, Sherbrooke, Québec, Canada, J1K-2R1,*

[2] *Department of Engineering Science, University of Electro-Communications, Ch Tokyo 182-8585, Japan*

(Dated: February 15, 2017)

In the framework of the weak coupling renormalization group technique we examine the possible instabilities of the extended quasi-one-dimensional electron gas model with both intrachain and interchain electron-electron interactions, including the influence of umklapp scattering and the coupling of spins to a magnetic field. In the limit of purely repulsive intrachain interactions, we confirm the passage from singlet $d$-wave like superconductivity to an inhomogeneous FFLO state under magnetic field. The passage is accompanied by an anomalous increase of the upper critical field that scales with the antinesting distance from the quantum critical point joining superconductivity to antiferromagnetism in the phase diagram, as well as the strength of interactions. Adding weak repulsive interchain interactions promotes the passage from singlet to triplet $f$-wave superconductivity which is expanded under field by the development of a triplet FFLO state with zero angular momentum projection for the Cooper pairs. The connection between theory and experiments on the anomalous upper critical field in the Bechgaard salts is discussed.

PACS numbers: 74.20.Mn,74.25Dw,74.70.Kn

## I. INTRODUCTION

The $(TMTSF)_2X$ series of organic conductors, also dubbed the Bechgaard salts series, stands out among the first examples of correlated electron systems showing the emergence of superconductivity (SC) following the suppression of a spin-density-wave state (SDW). This is found to occur when either pressure is applied or by chemical means, from anion $X$ substitution.[1–3]. This proximity has fostered a lot of debate around the nature of the SC order parameter in these materials, and in particular its transformations in magnetic field which will be the main theoretical focus of the present work.

The proximity of SC to SDW in the phase diagram of these quasi-one dimensional (quasi-1D) materials was soon interpreted as a sign of an intimate connection between both ordered states, suggesting that magnetism is directly involved in the development of a SC order parameter. This led to propose that short-range antiferromagnetic fluctuations of the metallic phase, can act as the source of Cooper pairing for electrons[4–8]. A singlet d-wave (SCd) gap with nodes on the Fermi surface was thus predicted to be the most favourable order parameter for superconductivity, whereas singlet $s$-wave and triplet $p$-wave pairings were found to be both suppressed by SDW correlations[5].This was regarded as consistent with the power law temperature dependence observed in the nuclear spin relaxation rate[9,10] and the high sensitivity of superconductivity to impurity scattering[11–14]. However, the singlet d-wave scenario was later on challenged with the puzzling observation in $(TMTSF)_2ClO_4$ of a thermally activated behaviour of thermal conductivity below $T_c$[15], a behaviour that has since been found consistent with the penetration depth extracted from muon spin rotation measurements on the same material[16]. When combined to the aforementioned impurity effect[17], thermal activation may point to a nodeless triplet $p$-wave SC gap, clearly in conflict with the predictions of microscopic calculations.

On a theoretical basis, the possibility of triplet SC other than $p$-wave in purely repulsive quasi-1D electron systems has been examined in different ways. From RPA-like approaches[18], it was found that triplet $f-$wave superconductivity (SCf) can compete with SCd if charge-density-wave (CDW) and SDW fluctuations become of equal importance, a situation that can be reproduced microscopically at sufficiently strong long-range Coulomb interaction along the chains. Such an incursion of SCf besides SCd in the calculated phase diagram of quasi-1D electron gas model was confirmed by the renormalization group (RG) method when the long-range part of the Coulomb term dominates other contributions for purely intrachain interactions[19]. When interchain Coulomb interaction is included, even weak in amplitude, it was shown from the RG method that bond centered charge-density wave, also called bond-order (BOW) fluctuations are enhanced besides SDW, which can turn SCd unstable in favor of a SCf triplet ordered state[20].

In the interval, the triplet scenario for superconductivity in the Bechgaard salts was further promoted from experiments carried out under magnetic field. This was borne out by a constant and temperature independent NMR Knight shift in the superconducting state of pressurized $(TMTSF)_2PF_6$[21]. The violation from electrical transport measurements of the Glogston criteria or Pauli limit for the critical field of singlet SC was also understood in terms of triplet pairing[22–26]. Resistivity data show the presence of superconductivity up to a critical field $H^r_{c2}$ standing well above the expected Pauli limiting field $H_P$ known to be bounded by the size of $T_c$ for

singlet Cooper pairing. These experiments were all conducted for field oriented in the $ab'$ plane of highest conduction, an orientation that quenches most of the orbital pair breaking effect, as a result of the strong anisotropy in the electron motion. In these conditions, homogeneous superconductivity can be sustained at arbitrary field if the SC order parameter has a triplet character[27,28].

Lower field NMR experiments that were subsequently conducted in $(TMTSF)_2ClO_4$ modified this view[29]. They revealed that the Knight shift in the superconducting state is actually suppressed in low field, giving then firm evidence for a singlet SC ground state. However, as the field is increased and crosses some threshold, the Knight shift and nuclear relaxation rate recover their respective normal state values. This arises while superconductivity persists in electrical transport, consistently with the aforementioned violation of the Pauli limit in the $ab'$ plane.

Theoretically, it was proposed from various mean-field approaches that NMR and transport experiments could be reconciled if the SC order parameter experiences a singlet to triplet transition under magnetic field[30–34]. A transition toward a SCf state under field was found to occur using the RG approach to a coupled two-chain version of this problem[35]. A second possibility put forward in the framework of mean-field theory is a transition toward an inhomogeneous FFLO singlet state under field[27,28,34,36], whose conditions of occurence are particularly optimized for an open quasi-1D Fermi surface. The existence of a field-induced FFLO state in the Bechgaard salts has received a certain empirical support from the observation of an anisotropic onset of the resistive transition in $(TMTSF)_2ClO_4$ at $H^r_{c2}$ in the $ab'$ plane[37,38]. Moreover, recent specific heat experiments performed on $(TMTSF)_2ClO_4$ for similar field orientation[39,40], revealed that $H^r_{c2}$ is preceded by a clear thermodynamic signature of the Pauli limit $H_P$. Besides confirming the singlet nature of the ground state at low field, this critical field scale corresponds to the transition seen by NMR under field.

In a shortened version of the present work, Fuseya *et al.*,[41] examined the field dependence of Cooper pairing from the RG approach to the repulsive quasi-1D electron gas model at incommensurate band filling. The magnetic field was exclusively coupled to spins without pair breaking effects of orbital origin so as to simulate the weakness of the orbital pair breaking for a field oriented in the $ab'$ plane. The calculations revealed that quantum fluctuations linked to the interplay between SDW and SCd have a sizeable impact on the upper critical field $H_{c2}$. The $H_{c2}(T)$ critical line shows a pronounced upturn at low temperature that largely exceeds the predicted Pauli limit. The difference was found to be non-universal for the ratio $H_{c2}(T)/T_c$, and SCd was shown to become unstable against the formation of a d-wave FFLO (dFFLO) state. No indication for field-induced uniform triplet superconductivity was obtained.

In the present work, we carry on the program of Ref.[41] a step further and extend the RG calculations under magnetic field to the case where half-filling umklapp scattering is present. Umklapp scattering is a key scattering ingredient in systems like the Bechgaard salts which presents some half-filling band character. It is also essential in the quantum criticality associated with the sequence of SDW-SCd instabilities found in these materials[6,8,42–46]. The instability of SCd against the formation of dFFLO state is confirmed under field, together with its strength correlated to the distance to the quantum critical point along the antinesting axis or the strength of interactions. We also investigate the influence of interchain Coulomb interaction in order to examine if the singlet to triplet transition induced by this interaction is expanded under field. This is found to be the case with the incursion under field of a triplet $f$-wave FFLO state with zero spin projection for the Cooper pairs, a state that precedes uniform SCf type of superconductivity along the interchain interaction axis.

In Sec. II, we introduce the extended quasi-1D electron gas model and the RG method in the presence of a Zeeman coupling of spins to a magnetic field. In Sec. III, we examine the modification of the phase diagram of the electron gas under magnetic field and the crossover to an inhomogeneous d-wave FFLO in the limit of purely intrachain repulsive interactions. The resulting anomalies in the upper critical field are discussed. In Sec. IV, the influence interchain repulsive interactions on the possible transitions toward triplet superconducting orders under field is investigated. We conclude in Sec. V.

## II. THE EXTENDED ELECTRON GAS MODEL IN A MAGNETIC FIELD

### A. Model

We consider a linear array of $N_P$ weakly coupled metallic chains of length $L$, separated by the interchain distance $d_b(\equiv 1)$. The partition function is expressed as a functional integral over the anticommuting $\psi's$

$$Z = \int\int \mathfrak{D}\psi^*\mathfrak{D}\psi \; e^{S_0[\psi^*,\psi]+S_I[\psi^*,\psi]}, \qquad (1)$$

where the quadratic part of the action is given by

$$S_0[\psi^*,\psi] = \sum_{\boldsymbol{k},\sigma} \psi^*_{p,\sigma}(\bar{k})[i\omega_n - E_{p,\sigma}(\boldsymbol{k})]\psi_{p,\sigma}(\bar{k}), \qquad (2)$$

where $\bar{k} = (\boldsymbol{k},\omega_n)$, $\boldsymbol{k} = (k,k_b)$ is the longitudinal and transverse wave vectors, and $\omega_n$ the fermion Matsubara frequencies. The spectrum of the electron gas model, in the presence of a Zeeman coupling of spins to a magnetic field $H$, takes the form

$$E_{p,\sigma}(\boldsymbol{k}) = v_F(pk - k_F) + \xi_b(k_b) - \sigma h, \qquad (3)$$

where $p = \pm$ refers to right/left moving carriers along the chains of velocity $v_F$, with $k_F$ as the 1D Fermi wave

vector ($\hbar = 1$ and $k_B = 1$ throughout). Here $h = \mu_B H$ and $\sigma = \pm$ is the spin index. The transverse part of the electron gas spectrum is

$$\xi_b(k_b) = -2t_b \cos k_b - 2t'_b \cos 2k_b, \tag{4}$$

where $t_b$ is the first nearest-neighbours transverse hopping, whereas the second nearest-neighbour hopping $t'_b \ll t_b$ is the anitinesting tuning parameter that simulates the main effect of pressure in the model.

In the g-ology picture of interactions, the two-body part of the action can be written in the form

$$\begin{aligned} S_I[\psi^*,\psi] = -\frac{T}{LN_P}\pi v_F \sum_{\{\bar{k},\sigma\}} \Big\{ & g_{\parallel}(\boldsymbol{k}^-_{F,1},\boldsymbol{k}^+_{F,2};\boldsymbol{k}^-_{F,3},\boldsymbol{k}^+_{F,4})\psi^*_{-\sigma}(\bar{k}_1)\psi^*_{+,\sigma}(\bar{k}_2)\psi_{-,\sigma}(\bar{k}_3)\psi_{+,\sigma}(\bar{k}_4) \\ & + g_{1\perp}(\boldsymbol{k}^-_{F,1},\boldsymbol{k}^+_{F,2};\boldsymbol{k}^-_{F,3},\boldsymbol{k}^+_{F,4})\psi^*_{-,\sigma}(\bar{k}_1)\psi^*_{+,-\sigma}(\bar{k}_2)\psi_{-,-\sigma}(\bar{k}_3)\psi_{+,\sigma}(\bar{k}_4) \\ & + g_{2\perp}(\boldsymbol{k}^+_{F,1},\boldsymbol{k}^-_{F,2};\boldsymbol{k}^-_{F,3},\boldsymbol{k}^+_{F,4})\psi^*_{-,\sigma}(\bar{k}_1)\psi^*_{+,-\sigma}(\bar{k}_2)\psi_{+,-\sigma}(\bar{k}_3)\psi_{-,\sigma}(\bar{k}_4) \\ & + \frac{1}{2}\big[\, g_{3\perp}(\boldsymbol{k}^+_{F,1},\boldsymbol{k}^+_{F,2};\boldsymbol{k}^-_{F,3},\boldsymbol{k}^-_{F,4})\psi^*_{+,\sigma}(\bar{k}_1)\psi^*_{+,-\sigma}(\bar{k}_2)\psi_{-,-\sigma}(\bar{k}_3)\psi_{-,\sigma}(\bar{k}_4) + \text{c.c.}\big]\Big\} \\ & \times \delta_{\bar{k}_1+\bar{k}_2,\bar{k}_3+\bar{k}_4(\pm\bar{G})}. \end{aligned} \tag{5}$$

The interaction parameters are defined for ingoing and outgoing electrons on the open Fermi surface $\boldsymbol{k}^p_F(k_b) = (pk_F(k_b), k_b)$ consisting of two ($p = \pm$) sheets parametrized by $k_b$ from the condition $E_p(\boldsymbol{k}^p_F) = 0$ in zero field. We have in order, the total backscattering amplitude for parallel spins, $g_{\parallel} = g_{1\parallel} - g_{2\parallel}$, which incorporates by exchange a forward scattering contribution; the forward scattering for antiparallel spins, $g_{2\perp}$; and umklapp scattering $g_{3\perp}$ between antiparallel spins for which the longitudinal lattice vector $\bar{G} = (0, 4k_F, 0)$ is involved in momentum conservation. All the couplings are dimensionless and normalized by $\pi v_F$.

In the framework of the extended electron gas model[20,47], the bare interactions superimpose a purely intrachain contribution and an interchain part between nearest-neighbour chains,

$$\begin{aligned} g_{i,\alpha}(\bar{k}_b) &\equiv g_{i,\alpha}(k_{b1}, k_{b2}, k_{b3}) \\ &= g_{i,\alpha} + 2\mathfrak{g}_{i,\alpha}\cos(k_{b1} - k_{b2}), \end{aligned} \tag{6}$$

where $i = 1, 2, 3$ and $\alpha = \parallel, \perp$ for the spins orientation. At the bare level, the transverse momentum dependence is coming solely from the interchain coupling, $\mathfrak{g}_{i,\alpha}$, a dependence that is modified on the Fermi surface by the RG flow of the coupling constants.

We will fix the range of the main parameters of the above model in order to simulate the experimental phase diagram of the Bechgaard salts in zero field. From band calculations[48,49], we shall take $E_F = v_F k_F = 3000$K for typical range of longitudinal Fermi energy and $t_b = 200$K for the amplitude of the transverse hopping along the $b$ direction. The antinesting amplitude $t'_b$ of the spectrum will be kept small compared to $t_b$ and will serve as a tuning parameter to mimic the effect of pressure. As for interactions, although it exists a large range of possible values able to generate a zero field phase diagram compatible with observations for the Bechgaard salts, we can follow the arguments of earlier works to obtain a reasonable set of figures for the intrachain couplings[20,43–46]. For instance, the bare intrachain backscattering amplitude can be fixed to $g_{1,\alpha} \simeq 0.32$, consistently with the range of values extracted from the enhancement of uniform susceptibility measurements[50]. The presence of a small dimerization gap $\Delta_D \ll E_F$, in the middle of an otherwise three-quarter filled band[48,49], leads to weak half-filling umklapp scattering, $g_{3\perp} \approx g_{1\perp}\Delta_D/E_F$[42,51,52]. This gives for umklapp the range of values $g_{3\perp} \approx 0.02...0.03$. The bare forward scattering amplitude can then be adjusted to $g_{2,\alpha} \simeq 0.64$, so that the calculated temperature scale of the SDW instability from RG at relatively low antinesting falls in the range of observed values $T_{\text{SDW}} \sim 10$K for the Bechgaard salts at low pressure[2]. With the above figures, a SDW to SCd sequence of instabilities can be obtained by the RG (e.g., $h = 0$ critical line of Fig. 1 obtained, at $g_{3\perp} = 0.025$), which is compatible with experiments[2,3]. Finally, regarding the amplitudes of repulsive interchain interaction $\mathfrak{g}_{i,\alpha}$, they will be taken variable, but kept small in comparison to their respective intrachain counterparts $g_{i,\alpha}$.

### B. Renormalization group equations

We apply a Kadanoff-Wilson RG approach to the extended quasi-1D electron model introduced in the previous subsection. The approach, which has been detailed in previous works[20,41,44] consists in the perturbative successive partial integrations of electron degrees of freedom in the partition function $Z$ on energy shells of thickness $\Lambda(\ell)d\ell$ at energy distance $\Lambda(\ell)=\Lambda_0 e^{-\ell}$ above and below the Fermi surface, where $\Lambda_0\equiv E_F$ is the initial cutoff fixed at the Fermi energy. Each energy shell is divided into $N_p$ patches, in which a transverse momentum integration is carried out for the internal variables of the logarithmically singular electron-electron (Copper) and electron-hole (Peierls) loops of the scattering channels.

At the one-loop level, the RG flow equations for the 3-momentum dependent scattering amplitudes $g_{i,\alpha}$ at non zero magnetic field are

$$\begin{aligned}
\partial_\ell g_{\parallel}(\bar{k}_b) =& -\langle\, g_{\parallel}(\bar{k}_{b1})g_{\parallel}(\bar{k}_{b2})\mathcal{I}^0_P(k_b,q_P)\,\rangle_{k_b} - \langle\, g_{1\perp}(\bar{k}_{b1})g_{1\perp}(\bar{k}_{b2})\mathcal{I}^{4h}_P(k_b,q_P)\,\rangle_{k_b}\\
&+\langle\, g_{\parallel}(\bar{k}_{b3})g_{\parallel}(\bar{k}_{b2})\mathcal{I}^0_C(k_b,q_C)\,\rangle_{k_b} - \langle\, g_{3\perp}(\bar{k}_{b1})g_{3\perp}(\bar{k}_{b2})\mathcal{I}^{4h}_P(k_b,-q_P)\,\rangle_{k_b}\\
\partial_\ell g_{1\perp}(\bar{k}_b) =& -\langle\, \big[g_{\parallel}(\bar{k}_{b1})g_{1b}(\bar{k}_{b2})+g_{\parallel}(\bar{k}_{b2})g_{1\perp}(\bar{k}_{b3})\big]\big(\mathcal{I}^0_P(k_b,-q_{bP})+\mathcal{I}^{4h}_P(k_b,-q_P)\big)/2\,\rangle_{k_b}\\
&+\langle\, \big[g_{2\perp}(\bar{k}_{b3})g_{1\perp}(\bar{k}_{b1})+g_{2\perp}(\bar{k}_{b4})g_{1\perp}(\beta_{b1})\big]\big(\mathcal{I}^{4h}_C(k_b,q_{bC})+\mathcal{I}^0_C(k_b,q_C)\big)/2\,\rangle_{k_b},\\
\partial_\ell g_{2\perp}(\bar{k}_b) =& -\langle\, g_{1\perp}(\bar{k}_{b3})g_{1\perp}(\bar{k}_{b4})\mathcal{I}^{4h}_C(k_b,q_C)\,\rangle_{k_b} + \langle\, g_{2\perp}(\bar{k}_{b3})g_{2\perp}(\bar{k}_{b4})\mathcal{I}^0_C(k_b,q_C)\,\rangle_{k_b}\\
&-\langle\, \big[g_{2\perp}(\bar{k}_{b1})g_{2\perp}(\bar{k}_{b3})+g_{3\perp}(\bar{k}_{b1})g_{3\perp}(\bar{k}_{b2})\big]\mathcal{I}^0_P(k_b,-q_P)\,\rangle_{k_b},\\
\partial_\ell g_{3\perp}(\bar{k}_b) =& -\langle\, g_{\parallel}(\bar{k}_{b1})g_{3\perp}(\bar{k}_{b2})\big(\mathcal{I}^0_P(k_b,q_P)+\mathcal{I}^{4h}_P(k_b,q_P)\big)/2\,\rangle_{k_b}\\
&+\langle\, g_{\parallel}(\bar{k}_{b2})g_{3\perp}(\bar{k}_{b1})\big(\mathcal{I}^{4h}_P(k_b,-q_P)+\mathcal{I}^0_P(k_b,-q_P)\big)/2\,\rangle_{k_b}\\
&-\langle\, g_{2\perp}(\bar{k}_{b5})g_{3\perp}(\bar{k}_{b6})\mathcal{I}^0_P(k_b,q'_P)+g_{2\perp}(\bar{k}_{b5})g_{3\perp}(\bar{k}_{b6})\mathcal{I}^0_P(k_b,-q'_P)\,\rangle_{k_b},
\end{aligned}\tag{7}$$

where $\langle\ldots\rangle_{k_b}=1/N_P\sum_{k_b}\ldots$ and

$$\begin{aligned}
\bar{k}_{b1}&=(k_b,k_{b4},k_{b1})\\
\bar{k}_{b2}&=(k_b,k_{b2},k_{b3})\\
\bar{k}_{b3}&=(k_{b1},k_{b2},k_b)\\
\bar{k}_{b4}&=(k_{b3},k_{b4},k_b)\\
\bar{k}_{b5}&=(k_b,k_{b4},k_{b2})\\
\bar{k}_{b6}&=(k_{b1},k_b,k_{b3})
\end{aligned}$$

$q_P^{(\prime)}=k_{b3}-k_{b2,1}=k_{b1,2}-k_{b4}$ and $q_C=k_{b1,3}+k_{b2,4}$. The on-shell Peierls ($\nu=P$) and Cooper ($\nu=C$) loops at finite $T$ and $h$ are given by

$$\begin{aligned}
\mathcal{I}^{\kappa h}_\nu(k_b,q^{(\prime)}_\nu) =& \frac{\Lambda(\ell)}{2}\sum_{\lambda=\pm1}\int_{k_b-\frac{\pi}{N_P}}^{k_b+\frac{\pi}{N_P}}\frac{dk_b}{2\pi}\\
&\times\frac{\theta(|\Lambda(\ell)+\lambda A^{\kappa h}_\nu|-\Lambda(\ell))}{2\Lambda(\ell)+\lambda A^{\mu h}_\nu}\\
&\times\Big[\tanh[\beta\Lambda(\ell)/2]+\tanh[\beta(\Lambda(\ell)/2+\lambda A^{\kappa h}_\nu/2)]\Big],
\end{aligned}\tag{8}$$

where for the loop field dependence, $\kappa=0,4$. Here $\theta(x)$ is the Heaviside function [$\theta(0)\equiv\frac{1}{2}$], and

$$\begin{aligned}
A^{\kappa h}_\nu(k_b,q^{(\prime)}_\nu) =& -\xi_b(k_b)-\eta_\nu\xi_b(\eta_\nu k_b+q^{(\prime)}_\nu)\\
&+\eta_\nu\xi_b(\eta_\nu k_{b2(4)}+q^{(\prime)}_\nu)+\xi_b(k_{b2(4)})+\kappa h,
\end{aligned}\tag{9}$$

for which $\eta_{P,C}=\pm1$.

To find out the nature of instabilities of the electron system, we compute the susceptibilities associated with the different possibilities of staggered density-wave and Cooper pairing correlations. Under successive partial integrations of the RG transformation, the linear coupling of pair of carriers to an external source field $h_\mu$ in the correlation channel $\mu$, yields the generic expression of the normalized temperature dependent susceptibility ($\tilde{\chi}_\mu=\pi v_F\chi_\mu$) at the wave vector $\boldsymbol{q}_\mu$:

$$\tilde{\chi}_\mu(\boldsymbol{q}_\mu)=2\int_0^\infty\langle z^2_\mu(k_b)\mathcal{I}^{\kappa_\mu h}_\mu(k_b,q_\mu)\rangle_{k_b}d\ell,\tag{10}$$

where $z_\mu(k_b)$ is the renormalization factor for the source-pair vertex. It obeys the flow equation

$$\partial_\ell z_\mu(k_b)=\frac{1}{2}\langle f_\mu(k'_b)g_\mu(\bar{k}'_b)\mathcal{I}^{\kappa_\mu h}_\mu(k'_b,q_\mu)\rangle_{k'_b}.\tag{11}$$

where $g_\mu$ is a momentum dependent combination of couplings for the correlation of the channel $\mu$ and $f_\mu(k_b)$ is

a form factor associated with the nature of correlations.

If we first look at the density-wave susceptibilities for which $f_\mu = 1$, we have in the charge sector, the site-centred ($\mu$ = CDW) and bond-centred ($\mu$ = BOW) charge-density wave susceptibilities, corresponding to the following combinations of couplings at the modulation (nesting) wave vector $\boldsymbol{q}_{\rm CDW} = \boldsymbol{q}_{\rm BOW} = (2k_F, \pi)$,

$$g_\mu \mathcal{I}_\mu^{\kappa_\mu h}\big|_{\mu={\rm CDW,BOW}} = -\big[g_{1\perp}(k'_b+\pi, k_b, k_b+\pi) + g_{\parallel}(k'_b+\pi, k_b, k_b+\pi) \pm g_{3\perp}(k'_b+\pi, k_b+\pi, k_b)\big]\mathcal{I}_P^{2h}(k'_b, \pi). \tag{12}$$

In the spin sector, the site-centred SDW susceptibility is likely to become singular. In presence of a magnetic field along $z$, the rotational symmetry is broken, which splits this susceptibility into longitudinal ($\tilde{\chi}_{{\rm SDW}_z}$) and transverse ($\tilde{\chi}_{{\rm SDW}_{xy}}$) components for which,

$$g_\mu \mathcal{I}_\mu^{\kappa_\mu h}\big|_{\mu={\rm SDW}_z,{\rm SDW}_{xy}} = \big[g_{2\perp}(k'_b+\pi, k_b, k_b+\pi) + g_{3\perp}(k'_b+\pi, k_b+\pi, k'_b)\big]\mathcal{I}_P^{2h,0}(k'_b, \pi) \tag{13}$$

If we consider in the second place the SC susceptibilities at $\boldsymbol{q}_\mu = 0$ that may be potentially singular in the presence of a magnetic field, we have for the singlet SC channel,

$$f_\mu g_\mu \mathcal{I}_\mu^{\kappa_\mu h} = -f_\mu(k'_b)\big[g_{1\perp}(k'_b, -k'_b, k_b) + g_{2\perp}(k'_b, -k'_b, k_b)\big]\mathcal{I}_C^{2h}(k'_b, 0). \tag{14}$$

For singlet s-wave susceptibility, $\tilde{\chi}_{\rm SS}$, $f_{\rm SS} = 1$; for d-wave susceptibility, $\tilde{\chi}_{\rm SCd}$, $f_{\rm SCd}(k_b) = \sqrt{2}\cos k_b$; for $g$-wave, $\tilde{\chi}_{\rm SCg}$, $f_{\rm SCg} = \sqrt{2}\cos 2k_b$, etc.

For the triplet channel at $\boldsymbol{q}_\mu = 0$, the SC susceptibilities are governed by the expressions

$$f_\mu g_\mu \mathcal{I}_\mu^{\kappa_\mu h} = f_\mu(k'_b)\big[g_{1\perp}(k'_b, -k'_b, k_b) - g_{2\perp}(k'_b, -k'_b, k_b)\big]\mathcal{I}_C^{2h}(k'_b, 0), \tag{15}$$

for antiparallel spins at $S_z = 0$, whereas for parallel spins at $S_z = \pm 1$,

$$f_\mu g_\mu \mathcal{I}_\mu^{\kappa_\mu h} = f_\mu(k'_b) g_{\parallel}(k'_b, -k'_b, k_b)\mathcal{I}_C^{0}(k'_b, 0), \tag{16}$$

For both cases, we have for $p$-wave susceptibility, $\tilde{\chi}_{\rm SCp}$, $f_{\rm SCp} = 1$; $f$-wave $\tilde{\chi}_{\rm SCf}$, $f_{\rm SCf} = \sqrt{2}\cos k_b$; etc.

Now for superconductivity, it is possible for electrons of opposite spins to form Cooper pairs with a nonzero momentum $\boldsymbol{q}_h = (2h/v_F, 0)$ in a FFLO state. This case requires a separate treatment of the pair vertex $z_\mu$[41], which actually splits into $z_\mu^{\uparrow\downarrow}$ and $z_\mu^{\downarrow\uparrow}$ for opposite spins. For singlet FFLO, these are governed by

$$\partial_\ell z_\mu^{\uparrow\downarrow(\downarrow\uparrow)}(k_b) = -\Big\langle f_\mu(k'_b)\big[g_{1\perp}(-k'_b, k'_b, -k_b) z_\mu^{\downarrow\uparrow(\uparrow\downarrow)}(k'_b) \times \mathcal{I}_C^{0(4h)}(k'_b, 0) + g_{2\perp}(-k'_b, k'_b, -k_b) z_\mu^{\uparrow\downarrow(\downarrow\uparrow)}(k'_b) \times \mathcal{I}_C^{4h(0)}(k'_b, 0)\big]\Big\rangle_{k'_b}, \tag{17}$$

where for $s$-wave FFLO, $f_{\rm sFFLO} = 1$; d-wave FFLO, $f_{\rm dFFLO}(k_b) = \sqrt{2}\cos k_b$; etc.

It is also possible in principle for triplet Cooper pairing with zero total spin projection, $S_z = 0$, to develop an inhomogeneous FFLO state following the equations

$$\partial_\ell z_\mu^{\uparrow\downarrow(\downarrow\uparrow)}(k_b) = \Big\langle f_\mu(k'_b)\big[g_{1\perp}(-k'_b, k'_b, -k_b) z_\mu^{\downarrow\uparrow(\uparrow\downarrow)}(k'_b) \times \mathcal{I}_C^{0(4h)}(k'_b, 0) - g_{2\perp}(-k'_b, k'_b, -k_b) z_\mu^{\uparrow\downarrow(\downarrow\uparrow)}(k'_b) \times \mathcal{I}_C^{4h(0)}(k'_b, 0)\big]\Big\rangle_{k'_b}, \tag{18}$$

where for $S_z = 0$ of $p$-wave, $f_{\rm pFFLO} = 1$; $f$-wave, $f_{\rm fFFLO} = \sqrt{2}\cos k_b$; etc.

The corresponding temperature dependent susceptibilities for the whole set of FFLO states take the following form

$$\tilde{\chi}_\mu(\boldsymbol{q}_h) = \int_0^\infty \langle\big[\,[z_\mu^{\uparrow\downarrow}(k_b)]^2 \mathcal{I}_{C\ell}^{0}(k_b, 0) + [z_\mu^{\downarrow\uparrow}(k_b)]^2 \mathcal{I}_{C\ell}^{4h}(k_b, 0)\big]\rangle_{k_b} d\ell. \tag{19}$$

## III. RESULTS FOR THE MODEL WITH INTRACHAIN INTERACTIONS

We first examine the results of integration of the above RG equations for $\mathfrak{g}_{i,\alpha} = 0$ in Eq. (6), namely when only intrachain interactions are present. In zero magnetic field the sequence of instabilities obtained for the input parameters of model given in Sec. II A coincides with the one found in previous works[45,46]. Thus, at relatively low antinesting amplitude $t'_b$ , a singularity in $\tilde{\chi}_{\rm SDW}$ at $\boldsymbol{q}_{\rm SDW} = (2k_F, \pi)$ is found from (10) and (13). The critical temperature $T_{\rm SDW}$ is traced in Fig. 1, which decreases monotonically by increasing $t'_b$. Close to the critical value $t'^*_b$ ($\simeq$ 32K, $t'^*_b/t_b \simeq 0.16$), $T_{\rm SDW}$ drops rapidly until $t'^*_b$ is reached and the system becomes unstable against the formation of a SCd state, with the divergence of $\tilde{\chi}_{\rm SCd}$ coming from the singularity of (14) at a maximum $T_c \sim 1$K [See Fig. 2 (a)]; $T_c$ then closes the sequence by its steady decrease with $t'_b > t'^*_b$, as shown in Fig. 1. The typical momentum profile of the SC combination of couplings $g_{\rm SCd}(k'_b, -k'_b, k_b)$ in the $k_b k'_b$ plane for temperature close to $T_c$, plane shows pronounced modulations compatible with the form factor $f_{\rm SCd}$ for SCd superconductivity. According to Fig. 3 (b), this modulation in momentum space is intimately connected with the amplitude and anisotropy developed by umklapp, $g_{3\perp}(k'_b, -k'_b, k_b)$, along the lines $k'_b = \pm k_b \pm \pi$, and which from (13), is directly involved in the strength of SDW correlations responsible for SCd pairing.

For non zero magnetic field, the SDW instability at low $t'_b$ is now taken place for spins oriented in the $xy$ plane transverse to the field. The amplitude of $T_{\rm SDW}$ obtained in Fig. 1 is slightly reinforced compared to zero field. This reinforcement of antiferromagnetism agrees

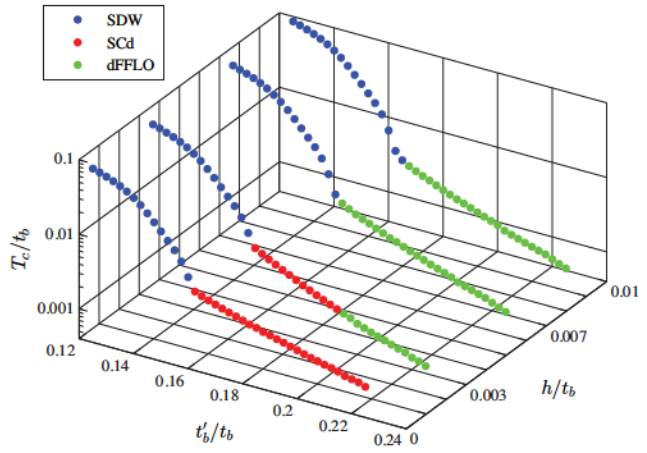


FIG. 1. The phase diagram of the quasi-1D electron gas model with intrachain interactions as a function of magnetic field.

with an increase of the critical $t_b'^*$ with $h$. At very low field, this presents as an increase of the maximum SCd $T_c$ with $h$, which is possible because orbital pair breaking is absent from the model. However, the SDW→SCd sequence of instabilities is rapidly altered under field. As shown in Fig. 1, where an incursion of a dFFLO instability takes place along the antinesting axis, as signalled by a singularity of $\tilde{\chi}_{\rm dFFLO}(\boldsymbol{q}_h)$ coming from (17) at a nonzero pairing momentum $\boldsymbol{q}_h = (2h/v_F, 0)$. The related divergence occurs at a $T_c$ that is steadily suppressed under field, but whose amplitude is significantly enhanced compared to mean-field calculations in which the interplay between the Cooper and density-wave pairing is neglected[34,41]. From Fig. 3 (c), the combination of couplings $g_{1\perp}(k'_b, -k'_b, k_b) + g_{2\perp}(k'_b, -k'_b, k_b)$ entering in (17) for singlet FFLO superconductivity presents also d-wave like modulations in the $k_b k'_b$ plane, but of weaker amplitude compared to the zero field situation.

Regarding triplet superconductivity, we see from Fig. 2 (a) that apart from a regular enhancement of $\chi_{\rm SCf}$ at low temperature no crossover to triplet superconductivity is found under field when only intrachain interactions are present. This result differs from the mean-field phenomenology when both singlet and triplet pairing interactions are present[30–32]

### A. $H$-$T$ phase diagram

In the superconducting sector of the phase diagram of Fig. 1, one can follow the critical temperature $T_c(h)$ with field, or conversely the upper critical field profile $h_{c2}(T)$ with temperature of Fig. 4. At very low field, the slope $dh_{c2}/dT$ is at first positive, indicating that $T_c$ increases with $h$. This results from the strengthening of SDW correlations, which as the source of Cooper pairing in the SCd channel, exceeds the field pair breaking effect on the singlet state in (10) and (14). As previously mentioned, this enhancement of $T_c$ takes place because orbital effect caused by the field is absent in the present model. At higher field, however, singlet pair breaking dominates and $T_c$ decreases, as shown in Fig. 4. The values of $h_{c2}$ are systematically above the mean-field result for the pure Pauli limit (dashed lines of Fig. 4)[53]. Instead of extrapolating to a field close to $h_P$ in the low temperature limit, $h_{c2}$ continues until a crossover to an inhomogeneous $d$FFLO state is achieved. In the dFFLO regime, $h_{c2}$ not only exceeds the Pauli limiting field $h_P(\simeq 1.25T_c)$, but also the Pauli limit of FFLO state for isotropic 2D ($h_P \simeq 1.78T_c$) and 3D ($h_P \simeq 1.34T_c$) superconductors[53].

Another important feature of the present results[41], which contrasts with mean-field type of calculations, is the non-universality of the ratio $h_{c2}/T_c$, as a function of either the antinesting amplitude $t'_b$ [Fig. 4 (a)] or inter-

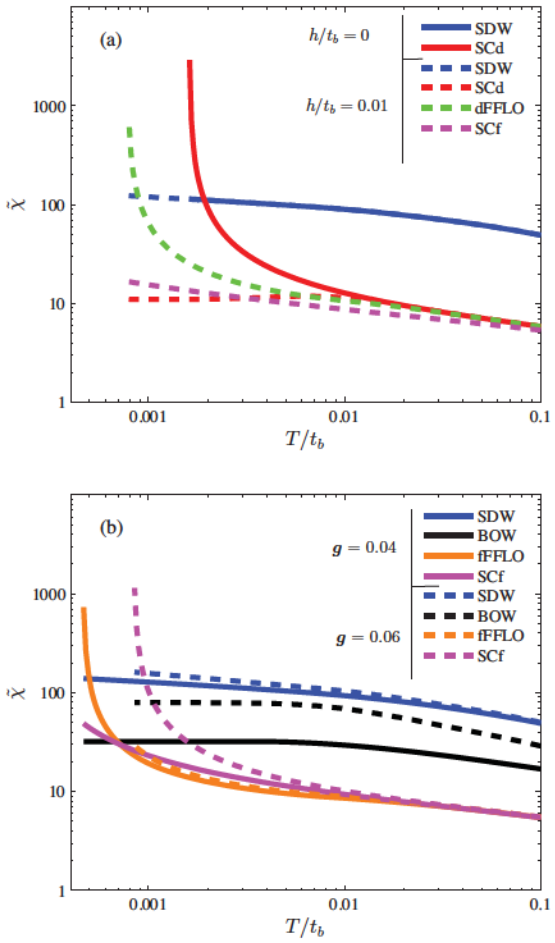


FIG. 2. Temperature dependence of the susceptibilities in the normal phase of the superconducting sector of the phase diagram at $t'_b/t_b = 0.21$. (a): For intrachain couplings only, $\mathfrak{g}_i = 0$ at zero and finite magnetic fields. (b): For finite interchain couplings $\mathfrak{g}_i \neq 0$ at $h/t_b = 0.01$.

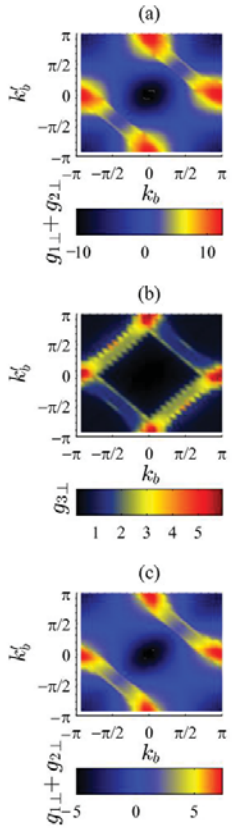


FIG. 3. Low temperature renormalized effective scattering amplitudes at $t_b'/t_b = 0.21$ for singlet Cooper pairing $g_{1\perp}(k_b', -k_b', k_b) + g_{2\perp}(k_b', -k_b', k_b)$ in the $k_b, k_b'$ plane for the normal phase of (a) : SCd ($h = 0$); (b): umklapp amplitude $g_{3\perp}(k_b', -k_b', k_b)$ at $h = 0$; (c) : dFFLO ($h/t_b = 0.01$).

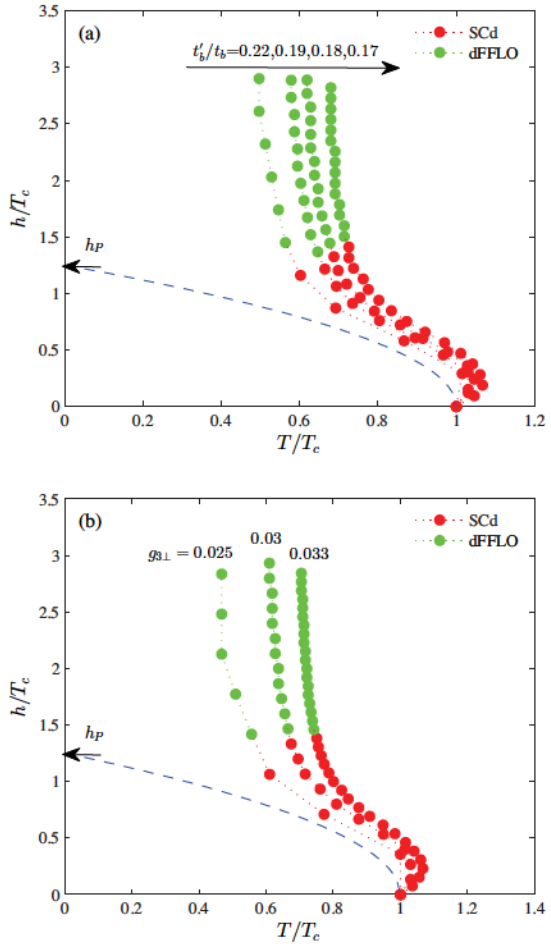


FIG. 4. The variation of the normalized upper critical field $h_{c2}/T_c$ with temperature for (a) : various $t_b'$ and (b) : different amplitudes of umklapp scattering $g_{3\perp}$ at $t_b'/t_b = 0.22$. The dashed line is mean-field result for the upper critical field in the Pauli limit.

action [e.g., $g_{3\perp}$, in Fig. 4 (b)]. At the root of this lack of universality stands SDW fluctuations as the source of Cooper pairing. In this respect, the RG flow equations (7) tell us that, in contrast to mean-field theory, the coupling components defining the effective singlet pairing interaction $g_{1\perp} + g_{2\perp}$ entering in $\tilde{\chi}_{\rm dFFLO}$ from (17), are continuously altered by SDW correlations in the course of decreasing $\Lambda(\ell)$ (See also Fig. 3). The initial values of couplings or antinesting modify this energy scale dependent interference effect. This indicates that in practice, the observation of the lack of universality in the anomalous upper critical field, as a function of the applied pressure in the Bechgaard salts for instance, would be a distinctive signature of fluctuation induced unconventional pairing in the material[41]. On experimental side, there are some indications that this is indeed the case[54].

## IV. INTERCHAIN INTERACTIONS

We now turn to the influence of interchain electron-electron repulsive interactions introducing a non zero $\mathfrak{g}_{i,\alpha}$ in the interaction parameters (6) of the extended quasi-1D electron gas model[20,47]. We shall take for simplicity the transverse backward and forward scattering amplitudes equal by putting, $\mathfrak{g}_{1,\alpha} = \mathfrak{g}_{2,\alpha} \equiv \mathfrak{g}$, for both parallel ($\alpha = \|$) and perpendicular ($\alpha = \perp$) spins. As for the transverse umklapp amplitude, we have the following ratio with backward scattering, $\mathfrak{g}_{3\perp}/\mathfrak{g} = g_{3\perp}/g_{1\perp}$, which is the same as for intrachain interactions discussed in Sec. III A.

We first review the case in zero magnetic field, which was examined by Nickel *et al.*[20]. By increasing the amplitude of $\mathfrak{g}$, the SDW→SCd sequence of instabilities tuned by $t_b'$ is modified from the relatively small value, $\mathfrak{g} \simeq 0.04$, of interchain repulsion. According to Fig. 5 (a), a triplet $f$-wave instability in $\tilde{\chi}_{\rm SCf}$ of (15-16) gets into the sequence that becomes SDW→SCd→SCf. By increasing $\mathfrak{g}$, it transforms into SDW→SCf, where SDW is connected directly to SCf at the quantum critical point $t_b'^*$. The emergence of SCf state emerges from the rise of BOW fluctuations which are detrimental to singlet SCd pair-

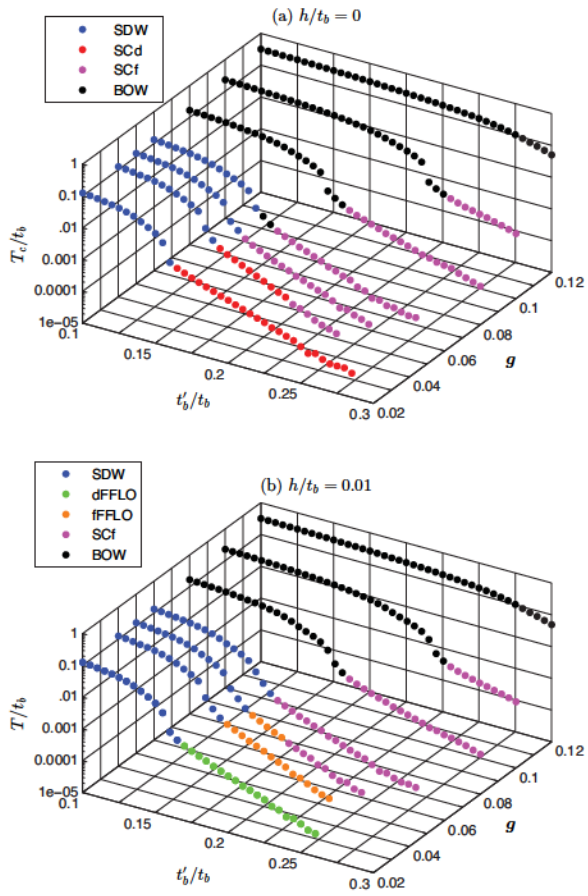


FIG. 5. Phase diagram of the extended quasi-electron gas model at (a): $h = 0$, and (b): $h/t_b = 0.01$.

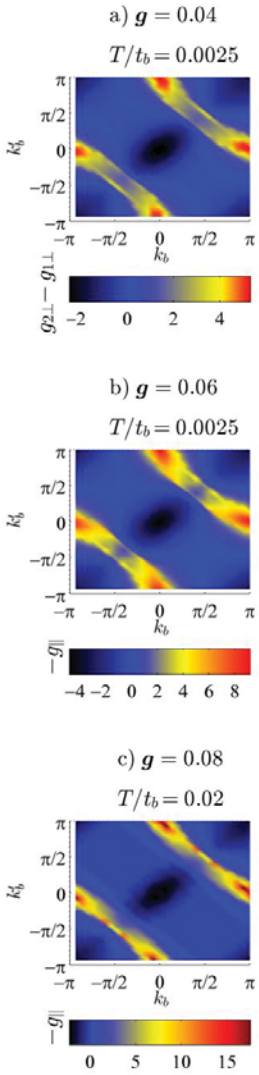


FIG. 6. Low temperature effective scattering amplitudes close to $T_c$ in the momentum space at $h/t_b = 0.01$, for: (a) $g_{2\perp}(k'_b, -k'_b, k_b) - g_{1\perp}(k'_b, -k'_b, k_b)$ for fFFLO ; (b) and (c) $g_{\parallel}(k'_b, -k'_b, k_b)$ for $SCf_1$.

ing. This sequence is soon modified by the incursion of a BOW instability from (12) in the sequence near $t'^*_b$, as shown in Fig. 5 (a). By increasing further $\mathfrak{g}$, near 0.1, makes the SDW unstable and yields the sequence BOW→SCf. This is also associated with the smearing of the quantum critical region to the benefit of the BOW ordering. Apart from few details at the quantitative level, the present results confirm those of Nickel *et al*[20].

If we now switch on the effect of magnetic field, we observe that the range of influence of triplet superconductivity is enlarged along the $\mathfrak{g}$ axis. Thus from $\mathfrak{g} \simeq 0.04$ and for $h/t_b \gtrsim 0.004$, the dFFLO state of Fig. 1 becomes unstable against the formation of a triplet fFFLO, $S_z = 0$, state governed by the divergence of (18), as shown in Fig. 2 (b) at $\mathfrak{g} = 0.04$. The related combination of couplings $g_{2\perp}(k'_b, -k'_b, k_b) - g_{1\perp}(k'_b, -k'_b, k_b)$ in the $k'_b k_b$ plane is plotted in Fig. 6 (a) close to $T_c(h)$. One observes pronounced modulations in momentum space compatible with $f_{\text{fFFLO}} = \sqrt{2}\cos k_b^{(\prime)}$ and peaks at $k_b^{(\prime)} = 0, \pm\pi$, along the lines $k'_b = -k_b \pm \pi$, which results mainly from SDW scattering. According to Fig. 2 (b), in this range of $\mathfrak{g}$, SDW correlations are by far dominant down to very close to $T_c(h)$ and act as the main source of interchain pairing for the fFFLO state at $S_z = 0$. It is worth mentioning that its existence has not been reported from mean-field theory analysis[34]. However, the FFLO mixing with triplet superconductivity has been found from this analysis and from DMRG in the two-legs ladders systems at strong coupling[55].

When $\mathfrak{g}$ further increases to reach $\mathfrak{g} \simeq 0.05$, the fFFLO state becomes in turn unstable to the benefit of uniform triplet $SCf_1$ state at $S_z = 1$, and a sequence of instabilities, SDW→$SCf_1$ along $t'_b$, as indicated in Fig. 5 (b). This sequence in the above $\mathfrak{g}$ range is similar to the one found in Fig. 5 (a) in the absence of field. Following (16), the $SCf_1$ pairing is directly connected to the combination of couplings $g_{\parallel}(k'_b, -k'_b, k_b)$ for parallel spins. From Fig. 6 (b), $g_{\parallel}$ presents strong modulations in the $k'_b k_b$

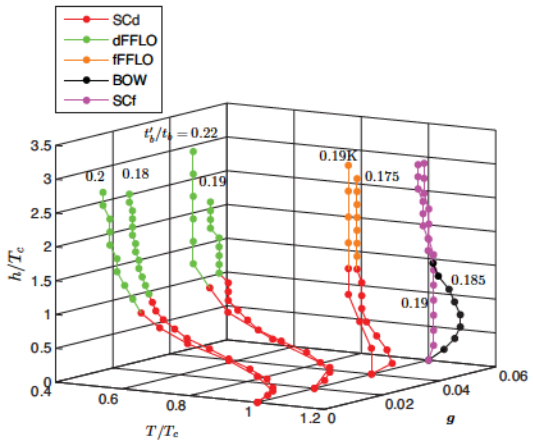


FIG. 7. The evolution of $h_{c2}$ *vs* temperature for various $t'_b$ and as a function of interchain coupling $\mathfrak{g}$.

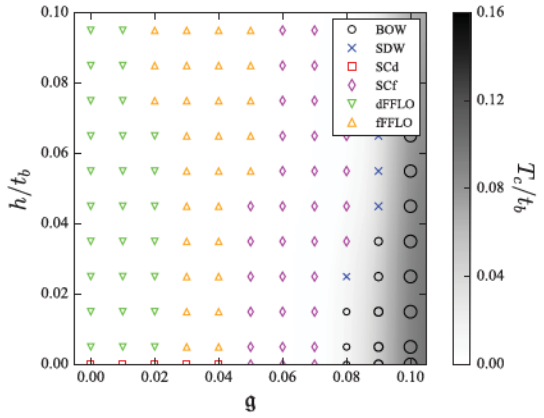


FIG. 8. The phase diagram in the $\mathfrak{g} - h$ plane for $t'_b/t_b = 0.2$.

plane near $T_c(h)$, which are consistent with the form factor $f_{\rm SCf} = \sqrt{2}\cos k_b^{(\prime)}$. As meant by the couplings involved in the BOW susceptibility in (12), peaks along the lines $k'_b = -k_b \pm \pi$ are consistent with the presence of strong BOW correlations which acts as the main source of $SCf_1$ pairing[18,20,35]. As displayed in Fig. 2 (b), the amplitude of BOW correlations are close in amplitude to SDW.

At $\mathfrak{g} \gtrsim 0.08$, the SDW state becomes in its turn unstable at low $t'_b$ in favour of a BOW state and the sequence BOW$\rightarrow$SCf$_1$ as a function of $t'_b$. The importance of BOW growth at the expense of SCf along the $\mathfrak{g}$ axis, as found in the absence of field [Figs 5 (a) and (b)]. This is reflected in Fig. 6 (c) for the modulation of the relevant coupling, $g_{\parallel}$, for $SCf_1$ in the $k'_b k_b$ plane, which is less pronounced on the negative side.

It is instructive to trace the temperature dependence of the critical field $h_{c2}(T)$ for the above selected ranges of interchain coupling $\mathfrak{g}$. At very low $\mathfrak{g}$, the Fig. 7 shows that under field, we have the expected sequence of instabilities SCd$\rightarrow$dFFLO previously found in Fig. 4 at $\mathfrak{g} = 0$. The violation of the Pauli limit in the dFFLO regime is dependent on antinesting and is reduced upon increasing $t'_b$. At higher $\mathfrak{g}$, when fFFLO becomes possible, the crossover of SCd to fFFLO under field is much more rapid and the violation of the Pauli limit, consequently more pronounced, with an almost vertical upturn of $h_{c2}$. Increasing further $\mathfrak{g}$, the vertical rise of the $h_{c2}$ line for $SCf_1$ does not lead to a crossover to another state, except for $t'_b$ close to the junction with BOW order, where one can start with a BOW state at low field and which is followed at sufficiently high field by a reentrant triplet $SCf_1$ state.

By way of closing the section, we give in Fig. 8 the phase diagram in the $\mathfrak{g}h$ plane which displays the transformation of ordered phases under magnetic field when the interchain interaction is varied at a fixed at $t'_b$ in the superconducting sector at $\mathfrak{g} = 0$. From the Figure, we observe that for a sizeable interval of weak repulsive $\mathfrak{g}$, the possible modifications of superconductivity expands under magnetic field to the benefit of FFLO states. These are not exclusively restricted to the $d$-wave sector, but also belong to the triplet $f$-wave sector at $S_z = 0$. Thus at relatively weak interchain repulsion, the sequences SCd $\rightarrow$ dFFLO, SCd $\rightarrow$ dFFLO $\rightarrow$ fFFLO and SCd $\rightarrow$ fFFLO are possible transformations of superconductivity within an accessible range of magnetic field ($h/t_b < 0.1$). It is worth noting that no SCd $\rightarrow$ SCf transition, from singlet to triplet uniform superconductivity, is predicted under field over all the range of $\mathfrak{g}$ covered, this at variance with previous mean-field results[34]. Furthermore, as previously discussed for stronger interchain interaction, namely when instead of superconductivity, a BOW order is favoured in zero field, the sequences BOW $\rightarrow$ SCf and BOW $\rightarrow$ SDW$_{xy}$ $\rightarrow$ SCf can be found showing the stabilization of uniform SCf from density-wave phases under sufficiently high magnetic field.

## V. SUMMARY AND CONCLUDING REMARKS

In this work we employed the weak coupling renormalization group method to examine the possible instabilities of the extended quasi-1D electron gas model with half-filling umklapp scattering and the presence of a magnetic field. The field is Zeeman coupled to spin degrees of freedom exclusively, which simulates the weakness of orbital pair breaking effect that characerizes specific planar field orientations in low dimensional superconductors like the Bechgaard salts.

For purely intrachain repulsive interactions, the SCd state of the electron gas is suppressed under field, evolving toward inhomogenous d-wave FFLO superconductivity rather than uniform triplet superconductivity. The dFFLO state is accompanied by a violation of the Pauli limiting field $H_P$ for singlet superconductivity, which is particularly enhanced by the constructive quantum interference between Cooper pairing and antiferromagnetic

fluctuations. The enhancement is then found to scale in a non universal way with both the interaction and the distance to the quantum critical point joining superconductivity and the spin-density-wave state in the phase diagram. These results obtained in the presence of half-filling umklapp scattering broaden the impact of an earlier study made at incommensurate band filling[41].

For the extended version of the quasi-electron electron gas model when interchain Coulomb interaction is included and a transition from d-wave to triplet $f$-wave superconductivity becomes possible. We find that its range of stability is somewhat enlarged by the magnetic field as one moves along the axis of interchain repulsion. The calculations reveal the existence of an intermediate $f$-wave FFLO state of zero total spin projection, which emerges within a finite interval of interchain Coulomb repulsion interaction before the onset of uniform $f$-wave superconductivity.

The possible field-induced FFLO states obtained provide an interesting avenue of interpretation for the persistant superconductivity in resistivity experiments observed well above the Pauli limiting field of the Bechgaard salts when they are very close to their quantum critical point. The results also allow the possibility for a direct experimental test of the theory from future resistivity experiments that would be conducted on a large pressure interval, in order to check if the anomalous enhancement of the upper critical field is suppressed in the limit of high pressure, as predicted[41]. Existing resitivity data on a $(TMTSF)_2PF_6$[54], though obtained in a limited range of pressures close to the critical value, head in this direction.

From the renormalization group viewpoint developed in the present work, it is not clear a priori which one of the $d$ and $f$ FFLO states is likely to be more favorable in systems like the Bechgaard salts. Both phases are occurring relatively close one another and both are falling in a reasonable range of parameters for these materials. It must be said, however, that the currently observed violation of the Pauli limit in the Bechgaard salts is significantly less pronounced than predicted in the triplet case. This would in turn tip the balance in favour of the singlet dFFLO scenario for the high field superconducting phase in the Bechgard salts.

## ACKNOWLEDGMENTS

We thank Samuel Desrosiers for his help on computational aspects of this work. C.B. thanks the National Science and Engineering Research Council of Canada (NSERC) under Grant No. RGPIN-2016-06017, and the Réseau Québécois des Matériaux de Pointe (RQMP) for financial support. Simulations were performed on computers provided by Canadian Foundation for Innovation, the Ministère de l'Éducation des Loisirs et du Sport (Québec), Calcul Québec, and Compute Canada.

[1] D. Jérome, A. Mazaud, M. Ribault, and K. Bechgaard, J. Phys. (Paris) Lett. **41**, L95 (1980).
[2] D. Jérome and H. J. Schulz, Adv. Phys. **31**, 299 (1982).
[3] N. Doiron-Leyraud, P. Auban-Senzier, S. René de Cotret, C. Bourbonnais, D. Jérome, K. Bechgaard, and L. Taillefer, Phys. Rev. B **80**, 214531 (2009).
[4] V. J. Emery, Synth. Met. **13**, 21 (1986).
[5] M. T. Béal-Monod, C. Bourbonnais, and V. J. Emery, Phys. Rev. B **34**, 7716 (1986).
[6] L. G. Caron and C. Bourbonnais, Physica B + C **143**, 453 (1986).
[7] D. J. Scalapino, E. Loh, and J. E. Hirsch, Phys. Rev. B **34**, R8190 (1986).
[8] C. Bourbonnais and L. G. Caron, Europhys. Lett. **5**, 209 (1988).
[9] M. Takigawa, H. Yasuoka, and G. Saito, J. Phys. Soc. Jpn **56**, 873 (1987).
[10] Y. Hasegawa and H. Fukuyama, J. Phys. Soc. Jpn. **56**, 877 (1987).
[11] M.-Y. Choi, P. Chaikin, S. Z. Huang, P. Haen, E. M. Engler, and R. L. Greene, Phys. Rev. B **25**, 6208 (1982).
[12] S. Tomic, D. Jerome, D. Mailly, M. Ribault, and K. Bechgaard, J. Phys. (Paris) Coll. 44, C31075 (1983).
[13] C. Coulon, P. Delhaes, J. Amiell, J. P. Manceau, J. M. Fabre, and L. Giral, J. Phys. (Paris) **43**, 1721 (1982).
[14] N. Joo, P. Auban-Senzier, C. R. Pasquier, D. Jérome, and K. Bechgaard, Europhys. Lett. **72**, 645 (2005).
[15] S. Belin and K. Behnia, Phys. Rev. Lett. **79**, 2125 (1997).
[16] F. L. Pratt, T. Lancaster, S. J. Blundell, and C. Baines, Phys. Rev. Lett. **110**, 107005 (2013).
[17] A. A. Abrikosov, J. Low Temp. Phys **53**, 359 (1983).
[18] K. Kuroki, R. Arita, and H. Aoki, Phys. Rev. B **63**, 094509 (2001); S. Onari, R. Arita, K. Kuroki, and H. Aoki, Phys. Rev. B **70**, 094523 (2004); Y. Tanaka and K. Kuroki, Phys. Rev. B **70**, 0605502(R) (2004).
[19] Y. Fuseya and Y. Suzumura, J. Phys. Soc. Jpn. **74**, 1263 (2005).
[20] J. C. Nickel, R. Duprat, C. Bourbonnais, and N. Dupuis, Phys. Rev. Lett. **95**, 247001 (2005); Phys. Rev. B **73**, 165126 (2006).
[21] I. J. Lee, S. Brown, W. G. Clark, M. J. Strouse, M. J. Naughton, W. Kang, and P. M. Chaikin, Phys. Rev. Lett. **88**, 17004 (2002).
[22] R. Brusetti, M. Ribault, D. Jerome, and K. Bechgaard, J. Phys. (Paris) **43**, 801 (1982).
[23] L. P. Gorkov and D. Jérome, J. Phys. Lett. **46**, L643 (1985).
[24] I. J. Lee, M. J. Naughton, G. M. Danner, and P. M. Chaikin, Phys. Rev. Lett. **78**, 3555 (1997).
[25] I. J. Lee, A. P. Hope, M. J. Leone, and M. J. Naughton, Synth. Met. **70**, 747 (1995).
[26] I. J. Lee, P. M. Chaikin, and M. J. Naughton, Phys. Rev. B **62**, R14669 (2000).
[27] A. G. Lebed, JETP Lett. **44**, 114 (1986).
[28] N. Dupuis, G. Montambaux, and C. A. R. S. de Melo, Phys. Rev. Lett. **70**, 2613 (1993).

[29] J. Shinagawa, Y. Kurosaki, F. Zhang, C. Parker, S. E. Brown, D. Jérome, K. Bechgaard, and J. B. Christensen, Phys. Rev. Lett. **98**, 147002 (2007).
[30] H. Shimahara, Phys. Rev. B **61**, R14936 (2000).
[31] N. Belmechri, G. Abramovici, M. Heritier, S. Haddad, and S. Charfi-Kaddour, EPL **80**, 37004 (2007).
[32] N. Belmechri, G. Abramovici, and M. Heritier, EPL **82**, 47009 (2008).
[33] H. Aizawa, K. Kuroki, and Y. Tanaka, Phys. Rev. B **77**, 144513 (2008).
[34] H. Aizawa, K. Kuroki, T. Yokoyama, and Y. Tanaka, Phys. Rev. Lett. **102**, 016403 (2009).
[35] K. Kajiwara, M. Tsuchiizu, Y. Suzumura, and C. Bourbonnais, J. Phys. Soc. Jpn. **78**, 104702 (2009).
[36] A. G. Lebed, Phys. Rev. Lett. **107**, 087004 (2011).
[37] S. Yonezawa, S. Kusaba, Y. Maeno, P. Auban-Senzier, C. Pasquier, K. Bechgaard, and D. Jerome, Phys. Rev. Lett. **100**, 117002 (2008).
[38] S. Yonezawa, S. Kusaba, Y. Maeno, P. Auban-Senzier, C. Pasquier, and D. Jerome, J. Phys. Soc. Jpn **77**, 054712 (2008).
[39] S. Yonezawa, Y. Maeno, K. Bechgaard, and D. Jerome, Phys. Rev. B **85**, 140502(R) (2012).
[40] D. Jérome and S. Yonezawa, C. R. Physique **17**, 357 (2016).
[41] Y. Fuseya, C. Bourbonnais, and K. Miyake, Europhys. Lett. **100**, 5708 (2012).
[42] V. J. Emery, R. Bruinsma, and S. Barisic, Phys. Rev. Lett. **48**, 1039 (1982).
[43] C. Bourbonnais and A. Sedeki, Phys. Rev. B **80**, 085105 (2009).
[44] A. Sedeki, D. Bergeron, and C. Bourbonnais, Phys. Rev. B **85**, 165129 (2012).
[45] M. Shahbazi and C. Bourbonnais, Phys. Rev. B **92**, 195141 (2015).
[46] M. Shahbazi and C. Bourbonnais, Phys. Rev. B **94**, 195153 (2016).
[47] L. P. Gor'kov and I. E. Dzyaloshinskii, Sov. Phys. JETP **40**, 198 (1974).
[48] P. M. Grant, J. Phys. (Paris) Coll. **44**, C3847 (1983).
[49] L. Ducasse, A. Abderrabba, J. Hoarau, M. Pesquer, B. Gallois, and J. Gaultier, J. Phys. C **19**, 3805 (1986).
[50] P. Wzietek, F. Creuzet, C. Bourbonnais, D. Jerome, K. Bechgaard, and P. Batail, J. Phys. I **3**, 171 (1993).
[51] S. Barisic and S. Brazovskii, in *Recent Developments in Condensed Matter Physics*, Vol. 1, edited by J. T. Devreese (Plenum, New York, 1981) p. 327.
[52] K. Penc and F. Mila, Phys. Rev. B **50**, 11 429 (1994).
[53] Y. Matsuda and H. Shimahara, J. Phys. Soc. Jpn. **76**, 051005 (2007).
[54] I. J. Lee, M. J. Naughton, and P. M. Chaikin, Phys. Rev. Lett. **88**, 207002 (2002).
[55] G. Roux, S. White, S. Capponi, and D. Poilblanc, Phys. Rev. Lett. **97**, 087207 (2006).

Chapter 3

# Boltzmann equation and transport

## 3.1 Transport in strongly correlated systems

In strongly correlated electron systems the transport properties frequently show deviations from the normal Fermi-liquid behavior observed in conventional metals. A striking example is the case of high $T_c$ superconductors whose almost all transport coefficients have exhibited deviations from the conventional Fermi-liquid ones: the resistivity in the normal (high temperature) state of the cuprate superconductors increases linearly in temperature, and both Hall coefficient ($R_H$) and Seebeck coefficient ($Q$) vary strongly with temperature and even in some compounds can show sign reversal [137, 138, 139, 140]. Non-Fermi-liquid-like behaviors are also found in other strongly correlated systems such as organic superconductors [141, 142, 143, 130, 21, 67] and heavy-fermion systems [144]. Remarkably, non-Fermi-liquid behavior is often found near the so called quantum critical point in the phase diagram, where a magnetic ordering temperature is driven to zero by tuning some external control parameter [145, 146, 147, 148, 149, 6]. The simultaneous appearance of superconductivity and non-Fermi-liquid behavior in the vicinity of such a quantum critical point indicates a link between unconventional transport at low temperatures and quantum fluctuations. Studying the transport phenomena in these systems give us important information about the nature of electronic correlations between the carriers.

The regime of the phase diagram with strong correlations is often regarded as a renormalized Fermi-liquid regime with strong fluctuations (superconducting and/or magnetic). The anomalous transport can thus be described by a Boltzmann theory which focuses on the coherent part of low-energy quasi-particles. In this work we investigate the anomalous transport properties in a quasi-one-dimensional Fermi liquid with strong scattering anisotropy by a full solution of the

semi-classical Boltzmann equation, which stands beyond the simple relaxation time approximation, for both the incoming and outgoing scattering processes.

## 3.2 Boltzmann equation

One of the simplest approaches to transport phenomena is the semi-classical Boltzmann theory. In terms of statistical physics, the semi-classical Boltzmann equation describes the time evolution of the Fermi distribution function $f(\boldsymbol{r},\boldsymbol{k},t)$ where $f(\boldsymbol{r},\boldsymbol{k},t)d\boldsymbol{r}d\boldsymbol{k}$ is the number of electrons (wave packets) at point $\boldsymbol{r}$ with wave number $\boldsymbol{k}$ in the phase space volume $d\boldsymbol{r}d\boldsymbol{k}$. Its time variation is due to three effects: diffusion, drift, and scattering. Diffusion is caused by any gradient in the electron concentration from point to point, whereas the drift is caused by external forces (diffusion in $\boldsymbol{k}$ space). Collisions change the distribution function due to mutual interaction between electrons or through their collision with obstacles in the lattice. The total distribution change rate is therefore given by:

$$\begin{aligned}\left(\frac{df(\boldsymbol{r},\boldsymbol{k},t)}{dt}\right) &= \left(\frac{\partial f}{\partial t}\right)_{\text{diffusion}} + \left(\frac{\partial f}{\partial t}\right)_{\text{drift}} + \left(\frac{\partial f}{\partial t}\right)_{\text{collisions}} \\ &= -\boldsymbol{v}_k \cdot \frac{\partial f}{\partial \boldsymbol{r}} - \dot{\boldsymbol{k}} \cdot \frac{\partial f}{\partial \boldsymbol{k}} + \left(\frac{\partial f}{\partial t}\right)_{\text{collisions}},\end{aligned} \tag{3.1}$$

where $\dot{\boldsymbol{k}} = \frac{e}{\hbar}(\boldsymbol{E} + \frac{1}{c}\boldsymbol{v}_k \times \boldsymbol{H})$ with $e$ ($e < 0$) the charge of electron and $\boldsymbol{E}$ and $\boldsymbol{H}$ as the electric and magnetic field. The collision term in equation (3.1) represents different microscopic scattering mechanisms between quasi-particles and is called the collision integral.

Let us first consider, for example, the case of impurity-scattering. Defining the scattering rate $\Gamma_{k\to k'}$ with which a quasi-particle scatters off an impurity scatterer from the momentum state $\boldsymbol{k}$ to the state $\boldsymbol{k}'$, the rate of change of distribution function due to scattering can be described as follows:

$$\left(\frac{\partial f(\boldsymbol{k})}{\partial t}\right)_{\text{collisions}} = \sum_{\boldsymbol{k}'} \left\{\Gamma_{k'\to k} f(\boldsymbol{k}')[1 - f(\boldsymbol{k})] - \Gamma_{k\to k'} f(\boldsymbol{k})[1 - f(\boldsymbol{k}')]\right\}, \tag{3.2}$$

where the occupation factors $f$ and $1 - f$ assure that the quasi-particle is going from an occupied to an empty state. Note that from now on we have dropped the variables $\boldsymbol{r}$ and $t$ from the distribution function for simplicity. The scattering rate is obtained from the well-known Fermi Golden Rule based on first-order time-dependent perturbation theory:

$$\Gamma_{k\to k'} = \frac{2\pi}{\hbar} |\langle \boldsymbol{k}|W|\boldsymbol{k}'\rangle|^2 \delta(\varepsilon_k - \varepsilon_{k'}), \tag{3.3}$$

where it is assumed that the perturbation $W$ does not vary with time after its sudden inset. In the presence of static external forces, a steady state occurs due to the compensation of external forces through dissipative quasi-particle interactions after sufficiently long time and thus $(\frac{df(\boldsymbol{r},\boldsymbol{k},t)}{dt})$ in equation (3.1) must vanish. In other words, in this steady state the distribution function does not depend explicitly on time even though the system remains in a non-equilibrium configuration. From equations (3.1) and (3.2), we obtain the following Boltzmann equation of integro-differential form:

$$\boldsymbol{v}_k \cdot \frac{\partial f}{\partial \boldsymbol{r}} + \frac{e}{\hbar}(\boldsymbol{E} + \frac{1}{c}\boldsymbol{v}_k \times \boldsymbol{H}) \cdot \frac{\partial f}{\partial \boldsymbol{k}} = \sum_{k'} \{\Gamma_{k'\to k} f(\boldsymbol{k}')[1 - f(\boldsymbol{k})] - \Gamma_{k\to k'} f(\boldsymbol{k})[1 - f(\boldsymbol{k}')]\}, \tag{3.4}$$

Now, we discuss the scattering between two quasi-particles in an interacting Fermi gas contained in volume of V, in which one particle scatters from a momentum state $\boldsymbol{k}$ to the momentum state $\boldsymbol{k}_3$ and another particle scatters from the state $\boldsymbol{k}_2$ to $\boldsymbol{k}_4$, as well as the inverse process. The first process reduces $f(\boldsymbol{k})$ while the inverse process increases the distribution function. Thus, there is a momentum exchange of $\boldsymbol{k}_3 - \boldsymbol{k}_2 = \boldsymbol{k} - \boldsymbol{k}_4$. The corresponding collision integral is of the form:

$$\left(\frac{\partial f(\boldsymbol{k})}{\partial t}\right)_{\text{collisions}} = -\frac{1}{\mathrm{V}} \sum_{\boldsymbol{k}_2,\boldsymbol{k}_3,\boldsymbol{k}_4} \Gamma(\boldsymbol{k},\boldsymbol{k}_2;\boldsymbol{k}_3,\boldsymbol{k}_4)\{f(\boldsymbol{k})f(\boldsymbol{k}_2)[1 - f(\boldsymbol{k}_3)][1 - f(\boldsymbol{k}_4)] - [1 - f(\boldsymbol{k})][1 - f(\boldsymbol{k}_2)]f(\boldsymbol{k}_3)f(\boldsymbol{k}_4)\}, \tag{3.5}$$

where the first (second) term represents the outgoing (incoming) scattering process. The scattering rate is given by:

$$\Gamma(\boldsymbol{k},\boldsymbol{k}_2;\boldsymbol{k}_3,\boldsymbol{k}_4) = \frac{1}{2}|W_{\boldsymbol{k},\boldsymbol{k}_2;\boldsymbol{k}_3,\boldsymbol{k}_4} - W_{\boldsymbol{k},\boldsymbol{k}_2;\boldsymbol{k}_4,\boldsymbol{k}_3}|^2 \times \delta_{\boldsymbol{k}+\boldsymbol{k}_2,\boldsymbol{k}_3+\boldsymbol{k}_4} \frac{2\pi}{\hbar}\delta(\varepsilon_{\boldsymbol{k}} + \varepsilon_{\boldsymbol{k}_2} - \varepsilon_{\boldsymbol{k}_3} + \varepsilon_{\boldsymbol{k}_4}). \tag{3.6}$$

Here $W_{\boldsymbol{k},\boldsymbol{k}_2;\boldsymbol{k}_3,\boldsymbol{k}_4} = \langle \boldsymbol{k}\boldsymbol{k}_2|W|\boldsymbol{k}_3\boldsymbol{k}_4\rangle$ is the interaction vertex matrix element obtained from the Fermi Golden rule, and $\varepsilon_{\boldsymbol{k}}$ is the energy of each quasi-particle. The form of collision integral leads to the conservation of the total momentum, total energy, and the number of particles. Because of these conservation laws, the non-equilibrium distribution function cannot be relaxed with a finite total momentum. In order to have a finite contribution of the two-particle scattering to the relaxation of distribution function, the momentum should be transferred to the lattice. This can be realized by umklapp scattering. In this two-particle scattering process, one particle scatters from the first to the second Brillouin zone and then scatters back to the first Brillouin zone through the transfer of reciprocal lattice vector $\boldsymbol{G}$ to the lattice. This way, the energy is conserved while the momentum conservation implies a delta function on momentum which is replaced by

$\delta_{k+k_2,k_3+k_4} \to \delta_{k+k_2,k_3+k_4\pm G}$.

### 3.2.1 Linearization of the collision integral

Solving the Boltzmann equation (3.1) is a difficult task due to the complicated non-linear dependence of the collision integral on the distribution function. In the case of the general form of the collision integral for particle-particle collisions, the Boltzmann equation involves six partial derivatives of the distribution function and the integrals of its forth power. In practice, one have to make simplifying assumptions. We should first note that the transport properties of the system are the consequence of its linear response to driving forces such as gradients of temperature, chemical or electrostatic potentials. Therefore, to a good approximation (if the driving forces are not too large) we only need to solve the Boltzmann equation up to linear order in external perturbation. In general, one can assume that the distribution function can be written as:

$$f(\boldsymbol{k}) = f^0(\boldsymbol{k}) + \delta f(\boldsymbol{k}), \tag{3.7}$$

where $f^0(\boldsymbol{k})$ is the equilibrium distribution function. The small $\delta f$ represents the deviation of distribution function from thermal equilibrium which is considered to be linear in the forces. Following the textbook [150], for small deviations from the global equilibrium one can introduce a normalized deviation $\phi(\boldsymbol{k})$ defined as:

$$f(\boldsymbol{k}) = \frac{1}{e^{\beta(\varepsilon_{\boldsymbol{k}}-\mu)-\phi(\boldsymbol{k})}+1}, \tag{3.8}$$

so that the distribution function can be expanded in powers of $\phi(\boldsymbol{k})$ as the following:

$$\begin{aligned} f &= f^0 + \left.\frac{\partial f}{\partial \phi}\right|_{\phi\to 0}\phi + \mathcal{O}(\phi^2) \\ &= f^0 + \frac{e^{\beta(\varepsilon_{\boldsymbol{k}}-\mu)}}{\left(e^{\beta(\varepsilon_{\boldsymbol{k}}-\mu)}+1\right)^2}\phi + \mathcal{O}(\phi^2). \end{aligned} \tag{3.9}$$

Writing $\dfrac{e^{\beta(\varepsilon_{\boldsymbol{k}}-\mu)}}{\left(e^{\beta(\varepsilon_{\boldsymbol{k}}-\mu)}+1\right)^2} = f^0(1-f^0)$, we obtain in linear order:

$$\delta f = f^0(1-f^0)\phi. \tag{3.10}$$

We can now write the collision integral in equations (3.5) and (3.1) in terms of $\delta f$ and $\phi$:

$$\begin{aligned}\left(\frac{\partial f(k)}{\partial t}\right)_{\text{collisions}} &= f^0(k)(1-f^0(k))\frac{d\phi(k)}{dt} + \mathcal{O}(\phi^2)\\ &= -\sum_{k_2,k_3,k_4} \Gamma(k,k_2,k_3,k_4)\times\{(f^0(k)+\delta f^0(k))(f^0(k_1)+\delta f^0(k_1)).\\ &\quad\times(1-f^0(k_3)-\delta f^0(k_3))(1-f^0(k_4)-\delta f^0(k_4))\\ &\quad-(1-f^0(k)-\delta f^0(k))(1-f^0(k_2)-\delta f^0(k_2))\\ &\quad\times(f^0(k_3)+\delta f^0(k_3))(f^0(k_4)+\delta f^0(k_4))\}\end{aligned}$$

Replacing $\delta f$ with (3.10) and keeping just linear terms in $\phi$, the expression within the braces in the right hand side of the above equation can be written:

$$\begin{aligned}\{\} =&\phi[f^0 f_3^0 f_4^0(1-f^0)(1-f_2^0)+f_2^0 f^0(1-f^0)(1-f_3^0)(1-f^0)]\\ &-\phi_3[f^0 f_2^0 f_3^0(1-f_3^0)(1-f_4^0)+f_4^0 f_3^0(1-f^0)(1-f_2^0)(1-f_3^0)]\\ &-\phi_4[f^0 f_2^0 f_4^0(1-f_4^0)(1-f_3^0)+f_3^0 f_4^0(1-f_4^0)(1-f^0)(1-f_2^0)]\\ &+\phi_2[f_2^0 f_3^0 f_4^0(1-f^0)(1-f_2^0)+f^0 f_2^0(1-f_2^0)(1-f_3^0)(1-f_4^0)],\end{aligned}\tag{3.11}$$

where for simplicity the $k$ dependence of $f$ and $\phi$ functions has been omitted. The above equation can be further simplified by using the following symmetry of the equilibrium distribution function:

$$f^0 f_2^0(1-f_3^0)(1-f_4^0) = f_3^0 f_4^0(1-f^0)(1-f_2^0).\tag{3.12}$$

Then we can write:

$$\begin{aligned}\{\} =&\phi[f_2^0 f^0(1-f^0)(1-f_3^0)(1-f_4^0)+f^0 f^0 f_2^0(1-f^3)(1-f_4^0)]\\ &-\phi_3[f^0 f_2^0 f_3^0(1-f_3^0)(1-f_4^0)+f^0 f_2^0(1-f_3^0)(1-f_3^0)(1-f_4^0)]\\ &-\phi_4[f^0 f^2 f_4^0(1-f_3^0)(1-f_4^0)+f^0 f_2^0(1-f_4^0)(1-f_3^0)(1-f_4^0)]\\ &+\phi_2[f^0 f_2^0(1-f_2^0)(1-f_3^0)(1-f_4^0)+f_2^0 f^0 f_2^0(1-f_3^0)(1-f_4^0)].\end{aligned}$$

After simplification, the collision integral in terms of $\phi$ becomes:

$$\begin{aligned}\frac{d\phi(k)}{dt} = \frac{-1}{f^0(k)(1-f^0(k))}\sum_{k_2,k_3,k_4}&\Gamma(k,k_2;k_3,k_4)\times\Big\{f^0(k)f^0(k_2)(1-f^0(k_3))(1-f^0(k_4))\\ &\times\left(\phi(k)+\phi(k_2)-\phi(k_3)-\phi(k_4)\right)\Big\}.\end{aligned}\tag{3.13}$$

In the steady state and up to linear order in external forces, plugging equations (3.7) and (3.10)

into (3.1) gives us the linearized Boltzmann equation:

$$\boldsymbol{v}_k \cdot \frac{\partial f^0(k)}{\partial \boldsymbol{r}} + e(\boldsymbol{E} + \boldsymbol{v}_k \times \boldsymbol{H}) \cdot \frac{\partial f^0(k)}{\partial \boldsymbol{k}} = f^0(k)(1 - f^0(k))\frac{d\phi(k)}{dt}. \tag{3.14}$$

Equation (3.13) can be rewritten in a more convenient form by defining an integral operator acting on $\phi$ as:

$$\mathcal{L}\phi(k) = \frac{1}{f^0(k)(1-f^0(k))} \sum_{k',k_2,k_3,k_4} \Gamma(k,k_2;k_3,k_4) \times f^0(k) f^0(k_2)(1-f^0(k_3))(1-f^0(k_4)) \\ \times \left(\delta_{k',k} + \delta_{k',k_2} - \delta_{k',k_3} - \delta_{k',k_4}\right)\phi(k'). \tag{3.15}$$

Here $\mathcal{L}$ is an integral operator and is called the collision operator. This leads to the following equation for $\phi$:

$$\frac{d\phi(k)}{dt} = -\mathcal{L}\phi(k) = -\sum_{k'} \mathcal{L}_{k,k'}\phi(k'). \tag{3.16}$$

## 3.3 Transport properties

We begin this section by considering the Boltzmann equation (3.14) in the absence of magnetic field and presence of a uniform static electric field $\boldsymbol{E}$ coming from a one-body electrostatic potential:

$$\boldsymbol{v}_k \cdot \frac{\partial f^0(k)}{\partial \boldsymbol{r}} + \frac{e}{\hbar}\boldsymbol{E} \cdot \frac{\partial f^0(k)}{\partial \boldsymbol{k}} = f^0(k)(1 - f^0(k))\frac{d\phi(k)}{dt}. \tag{3.17}$$

The partial derivatives of $f^0$ can be evaluated as follows:

$$\begin{aligned} \frac{\partial f^0(k)}{\partial \boldsymbol{r}} &= \frac{\partial f^0(k)}{\partial T}\boldsymbol{\nabla}_r T + \frac{\partial f^0(k)}{\partial \mu}\boldsymbol{\nabla}_r \mu \\ &= \frac{\beta}{T}(\varepsilon_k - \mu) f^0(k)(1 - f^0(k))\boldsymbol{\nabla}_r T + \beta f^0(k)(1 - f^0(k))\boldsymbol{\nabla}_r \mu. \end{aligned} \tag{3.18}$$

$$\frac{\partial f^0(k)}{\partial \boldsymbol{k}} = \frac{\partial f^0(k)}{\partial E(k)}\boldsymbol{\nabla}_k \varepsilon_k = -\beta f^0(k)(1 - f^0(k))\hbar \boldsymbol{v}_k. \tag{3.19}$$

Here $\boldsymbol{v}_k = 1/\hbar \boldsymbol{\nabla}_k \varepsilon_k$ is the group velocity of quasi-particle's wave packet at $\boldsymbol{k}$.

Replacing equations (3.18) and (3.19) into (3.17), we obtain:

$$\beta^2 k_B(\varepsilon_k - \mu)\boldsymbol{v}_k \,.\, \boldsymbol{\nabla}_r T - e\beta\boldsymbol{\mathcal{E}} \,.\, \boldsymbol{v}_k = \frac{d\phi(\boldsymbol{k})}{dt} = -\mathcal{L}\phi(\boldsymbol{k}), \tag{3.20}$$

with

$$\boldsymbol{\mathcal{E}} = \boldsymbol{E} + \frac{\boldsymbol{\nabla}_r \mu}{-e}. \tag{3.21}$$

The general electrochemical field $\boldsymbol{\mathcal{E}}$ is introduced as a summation of the external electric field and a finite gradient of the chemical potential caused by the change in the distribution of charge carriers which is itself a result of the thermal gradient.

The deviation function $\phi$, as the solution of Boltzmann equation, can be obtained by solving equation (3.20), which can be written as:

$$-\beta^2 k_B \mathcal{L}^{-1}(\varepsilon_k - \mu)\boldsymbol{v}_k \,.\, \boldsymbol{\nabla}_r T + e\beta\mathcal{L}^{-1}\boldsymbol{\mathcal{E}} \,.\, \boldsymbol{v}_k = \phi(\boldsymbol{k}), \tag{3.22}$$

where $\mathcal{L}^{-1}$ is the inverse of the collision operator.

### 3.3.1 Currents and response functions

In order to derive the expression for electrical resistivity and Seebeck coefficient, we need to consider the electrical and thermal current densities, which are respectively defined as:

$$j_e = \frac{e}{V}\sum_{\boldsymbol{k}} \boldsymbol{v}_k f(\boldsymbol{k}), \tag{3.23}$$

and

$$j_{\text{th}} = \frac{1}{V}\sum_{\boldsymbol{k}} (\varepsilon_k - \mu)\boldsymbol{v}_k f(\boldsymbol{k}). \tag{3.24}$$

Now for $f(\boldsymbol{k}) = f^0(\boldsymbol{k}) + \delta f = f^0(\boldsymbol{k}) + f^0(\boldsymbol{k})\big(1 - f^0(\boldsymbol{k})\big)\phi(\boldsymbol{k})$, the equilibrium part does not contribute to currents since the currents become odd functions of velocity. The non-equilibrium part $f^0(\boldsymbol{k})\big(1 - f^0(\boldsymbol{k})\big)\phi(\boldsymbol{k})$, however, is odd itself in $v$ so that the currents become even in velocity. The deviation $\phi$ solves equation (3.22).

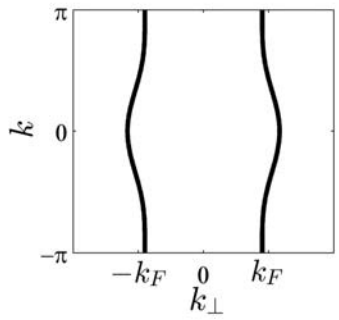


**Figure 3.1** The Fermi surface of the quasi-1D electron-gas model.

### Resistivity of the quasi-1D electron-gas

Now, we turn to our model of interest, the quasi-1D electron-gas model as introduced in detail in chapter 2. It consists of a linear array of $N_p$ weakly coupled conducting chains of length $L$ separated by the distance $d_\perp$. The energy spectrum reads:

$$\varepsilon_k^p = \hbar v_F(pk - k_F) + \epsilon_\perp(k_\perp). \tag{3.25}$$

The transverse part is given by

$$\epsilon_\perp(k_\perp) = -2t_\perp \cos k_\perp d_\perp - 2t'_\perp \cos 2k_\perp d_\perp. \tag{3.26}$$

In the absence of thermal gradient, the electric current along the $a$-axis becomes

$$j_a = \frac{2e}{LN_P d_\perp} \sum_k v_k^a f^0(k)(1 - f^0(k))\phi(k), \tag{3.27}$$

where $v_k^a$ is the electron velocity along the $a$ direction, and $\phi(k)$ solves equation:

$$\mathcal{L}\phi(k) = e\beta \mathcal{E}_a v_k^a. \tag{3.28}$$

The $f^0(1 - f^0)$ factor for all temperatures of interest is strongly peaked at the Fermi level. As a result, we can approximate $\phi(k)$ in equation 3.27 by its value at the Fermi wave vector $\phi(k_F^p) \equiv \phi_{k_\perp}$. This parametrizes the location of $\phi$ on the quasi-1D Fermi surface by $k_\perp$ from the condition $\varepsilon_{k_F^p}^p = 0$ which leads to $k_F^p = \left(k_F^p(k_\perp), k_\perp\right)$ (see figure 3.1). As for $v_k^a$, we use the longitudinal Fermi velocity $v_F$. Then

$$j_a = \frac{2e}{LN_P d_\perp} \sum_k v_F f^0(k)(1 - f^0(k))\phi_{k_\perp}. \tag{3.29}$$

Defining the normalized, dimensionless, deviation $\bar{\phi}_{k_\perp} = \phi_{k_\perp}/\beta e \mathcal{E}_a d_\perp$ and carrying out the energy integration using

$$\frac{1}{LN_P}\sum_{k} = \sum_{p}\int \frac{d\varepsilon_k^p}{2\pi\hbar v_F}\frac{1}{N_P}\sum_{k_\perp}', \tag{3.30}$$

in 3.29, we arrive at the following expression for the conductivity in the longitudinal direction:

$$\begin{aligned}\sigma_a &= \frac{e^2}{\hbar}\left(1/N_P\sum_{k_\perp}\bar{\phi}_{k_\perp}\right)\\ &= \frac{e^2}{\hbar}\left\langle\bar{\phi}_{k_\perp}\right\rangle_{k_\perp}',\end{aligned} \tag{3.31}$$

where $\left\langle\bar{\phi}_{k_\perp}\right\rangle$ is the deviation function averaged over the quasi-1D Fermi surface.

To calculate $\left\langle\bar{\phi}_{k_\perp}\right\rangle$, we note that in the framework of the electron-gas model, electron-electron umklapp scattering is the principal mechanism of momentum dissipation. It thus enters the scattering rate equation (3.6) as

$$\begin{aligned}\Gamma(k,k_2;k_3,k_4) = \frac{1}{2}|\langle k,k_2|g_3|k_3,k_4\rangle - \langle k,k_2|g_3|k_4,k_3\rangle|^2\\ \times\,\delta_{k+k_2,k_3+k_4+pG}\frac{2\pi}{\hbar}\delta(\varepsilon_k^p+\varepsilon_{k_2}^{p_2}-\varepsilon_{k_3}^{p_3}-\varepsilon_{k_4}^{p_4}),\end{aligned} \tag{3.32}$$

where $\langle k_1,k_2|g_3|k_3,k_4\rangle = \pi\hbar v_F g_3(k_{\perp 1},k_{\perp 2},k_{\perp 3},k_{\perp 4})$ is the normalized umklapp vertex function calculated at the Fermi level from RG whose temperature and momentum dependencies will play a key role in transport properties. Here $\boldsymbol{G} = (4k_F,0)$ is the longitudinal reciprocal lattice vector for the half-filling (Fermi wave vector $k_F = \pi/2a$) umklapp scattering.

As for the matrix elements of the collision operator, these take the form

$$\begin{aligned}\mathcal{L}_{k,k'} = \frac{1}{(LN_P)^2}\sum_{k_2,k_3,k_4}\Gamma(k,k_2;k_3,k_4)\frac{f^0(k_2)[1-f^0(k_3)][1-f^0(k_4)]}{[1-f^0(k)]}\\ \times(\delta_{k,k'}+\delta_{k_2,k'}-\delta_{k_3,k'}-\delta_{k_4,k'}).\end{aligned} \tag{3.33}$$

The above expression contains $i = 1,\ldots,4$ terms, namely one diagonal and three non-diagonal parts. This allows us to write:

$$\mathcal{L}_{k,k'} = \sum_{i=1}^{4}\mathcal{L}_{k,k'}^{[i]}. \tag{3.34}$$

By using the trick of reference [151], the momentum conservation delta function in (3.32) can be separated into its longitudinal and transverse components

$$\begin{aligned}\delta_{k+k_2,k_3+k_4+pG} &= \delta_{k_\perp+k_{2\perp},k_{3\perp}+k_{4\perp}} \times \frac{2\pi}{L}\delta(k+k_2-k_3-k_4-4pk_F) \\ &= \delta_{k_\perp+k_{\perp 2},k_{\perp 3}+k_{\perp 4}} \times \frac{2\pi}{L}\hbar v_F \delta(\varepsilon_k^p+\varepsilon_{k_2}^{p_2}+\varepsilon_{k_3}^{p_3}+\varepsilon_{k_4}^{p_4}-\Sigma),\end{aligned}$$

where

$$\Sigma = \epsilon_\perp(k_\perp)+\epsilon_\perp(k_{\perp 2})+\epsilon_\perp(k_{\perp 3})+\epsilon_\perp(k_{\perp 4}). \tag{3.35}$$

Equation (3.33) can therefore be decomposed in the following way:

$$\begin{aligned}\mathcal{L}^{[1]}_{k,k'} &= \frac{2\pi^3 v_F^2\hbar}{L^3 N_P{}^2}\sum_{k_2,k_3,k_4}|g_3(k_\perp,k_{2\perp},k_{3\perp})-g_3(k_\perp,k_{2\perp},k_{4\perp})|^2\times\delta_{k_\perp+k_{2\perp},k_{3\perp}+k_{4\perp}} \\ &\quad\times\delta(\varepsilon_k^p+\varepsilon_{k_2}^{p_2}-\varepsilon_{k_3}^{p_3}-\varepsilon_{k_4}^{p_4})\times\frac{f^0(k_2)(1-f^0(k_3))(1-f^0(k_4))}{(1-f^0(k))} \\ &\quad\times\delta_{k,k'}\delta(\varepsilon_k^p+\varepsilon_{k_2}^{p2}+\varepsilon_{k_3}^{p_3}+\varepsilon_{k_4}^{p_4}-\Sigma), \\ \mathcal{L}^{[2]}_{k,k'} &= \frac{2\pi^3 v_F^2\hbar}{L^3 N_P{}^2}\sum_{k_3,k_4}|g_3(k_\perp,k'_\perp,k_{3\perp})-g_3(k_\perp,k'_\perp,k_{4\perp})|^2\times\delta_{k_\perp+k'_\perp,k_{3\perp}+k_{4\perp}} \\ &\quad\times\delta(\varepsilon_k^p+\varepsilon_{k'}^{p'}-\varepsilon_{k_3}^{p_3}-\varepsilon_{k_4}^{p_4})\times\frac{f^0(k')(1-f^0(k_3))(1-f^0(k_4))}{(1-f^0(k))} \\ &\quad\times\delta(\varepsilon_k^p+\varepsilon_{k'}^{p'}+\varepsilon_{k_3}^{p_3}+\varepsilon_{k_4}^{p_4}-\Sigma_1), \\ \mathcal{L}^{[3]}_{k,k'} &= -\frac{2\pi^3 v_F^2\hbar}{L^3 N_P{}^2}\sum_{k_2,k_4}|g_3(k_\perp,k_{2\perp},k'_\perp)-g_3(k_\perp,k_{2\perp},k_{4\perp})|^2\times\delta_{k_\perp+k_{2\perp},k'_\perp+k_{4\perp}} \\ &\quad\times\delta(\varepsilon_k^p+\varepsilon_{k_2}^{p_2}-\varepsilon_{k'}^{p'}-\varepsilon_{k_4}^{p_4})\times\frac{f^0(k_2)(1-f^0(k'))(1-f^0(k_4))}{(1-f^0(k))} \\ &\quad\times\delta(\varepsilon_k^p+\varepsilon_{k_2}^{p_2}+\varepsilon_{k'}^{p'}+\varepsilon_{k_4}^{p_4}-\Sigma_2), \\ \mathcal{L}^{[4]}_{k,k'} &= -\frac{2\pi^3 v_F^2\hbar}{L^3 N_P{}^2}\sum_{k_2,k_3}|g_3(k_\perp,k_{2\perp},k_{3\perp})-g_3(k_\perp,k_{2\perp},k'_\perp)|^2\times\delta_{k_\perp+k_{2\perp},k_{3\perp}+k'_\perp} \\ &\quad\times\delta(\varepsilon_k^p+\varepsilon_{k_2}^{p_2}-\varepsilon_{k_3}^{p_3}-\varepsilon_{k'}^{p'})\times\frac{f^0(k_2)(1-f^0(k_3))(1-f^0(k'))}{(1-f^0(k))} \\ &\quad\times\delta(\varepsilon_k^p+\varepsilon_{k_2}^{p_2}+\varepsilon_{k_3}^{p_3}+\varepsilon_{k'}^{p'}-\Sigma_3),\end{aligned} \tag{3.36}$$

where $\Sigma_{1,2,3}$ are respectively obtained by substituting $k_{2\perp,3\perp,4\perp}$ for $k'_\perp$ in $\Sigma$ given in (3.35). Carrying

out the integration on energies, we arrive at

$$\begin{aligned}
\mathcal{L}^{[1]}_{k,k'} &= \frac{\pi^2}{\hbar {N_P}^2} \sum_{k_{\perp 3},k_{\perp 4}} |g_3(k_\perp, k_{\perp 3}+k_{\perp 4}-k_\perp, k_{\perp 3}, k_{\perp 4}) - g_3(k_\perp, k_{\perp 3}+k_{\perp 4}-k_\perp, k_{\perp 4}, k_{\perp 3})|^2 \\
&\times \frac{1+e^{-\beta\varepsilon^p_k}}{1+e^{\beta(\Sigma/2-\varepsilon^p_k)}} \frac{\Sigma/2 e^{\beta\Sigma/2}}{e^{\beta\Sigma/2}-1}\delta_{k,k'}, \\
\mathcal{L}^{[2]}_{k,k'} &= \frac{\pi^3 v_F}{L {N_P}^2} \sum_{k_{\perp 3},k_{\perp 4}} |g_3(k_\perp, k'_\perp, k_{\perp 3}, k_{\perp 4}) - g_3(k_\perp, k'_\perp, k_{\perp 4}, k_{\perp 3})|^2 \\
&\times \delta_{k_\perp+k'_\perp, k_{\perp 3}+k_{\perp 4}} \delta(\varepsilon^p_k + \varepsilon^{p'}_{k'} - \Sigma_1/2) \frac{1+e^{-\beta\varepsilon^p_k}}{1+e^{\beta\varepsilon^{p'}_{k'}}} \frac{(\varepsilon^p_k + \varepsilon^{p'}_{k'}) e^{\beta(\varepsilon^p_k+\varepsilon^{p'}_{k'})}}{e^{\beta(\varepsilon^p_k+\varepsilon^{p'}_{k'})}-1}, \\
\mathcal{L}^{[3]}_{k,k'} &= -\frac{\pi^3 v_F}{L {N_P}^2} \sum_{k_{\perp 2},k_{\perp 4}} |g_3(k_\perp, k_{\perp 2}, k'_\perp, k_{\perp 4}) - g_3(k_\perp, k_{\perp 2}, k_{\perp 4}, k'_\perp)|^2 \\
&\times \delta_{k_\perp+k_{\perp 2}, k'_\perp+k_{\perp 4}} \frac{1+e^{-\beta\varepsilon^p_k}}{1+e^{-\beta\varepsilon^{p'}_{k'}}} \frac{1}{(e^{\beta(\Sigma_2/2-\varepsilon^p_k)}+1)(e^{-\beta(\Sigma_2/2-\varepsilon^{p'}_{k'})}+1)}, \\
\mathcal{L}^{[4]}_{k,k'} &= -\frac{\pi^3 v_F}{L {N_P}^2} \sum_{k_{\perp 2},k_{\perp 3}} |g_3(k_\perp, k_{\perp 2}, k_{\perp 3}, k'_\perp) - g_3(k_\perp, k_{\perp 2}, k'_\perp, k_{\perp 3})|^2 \\
&\times \delta_{k_\perp+k_{\perp 2}, k_{\perp 3}+k'_\perp} \frac{1+e^{-\beta\varepsilon^p_k}}{1+e^{-\beta\varepsilon^{p'}_{k'}}} \frac{1}{(e^{\beta(\Sigma_3/2-\varepsilon^p_k)}+1)(e^{-\beta(\Sigma_3/2-\varepsilon^{p'}_{k'})}+1)}.
\end{aligned} \tag{3.37}$$

In the absence of temperature gradient, the linearized Boltzmann equation for the dimensionless $\bar{\phi}$ to be solved is

$$\sum_{i,k'} \mathcal{L}^{[i]}_{k,k'} \bar{\phi}_{k'} = 1, \tag{3.38}$$

with $\bar{\mathcal{L}} = \frac{\pi d_\perp}{v_F}\mathcal{L}$ as the dimensionless collision operator. Carrying out one more integration over

$\varepsilon^{p'}_{k'}$, the following four equations will be generated

$$\begin{aligned}
\mathcal{L}^{[1]}_{k_\perp,k'_\perp}\bar{\phi}_{k'_\perp} &= \frac{\pi^3 d_\perp}{2a\beta E_F {N_P}^2} \sum_{k'_\perp,k_{3\perp},k_{4\perp}} |\tilde{g}_3(k_\perp,k_{3\perp}+k_{3\perp}-k_\perp,k_{3\perp})-\tilde{g}_3(k_\perp,k_{3\perp}+k_{3\perp}-k_\perp,k_{4\perp})|^2 \\
&\times \left[\frac{1+e^{-\beta\varepsilon_k}}{1+e^{\beta(\Sigma/2-\varepsilon_k)}}\right]_{\varepsilon_k\sim 0} \frac{\Sigma/2e^{\beta\Sigma/2}}{e^{\beta\Sigma/2}-1}\delta_{k_\perp,k'_\perp}\bar{\phi}_{k'_\perp}, \\
\mathcal{L}^{[2]}_{k_\perp,k'_\perp}\bar{\phi}_{k'_\perp} &= \frac{\pi^3 d_\perp}{2a\beta E_F {N_P}^2} \sum_{k'_\perp,k_{3\perp},k_{4\perp}} |\tilde{g}_3(k_\perp,k'_\perp,k_{3\perp})-\tilde{g}_3(k_\perp,k'_\perp,k_{4\perp})|^2 \times \delta_{k_\perp+k'_\perp,k_{3\perp}+k_{4\perp}} \\
&\times \left[\frac{1+e^{-\beta\varepsilon^p_k}}{1+e^{\beta(\Sigma_1/2-\varepsilon^p_k)}}\right]_{\varepsilon^p_k\sim 0} \frac{\Sigma_1/2e^{\beta\Sigma_1/2}}{e^{\beta\Sigma_1/2}-1}\bar{\phi}_{k'_\perp}, \\
\mathcal{L}^{[3]}_{k_\perp,k'_\perp}\bar{\phi}_{k'_\perp} &= -\frac{\pi^3 d_\perp}{2a\beta E_F {N_P}^2} \sum_{k'_\perp,k_{2\perp},k_{4\perp}} |\tilde{g}_3(k_\perp,k_{2\perp},k'_\perp)-\tilde{g}_3(k_\perp,k_{2\perp},k_{4\perp})|^2 \times \delta_{k_\perp+k_{2\perp},k'_\perp+k_{4\perp}} \\
&\times \left[\frac{1+e^{-\beta\varepsilon^p_k}}{1+e^{\beta(\Sigma_2/2-\varepsilon^p_k)}}\right]_{\varepsilon^p_k\sim 0} \frac{\Sigma_2/2e^{\beta\Sigma_2/2}}{e^{\beta\Sigma_2/2}-1}\bar{\phi}_{k'_\perp}, \\
\bar{\mathcal{L}}^{[4]}_{k_\perp,k'_\perp}\bar{\phi}_{k'_\perp} &= -\frac{\pi^3 d_\perp}{2a\beta E_F {N_P}^2} \sum_{k'_\perp,k_{2\perp},k_{3\perp}} |\tilde{g}_3(k_\perp,k_{2\perp},k_{3\perp})-\tilde{g}_3(k_\perp,k_{2\perp},k'_\perp)|^2 \times \delta_{k_\perp+k_{2\perp},k_{3\perp}+k'_\perp} \\
&\times \left[\frac{1+e^{-\beta\varepsilon^p_k}}{1+e^{\beta(\Sigma_3/2-\varepsilon^p_k)}}\right]_{\varepsilon^p_k\sim 0} \frac{\Sigma_3/2e^{\beta\Sigma_3/2}}{e^{\beta\Sigma_3/2}-1}\bar{\phi}_{k'_\perp},
\end{aligned} \tag{3.39}$$

where as discussed above we put $\varepsilon^p_k$ on the Fermi surface.

After further manipulation and summing up all the above expressions we arrive at the final equation

$$\begin{aligned}
&\frac{\pi^3 d_\perp}{2a}\frac{T}{E_F}\frac{1}{N^2_P}\sum_{k'_\perp,k_{\perp3},k_{\perp4}} \Big\{ |g_3(k_\perp,k_{\perp3}+k_{\perp4}-k_\perp,k_{\perp3},k_{\perp4})-g_3(k_\perp,k_{\perp3}+k_{\perp4}-k_\perp,k_{\perp4},k_{\perp3})|^2 \\
&\times \frac{\beta\Sigma'/2}{\sinh(\beta\Sigma'/2)}\delta_{k_\perp,k'_\perp} + |g_3(k_\perp,k'_\perp,k_{\perp3},k_{\perp4})-g_3(k_\perp,k'_\perp,k_{\perp4},k_{\perp3})|^2\frac{\beta\Sigma''/2}{\sinh(\beta\Sigma''/2)}\delta_{k_\perp+k'_\perp,k_{\perp3}+k_{\perp4}} \\
&-2|g_3(k_\perp,k_{\perp3},k'_\perp,k_{\perp4})-g_3(k_\perp,k_{\perp3},k_{\perp4},k'_\perp)|^2\frac{\beta\Sigma''/2}{\sinh(\beta\Sigma''/2)}\delta_{k_\perp+k_{\perp3},k'_\perp+k_{\perp4}}\Big\}\bar{\phi}_{k'_\perp} = 1,
\end{aligned} \tag{3.40}$$

where

$$\begin{aligned}
\Sigma' &= \epsilon_\perp(k_\perp)+\epsilon_\perp(k_{\perp3}+k_{\perp4}-k_\perp)+\epsilon_\perp(k_{\perp3})+\epsilon_\perp(k_{\perp4}), \\
\Sigma'' &= \epsilon_\perp(k_\perp)+\epsilon_\perp(k'_\perp)+\epsilon_\perp(k_{\perp3})+\epsilon_\perp(k_{\perp4}).
\end{aligned} \tag{3.41}$$

The numerical solution of (3.40), using the results of the RG method for the computation of umklapp vertex function $g_3(k_{\perp 1}, k_{\perp 2}, k_{\perp 3}, k_{\perp 4})$ on the Fermi surface, gives us the values of $\bar{\phi}_{k_\perp}$ on the Fermi surface. Substituting these values in the expression (3.31), we compute the electrical resistivity. The results are given and discussed in detail in the following paper.

The Boltzmann theory in the second section of the paper is completely explained in the previous sections of this chapter as well as the step by step linearization procedure of the Boltzmann equation. The renormalization group calculation of the umklapp scattering in the third section is demonstrated in detail in chapter two of this thesis. The momentum and temperature variation of the umklapp scattering amplitude over the entire metallic phase is presented in section four of the paper. The next section contains the numerical results for the longitudinal resistivity. They are analyzed and discussed in terms of how the renormalized umklapp vertex function varies along the Fermi surface as a function of temperature. A full comparison of the results with experimental data is provided.

## Publication

- **Electrical transport near quantum criticality in low-dimensional organic superconductors**

**M. Shahbazi** and C. Bourbonnais, published in **Phys. Rev. B 92, 195141 (2015)**
I have developed an analytic as well as a numerical solution of the Boltzmann equation coupled to the renormalization group technique to calculate the electrical resistivity of a quasi-1D electron gas model. I have written all the computer programs. I have written all the manuscript. The co-author has participated to the correction of the manuscript for publication.

# Electrical transport near quantum criticality in low-dimensional organic superconductors

M. Shahbazi* and C. Bourbonnais†
*Regroupement Québecois sur les Matériaux de Pointe, Département de physique, Université de Sherbrooke, Sherbrooke, Québec, Canada J1K-2R1*

(Received 29 August 2015; revised manuscript received 24 October 2015; published 20 November 2015)

We propose a theory of longitudinal resistivity in the normal phase of quasi-one-dimensional organic superconductors near their quantum critical point where antiferromagnetism borders with superconductivity under pressure. The linearized semiclassical Boltzmann equation is solved numerically, fed in by the half-filling electronic umklapp scattering vertex as derived from one-loop renormalization-group calculations for the quasi-one-dimensional electron-gas model. The momentum and temperature dependence of umklapp scattering has an important impact on spin fluctuations and on the behavior of longitudinal resistivity in the the normal phase. Resistivity is found to be linear in temperature around the quantum critical point at which spin-density-wave order joins superconductivity along the antinesting axis, to gradually evolve towards the Fermi-liquid behavior in the limit of weak superconductivity. A critical analysis of the predictions is made from a comparison with experiments performed on the $(TMTSF)_2PF_6$ member of the Bechgaard salt series under pressure. Fair agreement between theory and experiment is then found in the low-temperature range linked to quantum criticality while deviations from predictions become apparent at high temperature.

DOI: 10.1103/PhysRevB.92.195141 PACS number(s): 74.25.fc, 71.10.Hf, 74.70.Kn

## I. INTRODUCTION

The quasi-one-dimensional (quasi-1D) organic conductors $(TMTSF)_2X$, called the Bechgaard salts, are known to be among the first examples of correlated electron systems in which superconductivity (SC) borders with antiferromagnetism or spin-density-wave order (SDW) in their phase diagram [1–4]. Both orderings are brought in close proximity by tuning pressure which can be achieved either hydrostatically or by chemical means. This results in a characteristic SDW-SC sequence of instabilities that shares many common traits with other unconventional superconductors including members of cuprate [5–7], heavy-fermion [8,9], and pnictide [9,10] series of compounds. This sequence is typically preceded by a metallic phase with unusual properties. For the Bechgaard salts, an anomalous metallic phase occurs nearby the critical pressure $P_c$, as a quantum critical point (QCP) connecting the ordering temperature $T_c$ for SC at its optimal value with the vanishing $T_{SDW}$ for SDW [3,4]. The temperature dependence of longitudinal resistivity near this point is found to depart from the $T^2$ behavior for a Fermi liquid. A detailed analysis has revealed that resistivity is instead linear in temperature close to $P_c$, as commonly found near a QCP [5]. It smoothly evolves toward the Fermi-liquid prediction as pressure is tuned away from $P_c$, in apparent correspondence with the gradual suppression of $T_c$ under pressure [11,12].

Generally linked to a QCP with SDW is the presence of spin fluctuations in the metallic state. These fluctuations may give rise to an important source of electron-electron umklapp scattering. As a mechanism of momentum dissipation, umklapp enters as a key determinant in the temperature dependence of resistivity [13,14]. In systems like the Bechgaard salts, this scattering process is primarily the consequence of a weak dimerization of the organic stacks which imparts a half-filled character to the electron band and allows the longitudinal transfer of charge carriers across the Fermi surface [15]. The existence of SDW fluctuations in the metallic phase of these materials has been amply borne out by NMR measurements [16–20]. The temperature dependence of the nuclear-spin relaxation rate $T_1^{-1}$ shows a pronounced enhancement of the Curie-Weiss form, at variance with the linear-$T$ Korringa law expected for a Fermi liquid. The amplitude of enhancement is in precise correspondence with the anomalous resistivity and the size of $T_c$ over the broad range of pressure where superconductivity is present [20,21], showing an intimate connection between SDW and Cooper pairing.

From a theoretical point of view, one-loop renormalization group (RG) studies on the quasi-1D electron-gas model with umklapp scattering have previously shown how the SDW-SC sequence of instabilities can be reproduced by varying the transverse next-to-nearest-neighbor hopping term $t'_\perp$, which acts as an antinesting term that simulates the role of pressure in the model [21,22]. Along the antinesting axis, a critical value $t'^*_\perp$ can be defined as the analog of the actual QCP at $P_c$. This is where $T_{SDW}$ is suppressed and a $d$-wave SC (SC$d$) instability appears at a maximum $T_c$. The SDW-SC$d$ pattern is also found to be accompanied by SDW fluctuations over a wide temperature domain of the nonordered state. Above $t'^*_\perp$ for instance, the calculated SDW susceptibility in the normal phase fits a Curie-Weiss form in agreement with the one extracted from NMR experiments. This enhancement of SDW correlations is mainly ascribed to the positive response of umklapp scattering to the growth of $d$-wave pairing [21,23].

From the one-loop electron-electron vertex functions obtained for the electron gas, the quasiparticle scattering rate has been computed from the self-energy [12,23]. Near $t'^*_\perp$, the rate develops a linear $T$ dependence above $T_c$, to which a Fermi-liquid $T^2$ component subsequently adds and grows as $t'_\perp$ distances from the QCP and $T_c$ decreases. This qualitatively agrees with the polynomial-$T$ analysis of resistivity data in systems like $(TMTSF)_2PF_6$ and $(TMTSF)_2ClO_4$ over the whole

*maryam.shahbazi@usherbrooke.ca
†claude.bourbonnais@usherbrooke.ca

 

pressure domain where superconductivity is found [11,12]. An alternative self-energy approach to resistivity data has been proposed from a hot-cold spots picture of the SDW nesting along the quasi-1D Fermi surface in the conventional framework of the QCP where superconductivity is neglected [24].

In this work we intend to push the calculation of longitudinal resistivity a step beyond the self-energy approach by solving the semiclassical Boltzmann equation which, with scattering in and out processes, incorporates some vertex corrections. This is achieved numerically with the aid of the RG method which is employed to compute the momentum and temperature-dependent umklapp scattering vertex function entering the collision term of the Boltzmann equation. The approach allows us to focus on renormalized scattering processes that do not conserve momentum and contribute to resistivity. Our procedure is similar in the outline with the one recently proposed by Buhmann *et al.* [25] in the study of transport properties of the hole-doped cuprate superconductors.

The results put forward below give the predictions of resistivity for a quasi-1D electron system with weak half-filling umklapp scattering over the whole temperature domain. This ranges from the known insulating-like 1D domain at high temperature down to the crossover to a higher dimensional regime in which instabilities of the electron gas against broken symmetry states can occur. In this low-temperature domain, the system is shown to develop a metallic linear-$T$ dependence as antinesting approaches its critical value $t_\perp'^*$ where SDW and SC$d$ orders meet. This quantum critical behavior in resistivity ensues from the anisotropic growth of half-filling umklapp scattering with lowering temperature, a consequence of reinforcement of commensurate SDW correlations by SC$d$ pairing in the metallic phase, which persists down to $T_c$. Above $t_\perp'^*$, the reinforcement undergoes a gradual decline that defines an extended region of quantum criticality where the temperature dependence of resistivity can fit a power-law dependence $\rho(T) \sim T^\alpha$ with an exponent $\alpha < 2$. The exponent approaches the Fermi-liquid limit $\alpha \simeq 2$ at low enough temperature and for sufficiently large $t_\perp'$, namely where $T_c$ becomes small. Anisotropy developed by umklapp scattering is found to have a sizable impact on the momentum dependence of the scattering rate extracted from resistivity. While the predictions are shown to be congruent with those of experiments carried out on the Bechgaard salts for the whole range of temperature associated to quantum criticality, the theory is unsuccessful to account for the different scattering mechanism in resistivity that apparently unfolds at higher temperature for these compounds.

The linearized Boltzmann transport theory is introduced in Sec. II and Appendix A. In Sec. III and Appendix B, we present the RG approach of the quasi-1D electron gas, from which the results for the phase diagram along with the temperature and momentum dependence of umklapp scattering vertex entering the Boltzmann equation are given. In Sec. IV, numerical results for resistivity and their analysis in terms of renormalized umklapp vertex function are detailed. A comparison with existing experiments performed on the $(TMTSF)_2PF_6$ member of the Bechgaard salts is presented. We summarize and conclude this work in Sec. V.

## II. BOLTZMANN EQUATION

The semiclassical Boltzmann equation describes the variation of the quasiparticle Fermi distribution function $f$ due to collisions and external forces. In the presence of a spatially uniform and static electric field $\boldsymbol{\mathcal{E}}$ coming from a one-body electrostatic potential, the Boltzmann equation reduces to the expression

$$\frac{df(\boldsymbol{k})}{dt} = e\,\boldsymbol{\mathcal{E}}\cdot\nabla_{\hbar\boldsymbol{k}} f = \left[\frac{\partial f(\boldsymbol{k})}{\partial t}\right]_{\rm coll}, \tag{1}$$

where $e$ is the electric charge. The collision integral for an array of $N_P$ chains of length $L$ takes the form

$$\begin{aligned}\left[\frac{\partial f(\boldsymbol{k})}{\partial t}\right]_{\rm coll} &= (LN_P)^{-2}\sum_{\boldsymbol{k}_2,\boldsymbol{k}_3,\boldsymbol{k}_4} w(\boldsymbol{k},\boldsymbol{k}_2;\boldsymbol{k}_3,\boldsymbol{k}_4)\\ &\times\{f(\boldsymbol{k})f(\boldsymbol{k}_2)[1-f(\boldsymbol{k}_3)][1-f(\boldsymbol{k}_4)]\\ &-[1-f(\boldsymbol{k})][1-f(\boldsymbol{k}_2)]f(\boldsymbol{k}_3)f(\boldsymbol{k}_4)\},\end{aligned} \tag{2}$$

for scattering in and out processes. The electron-electron (longitudinal umklapp) contribution to scattering rate $w$ is obtained from the Fermi "golden rule,"

$$\begin{aligned}w(\boldsymbol{k},\boldsymbol{k}_2;\boldsymbol{k}_3,\boldsymbol{k}_4) &= \tfrac{1}{2}|\langle\boldsymbol{k},\boldsymbol{k}_2|g_3|\boldsymbol{k}_3,\boldsymbol{k}_4\rangle - \langle\boldsymbol{k},\boldsymbol{k}_2|g_3|\boldsymbol{k}_4,\boldsymbol{k}_3\rangle|^2\\ &\times\delta_{\boldsymbol{k}+\boldsymbol{k}_2,\boldsymbol{k}_3+\boldsymbol{k}_4+\boldsymbol{G}}\frac{2\pi}{\hbar}\delta(\varepsilon_{\boldsymbol{k}}+\varepsilon_{\boldsymbol{k}_2}-\varepsilon_{\boldsymbol{k}_3}-\varepsilon_{\boldsymbol{k}_4}),\end{aligned} \tag{3}$$

where $\boldsymbol{G} = (4k_F,0)$ is the longitudinal reciprocal-lattice vector for half-filling umklapp scattering, and $k_F = \pi/(2a)$ is the longitudinal (1D) Fermi wave vector for dimerized chains.

To linearize the Boltzmann equation, we introduce the normalized deviation function $\phi_{\boldsymbol{k}}$ in the Fermi distribution function [26],

$$f(\boldsymbol{k}) = \frac{1}{e^{\beta\epsilon^p_{\boldsymbol{k}}-\phi_{\boldsymbol{k}}}+1}, \tag{4}$$

where $\beta = 1/T$ ($k_B = 1$). The electron energy spectrum is the one of the quasi-1D electron-gas model,

$$\epsilon^p_{\boldsymbol{k}} = \hbar v_F(pk - k_F) + \epsilon_\perp(k_\perp). \tag{5}$$

The spectrum comprises a longitudinal part linearized around the right/left 1D Fermi points $pk_F = \pm k_F$ with $v_F$ as the longitudinal Fermi velocity. The transverse part is given by

$$\epsilon_\perp(k_\perp) = -2t_\perp\cos k_\perp d_\perp - 2t'_\perp\cos 2k_\perp d_\perp, \tag{6}$$

where $t_\perp$ and $t'_\perp$ are the first and second nearest-neighbor interchain hopping terms and $d_\perp$ is the interchain distance.

The first-order expansion $f(\boldsymbol{k}) \simeq f^0(\boldsymbol{k}) + f^0(\boldsymbol{k})[1-f^0(\boldsymbol{k})]\phi_{\boldsymbol{k}}$ of the distribution function yields after substitution in (1),

$$\mathcal{L}\phi_{\boldsymbol{k}} = e\beta\mathcal{E}\cdot v_{\boldsymbol{k}}, \tag{7}$$

where $\mathcal{E} \sim \mathcal{O}(\phi)$. This is the linearized Boltzmann equation in which the collision operator $\mathcal{L}$ obeys the relation

$$\mathcal{L}\phi_{\boldsymbol{k}} = \sum_{\boldsymbol{k}'}\mathcal{L}_{\boldsymbol{k},\boldsymbol{k}'}\phi_{\boldsymbol{k}'}. \tag{8}$$

The matrix elements are of the form

$$\mathcal{L}_{\boldsymbol{k},\boldsymbol{k}'} = \frac{1}{(LN_P)^2}\sum_{\boldsymbol{k}_2,\boldsymbol{k}_3,\boldsymbol{k}_4}\frac{1}{2}|\langle \boldsymbol{k},\boldsymbol{k}_2|g_3|\boldsymbol{k}_3,\boldsymbol{k}_4\rangle - \langle \boldsymbol{k},\boldsymbol{k}_2|g_3|\boldsymbol{k}_4,\boldsymbol{k}_3\rangle|^2\frac{2\pi}{\hbar}\delta_{\boldsymbol{k}+\boldsymbol{k}_2,\boldsymbol{k}_3+\boldsymbol{k}_4+p\boldsymbol{G}} \delta\left(\varepsilon^p_{\boldsymbol{k}}+\varepsilon^{p_2}_{\boldsymbol{k}_2}-\varepsilon^{p_3}_{\boldsymbol{k}_3}-\varepsilon^{p_4}_{\boldsymbol{k}_4}\right) \times\frac{f^0(\boldsymbol{k}_2)[1-f^0(\boldsymbol{k}_3)][1-f^0(\boldsymbol{k}_4)]}{[1-f^0(\boldsymbol{k})]} \times(\delta_{\boldsymbol{k},\boldsymbol{k}'}+\delta_{\boldsymbol{k}_2,\boldsymbol{k}'}-\delta_{\boldsymbol{k}_3,\boldsymbol{k}'}-\delta_{\boldsymbol{k}_4,\boldsymbol{k}'}) = \sum_{i=1}^{4}\mathcal{L}^{[i]}_{\boldsymbol{k},\boldsymbol{k}'}, \quad (9)$$

which separates into a diagonal ($\mathcal{L}^{[1]}$) and three off-diagonal terms ($\mathcal{L}^{[2-4]}$). In Appendix A, each term is evaluated explicitly in the framework of the quasi-1D electron-gas model introduced in Sec. III.

For an electric field $\boldsymbol{\mathcal{E}} = \mathcal{E}_a\hat{a}$ oriented along the chain direction, the corresponding electrical current density $j_a = \sigma_a\mathcal{E}_a$ allows us to extract the conductivity $\sigma_a$, as the inverse of longitudinal resistivity $\rho_a$. To first order in $\phi$, the current density is given by

$$j_a = \frac{2e}{LN_Pd_\perp}\sum_{\boldsymbol{k}} v_F f(\boldsymbol{k}) \simeq \frac{2e}{LN_Pd_\perp}\sum_{\boldsymbol{k}} v_F f^0(\mathbf{k})[1-f^0(\boldsymbol{k})]\phi_{k_\perp}. \quad (10)$$

Since for all temperatures of interest, the product $f^0[1-f^0]$ is strongly peaked at the Fermi level, the deviation $\phi_{\boldsymbol{k}} \to \phi_{\boldsymbol{k}^p_F} \equiv \phi_{k_\perp}$ can be evaluated at the Fermi wave vector $\boldsymbol{k}^p_F = (k^p_F(k_\perp),k_\perp)$, whose location on the $p$ Fermi-surface sheet is entirely parametrized by $k_\perp$ from the equation $\epsilon^p_{\boldsymbol{k}^p_F} = 0$. By introducing the normalized deviation $\bar{\phi}_{k_\perp} = \phi_{k_\perp}/(\beta e\mathcal{E}_a d_\perp)$ and after an energy integration following (A4), the 2D conductivity or the inverse resistivity in the longitudinal direction becomes

$$\sigma_a = \rho_a^{-1} = \frac{e^2}{\hbar}\langle\bar{\phi}_{k_\perp}\rangle_{\rm FS}, \quad (11)$$

where $\langle\bar{\phi}_{k_\perp}\rangle_{\rm FS} = 1/N_P\sum_{k_\perp}\bar{\phi}_{k_\perp}$ is the deviation function averaged over the Fermi surface. The function $\bar{\phi}_{k_\perp}$ satisfies the equation

$$\sum_{i,k'_\perp}\bar{\mathcal{L}}^{[i]}_{k_\perp,k'_\perp}\bar{\phi}_{k'_\perp} = 1, \quad (12)$$

whose explicit expression is given in (A6) and for which we have introduced the dimensionless operator $\bar{\mathcal{L}}^{[i]} = \frac{\pi d_\perp}{v_F}\mathcal{L}^{[i]}$. The above expression is fed by the momentum and temperature dependence of the umklapp vertex function. This function is provided by the RG approach to the quasi-1D electron-gas model that is introduced next.

## III. RENORMALIZED UMKLAPP SCATTERING FOR THE ELECTRON-GAS MODEL

### A. Model

The quasi-1D electron-gas model in its standard form comprises, besides its one-electron energy spectrum (5), three electron-electron coupling constants that will be defined here on the Fermi-surface sheets $\boldsymbol{k}^p_F$. These are the backward and the forward scattering amplitudes $g_1(\boldsymbol{k}^-_{F,1},\boldsymbol{k}^+_{F,2};\boldsymbol{k}^-_{F,3},\boldsymbol{k}^+_{F,4})$ and $g_2(\boldsymbol{k}^+_{F,1},\boldsymbol{k}^-_{F,2};\boldsymbol{k}^-_{F,3},\boldsymbol{k}^+_{F,4})$ for normal scattering processes between right- and left-moving carriers, and $g_3(\boldsymbol{k}^p_{F,1},\boldsymbol{k}^p_{F,2};\boldsymbol{k}^{-p}_{F,3},\boldsymbol{k}^{-p}_{F,4})$ for umklapp scattering along the chains, whose momentum conservation involves the reciprocal-lattice vector $\boldsymbol{G} = (4k_F,0)$ at half filling. These coupling constants can be seen as phenomenological parameters of the model whose range at the bare level can be fixed from experimental data. We will follow [21–23], and use the typical values (normalized by $\hbar\pi v_F$) $g_1 \simeq 0.32$ and $g_2 \simeq 0.64$ for the two normal processes, consistent with the observed enhancement of uniform magnetic susceptibility [27] and the scale of $T_{\rm SDW}$ at low pressure [28,29]. As for the umklapp term, its bare value is primarily proportional to the dimerization gap $\Delta_D$ [30] of the organic stacks ($g_3 \approx g_1\Delta_D/E_F$) [31,32], which is small in the Bechgaard salts. Although rather weak at the bare level, umklapp processes have a strong influence on spin fluctuations at low energy and enter as a key determinant in the temperature dependence of longitudinal resistivity as we will see. The bare umklapp amplitude will thus be varied in the interval $g_3 \simeq 0.02\ldots0.035$, in accordance with the range of values expected for $\Delta_D$ [30]. For the model spectrum (5), we shall use $E_F = 3000$ K and $t_\perp = 200$ K for the Fermi energy and transverse hopping, as representative figures of the band structure for the Bechgaard salts [33,34]. The transverse second nearest-neighbor hopping $t'_\perp$ is an effective parameter of the band calculations which introduces nesting alterations [35]; this will be the only parameter to be varied continuously to simulate pressure effects [36].

We follow the lines of previous works and apply the Kadanoff-Wilson RG approach to the quasi-1D electron-gas model which is outlined in Appendix B [22,23,37,38]. Each constant energy surface is first divided into $N_P(=60)$ patches, each centered on a discrete value of $k_\perp$ parametrizing each Fermi sheet $\boldsymbol{k}^p_F = (k^p_F(k_\perp),k_\perp)$. The successive integration of electronic degrees of freedom as a function of the energy distance from the Fermi surface comprises perturbative contributions to the scattering amplitudes coming from closed loops, vertex corrections, and ladder diagrams of the density-wave (Peierls) and electron-electron (Cooper) scattering channels. The resulting RG flow equations for the $k_\perp$-dependent scattering amplitudes $g_{1,2,3}(k_{\perp 1},k_{\perp 2};k_{\perp 3},k_{\perp 4})$ on the Fermi surface are reproduced in (B1) of Appendix B. Their $k_\perp$ dependence takes into account the transverse momentum variables in both Peierls and Cooper channels, along with the longitudinal momentum transfer in each channel which is adjusted so that the momentum of ingoing and outgoing particles fall on the warped Fermi surface.

These flow equations are completed by those of the susceptibilities $\chi_\mu(q_0)$ given in (B4). These serve to signal an instability against either $\mu =$ SDW or $\mu =$ SC$d$ types of

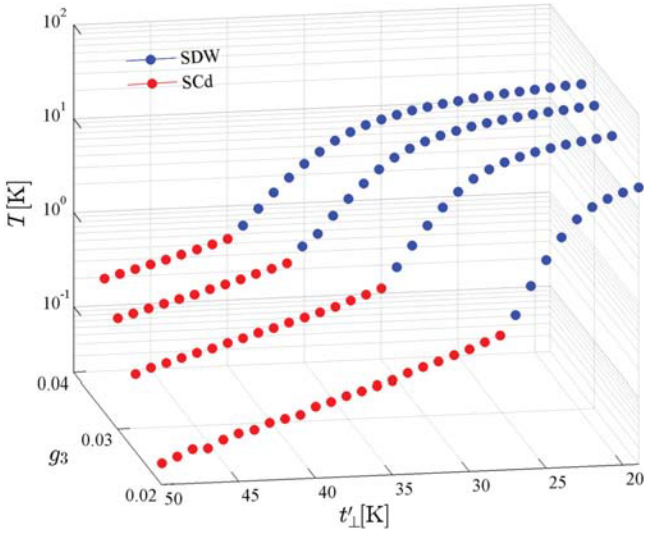


FIG. 1. (Color online) Calculated phase diagram of the quasi-one-dimensional electron-gas model showing the SDW-SC$d$ sequence of instabilities as a function of antinesting $t'_\perp$ and initial $g_3$ (for the model parameters used in the calculations, see Sec. III A).

ordering at the corresponding wave vectors $\boldsymbol{q}_0 = (2k_F,\pi)$ and $\boldsymbol{q}_0 = 0$.

### B. Phase diagram

The integration of the flow equations for the scattering amplitudes (B1) and susceptibilities (B4) and (B5) leads to their corresponding renormalized values at temperature $T$. For the above set of model parameters, the singularities in $\chi_{\rm SDW}(2k_F,\pi)$ and $\chi_{{\rm SC}d}(0)$ at temperatures $T_{\rm SDW}$ and $T_{{\rm SC}d}$ enable us to follow the SDW-SC$d$ sequence of instabilities as a function of the antinesting parameter $t'_\perp$ and initial $g_3$. The resulting phase diagrams are shown in Fig. 1. The variation of $T_{\rm SDW}$ shows a characteristic monotonic decrease with $t'_\perp$ up to the approach of the critical value $t'^*_\perp$ where $T_{\rm SDW}$ undergoes a rapid decrease, followed by the emergence of a SC$d$ instability. The latter reaches its maximum $T_c$ at $t'^*_\perp$, followed by its steady decrease for larger $t'_\perp$. The impact of increasing the initial $g_3$ on this sequence is to magnify antiferromagnetism and $T_{\rm SDW}$, which ultimately translates into an increase of the critical $t'^*_\perp$ and an enhancement of $d$-wave Cooper pairing, as shown by the upward shift of the $T_c$ line in Fig. 1.

### C. Umklapp scattering

In the SDW sector of the phase diagram, the umklapp scattering amplitude $g_3$ develops like $\chi_{\rm SDW}$ a singular growth at the approach of $T_{\rm SDW}$. For $t'_\perp < t'^*_\perp$ and different temperatures, Fig. 2(a) shows the contour plot of $g_3(k_{\perp 1}, -k_{\perp 1},k_{\perp 2})$ projected in the $(k_{\perp 1},k_{\perp 2})$ plane at zero transverse momentum for the pairs of ingoing and outgoing particles. As shown in Fig. 2(a), the maximum of scattering intensity is mainly concentrated along the lines $k_{\perp 2} = \pm(\mp)k_{\perp 1} \pm \pi$, which is congruent with the transverse component of the SDW correlation wave vector $\boldsymbol{q}_0 = (2k_F,\pi)$. Along these lines, the singular growth is the strongest around the spots $(0, \pm\pi)$ and $(\pm\pi,0)$, whose components differ from the points

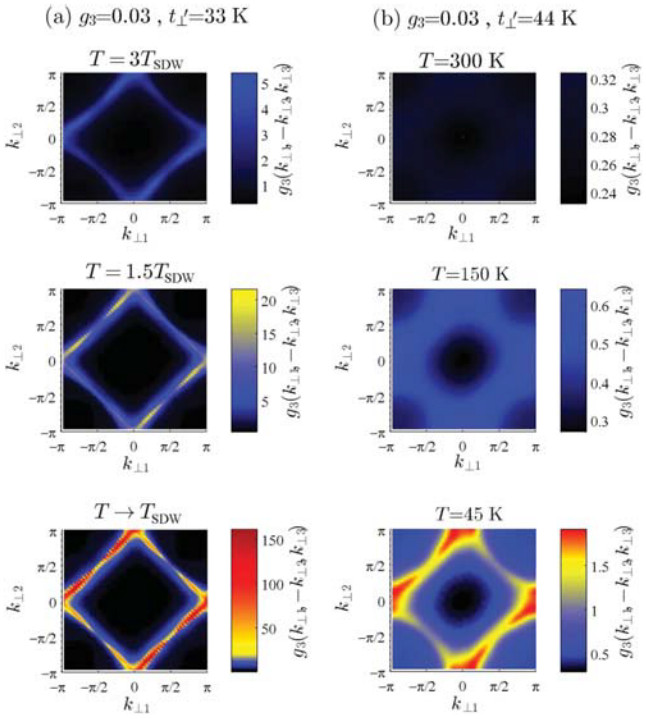


FIG. 2. (Color online) Renormalized umklapp scattering amplitude projected in the $(k_{\perp 1},k_{\perp 2})$ plane in the normal phase at different temperatures for the initial $g_3 = 0.03$ ($t'^*_\perp = 38$ K). (a) $t'_\perp = 33$ K ($< t'^*_\perp$); (b) $t'_\perp = 44$ K ($> t'^*_\perp$) (for other model parameters used in the calculations, see Sec. III A).

$k_\perp = \pm\pi/4, \pm 3\pi/4$ on the Fermi surface where nesting is predicted to be optimal for the spectrum (5). The fact that the warmest regions of scattering on the Fermi surface differ from the nesting prediction reflects the influence of Cooper scattering channel in the anisotropic flow of $g_3$ in Eq. (B1).

If we now consider the low-temperature variation of umklapp in the SC$d$ sector of the phase diagram at $t'_\perp > t'^*_\perp$, we note according to Fig. 3 that $g_3$ is no longer singular for all temperatures down to $T_c$. However, as temperature is decreasing we still observe an enhancement of $g_3$ along the SDW lines of scattering $k_{\perp 2} = \pm(\mp)k_{\perp 1} \pm \pi$. These are associated with peaks at $k_\perp = 0, \pm\pi$ on the Fermi surface whose amplitude increases with the bare $g_3$, as shown in Fig. 3. According to the combination $g_{\rm SDW} = g_2 + g_3$ of couplings entering in the SDW susceptibility [see Eq. (B6)], a positive increase in umklapp goes hand in hand with an increase of SDW spin correlations. This has been shown to yield a temperature dependence for $\chi_{\rm SDW}(\boldsymbol{q}_0) \sim 1/(T+\Theta)$ of the Curie-Weiss form in the same temperature domain, with an energy scale $\Theta$ for SDW correlations approaching zero at $t'^*_\perp$ and raising linearly with $t'_\perp$ from the QCP [21,23,39]. Occurring despite poor nesting conditions, the enhancement in both $g_3$ and SDW susceptibility results from a positive feedback of $d$-wave Cooper pairing on SDW correlations at the core of the flow equations (B1); these mix on the same footing the Peierls (density-wave) and Cooper scattering for electrons. As mentioned earlier, the reinforcement is made possible by a $k_\perp$-dependent coupling of $g_3$ to normal scattering processes $g_2$ and $g_1$ in the flow equations (B1). According to

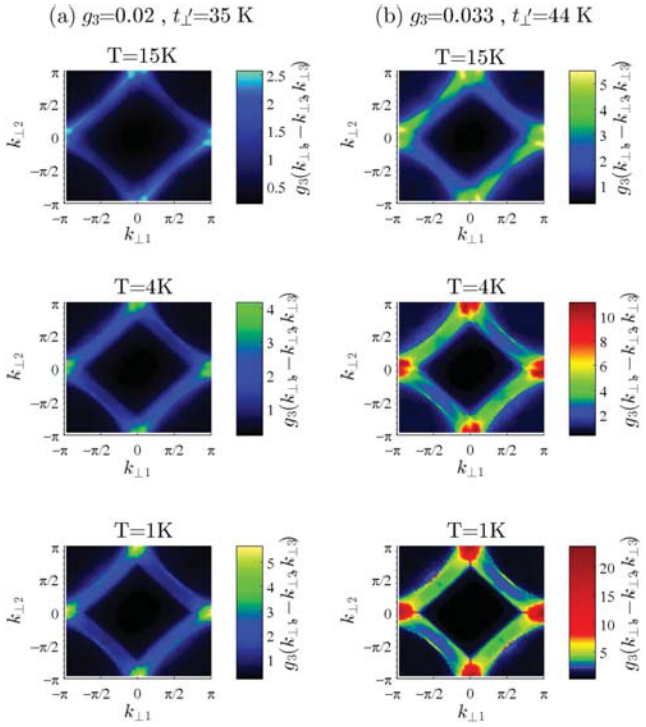


FIG. 3. (Color online) Renormalized umklapp scattering amplitude projected in the $(k_{\perp 1},k_{\perp 2})$ plane in the normal phase of the SC$d$ sector of the phase diagram,as obtained at different temperatures and initial values of $g_3$ (for other model parameters used in the calculations, see Sec. III A).

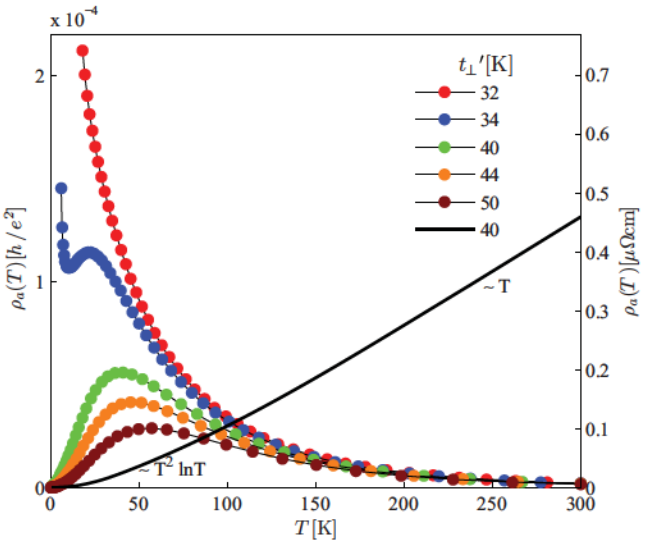


FIG. 4. (Color online) Calculated longitudinal resistivity over the whole temperature interval for different $t_\perp'$ at $g_3 = 0.03$ ($t_\perp'^* = 38$ K). The continuous line refers to the Fermi-liquid limit at constant scale-independent $g_3(= 0.03)$ yielding linear $T$ resistivity in the high-temperature 1D domain ($T > t_\perp = 200$ K) followed by a crossover toward a 2D $T^2 \ln T$ regime at low temperature (for other model parameters used in the calculations, see Sec. III A).

these, the first Fourier component in $\cos(k_{\perp 1}d_\perp)\cos(k_{\perp 2}d_\perp)$ of normal couplings—responsible for an attractive interchain or $d$-wave pairing between up and down spin electrons of first nearest-neighbor chains—grows singularly at the approach of $T_c$ and reinforces the effective antiferromagnetic exchange between electrons.

Anisotropy of umklapp scattering in momentum space along with its temperature dependence enter as key factors in the determination of resistivity at low temperature.

## IV. NUMERICAL RESULTS FOR THE BOLTZMANN EQUATION

We can now proceed to the numerical solution of the linearized semiclassical Boltzmann equation (12), using (A6) and the above RG results for the renormalized umklapp vertex part. The solutions for the normalized functions $\bar{\phi}_{k_\perp}$ have been obtained for $N_P = 60$ patches for the Fermi-surface sheet $k_F^p(k_\perp)$. This assures a convergence for the solutions of the Boltzmann equation (12) or (A6) that is independent of the discretization of the transverse Brillouin zone. Following (11), the temperature dependence of longitudinal resistivity can then be obtained by tuning the values of $t_\perp'$ and initial $g_3$.

### A. Dimensionality of the electron gas and resistivity

We first consider in Fig. 4 the general features of longitudinal resistivity over the whole temperature interval. This includes the high—effectively 1D—temperature domain at $T > t_\perp$, its crossover to the 2D region at $T < t_\perp$ where the warping of the Fermi surface becomes quantum mechanically coherent, and finally the temperature domain $T_\mu < T < t_\perp'$ where antinesting effects come into play at the approach of instabilities.

From Fig. 4, we see that in the 1D temperature region at $T > t_\perp$ for both SDW and SC$d$ sectors of the phase diagram, the resistivity is not metallic but grows with decreasing temperature. This is the result of relevant umklapp scattering whose flow toward Mott physics in the 1D domain is characterized by essentially no $k_\perp$ dependence, that is, no transverse correlations, as illustrated in Fig. 2(b) (top panel). Despite the absence of a charge gap, the growth of $g_3$ at $T > t_\perp$ is sufficiently rapid to completely overcome the linear-$T$ resistivity decrease obtained in the limit of a constant $g_3$ (continuous line of Fig. 4). This insulating like behavior is consistent with previous 1D results obtained in the presence of relevant $g_3$ [40,41].

When $t_\perp' < T < t_\perp$, the system crossovers to its 2D regime with antinesting effects remaining weak. In this temperature domain, the relevance of $g_3$ is still strong enough to outweigh the crossover toward the low-temperature Fermi-liquid $T^2 \ln T$-resistivity behavior found at constant $g_3$ [13,14] (continuous line of Fig. 4). Resistivity remains insulating in this region. It is only when $T$ is further lowered below $t_\perp'$ that the anisotropic growth of $g_3$ is significantly damped. At $t_\perp' > t_\perp'^*$, in the SC$d$ sector where umklapp, though still increasing, is no longer singular at finite $T$, resistivity goes through a maximum at $T \sim t_\perp'$ and is followed at lower temperature by a metallic behavior. Metallic behavior is also possible above $T_{\rm SDW}$ in the SDW sector of the phase diagram provided $t_\perp'$ is relatively close to the critical $t_\perp'^*$, as portrayed in

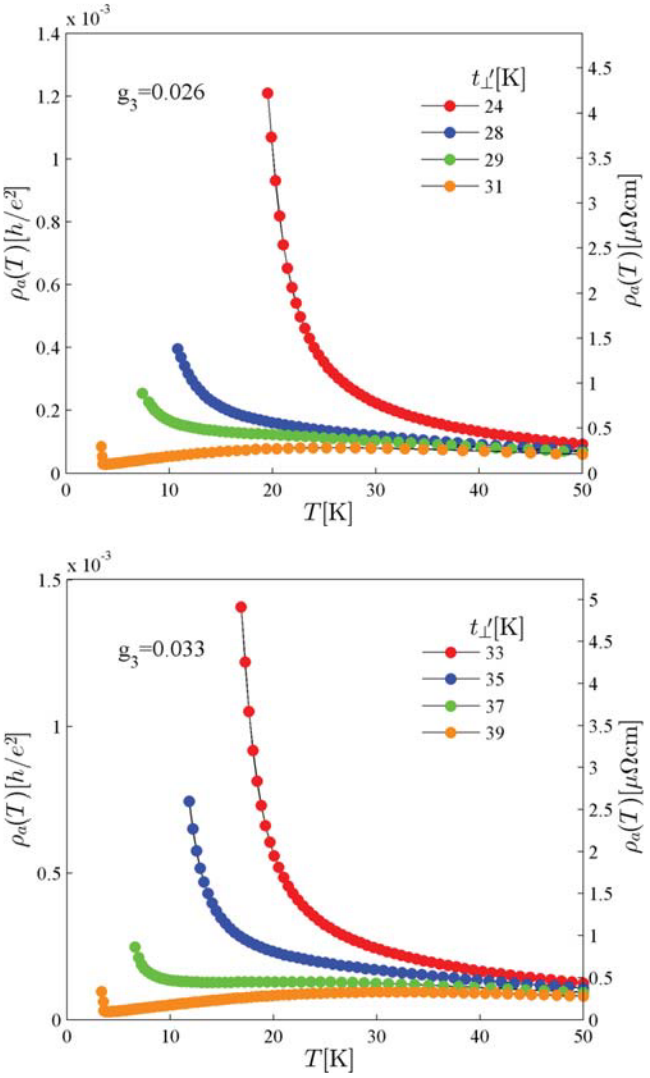


FIG. 5. (Color online) Calculated resistivity at low temperature in the SDW domain of the phase diagram for different $t'_\perp$ and $g_3$ (for other model parameters used in the calculations, see Sec. III A).

Fig. 4. As we will show next, however, metallicity is in general not equivalent to a Fermi-liquid behavior. Deviations from the latter are found and correlated to the distance from $t'^*_\perp$; it is only at strong $t'_\perp \gg t'^*_\perp$ that Fermi-liquid features tend to be restored when temperature is sufficiently small.

### B. Resistivity at quantum criticality and beyond

We now focus on the low-temperature profile of $\rho_a$ at $T_\mu < T < t'_\perp$ on either side of the QCP $t'^*_\perp$. Starting with the SDW side of the phase diagram, Fig. 5 displays the temperature dependence of resistivity in the normal phase of the SDW instability at different $t'_\perp$ and bare $g_3$ values. When $t'_\perp$ is relatively far below $t'^*_\perp$, resistivity remains insulating like with $d\rho_a/dT < 0$ down to $T_{\rm SDW}$. The growth of umklapp scattering and therefore of SDW fluctuations is sufficiently strong to maintain the source of inelastic scattering and the insulating response of the electron gas. In these conditions, the behavior varies weakly with the initial amplitude of $g_3$.

The temperature profile of resistivity qualitatively changes at the approach of $t'^*_\perp$. At $T \sim t'_\perp$, $\rho_a$ reaches a maximum followed by a crossover to a metallic behavior which persists down to very close to $T_{\rm SDW}$. The singularity in umklapp, being still present despite sizable nesting alterations, generates a resistivity upturn due to critical scattering, as in Figs. 4 and 5. In the metallic regime, however, the resistivity deviates from the Fermi-liquid prediction. A suitable way to describe these deviations is to express resistivity as a power law, $\rho_a(T) \sim T^{\alpha(T)}$, with a local exponent $\alpha(T)$ defined by

$$\alpha(T) = \frac{d}{d\ln T} \ln \rho_a(T). \tag{13}$$

The values of the exponent $\alpha$ are inserted in the calculated phase diagrams and shown in Fig. 7 for different bare amplitudes of $g_3$. Thus in approaching $t'^*_\perp$ from below the exponent $\alpha(T)$ crossovers from negative (insulating) to positive (metallic) values. Sufficiently close to $t'^*_\perp$, $T_{\rm SDW}$ is small and $\alpha(T)$ reaches unity for $T \lesssim 10$ K, which corresponds to the linear-$T$ resistivity usually associated to the QCP.

This linearity can be qualitatively understood if one considers that at low temperature resistivity is, roughly speaking, proportional to $T^2\langle g_3^2\rangle_{\rm FS}$. This would indicate that the average of the square of umklapp scattering over the Fermi surface, $\langle g_3^2\rangle_{\rm FS} \sim 1/T$, essentially grows as the inverse of temperature above the transition. Note that this temperature dependence is similar to the SDW susceptibility that goes like $\chi_{\rm SDW} \sim 1/T$ at $T \gg |\Theta|$ in this region [21,23].

If we now consider the SC$d$ region at $t'_\perp \geqslant t'^*_\perp$, the linearity continues to be seen over a finite region of the phase diagram. From Figs. 6 and 7, it can be found over a large temperature interval above $T_c$ near $t'^*_\perp$. However, a shift in the value of $\alpha(T)$ toward larger values takes place at low enough temperature especially if $g_3$ is relatively small initially. As a function of temperature a fan-shape-like region then unfolds from the neighborhood of $t'^*_\perp$ in which $\alpha(T) \simeq 1$. This region of linear resistivity in the phase diagram broadens as the bare $g_3$ increases and spin fluctuations in the normal phase and then $T_c$ are enhanced. Thus contrary to the situation expected for a classical QCP tied to SDW ordering alone [42], this region of linearity is not quickly followed as a function of $t'_\perp$ by a $T^2$ resistivity. The crossover region $1 < \alpha(T) < 2$ where deviations are present is rather wide and covers the whole region where superconductivity is present, as portrayed in Fig. 7 for different $g_3$. It is only in the low-temperature domain close to $T_c$ and for $t'_\perp$ well above $t'^*_\perp$ that the boundary with the Fermi-liquid limit appears and $T^2$ resistivity becomes visible (see Figs. 6 and 7), namely where $\langle g_3^2\rangle_{\rm FS}$ becomes essentially temperature independent. Similar features were found in previous RG calculations of the electron-electron scattering rate that included both normal and umklapp processes [23]. These were attributed to the presence of the superconducting instability that still influence the growth of the coupling constants; it gives rise to a positive feedback of SC$d$ pairing on umklapp scattering which can account for this extended quantum critical behavior.

It is also of interest to compare the present microscopic calculations to those of the phenomenological self-energy approach of Ref. [24] to quantum critical SDW effects of hot spots scattering on the Fermi surface. In the latter picture,

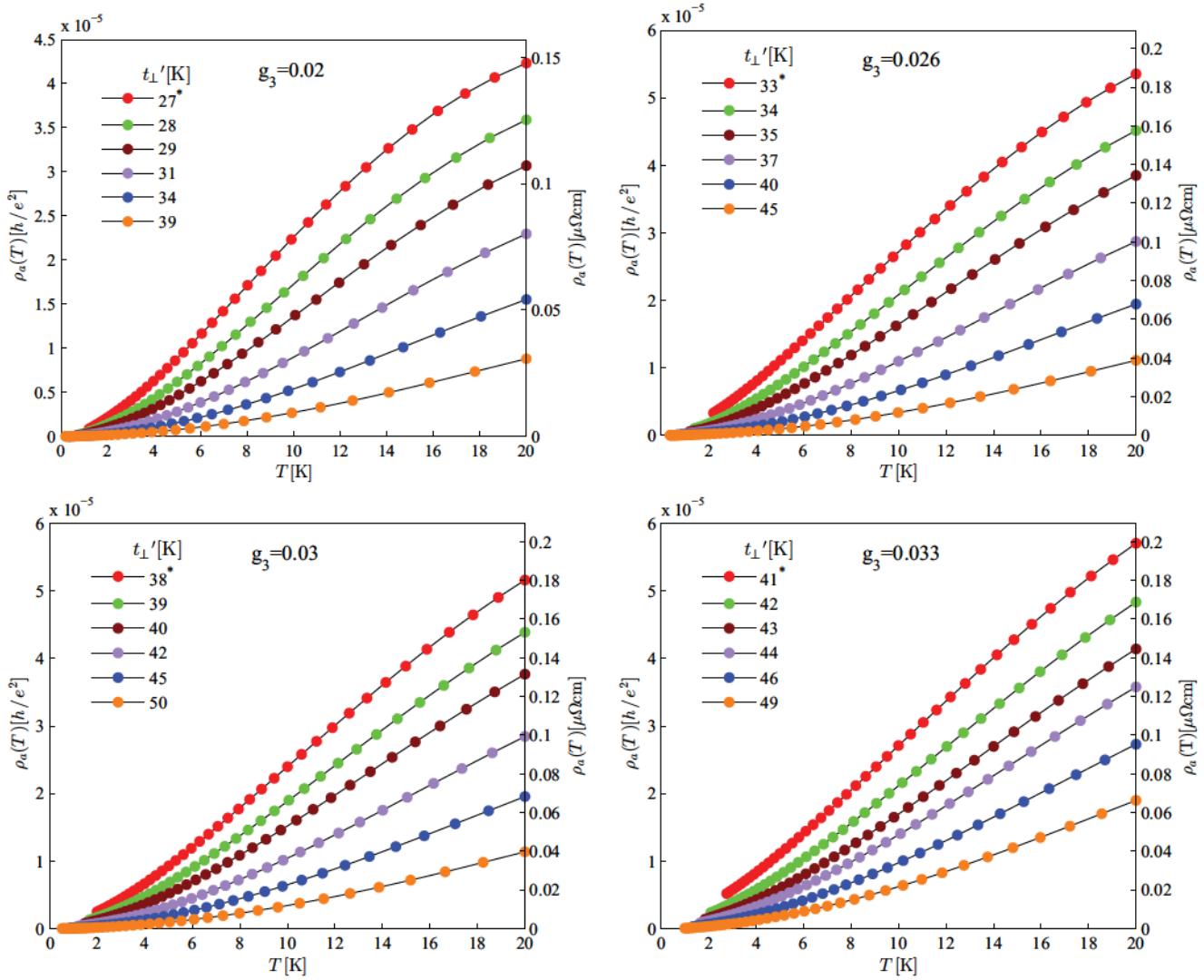


FIG. 6. (Color online) Calculated resistivity at low temperature in the SC$d$ domain of the phase diagram for different $t'_\perp$ and $g_3$ (for other model parameters used in the calculations, see Sec. III A).

resistivity at the hot spots ceases to be $T$-linear below some characteristic low-temperature scale $T_S$, which vanishes at the QCP, but increases as $t'_\perp$ grows away from $t'^*_\perp$ (Fig. 3 of Ref. [24]). Below this scale, resistivity then retrieves the Fermi-liquid $T^2$ behavior of the cold regions, a crossover line qualitatively similar in position with the recovery of a quadratic exponent $\alpha$ for resistivity sufficiently far from $t'^*_\perp$ and at low temperature in Fig. 7. In the present microscopic calculations, the conductivity or the inverse of resistivity sums, according to (11), the contributions from all cold and warm umklapp scattering regions on the Fermi surface.

### C. Anisotropy of the scattering rate

It is instructive to extract from the above results for resistivity some information about the momentum resolved—$k_\perp$-dependent—scattering rate. According to (11), the conductivity $\sigma_a = \sum_i \sigma_{k_{\perp i}}$ is a sum of contributions coming from each patch. One can associate to each contribution a patch resistivity $\rho_{k_{\perp i}} = (\sigma_{k_{\perp i}})^{-1}$ as an element of an array of parallel resistors proportional to a scattering rate at $k_F^p(k_{\perp i})$ on the Fermi surface.

Figure 8 shows the variation of $\rho_{k_{\perp i}}$ as a function of $k_{\perp i}$. In the SC$d$ regime, there are peaks at $k_\perp = 0$ and $\pm\pi$ indicating that the scattering rate is larger at these points. These warmer regions of scattering are the same as those of umklapp scattering amplitude along the Fermi surface in Fig. 3 and then differ from the positions $k_\perp = \pm\pi/4$ and $\pm 3\pi/4$ attributed to the best nesting conditions for the spectrum. The resulting momentum profile of $\rho_{k_{\perp i}}$ over the Fermi surface is also congruent with the one previously found by a direct RG calculation of the scattering rate from the one-particle self-energy at low temperature, which takes into account both normal and umklapp processes [23]. As stressed in Ref. [23] these warmer regions of scattering turn out to coincide with the locations of maximums for a $d$-wave gap along the Fermi surface. Since a single-scattering channel (Peierls) calculation would invariably lead to the best nesting points as the warmest spots of scattering on the Fermi surface, it follows that one can ascribe the shift in the spots on the Fermi surface to the

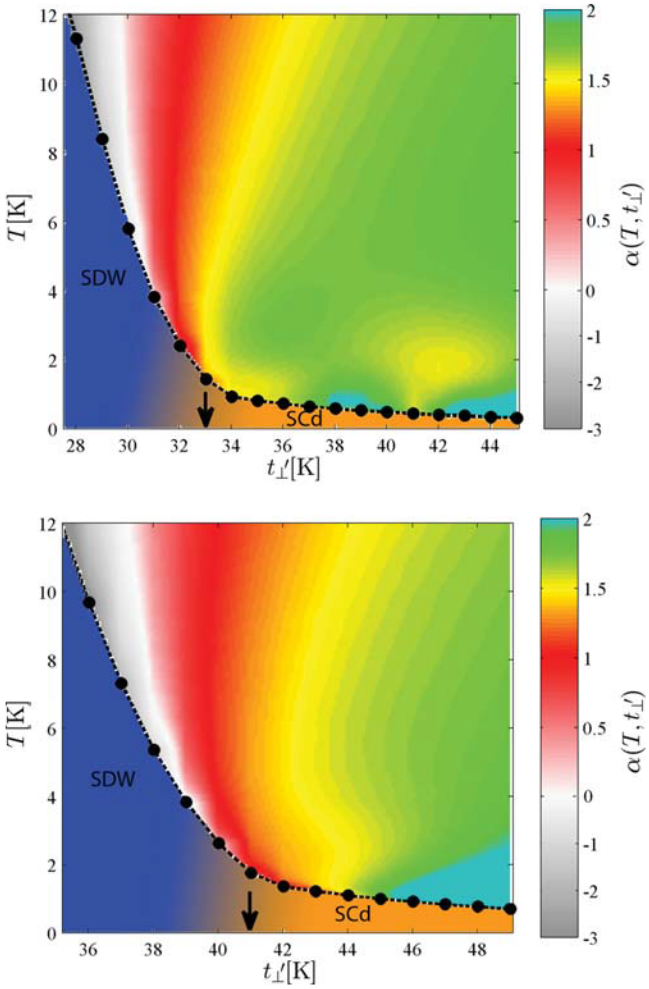


FIG. 7. (Color online) Variation of the power-law exponent $\alpha$ of resistivity in the phase diagram for $g_3 = 0.026$ (top) and $g_3 = 0.033$ (bottom). The arrows indicate the location of $t_\perp'^*$ (for other model parameters used in the calculations, see Sec. III A).

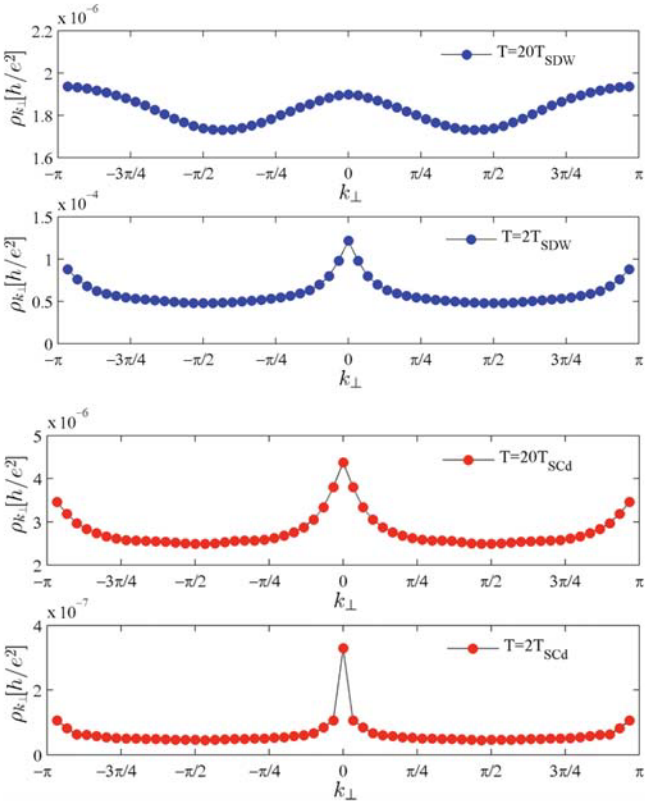


FIG. 8. (Color online) Variation of resistivity components along the Fermi surface at different temperatures: SDW (top) and SC$d$ (bottom) domains (for other model parameters used in the calculations, see Sec. III A).

presence of the interfering Cooper channel in the complete one-loop calculation (B1). The interference between both scattering channels being present in the SDW sector of the phase diagram as well, the anisotropy of $\rho_{k_\perp}$ is found to be similar above $T_{\rm SDW}$, as displayed in Fig. 8.

### D. Comparison with experiments

In the following we shall make some comparison of the above results with experiments. Starting with the SDW sector of the calculated phase diagram at low nesting deviations, the results displayed in Figs. 4 and 5 show the absence of metallic resistivity above $T_{\rm SDW}$. This is at variance to what is actually observed in system like $(TMTSF)_2PF_6$ series of the Bechgaard salts series below $P_c$ where a nearly $T^2$ behavior for resistivity is well known to be observed above the resistivity upturn at $T_{\rm SDW} \sim 10$ K [11,29,43,44] (see also Fig. 9). The temperature profile obtained for resistivity well below $t_\perp'^*$ is rather characteristic of the one seen in the cousin sulfur based compounds $(TMTTF)_2X$ ($X = PF_6$, Br, ...) at low pressure [45], which are characterized by a 1D Mott insulating gap at high temperature due to umklapp scattering, followed at lower temperature by a transition to an antiferromagnetic ground state [28,29,46]. Under moderate pressure, the normal phase of these systems becomes metallic with a power-law behavior down to $T_{\rm SDW}$ which would agree qualitatively with the calculated positive values for $\alpha$ found at low temperature not too far below $t_\perp'^*$ in Fig. 7. However in contrast to the results shown in Fig. 5, no maximum in resistivity is found experimentally for longitudinal resistivity at a scale that would correspond to $t_\perp'$ [29]. These discrepancies provide some indication that inelastic scattering at intermediate temperature and above would come from processes other than half-filling umklapp [47–49].

On the SC side, above the QCP at $P_c$, detailed resistivity measurements for $(TMTSF)_2PF_6$ have been performed in the low-temperature domain up to about 15 times $T_c$ ($T_c$ of the order of 1 K at $P_c$) [11,12]. The resistivity data are reproduced in Fig. 9. At the pressure of 11.8 kbar, close to the $P_c \simeq$ 9 kbar, resistivity is found to be $T-$linear ($\alpha = 1$) from up to $10T_c$ down to $T_c$ and even below when a small magnetic field is applied, as shown in the log-log plot of Fig. 9(b). As pressure is increased, the linearity decreases in strength and the resistivity develops some upward curvature which translates into a gradual increase of the power-law exponent $\alpha$, but which still remains smaller than the Fermi-liquid limit $\alpha = 2$. It is only at much larger pressure ($P = 20.8$ kbar in Fig. 9), when $T_c$ becomes small, that the $T^2$ behavior tends to be retrieved

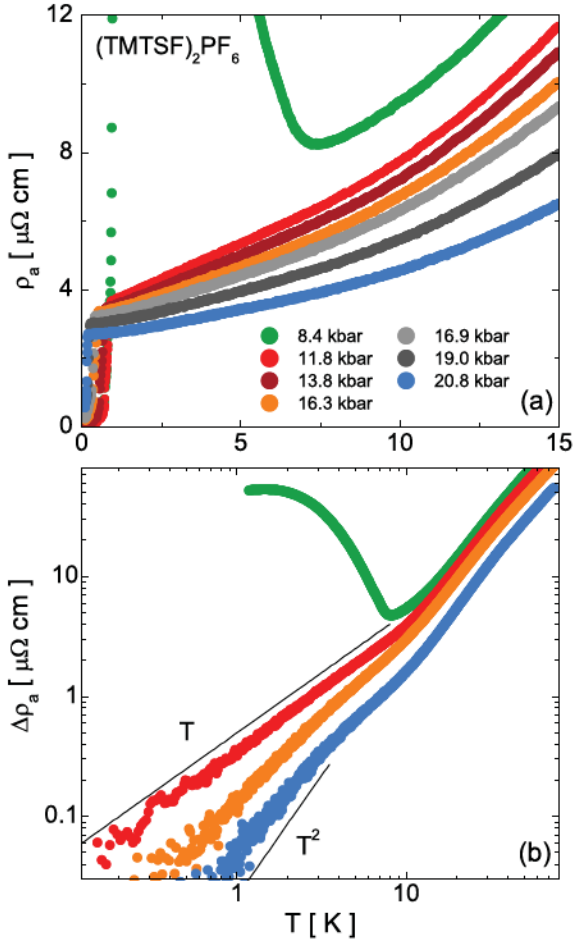


FIG. 9. (Color online) (a) Longitudinal resistivity of Ref. [11] observed at different pressures or $T_c$ for $(TMTSF)_2PF_6$. (b) Inelastic part of the data ($\Delta\rho_a = \rho_a - \rho_a^0$) traced in a log-log plot showing the growth of the power-law exponent $\alpha$ for resistivity with pressure (for other model parameters used in the calculations, see Sec. III A).

as shown in Fig. 9(b). Deviations to the Fermi-liquid behavior were found to scale with the size of $T_c$ [11,12].

These features are consistent with the results of Fig. 7 where deviations from linearity develop with increasing the antinesting parameter so that the resistivity exponent reaches 2 when the superconducting phase is about to disappear. The calculated evolution of the exponent $\alpha$ near $t_\perp'^*$ and above is in qualitative agreement with the results of Fig. 9.

The theory, however, fails to predict the restoration of an apparent Fermi-liquid $T^2$ behavior in the intermediate-temperature region, namely above the domain of anomalous resistivity. As mentioned above, this Fermi-liquid behavior is also found in the SDW sector of the phase diagram above $T_{SDW} \sim 10$ K (see Fig. 9). In the present approach, this would indicate that the system crosses over to a state where umklapp renormalization becomes essentially absent, in spite of reinforced nesting properties resulting from either a temperature increase or a reduction of $t_\perp'$. These features are at variance with the results of the present model that invariably predicts the reverse. For systems like the Bechgaard salts with one type of carrier tied to a single-component Fermi surface, these features may indicate that a "colder" source of inelastic scattering [50], not included in the present calculations, gains in importance at higher temperature. It surpasses around 10 K the anomalous power-law behavior resulting from the sole basis of electronic half-filled umklapp scattering. This is also inferred from the calculated values of 3D resistivity for the present model. The actual resistivity is obtained from the product of the 2D part by the interchain lattice constant $c$, namely $\rho_a c$. For the Bechgaard salts, $c = 13.52$ Å [2] and the resistivity can then be expressed in $\mu\Omega$ cm units, as shown in the right-hand-side scale of Figs. 4–6. The comparison with Figs. 9(b) for the inelastic part of resistivity indicates that the data reach one order of magnitude larger values at 10 K, that is, where the change of regime occurs (see Fig. 9). It is worth noting that from nuclear relaxation rate experiments [4,17,19,27], a crossover in the properties of spin fluctuations is known to occur in the same temperature range. At what extent this change introduces an additional source of scattering for resistivity remains to be determined (see note in Ref. [51]).

## V. SUMMARY AND CONCLUDING REMARKS

We have studied the temperature and pressure dependence of electrical resistivity of the Bechgaard salts quasi-one-dimensional organic superconductors in the vicinity of their quantum critical point where superconductivity borders on spin-density-wave order under pressure. We have proceeded to the numerical solution of the semiclassical Boltzmann equation in which the collision umklapp electronic term has been computed by one-loop RG calculations in the framework of the quasi-1D electron-gas model with tunable nesting alterations.

The temperature dependence of longitudinal resistivity $\rho_a$ has thus been obtained over the whole temperature domain from the 1D high-temperature region, which is invariably insulating, down to the different effective 2D regimes where either an insulating SDW or SC$d$ instabilities are found depending on the strength of antinesting parameter $t_\perp'$. Antinesting proves to be the characteristic scale of the model for weakening the growth of umklapp term under scaling, allowing the onset of anomalous metallic resistivity near the quantum critical point $t_\perp'^*$ along the antinesting axis. Marked deviations from the Fermi-liquid $T^2$ behavior have been found and described in terms of power-law resistivity $\rho_a \sim T^\alpha$ in the chain direction. Linear resistivity is found within a characteristic fan-shape region of the phase diagram near $t_\perp'^*$, followed by a gradual increase of the exponent $\alpha$, reaching the Fermi-liquid limit at low enough temperature and sufficiently large antinesting or low superconducting $T_c$.

The quantum critical regime can be understood as an anomalous increase of umklapp scattering with lowering temperature, an enhancement that turns out to be nonuniform or anisotropic along the Fermi surface, with peaks at the positions where the Fermi velocity is purely longitudinal and nesting is relatively poor. This umklapp vertex renormalization being directly linked to an enhancement of SDW correlations, these can be equivalently considered as the source of anomalous inelastic scattering. The region of non-Fermi-liquid values of $\alpha$ are found to extend well beyond the confines of the

QCP vicinity, a consequence of the reinforcement of umklapp scattering or SDW fluctuations by $d$-wave Cooper pairing. This leads to the apparent correlation of $\alpha$ with the size of $T_c$.

The results have been shown to qualitatively account for the linear-$T$ longitudinal resistivity observed near the QCP of the Bechgaard salts phase diagram and for the gradual growth of $\alpha$ toward the Fermi-liquid behavior, as pressure moves away from the QCP and $T_c$ is suppressed. However, discrepancies between theory and experiment remain, namely in the temperature region above the domain of quantum criticality. The present approach to resistivity fails to reproduce the crossover to an apparent Fermi liquid in the intermediate-temperature domain, namely above that of quantum critical effects. A possible break down of the coherent quasiparticle picture implied in a Boltzmann approach to transport may be invoked, but this is apparently not supported by other experiments performed in this temperature range, especially from optical transport measurement which confirms the existence of coherent quasiparticles in this temperature range [52,53].

For systems like the Bechgaard salts with a simple open Fermi surface, this is likely to point to a mechanism of electron scattering that superimposes to that of half-filling umklapp with increasing temperature. This crossover is seemingly related to the one seen for spin fluctuations in nuclear relaxation experiments. This problem is currently under investigation.

## ACKNOWLEDGMENTS

The authors would like to thank H. Bakrim for his valuable comments on computing aspects of this work, and N. Doiron-Leyraud and P. Auban-Senzier for sharing their experimental data on the resistivity of the Bechgaard salts. C.B. thanks the National Science and Engineering Research Council of Canada (NSERC) and the Réseau Québécois des Matériaux de Pointe (RQMP) for financial support. Computational resources were provided by Calcul Québec and Compute Canada.

## APPENDIX A: LINEARIZED BOLTZMANN EQUATION

The linearized Boltzmann equation is of the form

$$\sum_{i,\boldsymbol{k}'} \mathcal{L}^{[i]}_{\boldsymbol{k},\boldsymbol{k}'} \phi_{\boldsymbol{k}'} = e\beta \mathcal{E} \cdot v_{\boldsymbol{k}}, \tag{A1}$$

where the collision operator given by expression (9) is the sum of four terms,

$$\sum_{i=1}^{4} \mathcal{L}^{[i]}_{\boldsymbol{k},\boldsymbol{k}'} = \frac{1}{(LN_P)^2} \sum_{\boldsymbol{k}_2,\boldsymbol{k}_3,\boldsymbol{k}_4} \frac{1}{2} |g_3(k_\perp,k_{\perp 2},k_{\perp 3},k_{\perp 4}) - g_3(k_\perp,k_{\perp 2},k_{\perp 4},k_{\perp 3})|^2 \frac{2\pi}{\hbar} \delta_{\boldsymbol{k}+\boldsymbol{k}_2,\boldsymbol{k}_3+\boldsymbol{k}_4+p\boldsymbol{G}}$$
$$\times \delta\left(\varepsilon^p_{\boldsymbol{k}} + \varepsilon^{p_2}_{\boldsymbol{k}_2} - \varepsilon^{p_3}_{\boldsymbol{k}_3} - \varepsilon^{p_4}_{\boldsymbol{k}_4}\right) \frac{f^0(\boldsymbol{k}_2)[1-f^0(\boldsymbol{k}_3)][1-f^0(\boldsymbol{k}_4)]}{[1-f^0(\boldsymbol{k})]} (\delta_{\boldsymbol{k},\boldsymbol{k}'} + \delta_{\boldsymbol{k}_2,\boldsymbol{k}'} - \delta_{\boldsymbol{k}_3,\boldsymbol{k}'} - \delta_{\boldsymbol{k}_4,\boldsymbol{k}'}). \tag{A2}$$

In the framework of the electron-gas model, we have used

$$\langle \boldsymbol{k}_1,\boldsymbol{k}_2|g_3|\boldsymbol{k}_3,\boldsymbol{k}_4\rangle = \pi\hbar v_F g_3(k_{\perp 1},k_{\perp 2},k_{\perp 3},k_{\perp 4})$$

for the (normalized) umklapp vertex functions evaluated on the Fermi surface. By separating the kinematics constraint on the momentum conservation into its longitudinal and transverse components [13], one has

$$\delta_{\boldsymbol{k}+\boldsymbol{k}_2,\boldsymbol{k}_3+\boldsymbol{k}_4+p\boldsymbol{G}} = \delta_{k_\perp+k_{\perp 2},k_{\perp 3}+k_{\perp 4}} \frac{2\pi}{L} \hbar v_F \delta(\varepsilon^p_{\boldsymbol{k}} + \varepsilon^{p_2}_{\boldsymbol{k}_2} + \varepsilon^{p_3}_{\boldsymbol{k}_3} + \varepsilon^{p_4}_{\boldsymbol{k}_4} - \Sigma), \tag{A3}$$

where $\Sigma = \epsilon_\perp(k_\perp) + \epsilon_\perp(k_{\perp 2}) + \epsilon_\perp(k_{\perp 3}) + \epsilon_\perp(k_{\perp 4})$.

The summation over the momentum vectors can be written as

$$\frac{1}{LN_P} \sum_{\boldsymbol{k}} = \sum_p \int \frac{d\varepsilon^p_{\boldsymbol{k}}}{2\pi\hbar v_F} \frac{1}{N_P} \sum_{k_\perp}. \tag{A4}$$

Carrying out the integration over the energy variables $(\varepsilon^{p_3}_{\boldsymbol{k}_3},\varepsilon^{p_4}_{\boldsymbol{k}_4})$ and $(\varepsilon^{p_2}_{\boldsymbol{k}_2},\varepsilon^{p_4}_{\boldsymbol{k}_4})$ for respectively the first and the last two terms of (A2), we arrive at the corresponding expressions entering the collision operator,

$$\mathcal{L}^{[1]}_{\boldsymbol{k},\boldsymbol{k}'} = \frac{\pi^2}{\hbar {N_P}^2} \sum_{k_{\perp 3},k_{\perp 4}} |g_3(k_\perp,k_{\perp 3}+k_{\perp 4}-k_\perp,k_{\perp 3},k_{\perp 4}) - g_3(k_\perp,k_{\perp 3}+k_{\perp 4}-k_\perp,k_{\perp 4},k_{\perp 3})|^2 \frac{1+e^{-\beta\varepsilon^p_{\boldsymbol{k}}}}{1+e^{\beta(\Sigma/2-\varepsilon^p_{\boldsymbol{k}})}} \frac{\Sigma/2e^{\beta\Sigma/2}}{e^{\beta\Sigma/2}-1} \delta_{\boldsymbol{k},\boldsymbol{k}'},$$

$$\mathcal{L}^{[2]}_{\boldsymbol{k},\boldsymbol{k}'} = \frac{\pi^3 v_F}{{LN_P}^2} \sum_{k_{\perp 3},k_{\perp 4}} |g_3(k_\perp,k'_\perp,k_{\perp 3},k_{\perp 4}) - g_3(k_\perp,k'_\perp,k_{\perp 4},k_{\perp 3})|^2 \delta_{k_\perp+k'_\perp,k_{\perp 3}+k_{\perp 4}} \delta\left(\varepsilon^p_{\boldsymbol{k}} + \varepsilon^{p'}_{\boldsymbol{k}'} - \Sigma_1/2\right) \frac{1+e^{-\beta\varepsilon^p_{\boldsymbol{k}}}}{1+e^{\beta\varepsilon^{p'}_{\boldsymbol{k}'}}} \frac{(\varepsilon^p_{\boldsymbol{k}} + \varepsilon^{p'}_{\boldsymbol{k}'}) e^{\beta(\varepsilon^p_{\boldsymbol{k}}+\varepsilon^{p'}_{\boldsymbol{k}'})}}{e^{\beta(\varepsilon^p_{\boldsymbol{k}}+\varepsilon^{p'}_{\boldsymbol{k}'})}-1},$$

$$\mathcal{L}^{[3]}_{\boldsymbol{k},\boldsymbol{k}'} = -\frac{\pi^3 v_F}{{LN_P}^2} \sum_{k_{\perp 2},k_{\perp 4}} |g_3(k_\perp,k_{\perp 2},k'_\perp,k_{\perp 4}) - g_3(k_\perp,k_{\perp 2},k_{\perp 4},k'_\perp)|^2 \delta_{k_\perp+k_{\perp 2},k'_\perp+k_{\perp 4}} \frac{1+e^{-\beta\varepsilon^p_{\boldsymbol{k}}}}{1+e^{-\beta\varepsilon^{p'}_{\boldsymbol{k}'}}} \frac{1}{(e^{\beta(\Sigma_2/2-\varepsilon^p_{\boldsymbol{k}})}+1)(e^{-\beta(\Sigma_2/2-\varepsilon^{p'}_{\boldsymbol{k}'})}+1)},$$

$$\mathcal{L}^{[4]}_{\boldsymbol{k},\boldsymbol{k}'} = -\frac{\pi^3 v_F}{L{N_P}^2}\sum_{k_{\perp 2},k_{\perp 3}} |g_3(k_\perp,k_{\perp 2},k_{\perp 3},k'_\perp) - g_3(k_\perp,k_{\perp 2},k'_\perp,k_{\perp 3})|^2 \delta_{k_\perp+k_{\perp 2},k_{\perp 3}+k'_\perp} \frac{1+e^{-\beta\varepsilon^p_{\boldsymbol{k}}}}{1+e^{-\beta\varepsilon^{p'}_{\boldsymbol{k}'}}} \frac{1}{(e^{\beta(\Sigma_3/2-\varepsilon^p_{\boldsymbol{k}})}+1)(e^{-\beta(\Sigma_3/2-\varepsilon^{p'}_{\boldsymbol{k}'})}+1)}, \tag{A5}$$

where $\Sigma_1$, $\Sigma_2$, and $\Sigma_3$ are obtained by substituting respectively $k_{\perp 2}$, $k_{\perp 3}$, and $k_{\perp 4}$ with $k'_\perp$ in the $\Sigma$ expression.

The normalized equation to solve numerically for the $\phi's$ reads

$$\sum_{i,\boldsymbol{k}'} \bar{\mathcal{L}}^{[i]}_{\boldsymbol{k},\boldsymbol{k}'}\bar{\phi}_{\boldsymbol{k}'} = 1,$$

where according to (A1) we have defined the normalized quantities $\pi d_\perp \mathcal{L}^{[i]}/v_F \to \bar{\mathcal{L}}^{[i]}$ and $\phi/(e\mathcal{E}_a\beta d_\perp) \to \bar{\phi}$. Carrying out the integration over $\varepsilon^{p'}_{\boldsymbol{k}'}$ and putting $\varepsilon^p_{\boldsymbol{k}} = 0$ on the Fermi surface, we arrive by rearranging the terms at the final equation,

$$\begin{aligned}
&\frac{\pi^3 d_\perp}{2a}\frac{T}{E_F}\frac{1}{N_P^2}\sum_{k'_\perp,k_{\perp 3},k_{\perp 4}} \Big\{ |g_3(k_\perp,k_{\perp 3}+k_{\perp 4}-k_\perp,k_{\perp 3},k_{\perp 4}) - g_3(k_\perp,k_{\perp 3}+k_{\perp 4}-k_\perp,k_{\perp 4},k_{\perp 3})|^2 \frac{\beta\Sigma'/2}{\sinh(\beta\Sigma'/2)}\delta_{k_\perp,k'_\perp} \\
&+ |g_3(k_\perp,k'_\perp,k_{\perp 3},k_{\perp 4}) - g_3(k_\perp,k'_\perp,k_{\perp 4},k_{\perp 3})|^2 \frac{\beta\Sigma''/2}{\sinh(\beta\Sigma''/2)}\delta_{k_\perp+k'_\perp,k_{\perp 3}+k_{\perp 4}} \\
&- 2|g_3(k_\perp,k_{\perp 3},k'_\perp,k_{\perp 4}) - g_3(k_\perp,k_{\perp 3},k_{\perp 4},k'_\perp)|^2 \frac{\beta\Sigma''/2}{\sinh(\beta\Sigma''/2)}\delta_{k_\perp+k_{\perp 3},k'_\perp+k_{\perp 4}} \Big\}\bar{\phi}_{k'_\perp} = 1,
\end{aligned} \tag{A6}$$

where

$$\Sigma' = \epsilon_\perp(k_\perp) + \epsilon_\perp(k_{\perp 3}+k_{\perp 4}-k_\perp) + \epsilon_\perp(k_{\perp 3}) + \epsilon_\perp(k_{\perp 4}), \quad \Sigma'' = \epsilon_\perp(k_\perp) + \epsilon_\perp(k'_\perp) + \epsilon_\perp(k_{\perp 3}) + \epsilon_\perp(k_{\perp 4}). \tag{A7}$$

We shall fix the ratio $d_\perp/a \simeq 1.05$ in (A6) from the known values of lattice constants in the Bechgaard salts for the longitudinal $\hat{a}$ (7.3 Å) and transverse $\hat{b}$ (7.7 Å) directions [2]. The solution of (A6) for the $\phi_{k_\perp}$ on the Fermi surface leads to the evaluation of conductivity (11) as the inverse of resistivity.

## APPENDIX B: ONE-LOOP RENORMALIZATION GROUP FOR THE ELECTRON GAS

### 1. Vertices

The renormalization-group approach to the quasi-1D electron gas is detailed in Refs. [21–23]. In the outline, the method starts with the segmentation of energy shells of thickness $\frac{1}{2}E_0(\ell)d\ell$, located at $\pm\frac{1}{2}E_0(\ell)$ from either side of the Fermi sheets, into $N_p$ patches, each centered at a particular value of the transverse momentum $k_\perp$, where $E_0(\ell) = E_0 e^{-\ell}$ is the scaled bandwidth at step $\ell$ and $E_0 \equiv 2E_F$ is the initial bandwidth. The successive partial trace integration of electron degrees of freedom in the partition function leads to the renormalization or flow of the scattering amplitudes $g_i$ as a function of $\ell$. At the one-loop level, the flow combines corrections from the electron-hole (Peierls) and electron-electron (Cooper) interfering channels of scattering and leads to the flow equations written in the compact form

$$\begin{aligned}
\partial_\ell g_1(k_{\perp 1},k_{\perp 2},k_{\perp 3},k_{\perp 4}) &= (-2g_1\circ g_1 + g_1\circ g_2 + g_2\circ g_1)\partial_\ell\mathcal{L}_P - (g_1\circ g_2 + g_2\circ g_1)\partial_\ell\mathcal{L}_C, \\
\partial_\ell g_2(k_{\perp 1},k_{\perp 2},k_{\perp 3},k_{\perp 4}) &= -(g_1\circ g_1 + g_2\circ g_2)\partial_\ell\mathcal{L}_C + (g_2\circ g_2 + g_3\circ g_3)\partial_\ell\mathcal{L}_P, \\
\partial_\ell g_3(k_{\perp 1},k_{\perp 2},k_{\perp 3},k_{\perp 4}) &= (-g_1\circ g_3 - g_3\circ g_1 + g_2\circ g_3 + g_3\circ g_2)\partial_\ell\mathcal{L}_P + 2g_2\bullet g_3\partial_\ell\mathcal{L}_P,
\end{aligned} \tag{B1}$$

where $\partial_\ell = \partial/\partial\ell$. $\mathcal{L}_{v=P,C}$ are the Peierls and Cooper loops whose derivative at finite temperature comprises an integration over the patch. These take the form

$$\partial_\ell\mathcal{L}_v(k_\perp,q^{(\prime)}_{\perp v}) = \frac{E_0(\ell)}{4N_P}\sum_{\mu=\pm 1}\int_{k_\perp-\pi/N_P}^{k_\perp+\pi/N_P}\frac{dk_\perp}{2\pi}\frac{\theta(|E_0(\ell)/2+\mu A_v| - E_0(\ell)/2)}{E_0(\ell)+\mu A_v}[\tanh[\beta E_0(\ell)/4] + \tanh[\beta(E_0(\ell)/4+\mu A_v/2)]], \tag{B2}$$

where

$$A_v(k_\perp,q^{(\prime)}_{\perp v}) = -\epsilon_\perp(k_\perp) - \eta_v\epsilon_\perp(\eta_v k_\perp + q^{(\prime)}_{\perp v}) + \eta_v\epsilon_\perp(\eta_v k_{\perp 2(4)} + q^{(\prime)}_{\perp v}) + \epsilon_\perp(k_{\perp 2(4)}) \tag{B3}$$

with $q^{(\prime)}_{\perp P} = k_{\perp 3} - k_{\perp 2} = k_{\perp 1} - k_{\perp 4} (k_{\perp 3} - k_{\perp 1} = k_{\perp 2} - k_{\perp 4})$ and $q_{\perp C} = k_{\perp 1} + k_{\perp 2} = k_{\perp 3} + k_{\perp 4}$; $\eta_P = 1$ and $\eta_C = -1$. $\theta(x)$ is the Heaviside function [$\theta(0) \equiv \frac{1}{2}$].

The momentum dependence of couplings in the discrete convolution products "$\circ$" over the internal $k_\perp$ loop variable on the right-hand side of (B1) are in order $g(k_\perp,k_{\perp 4},k_{\perp 1},k_\perp - q_{\perp P})g(k_\perp,k_{\perp 2},k_{\perp 3},k_\perp - q_{\perp P})$ for the Peierls channel, $g(k_{\perp 1},k_{\perp 2},k_\perp,q_{\perp C} - k_\perp)g(k_{\perp 3},k_{\perp 4},k_\perp,q_{\perp C} - k_\perp)$ for the Cooper channel, and $g(k_\perp,k_{\perp 4},k_{\perp 2},k_\perp - q'_{\perp P})g(k_{\perp 1},k_\perp,k_{\perp 3},k_{\perp 1} - q'_{\perp P})$ for the "$\bullet$" product of the off-diagonal Peierls channel.

### 2. Susceptibilities

The linear response of the electron system to a source field of SDW and SC$d$ order parameter leads to the corresponding expressions of the normalized static susceptibility

$$\bar{\chi}_\mu(\boldsymbol{q}_\mu) = 2\int_\ell [f_\mu(k_\perp) z_\mu(k_\perp)]^2 \partial_\ell \mathcal{L}_\mu d\ell \tag{B4}$$

for $\mu =$ SDW at $\boldsymbol{q}_0 = (2k_F,\pi)$ and $\mu =$ SC$d$ at $\boldsymbol{q}_0 = 0$.These are functions of the renormalization factor for the pair vertex $z_\mu$ in the corresponding channel which obeys the following flow equation:

$$\partial_\ell z_\mu(k_\perp) = (\partial_\ell \mathcal{L}_\mu) g_\mu z_\mu(k'_\perp), \tag{B5}$$

where

$$\begin{aligned} g_{\rm SDW} &= g_2(k'_\perp + \pi, k_\perp, k_\perp + \pi, k'_\perp) + g_3(k'_\perp - \pi, k_\perp + \pi, k_\perp, k'_\perp), \\ g_{{\rm SC}d} &= -g_1(-k'_\perp, k'_\perp, -k_\perp, k_\perp) - g_2(-k'_\perp, k'_\perp, -k_\perp, k_\perp), \end{aligned} \tag{B6}$$

are the combinations of momentum dependent scattering amplitudes that govern the flow for each susceptibility. The form factors $f_\mu$ assigned to the nature of ordered phases are $f_{\rm SDW} = 1$ and $f_{{\rm SC}d} = \sqrt{2}\cos k_\perp$.


[1] D. Jérome, A. Mazaud, M. Ribault, and K. Bechgaard, J. Phys. (Paris) Lett. **41**, 95 (1980).
[2] D. Jérome and H. J. Schulz, Adv. Phys. **31**, 299 (1982).
[3] C. Bourbonnais and D. Jérome, in *The Physics of Organic Superconductors and Conductors*, Springer Series in Materials Science Vol. 110, edited by A. Lebed (Springer, Heidelberg, 2008), p. 357.
[4] S. E. Brown, Physica C **514**, 279 (2015).
[5] L. Taillefer, Annu. Rev. Condens. Matter Phys. **1**, 51 (2010).
[6] N. P. Armitage, P. Fournier, and R. L. Greene, Rev. Mod. Phys. **82**, 2421 (2010).
[7] K. Jin, N. P. Butch, K. Kirshenbaum, J. Paglione, and R. L. Greene, Nature (London) **476**, 73 (2011).
[8] T. Tomita, K. Kuga, Y. Uwatoko, P. Coleman, and S. Nakatsuji, Science **349**, 506 (2015).
[9] D. J. Scalapino, Rev. Mod. Phys. **84**, 1383 (2012).
[10] G. R. Stewart, Rev. Mod. Phys. **83**, 1589 (2011).
[11] N. Doiron-Leyraud, P. Auban-Senzier, S. René de Cotret, C. Bourbonnais, D. Jérome, K. Bechgaard, and L. Taillefer, Phys. Rev. B **80**, 214531 (2009).
[12] N. Doiron-Leyraud, P. Auban-Senzier, S. R. de Cotret, C. Bourbonnais, A. Sedeki, D. Jérome, K. Bechgaard, and L. Taillefer, Eur. Phys. J. B **78**, 23 (2010).
[13] L. P. Gor'kov and M. Mochena, Phys. Rev. B **57**, 6204 (1998).
[14] A. T. Zheleznyak and V. M. Yakovenko, Eur. Phys. J. B **11**, 385 (1999).
[15] V. J. Emery, R. Bruinsma, and S. Barisic, Phys. Rev. Lett. **48**, 1039 (1982).
[16] C. Bourbonnais, F. Creuzet, D. Jérome, K. Bechgaard, and A. Moradpour, J. Phys. (Paris) Lett. **45**, 755 (1984).
[17] F. Creuzet, C. Bourbonnais, L. G. Caron, D. Jérome, and A. Moradpour, Synth. Met. **19**, 277 (1987).
[18] W. Wu, P. M. Chaikin, W. Kang, J. Shinagawa, W. Yu, and S. E. Brown, Phys. Rev. Lett. **94**, 097004 (2005).
[19] S. E. Brown, P. M. Chaikin, and M. J. Naughton, in *The Physics of Organic Superconductors and Conductors* (Ref. 3), p. 49.
[20] Y. Kimura, M. Misawa, and A. Kawamoto, Phys. Rev. B **84**, 045123 (2011).
[21] C. Bourbonnais and A. Sedeki, Phys. Rev. B **80**, 085105 (2009).
[22] J. C. Nickel, R. Duprat, C. Bourbonnais, and N. Dupuis, Phys. Rev. B **73**, 165126 (2006).
[23] A. Sedeki, D. Bergeron, and C. Bourbonnais, Phys. Rev. B **85**, 165129 (2012).
[24] H. Meier, P. Auban-Senzier, C. Pépin, and D. Jérome, Phys. Rev. B **87**, 125128 (2013).
[25] J. M. Buhmann, M. Ossadnik, T. M. Rice, and M. Sigrist, Phys. Rev. B **87**, 035129 (2013).
[26] H. Haug and A. P. Jauho, in *Quantum Kinetics in Transport and Optics of Semiconductors*, Springer Series in Solid-State Sciences Vol. 110, edited by M. Cardona and P. Fulde (Springer, Heidelberg, 2008), p. 3.
[27] P. Wzietek, F. Creuzet, C. Bourbonnais, D. Jérome, K. Bechgaard, and P. Batail, J. Phys. I (France) **3**, 171 (1993).
[28] B. J. Klemme, S. E. Brown, P. Wzietek, G. Kriza, P. Batail, D. Jérome, and J. M. Fabre, Phys. Rev. Lett. **75**, 2408 (1995).
[29] J. Moser, M. Gabay, P. Auban-Senzier, D. Jérome, K. Bechgaard, and J. M. Fabre, Eur. Phys. J. B **1**, 39 (1998).
[30] P. M. Grant, J. Phys. (Paris) Coll. **44**, C3-847 (1983).
[31] S. Barisic and S. Brazovskii, in *Recent Developments in Condensed Matter Physics*, edited by J. T. Devreese (Plenum, New York, 1981), Vol. 1, p. 327.
[32] K. Penc and F. Mila, Phys. Rev. B **50**, 11429 (1994).
[33] P. M. Grant, Phys. Rev. B **26**, 6888 (1982).
[34] L. Ducasse, A. Abderrabba, and B. Gallois, J. Phys. C **18**, L947 (1985).
[35] K. Yamaji, J. Phys. Soc. Jpn. **55**, 860 (1986); L. P. Gor'kov and A. Lebed, J. Phys. Lett. **45**, 433 (1984).
[36] The pressure increase of electronic band parameters introduces a smooth decrease of the normalized to the bandwidth couplings $g_i$ of the electron-gas model. This can be shown to introduce only quantitative changes compared to the case where solely $t'_\perp$ simulates the effect of pressure. See for example R. Duprat and C. Bourbonnais, Eur. Phys. J. B **21**, 219 (2001).
[37] C. Bourbonnais and L. G. Caron, Int. J. Mod. Phys. B **05**, 1033 (1991).

[38] C. Bourbonnais, B. Guay, and R. Wortis, in *Theoretical Methods for Strongly Correlated Electrons*, edited by D. Sénéchal, A. M. Tremblay, and C. Bourbonnais (Springer, Heidelberg, 2003), pp. 77–78.
[39] C. Bourbonnais and A. Sedeki, C. R. Phys. **12**, 532 (2011).
[40] L. P. Gor'kov and I. E. Dzyaloshinskii, JETP Lett. (USSR) **18**, 401 (1973).
[41] T. Giamarchi, Phys. Rev. B **44**, 2905 (1991).
[42] T. Moriya and K. Ueda, Rep. Prog. Phys. **66**, 1299 (2003).
[43] K. Bechgaard, C. Jacobsen, K. Mortensen, H. Pedersen, and N. Thorup, Solid State Commun. **33**, 1119 (1980).
[44] T. Vuletic, P. Auban-Senzier, C. Pasquier, S. Tomic, D. Jerome, M. Heritier, and K. Bechgaard, Eur. Phys. J. B **25**, 319 (2002).
[45] C. Coulon, P. Delhaes, S. Flandrois, R. Lagnier, E. Bonjour, and J. Fabre, J. Phys. (Paris) **43**, 1059 (1982).
[46] L. Balicas, K. Benhia, W. Kang, E. Canadell, M. R. P. Auban-Senzier, D. Jérome, and J. Fabre, J. Phys. I (France) **4**, 1539 (1994).
[47] T. Giamarchi, Physica B **230-232**, 975 (1997).
[48] A. Schwartz, M. Dressel, G. Grüner, V. Vescoli, L. Degiorgi, and T. Giamarchi, Phys. Rev. B **58**, 1261 (1998).
[49] M. Tsuchiizu, H. Yoshioka, and Y. Suzumura, J. Phys. Soc. Jpn. **70**, 1460 (2001).
[50] R. Hlubina and T. M. Rice, Phys. Rev. B **51**, 9253 (1995).
[51] The spin fluctuations that govern the temperature dependence of nuclear relaxation rate in the intermediate- and high-temperature domains have been shown to pertain to small $q$ wave vectors (see for example Refs. [17,21,27]). These fluctuations are distinct from those generated by the half-filling umklapp term $g_3$ of the SDW sector.
[52] C. S. Jacobsen, D. B. Tanner, and K. Bechgaard, Phys. Rev. Lett. **46**, 1142 (1981).
[53] M. Dressel, A. Schwartz, G. Gruner, and L. Degiorgi, Phys. Rev. Lett. **77**, 398 (1996).

**Seebeck coefficient**

When a temperature difference is maintained at the ends of a metal or a semiconductor sample and no electric current is allowed to flow, by an open circuit setup, there will be a steady-state electrostatic potential difference between high and low temperature regions of the sample. The thermoelectric power or the Seebeck coefficient $Q$ is defined as the ratio between the potential and the temperature differences, or in other terms, the ratio of induced electric field to the temperature gradient along the $a$ direction:

$$Q_a = \frac{-\Delta V_a}{\Delta T_a} \equiv \frac{\boldsymbol{\mathcal{E}}_a}{\boldsymbol{\nabla}_a T} \tag{3.42}$$

In this sub-section we obtain the expression of the longitudinal Seebeck coefficient for the upper hole-band of an array of $N_P$ dimerized chains at three-quarter filling:

$$E_k = \sqrt{2(t^2+\delta t^2)+2(t^2-\delta t^2)\cos ka} + \epsilon_\perp(k_\perp), \tag{3.43}$$

where $t \pm \delta t$ are the transfer integrals within and between the dimers ($\delta t > 0$ , $\delta t \ll t$). The transverse part of the spectrum is given by:

$$\epsilon_\perp(k_\perp) = 2t_\perp \cos k_\perp d_\perp + 2t'_\perp \cos 2k_\perp d_\perp, \tag{3.44}$$

where for hole carriers, the hopping transverse to chains and the anti-nesting parameter, $t_\perp$ and $t'_\perp$, are both positive.

If we define the driving fields as $\boldsymbol{F} = \begin{pmatrix} \boldsymbol{\mathcal{E}}_a \\ -\boldsymbol{\nabla}_a T \end{pmatrix}$ , then the thermal and electric current densities can be related to the driving fields *via* a response function matrix defined as

$$\begin{pmatrix} j_e^a \\ j_{\text{th}}^a \end{pmatrix} = \begin{bmatrix} K_{11} & K_{12} \\ K_{21} & K_{22} \end{bmatrix} \begin{pmatrix} \boldsymbol{\mathcal{E}}_a \\ -\boldsymbol{\nabla}_a T \end{pmatrix}. \tag{3.45}$$

For a longitudinal (along the $a$-axis) electric field and a longitudinal thermal gradient, the electric current density along the chain direction reads:

$$j_e^a = K_{11}\mathcal{E}_a - K_{12}\nabla_a T. \tag{3.46}$$

Setting $j_e^a = 0$ for open-circuit condition, we can express the longitudinal Seebeck coefficient in

terms of the $K_{ij}$ coefficients:

$$Q_a = \frac{\boldsymbol{\mathcal{E}}_a}{\boldsymbol{\nabla}_a T} = \frac{K_{12}}{K_{11}}. \tag{3.47}$$

Taking into account the full equation for the normalized deviation from thermal equilibrium, equation (3.22), and inserting it to the expression (3.27) for the longitudinal current density, the transport coefficients take the following forms

$$K_{11} = \frac{2e^2}{LN_\perp d_\perp} \sum_{\boldsymbol{k}} v_{\boldsymbol{k}}^a f^0(\boldsymbol{k})(1 - f^0(\boldsymbol{k}))\beta \mathcal{L}^{-1} \mathcal{E}_a v_{\boldsymbol{k}}^a. \tag{3.48}$$

$$K_{12} = \frac{2e}{LN_\perp d_\perp} \sum_{\boldsymbol{k}} v_{\boldsymbol{k}}^a f^0(\boldsymbol{k})(1 - f^0(\boldsymbol{k}))\beta^2 k_B \mathcal{L}^{-1}(E_{\boldsymbol{k}} - \mu)\nabla_a T v_{\boldsymbol{k}}^a. \tag{3.49}$$

We define the thermal $\phi_{\boldsymbol{k}}^T$ and the electrical $\phi_{\boldsymbol{k}}^{\mathcal{E}}$ deviations as

$$\phi_{\boldsymbol{k}}^{\mathcal{E}} = e\beta \mathcal{L}^{-1} \mathcal{E}_a v_{\boldsymbol{k}}^a. \tag{3.50}$$

$$\phi_{\boldsymbol{k}}^T = \beta^2 k_B \mathcal{L}^{-1}(E_{\boldsymbol{k}} - \mu)\nabla_a T v_{\boldsymbol{k}}^a. \tag{3.51}$$

Dividing $K_{12}$ to $K_{11}$, and in order to obtain the right unit for the Seebeck coefficient in (3.47) as $[Q] \sim \frac{k_B}{e}$, we introduce the quantities

$$\bar{\phi}_{\boldsymbol{k}}^{\mathcal{E}} = \phi_{\boldsymbol{k}}^{\mathcal{E}} / (e\beta v_{\boldsymbol{k}_F}^a \mathcal{E}_a),$$

$$\bar{\phi}_{\boldsymbol{k}}^T = \phi_{\boldsymbol{k}}^T / [\beta^2 k_B v_{\boldsymbol{k}_F}^a (E_{\boldsymbol{k}} - \mu)\nabla_a T],$$

which both have the unit of time. Here the particle velocity has been evaluated at the Fermi level due to the peak of $f^0(1 - f^0)$ factor at the Fermi level. Therefore, we can write

$$\begin{aligned} Q_a = \frac{K_{12}}{K_{11}} &= \frac{\frac{2e\beta^2 k_B}{LN_P} \sum_{\boldsymbol{k}} {v_{\boldsymbol{k}}^a}^2 f^0(\boldsymbol{k})\big(1 - f^0(\boldsymbol{k})\big)(E_K - \mu)\bar{\phi}_{\boldsymbol{k}}^T}{\frac{2\beta e^2}{LN_P} \sum_{\boldsymbol{k}} {v_{\boldsymbol{k}}^a}^2 f^0(\boldsymbol{k})\big(1 - f^0(\boldsymbol{k})\big)\bar{\phi}_{\boldsymbol{k}}^{\mathcal{E}}} \\ &= \frac{k_B}{e} \frac{\int dE N(E) f^0(E)\big(1 - f^0(E)\big)(E - \mu) \sum_{k_\perp} {v_{E,k_\perp}^a}^2 \bar{\phi}_{E,k_\perp}^T}{\int dE N(E) f^0(E)\big(1 - f^0(E)\big) \sum_{k_\perp} {v_{E,k_\perp}^a}^2 \bar{\phi}_{E,k_\perp}^{\mathcal{E}}}. \end{aligned} \tag{3.52}$$

With a Sommerfeld expansion of nominator and denominator, we arrive at the following expression for the Seebeck coefficient

$$Q_a = \frac{\pi^3}{3}\frac{k_B^2 T}{e}\left\{\left[\frac{d\ln\langle N(E,k_\perp)\rangle_{k_\perp}}{dE} + 2\frac{d\ln\langle v^a_{E,k_\perp}\rangle_{k_\perp}}{dE}\right] + \frac{\partial\ln\langle\bar{\phi}_{E,k_\perp}\rangle_{k_\perp}}{\partial E}\right\}_{E=0}, \tag{3.53}$$

where the first and the second terms are respectively the energy derivative of the density of states per spin, $\langle N(E,k_\perp)\rangle_{k_\perp} (= \pi^{-1}\langle|\partial k/\partial E_k|\rangle_{k_\perp})$, and the derivative of the longitudinal velocity $\langle v^a_{E,k_\perp}\rangle_{k_\perp} (= \hbar^{-1}\langle\partial E_k/\partial k\rangle_{k_\perp})$ both averaged over the Fermi surface for a filling of one hole per dimer ($\langle\ldots\rangle_{k_\perp} = N_P^{-1}\sum_{k_\perp}\ldots$). The third term is proportional to the energy derivative of $\langle\bar{\phi}'_{E=0,k_\perp}\rangle_{k_\perp}$ averaged over the Fermi surface for the normalized deviations $\bar{\phi}^{\mathcal{E}} = \bar{\phi}^T \equiv \bar{\phi}$, namely the scattering time.

The Boltzmann equation to solve for the scattering time yields

$$\mathcal{L}\bar{\phi}_k = \sum_{i,k'}\mathcal{L}^{[i]}_{k,k'}\bar{\phi}_{k'} = 1, \tag{3.54}$$

on which performing the same procedure as in the case of resistivity, we arrive at the final equation

$$\begin{aligned}
&\frac{\pi}{\beta\hbar}\frac{1}{N_P^2}\sum_{k'_\perp,k_{\perp 3},k_{\perp 4}}\Big\{\left|g_3(k_\perp,k_{\perp 3}+k_{\perp 4}-k_\perp;k_{\perp 3},k_{\perp 4}) - g_3(k_\perp,k_{\perp 3}+k_{\perp 4}-k_\perp;k_{\perp 4},k_{\perp 3})\right|^2\delta_{k_\perp,k'_\perp}\\
&\times\frac{\beta\Sigma'/4\cosh(\beta E/2)}{\cosh(\beta(\Sigma'/4-E/2))\sinh(\beta\Sigma'/4)} + \left|g_3(k_\perp,k'_\perp;k_{\perp 3},k_{\perp 4}) - g_3(k_\perp,k'_\perp;k_{\perp 4},k_{\perp 3})\right|^2\\
&\times\frac{\beta\Sigma''/4\cosh(\beta E/2)}{\cosh(\beta(\Sigma''/4-E/2))\sinh(\beta\Sigma''/4)}\delta_{k_\perp+k'_\perp,k_{\perp 3}+k_{\perp 4}} - 2\left|g_3(k_\perp,k_{\perp 3};k'_\perp,k_{\perp 4}) - g_3(k_\perp,k_{\perp 3};k_{\perp 4},k'_\perp)\right|^2\\
&\times\frac{\beta\Sigma''/4\cosh(\beta E/2)}{\cosh(\beta(\Sigma''/4-E/2))\sinh(\beta\Sigma''/4)}\delta_{k_\perp+k_{\perp 3},k'_\perp+k_{\perp 4}}\Big\}\bar{\phi}_{E,k'_\perp} = 1,
\end{aligned} \tag{3.55}$$

with $\Sigma' = \epsilon_\perp(k_\perp) + \epsilon_\perp(k_{\perp 3}+k_{\perp 4}-k_\perp) + \epsilon_\perp(k_{\perp 3}) + \epsilon_\perp(k_{\perp 4})$ and $\Sigma'' = \epsilon_\perp(k_\perp) + \epsilon_\perp(k'_\perp) + \epsilon_\perp(k_{\perp 3}) + \epsilon_\perp(k_{\perp 4})$.

We solve (3.55) numerically, with the RG calculated umklapp vertex function, to find $\bar{\phi}_{E,k_\perp}$. We then insert this into the third term of equation (3.53) and compute the longitudinal Seebeck coefficient. The results are given and discussed in detail in the following paper. We present the temperature variation of the Seebeck coefficient over the whole temperature interval of the phase diagram for the model and study its link to the energy profile of the anisotropic inelastic scattering time. A critical analysis of the results is made from a comparison with the existing experiments.

## Publication

- **Seebeck coefficient in correlated low-dimensional organic metals**

**M. Shahbazi** and C. Bourbonnais, published in **Phys. Rev. B 94, 195153 (2016)**
I have developed an analytic as well as a numerical solution of the Boltzmann equation coupled to the renormalization group technique to calculate the Seebeck coefficient of a quasi-1D electron gas model. I have written all the computer programs. I have written all the manuscript. The co-author has participated to the correction of the manuscript for publication.

# Seebeck coefficient in correlated low-dimensional organic metals

M. Shahbazi* and C. Bourbonnais†
*Regroupement Québecois sur les Matériaux de Pointe, Département de physique, Université de Sherbrooke, Sherbrooke, Québec, Canada J1K-2R1*
(Received 18 September 2016; revised manuscript received 12 November 2016; published 29 November 2016)

We study the influence of inelastic electron-electron scattering on the temperature variation of the Seebeck coefficient in the normal phase of quasi-one-dimensional organic superconductors. The theory is based on the numerical solution of the semiclassical Boltzmann equation for which the collision integral equation is solved with the aid of the renormalization-group method for the electronic umklapp scattering vertex. We show that the one-loop renormalization-group flow of momentum and temperature-dependent umklapp scattering, in the presence of nesting alterations of the Fermi surface, introduce electron-hole asymmetry in the energy dependence of the anisotropic scattering time. This is responsible for the enhancement of the Seebeck coefficient with respect to the band $T$-linear prediction and even its sign reversal around the quantum critical point of the phase diagram, namely, where the interplay between antiferromagnetism and superconductivity and also the strength of spin fluctuations are the strongest. A comparison of the results with available data on low-dimensional organic superconductors is presented and critically discussed.

DOI: 10.1103/PhysRevB.94.195153

## I. INTRODUCTION

In the past few years we have seen expanding interest in the Seebeck coefficient as a sensitive probe of fluctuations encased in the quantum critical behavior of correlated electrons. This has been exemplified both experimentally and theoretically for quantum critical points in heavy fermions [1–5] and pnictides [6] and for hole- [7–10] and electron-doped [11,12] cuprates. In organic superconductors like the Bechgaard salt $(TMTSF)_2X$ series, also known to exhibit quantum criticality, the measurements of the Seebeck coefficient have been the subject of numerous reports following their discovery [13–19] until very recently [20]. However, these works have found very little theoretical echo as to the possible part played by quantum fluctuations in the thermoelectric response seen in these correlated quasi-one-dimensional (quasi-1D) metals. This topic, which has remained essentially unexplored so far [21], will be the main focus of the present work.

The quantum critical behavior of the Bechgaard salts is known to result from the juncture of a declining spin-density-wave (SDW) state with the onset of a superconducting (SC) dome under pressure [22–26]. The signatures of quantum criticality have been chiefly revealed by the observation of linear-$T$ resistivity [27], whose strength scales with the distance from the quantum critical point (QCP) along the pressure axis. Among other fingerprints of quantum criticality, linear resistivity was also found to scale with the amplitude of SDW fluctuations seen by NMR and with the size of the critical temperature $T_c$ for superconductivity [25,28–30].

The contributions of the renormalization-group (RG) approach to the understanding of these quantum critical features were the purpose of several works in the past [31–33]. In the framework of the quasi-1D electron-gas model, for instance, that is how the characteristic sequence of instability lines and the scaling of spin fluctuations with the size of $T_c$ could be fairly well simulated when the antinesting amplitude of the quasi-1D electron band structure was used as a tuning parameter for the QCP [33–35].

More recently, the RG calculations for the umklapp vertex were shown to serve as an input to the linearized Boltzmann theory of electrical transport [36]. From this combination of techniques, first proposed by Buhmann *et al.* [9] in the context of the two-dimensional (2D) Hubbard model for the cuprates, the metallic resistivity across the QCP could be calculated along the pressure (antinesting) axis, and the results could be congruently compared with experiments in the Bechgaard salts [27].

In this work we further exploit the RG-Boltzmann approach and derive the Seebeck coefficient for correlated quasi-1D metals. The numerical integration of the linearized Boltzmann equation when fed in by the RG umklapp vertex function allows a microscopic determination of the energy variation of the anisotropic electron-electron scattering time across the Fermi surface. This variation is mostly influenced by SDW fluctuations and is anisotropic on the Fermi surface. It introduces deviations with respect to a positive and linear-$T$ Seebeck coefficient obtained in the band limit for hole carriers in materials like the Bechgaard salts. The deviations take the form of enhancements that can be not only positive but also negative or electronlike in character. The latter can lead to the sign reversal of the Seebeck coefficient, especially in the neighborhood of the QCP where the interplay between SDW and SC, together with the amplitude of the SDW fluctuations in the metallic state, is the strongest. These results offer an interesting avenue of understanding for the sign reversal of the Seebeck coefficient occurring in the Bechgaard salts near their QCP.

The theory is broadened to systems with stronger umklapp scattering that favors a Mott instability in the 1D portion of their metallic state and which can be approached by the weak-coupling RG from the high-temperature domain. The results are compared to the measurements of the Seebeck coefficient for prototype members of the sulfur-based compounds, the $(TMTTF)_2X$, known as the Fabre salts series [37].

*maryam.shahbazi@usherbrooke.ca
†claude.bourbonnais@usherbrooke.ca

 

These compounds are characterized by a more pronounced dimerization of the organic stacks which magnifies umklapp scattering and favors a crossover toward a 1D Mott insulating state.

In Sec. II, we use the linearized Boltzmann theory to derive the expression of the Seebeck coefficient for a quasi-1D three-quarter-filled hole band of a lattice of weakly dimerized chains. In Sec. III, the momentum-resolved renormalized umklapp vertex entering the Boltzmann equation is computed by the RG in the conditions of the quasi-1D electron-gas model simulating the sequence of instabilities found in the Bechgaard salts. In Sec. IV, we present the temperature variations of the Seebeck coefficient across the quantum critical point of the model and examine their link to the energy profile of the inelastic scattering time. In Sec. V, a comparison of the results is made with available data for $(TMTSF)_2X$ and on a broader basis for the more correlated compounds $(TMTTF)_2X$. We conclude in Sec. VI.

## II. LINEARIZED BOLTZMANN THEORY OF THE SEEBECK COEFFICIENT

We consider the semiclassical Boltzmann equation for the variation of the quasiparticle Fermi distribution function $f$ in the presence of collisions and a thermal gradient $\nabla_r T$. In steady-state conditions, it takes the form

$$\left[\frac{\partial f(\boldsymbol{k})}{\partial t}\right]_{\rm coll} = e\,\boldsymbol{\mathcal{E}}\cdot\nabla_{\hbar\boldsymbol{k}} f - \frac{(E_{\boldsymbol{k}}-\mu)}{T}\nabla_r T\cdot\nabla_{\hbar\boldsymbol{k}} f, \quad (1)$$

where $E_{\boldsymbol{k}}$ is the carrier spectrum, $\mu$ is the chemical potential, $e$ is the electron charge, and $\boldsymbol{\mathcal{E}}$ is the electric field set up by the thermal gradient. The collision integral for an array of $N_P$ chains of length $L$ takes the form

$$\begin{aligned}\left[\frac{\partial f(\boldsymbol{k})}{\partial t}\right]_{\rm coll} =& -(LN_P)^{-2}\sum_{\boldsymbol{k}_2,\boldsymbol{k}_3,\boldsymbol{k}_4}\frac{1}{2}|\langle \boldsymbol{k},\boldsymbol{k}_2|g_3|\boldsymbol{k}_3,\boldsymbol{k}_4\rangle \\ &- \langle \boldsymbol{k},\boldsymbol{k}_2|g_3|\boldsymbol{k}_4,\boldsymbol{k}_3\rangle|^2\frac{2\pi}{\hbar}\delta_{\boldsymbol{k}+\boldsymbol{k}_2,\boldsymbol{k}_3+\boldsymbol{k}_4\pm\boldsymbol{G}} \\ &\times\delta\big(E_{\boldsymbol{k}}+E_{\boldsymbol{k}_2}-E_{\boldsymbol{k}_3}-E_{\boldsymbol{k}_4}\big) \\ &\times\{f(\boldsymbol{k})f(\boldsymbol{k}_2)[1-f(\boldsymbol{k}_3)][1-f(\boldsymbol{k}_4)] \\ &-[1-f(\boldsymbol{k})][1-f(\boldsymbol{k}_2)]f(\boldsymbol{k}_3)f(\boldsymbol{k}_4)\}. \quad (2)\end{aligned}$$

From Fermi's golden rule, the transition probability per unit of time is related to the matrix element $\langle \boldsymbol{k},\boldsymbol{k}_2|g_3|\boldsymbol{k}_3,\boldsymbol{k}_4\rangle$ for longitudinal umklapp processes, where $\boldsymbol{G}=(4k_F,0)$ is the longitudinal reciprocal lattice wave vector and $k_F$ is the 1D Fermi wave vector.

We proceed to the linearization of the Boltzmann equation by introducing [38]

$$f(\boldsymbol{k}) = \frac{1}{e^{\beta(E_{\boldsymbol{k}}-\mu)-\phi_{\boldsymbol{k}}}+1}, \quad (3)$$

where $\phi_{\boldsymbol{k}}$ is a normalized deviation to thermal equilibrium and $\beta=1/k_BT$. In the tight-binding approximation, the hole band spectrum for a linear array of $N_P$ weakly coupled dimerized chains is given by

$$E_{\boldsymbol{k}} = \sqrt{2(t^2+\delta t^2)+2(t^2-\delta t^2)\cos ka}+\epsilon_\perp(k_\perp), \quad (4)$$

where $t\pm\delta t$ are the transfer integrals within and between the dimers ($\delta t>0, \delta t\ll t$). Here $a$ is the lattice spacing along the chains, namely, the distance between dimers. The transverse part of the hole spectrum is given by

$$\epsilon_\perp(k_\perp) = 2t_\perp\cos k_\perp d_\perp + 2t'_\perp\cos 2k_\perp d_\perp, \quad (5)$$

where $t_\perp$ and $t'_\perp$ are the first- and second-nearest-neighbor transfer integrals in the direction perpendicular to the chains.

For small deviations with respect to equilibrium, the Fermi distribution becomes

$$f(\boldsymbol{k}) \simeq f^0(\boldsymbol{k}) + f^0(\boldsymbol{k})[1-f^0(\boldsymbol{k})]\phi_{\boldsymbol{k}}, \quad (6)$$

where $f^0(\boldsymbol{k})$ is the equilibrium distribution at $\phi_{\boldsymbol{k}}=0$. Inserting (6) in Eqs. (1) and (2) leads to the linearized Boltzmann equation

$$\begin{aligned}\mathcal{L}\phi_{\boldsymbol{k}} &= e\beta\mathcal{E}\cdot\boldsymbol{v}_{\boldsymbol{k}} - \beta^2 k_B(E_{\boldsymbol{k}}-\mu)\boldsymbol{v}_{\boldsymbol{k}}\cdot\nabla_r T \\ &\equiv \mathcal{L}\phi^{\mathcal{E}}_{\boldsymbol{k}} - \mathcal{L}\phi^{T}_{\boldsymbol{k}}. \quad (7)\end{aligned}$$

The collision operator $\mathcal{L}$ satisfies the integral equation

$$\mathcal{L}\phi^j_{\boldsymbol{k}} = \sum_{\boldsymbol{k}'}\mathcal{L}_{\boldsymbol{k},\boldsymbol{k}'}\phi^j_{\boldsymbol{k}'} \quad (j=\mathcal{E},T), \quad (8)$$

where the kernel is given by

$$\begin{aligned}\mathcal{L}_{\boldsymbol{k},\boldsymbol{k}'} =& (LN_P)^{-2}\sum_{\boldsymbol{k}_2,\boldsymbol{k}_3,\boldsymbol{k}_4}\frac{1}{2}|\langle \boldsymbol{k},\boldsymbol{k}_2|g_3|\boldsymbol{k}_3,\boldsymbol{k}_4\rangle \\ &- \langle \boldsymbol{k},\boldsymbol{k}_2|g_3|\boldsymbol{k}_4,\boldsymbol{k}_3\rangle|^2\frac{2\pi}{\hbar}\delta_{\boldsymbol{k}+\boldsymbol{k}_2,\boldsymbol{k}_3+\boldsymbol{k}_4\pm\boldsymbol{G}} \\ &\times\delta\big(E_{\boldsymbol{k}}+E_{\boldsymbol{k}_2}-E_{\boldsymbol{k}_3}-E_{\boldsymbol{k}_4}\big) \\ &\times\frac{f^0(\boldsymbol{k}_2)[1-f^0(\boldsymbol{k}_3)][1-f^0(\boldsymbol{k}_4)]}{[1-f^0(\boldsymbol{k})]} \\ &\times\big(\delta_{\boldsymbol{k},\boldsymbol{k}'}+\delta_{\boldsymbol{k}_2,\boldsymbol{k}'}-\delta_{\boldsymbol{k}_3,\boldsymbol{k}'}-\delta_{\boldsymbol{k}_4,\boldsymbol{k}'}\big) \\ =& \sum_{i=1}^{4}\mathcal{L}^{[i]}_{\boldsymbol{k},\boldsymbol{k}'}, \quad (9)\end{aligned}$$

which can be written as the sum of four contributions. The explicit expressions for the diagonal ($\mathcal{L}^{[1]}$) and off-diagonal ($\mathcal{L}^{[2-4]}$) terms are calculated according to Ref. [36] in the limit of the quasi-1D electron-gas model. Their expressions, given in the Appendix, are generalizations at arbitrary energy distance from the Fermi level.

The electric current density along the chains resulting from a longitudinal thermal gradient $\nabla_a T$ and the induced electric field $\mathcal{E}_a$ in leading order is given by

$$\begin{aligned}j_a &= \frac{2e}{LN_\perp d_\perp}\sum_{\boldsymbol{k}}v^a_{\boldsymbol{k}}f(\boldsymbol{k}) \\ &\simeq \frac{2e}{LN_\perp d_\perp}\sum_{\boldsymbol{k}}v^a_{\boldsymbol{k}}f^0(\boldsymbol{k})[1-f^0(\boldsymbol{k})]\big(\phi^{\mathcal{E}}_{\boldsymbol{k}}-\phi^T_{\boldsymbol{k}}\big), \quad (10)\end{aligned}$$

where $v^a_{\boldsymbol{k}}$ is the carrier velocity along the $a$ direction. Introducing the normalized deviations $\bar{\phi}^{\mathcal{E}}_{\boldsymbol{k}}=\phi^{\mathcal{E}}_{\boldsymbol{k}}/(e\beta v^a_{\boldsymbol{k}_F}\mathcal{E}_a)$ and $\bar{\phi}^T_{\boldsymbol{k}}=\phi^T_{\boldsymbol{k}}/[\beta^2k_Bv^a_{\boldsymbol{k}_F}(E_{\boldsymbol{k}}-\mu)\nabla_aT]$, which have units of time, this expression can be recast in the form

$$j_a = K_{11}\mathcal{E}_a - K_{12}\nabla_aT. \quad (11)$$

In the absence of charge current ($j_a = 0$), this leads to the expression of longitudinal Seebeck coefficient $Q_a$ as the ratio

$$Q_a = \frac{\mathcal{E}_a}{\nabla_a T} = \frac{K_{12}}{K_{11}}. \tag{12}$$

Since the product $f^0[1 - f^0]$ is strongly peaked at the Fermi level $E_{\boldsymbol{k}} - \mu \equiv E = 0$, a Sommerfeld expansion of the matrix elements $K_{11}$ and $K_{12}$ yields the following expression for the Seebeck coefficient:

$$Q_a = \frac{\pi^3}{3}\frac{k_B^2 T}{|e|}\left\{\left[-\frac{d\ln\langle N(E,k_\perp)\rangle_{k_\perp}}{dE} - 2\frac{d\ln\langle v^a_{E,k_\perp}\rangle_{k_\perp}}{dE}\right] - \frac{\partial\ln\langle\bar{\phi}_{E,k_\perp}\rangle_{k_\perp}}{\partial E}\right\}_{E=0} = Q_a^0 + Q_a^c, \tag{13}$$

which can be separated into two contributions. The first, denoted $Q_a^0$, is the sum of the two terms in brackets, which corresponds to the band contribution. It is linked to the energy derivatives of the density of states per spin $\langle N(E,k_\perp)\rangle_{k_\perp}$ $(= \pi^{-1}\langle|\partial k/\partial E_{\boldsymbol{k}}|\rangle_{k_\perp})$, and of the longitudinal velocity $\langle v^a_{E,k_\perp}\rangle_{k_\perp}$ $(= \hbar^{-1}\langle\partial E_{\boldsymbol{k}}/\partial k\rangle_{k_\perp})$. Both quantities are averaged over the Fermi surface for a filling of one hole per dimer ($\langle\cdots\rangle_{k_\perp} = N_P^{-1}\sum_{k_\perp}\cdots$). The second contribution, $Q_a^c$, is associated with collisions; it is proportional to the energy derivative $\langle\bar{\phi}'_{E=0,k_\perp}\rangle_{k_\perp}$ averaged over the Fermi surface for the normalized deviations $\bar{\phi}^{\mathcal{E}} = \bar{\phi}^T \equiv \bar{\phi}$, namely, the scattering time. The latter obeys the single integral equation

$$\mathcal{L}\bar{\phi}_{\boldsymbol{k}} = \sum_{i,\boldsymbol{k}'}\mathcal{L}^{[i]}_{\boldsymbol{k},\boldsymbol{k}'}\bar{\phi}_{\boldsymbol{k}'} = 1, \tag{14}$$

whose explicit expression is given in (A6). Here $\bar{\phi}_{\boldsymbol{k}} \to \bar{\phi}_{E,k_\perp}$ can be expressed as a function of the energy distance from the Fermi surface and the angle parametrized by $k_\perp$. Expression (13) is reminiscent of the Mott formula for the Seebeck coefficient [21,39]. It should be stressed, however, that the scattering term results from the solution of the $\boldsymbol{k}$-dependent integral equation (14), which goes beyond the relaxation-time approximation used for the Mott result [40].

## III. RENORMALIZED UMKLAPP VERTEX

### A. The quasi-one-dimensional electron-gas model

The temperature variation of the momentum-dependent umklapp vertex part entering the collision operator of the Boltzmann equation (9) is calculated using the renormalization-group technique in the framework of the quasi-one-dimensional electron-gas model. In the model the longitudinal part of the lattice model for the hole spectrum $E_{\boldsymbol{k}}$ in (4) is linearized with respect to the 1D Fermi points $\pm k_F$. This gives

$$E_{\boldsymbol{k}} - \mu \approx \epsilon^p_{\boldsymbol{k}} = -\hbar v_F(pk - k_F) + \epsilon(k_\perp), \tag{15}$$

where $p = \pm$ refers to right- and left-moving carriers along the chains and $v_F = (t^2 - \delta t^2)a/(\hbar\sqrt{2t^2 + 2\delta t^2})$ is the longitudinal Fermi velocity. According to band calculations, the hopping integrals will be fixed at $t/k_B = 2700$ K and $t_\perp/k_B = 200$ K as typical figures for hopping integrals in compounds like the Bechgaard salts. A second harmonic is added to the transverse tight-binding spectrum which acts as an antinesting tuning parameter $t'_\perp \ll t_\perp$. Antinesting is considered the main parameter simulating the pressure in the model.

Particles interact through three coupling constants defined on the warped Fermi surface sheets $\boldsymbol{k}^p_F(k_\perp) = (k^p_F(k_\perp), k_\perp)$, as parametrized by $k_\perp$ from the condition $\epsilon^p(\boldsymbol{k}^p_F) = 0$ (see the top panel in Fig. 4 below). These are the backward- and forward-scattering amplitudes $g_1(\boldsymbol{k}^-_{F,1},\boldsymbol{k}^+_{F,2};\boldsymbol{k}^-_{F,3},\boldsymbol{k}^+_{F,4})$ and $g_2(\boldsymbol{k}^+_{F,1},\boldsymbol{k}^-_{F,2};\boldsymbol{k}^-_{F,3},\boldsymbol{k}^+_{F,4})$ and the longitudinal umklapp scattering $g_3(\boldsymbol{k}^p_{F,1},\boldsymbol{k}^p_{F,2};\boldsymbol{k}^{-p}_{F,3},\boldsymbol{k}^{-p}_{F,4})$. All couplings are normalized by $\hbar\pi v_F$ and develop from renormalization a momentum dependence on three independent transverse momentum variables.

We will follow previous works [33,34,36] and fix the bare initial repulsive values of the couplings consistently with different experiments and band calculations. Thus for the bare backward scattering, by taking $g_1 \approx 0.32$, one can reasonably account for the observed temperature-dependent enhancement of uniform susceptibility [41]. For the bare longitudinal umklapp term $g_3$, its bare amplitude is nonzero but very weak, owing to the small dimerization of the organic stacks that introduces some half-filled character to the band. This yields $g_3 \approx g_1(2\delta t/t)$ as a result of the modulation $\delta t$ of longitudinal hopping integrals responsible for the dimerization gap [42,43]. According to band calculations at low pressure [44], $\delta t/t \approx 0.05, \ldots, 0.1$, suggesting we take $g_3 \approx 0.025$ in the following calculations. From these figures, the amplitude of the bare forward scattering can be finally adjusted to the value $g_2 \approx 0.64$ in order to get from the low-$t'_\perp$ RG calculations (see Fig. 1) the right order of magnitude for the observed SDW scale, namely, $T_{\rm SDW} \sim 10$ K for $(\mathrm{TMTSF})_2X$ at ambient pressure [22]. As a function of $t'_\perp$, the application of the RG generates a phase diagram compatible with the

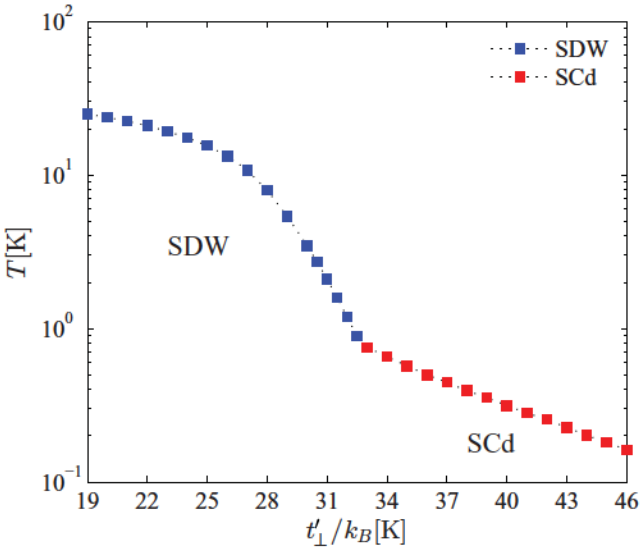


FIG. 1. Renormalization-group results for the phase diagram of the quasi-1D electron-gas model as a function of the antinesting tuning parameter $t'_\perp$ and for the model parameters specified in Sec. III A.

experimental situation [22,27]. There is nothing special in the above choice. Actually, at small umklapp, there exists a whole range of reasonable coupling parameters that would yield a phase diagram comparable to Fig. 1 and then results similar to those for the Seebeck coefficient.

As will discussed in more detail in Sec. V A, one can extend the analysis to the more correlated sulfur-based Fabre salt series $(TMTTF)_2X$ characterized by smaller band parameters and stronger umklapp scattering owing to a larger dimerization of the organic stacks.

### B. Renormalization-group results

The RG approach to the above quasi-1D electron-gas model has been described in detail in previous works [32–36]. In essence, it consists of the segmentation of infinitesimal energy shells on either side of the Fermi sheets into $N_P$ patches, whose internal transverse momentum integration in the loop calculations leads to as many $k_\perp$ values. Successive integrations of electronic degrees of freedom on these shells from the (Fermi) energy cutoff $E_F/k_B[=\pi t/(2k_B\sqrt{2})] \equiv$ 3000 K down to zero at the Fermi surface result in the flow of the coupling constants toward their momentum-dependent values as a function of temperature. This is carried out until a singularity is reached in the coupling constants which signals an instability of the electron gas against the formation of a broken-symmetry state at a given temperature.

For the repulsive sector with these $(TMTSF)_2X$ model parameters, this can occur in either a SDW or $d$-wave SC (SCd) channel depending on the amplitude of antinesting $t'_\perp$. The characteristic sequence of instabilities obtained for $N_P = 60$ patches is reviewed in Fig. 1 [36]. At relatively low nesting deviations the magnetic scale $T_{\rm SDW}$ dominates; it drops with $t'_\perp$ down to the critical value $t'^*_\perp$, where instead of a plain quantum critical behavior for antiferromagnetism for which $T_{\rm SDW}$ would reach zero, the ending of $T_{\rm SDW}$ gives rise to an SCd instability at its maximum $T_c$. The latter then steadily falls off with further increasing $t'_\perp$.

The normal phase we are interested in for the Seebeck coefficient is characterized by spin fluctuations. This is, of course, found in the SDW sector of the phase diagram where the SDW susceptibility $\chi_{\rm SDW}(q_0)$ at the best nesting wave vector of $\epsilon^p_k$ at $q_0 = (2k_F,\pi/d_\perp)$ develops a singularity at $T_{\rm SDW}$. In the SCd sector, an enhancement, although nonsingular, is still present. It takes the form of a Curie-Weiss temperature profile $\chi_{\rm SDW} \sim (T+\Theta)^{-1}$ over a large temperature domain above $T_c$ ($\Theta \geqslant 0$). The enhancement is quantum critical at $t'^*_\perp$ ($\Theta = 0$) and then decays with the decrease of $T_c$ and the rise of the Curie-Weiss scale $\Theta$ along the antinesting axis [33].

These short-range SDW correlations of the metallic phase are directly related to the enhancement of umklapp scattering entering the collision operator of the Boltzmann equation. In Fig. 2, we show the temperature and momentum dependence of $g_3$ on the Fermi surface, as projected in the $(k_{\perp 1},k_{\perp 3})$ plane when $k_{\perp 1} = -k_{\perp 2}$ and $k_{\perp 3} = -k_{\perp 4}$. On the SDW side, the top panel of Fig. 2(a) refers to the high-temperature range ($T > t_\perp$), which shows no structure in the transverse momentum plane for $g_3$, indicating that SDW correlations are essentially 1D in character and confined along chains. As temperature is lowered below $t_\perp$, transverse short-range order

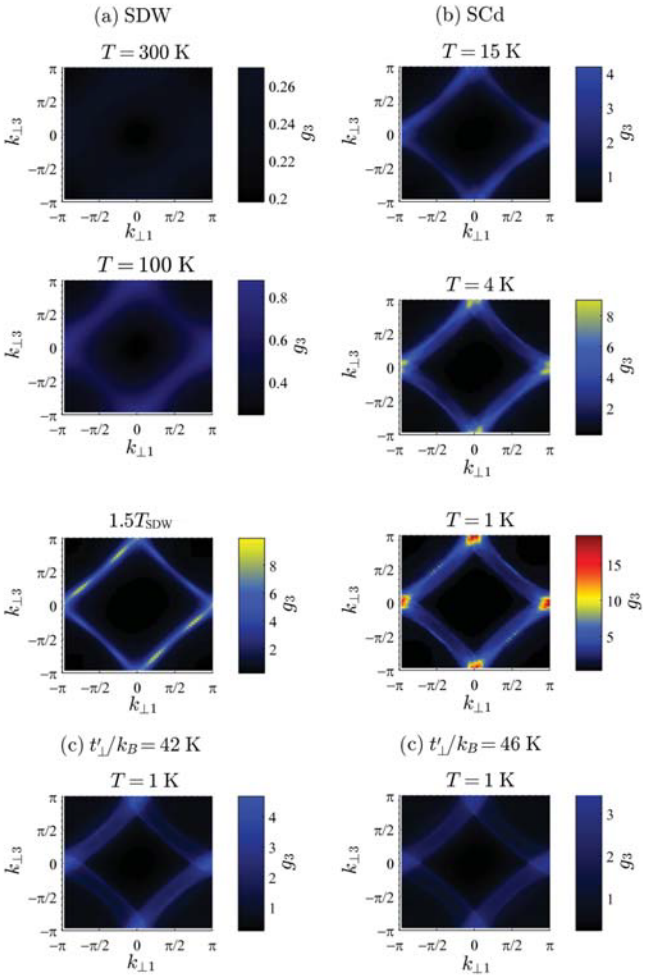


FIG. 2. Renormalized umklapp scattering amplitude $g_3(k_{\perp 1}, -k_{\perp 1}; k_{\perp 3}, -k_{\perp 3})$, projected in the $(k_{\perp 1},k_{\perp 3})$ plane at different temperatures for the metallic phase model parameters specified in Sec. III A. (a) SDW, $t'_\perp/k_B = 25$ K ($<t'^*_\perp/k_B$), (b) SCd, $t'_\perp/k_B =$ 35 K ($>t'^*_\perp/k_B$), and (c) SCd, $t'_\perp/k_B = 42$ and 46 K at $T = 1$ K.

starts to develop, as shown by more intense scattering along the lines $k_{\perp 1} = k_{\perp 3} \pm \pi$ ($d_\perp = 1$). This is in accordance with the transverse momentum transfer associated with the best nesting wave vector $q_0$ of the spectrum (15). When the lowest temperature is reached, peaks of stronger intensity appear on the corners at $k_{\perp 1,3} = 0, \pm\pi$ and at the best nesting points $\pm\pi/4, \pm 3\pi/4$ of the spectrum (15). These refer to warmer regions of scattering on the Fermi surface at the approach of the critical domain of the SDW instability.

On the SCd side of the phase diagram, in Fig. 2(b), we see a pronounced but nonsingular anisotropic increase of umklapp scattering; peaks are confined around $k_{\perp 1,3} = 0, \pm\pi$ on the Fermi surface, where enhanced scattering is found as the temperature is lowered. This enhancement occurs despite the flow of coupling constants towards a SCd fixed point indicative of positive interference between both instabilities. This increase goes hand in hand with the one of SDW correlations in this temperature region, which are directly involved in the mechanism of $d$-wave Cooper pairing [45–47]. By increasing $t'_\perp$ further, although the same anisotropy of

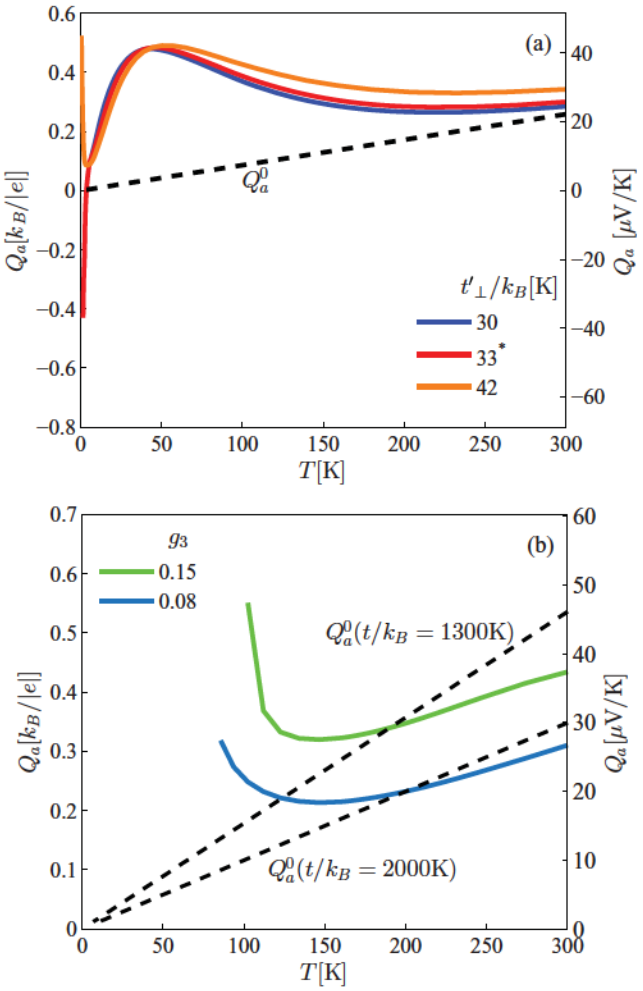


FIG. 3. The longitudinal Seebeck coefficient as a function of temperature for (a) different values of antinesting $t'_\perp$ in the metallic phase and (b) model parameters in the more correlated case with stronger umklapp scattering and lower amplitudes of hopping integrals [$t'_\perp/k_B = 15$ K, $t_\perp/k_B = 100$ K; see Sec. V A on $(TMTTF)_2X$ salts]. The dashed lines gives the band contribution $Q_a^0$ of Eq. (13) for constant relaxation time in energy.

umklapp enhancement persists, its amplitude scales down with the reduction of $T_c$, as displayed in Fig. 2(c).

The consequence of this anisotropic growth of umklapp scattering on the temperature dependence of the Seebeck coefficient will be analyzed next.

## IV. NUMERICAL RESULTS FOR THE SEEBECK COEFFICIENT

### A. High-temperature domain

The temperature dependence of the Seebeck coefficient (13), as obtained from the numerical solution of (A6) for the $(TMTSF)_2X$ model parameters, is shown in Fig. 3(a) in the whole temperature interval of interest. By comparing the amplitude of the two contributions to the Seebeck coefficient in (13), we observe that apart from the high-1D-temperature region, the amplitude of the last term related to scattering

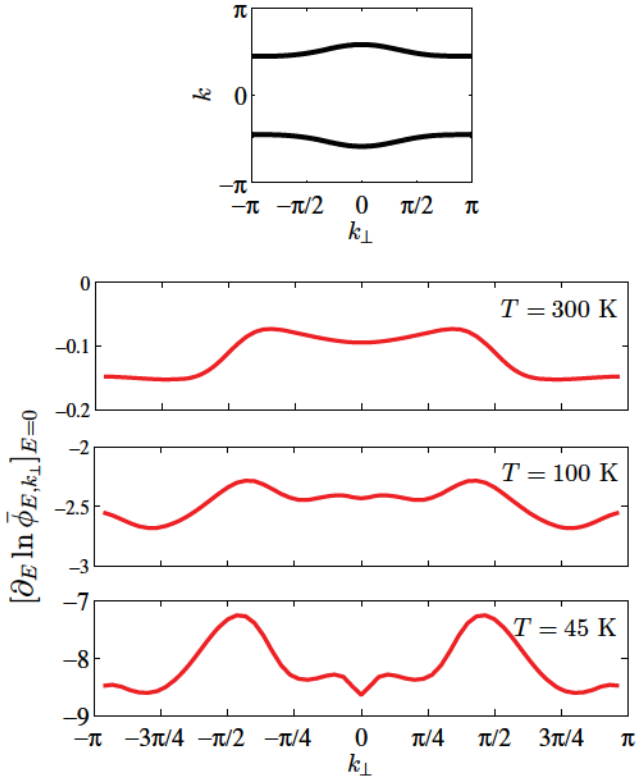


FIG. 4. Open Fermi surface of the quasi-1D electron-gas model (top) and typical variations of the scattering time along the Fermi surface for different high temperatures ($t'_\perp = t'^*_\perp$; bottom).

dominates the band contribution $Q_a^0$ [dashed line in Fig. 3(a)] over most of the temperature interval. This gives rise to a shallow minimum for the Seebeck coefficient below which the normalized energy derivative $\bar{\phi}'_{E=0,k_\perp}/\bar{\phi}_{E=0,k_\perp}$ of the normalized scattering time on the Fermi surface grows in importance, as indicated in the lower panels of Fig. 4. The derivative is negative, and according to (13), it gives a positive $Q_a^c$, as normally expected for hole carriers whose velocity and scattering time decrease with increasing energy.

By lowering the temperature the scattering time derivative gains in amplitude and develops, like $g_3$ in Fig. 2, anisotropy over the Fermi surface with maximums at $k_\perp = 0, \pm\pi$ and $\pm\pi/4, \pm 3\pi/4$. This leads to a smooth increase of the Seebeck coefficient that levels off at a maximum value around the antinesting $t'_\perp$ scale. This is followed in Fig. 3(a) by a rapid drop at lower temperature which is nearly linear; it evolves toward anomalous features in the amplitude or the sign of the Seebeck coefficient depending on the distance to the critical value $t'^*_\perp$ in the phase diagram. This will be discussed in more detail below.

### B. Low-temperature domain and quantum criticality

The results for the Seebeck coefficient in the metallic low-temperature part of the phase diagram are presented in Fig. 5(a) for different values of the antinesting parameter $t'_\perp$. On the SDW side, for $t'_\perp$ relatively well below the critical $t'^*_\perp/k_B$ (=33 K), the decrease of the Seebeck coefficient with lowering

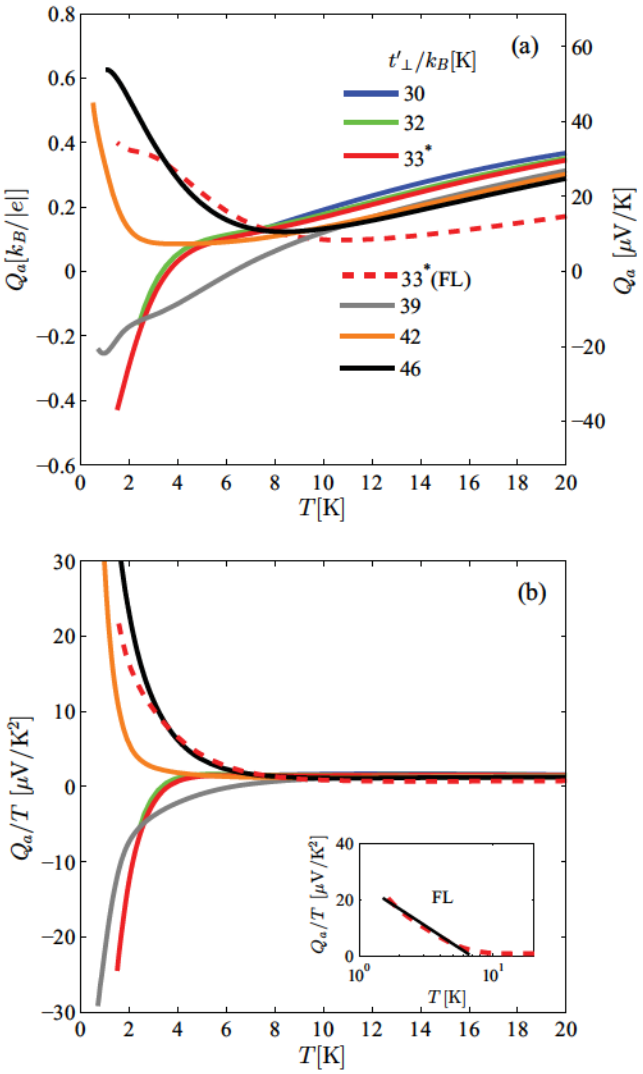


FIG. 5. (a) The longitudinal Seebeck coefficient $Q_a$ and (b) the ratio $Q_a/T$ as a function of $T$ at low temperature and different values of antinesting $t'_\perp$. The value with an asterisk stands for the critical $t'^*_\perp$. The dashed line corresponds to the Fermi liquid limit using a momentum- and temperature-independent $g_3$ ($=0.025$) at $t'^*_\perp$. The inset in (b) displays the enhancement on a logarithmic temperature scale. The solid line refers to $Q_a/T \sim \ln T$.

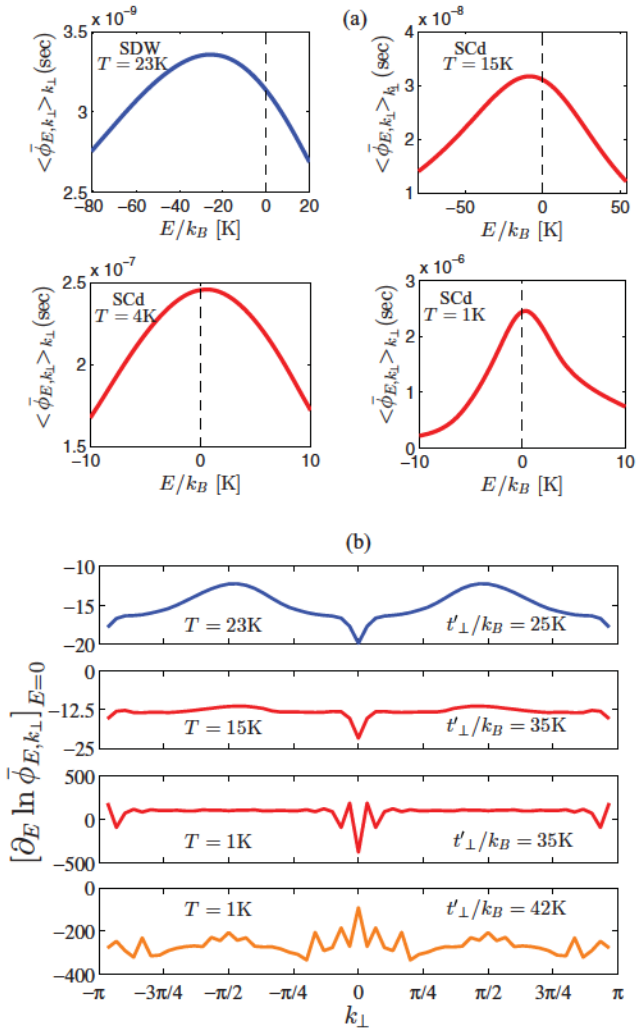


FIG. 6. (a) Variation of the normalized scattering time as a function of energy near the Fermi level at low temperature. Here $t'_\perp/k_B = 25$ and 35 K for the blue and red curves, respectively. (b) The anisotropy of the normalized energy derivative of the scattering time along the Fermi surface at low temperature for different $t'_\perp$.

temperature is nearly linear, as indicated by the constant ratio $Q_a/T$ in Fig. 5(b) when the temperature is lowered. Here the slope for $Q_a$ is steeper than for the band contribution $Q_a^0$ [dashed line in Fig. 3(a)]. The dominant contribution to the Seebeck coefficient comes from $Q_a^c$, which is positive, resulting from a peak in the energy-dependent quasiparticle scattering time located on the occupied side of the Fermi level at $E < 0$, as shown in the top left panel of Fig. 6(a) above the SDW instability. It is worth noting that in these metallic conditions of the SDW state, the calculated scattering time at the Fermi level ($\sim 10^{-9}$ s) is significantly larger than the one found from the Drude theory of the conductivity of the Bechgaard salts above the SDW state [48] (see the note in Ref. [49]).

By raising $t'_\perp$, the temperature scale $T_{\rm SDW}$ in Fig. 1 decays, and at the approach of $t'^*_\perp$ from below, the Seebeck coefficient develops an anomalous enhancement that is opposite in sign. This is depicted by the green lines in Fig. 5. The effect is reinforced when the electron system ultimately enters the SCd domain at $t'^*_\perp$ where $T_c$ is maximum. This indicates that the collision contribution $Q_a^c$ is still negative or electronlike in character and that it exceeds $Q_a^0$ in amplitude. The sign reversal of the Seebeck coefficient refers to an increase of the scattering time with energy and then to a different asymmetry in the quasiparticle resonance peak of $\langle \bar{\phi}_{E,k_\perp} \rangle$. According to Fig. 6(a), when the temperature is lowered, the latter is shifted from the occupied to the unoccupied side just above the Fermi level at $E > 0$. As for the anisotropy profile of $\bar{\phi}'/\bar{\phi}$ over the Fermi surface, the third panel in Fig. 6(b) reveals that this electronlike component of the Seebeck coefficient comes in large part from the cold regions of scattering, namely, away from the warmer spots centered in $k_\perp = 0$ and $\pm\pi$ in the SCd

sector [see Fig. 2(b)]. In the latter regions large oscillations of $\bar{\phi}'/\bar{\phi}$ between positive and negative values tend to average out their contributions to a net positive contribution to the Seebeck coefficient. It is worth noting that the change in sign of the Seebeck coefficient, obtained by tuning $t'_\perp$ across $t'^*_\perp$, occurs in the metallic state, that is, in the absence of any reconstruction of the Fermi surface.

Further above $t'^*_\perp$, the negative enhancement of the Seebeck coefficient weakens and finally transforms into a positive upturn, as shown in Fig. 5. The latter is consistent with a quasiparticle resonance in the scattering time whose peak shifts back below the Fermi level with a negative slope in $\langle \bar{\phi}'_{E=0,k_\perp} \rangle_{k_\perp}$, as shown in the bottom panel in Fig. 6(b). This contributes positively to $Q_a^c$. At sufficiently large $t'_\perp$, namely, when nesting alterations become large, the $g_3$ coupling renormalizes less and less with a concomitant weaker anisotropy, as illustrated in Fig. 2(c). In these conditions the Seebeck coefficient should tend to that of a Fermi liquid. This is confirmed when one imposes a momentum- and temperature-independent $g_3$ in the calculations of the scattering time in (A6), which simulates the conditions of a Fermi liquid. This is shown by the dashed lines in Fig. 5. It is worth noting that the Fermi liquid result for the quasi-1D electron-gas model differs from the linear-$T$ band term $Q_a^0$. The corresponding ratio $Q_a/T$ in Fig. 5(b) displays a low-temperature variation whose curvature in $T$ slightly exceeds a logarithmic enhancement [inset of Fig. 5(b)]. It is worth pointing out that for a quasi-1D Fermi liquid, the scattering time is energy dependent and goes as $\sim E^2 \ln E$ with logarithmic corrections; it is also asymmetric with respect to the Fermi level due to the presence of antinesting [36,50]. According to Fig. 5(b), the effect of umklapp renormalization leads to enhancements also stronger than logarithmic. Note that previous calculations of fluctuation effects, except this time on the band or thermodynamic contribution $Q_a^0$, predict logarithmic corrections near a quantum critical point [4].

Following the example of resistivity [36], one can define from $t'^*_\perp$ the zone of influence of quantum criticality where anomalous signs and enhancement of the Seebeck coefficient are found. This is portrayed in Fig. 7. As pointed out previously [31,33,34,36], $t'^*_\perp$ defines a quantum critical point where the entanglement or mutual reinforcement between SDW and SCd instabilities is the strongest, $T_c$ is the highest, and spin fluctuations are quantum critical down to $T_c$ [33]. This is apparently responsible for the electron-type asymmetry in the energy dependence of electron-electron scattering time and therefore for the sign reversal of the Seebeck coefficient.

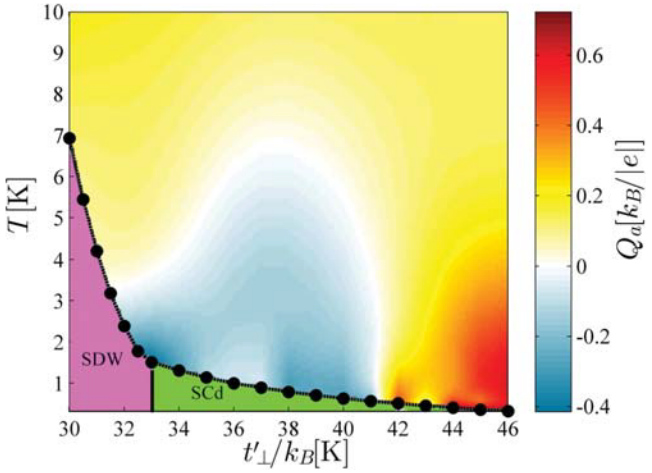


FIG. 7. Amplitude of the Seebeck coefficient at low temperature as a function of antinesting.

The amplitude of reinforcement between SDW and SCd pairings is correlated to the size of $T_c$. This is reflected in Figs. 2(b) and 2(c) by the anisotropic flow of $g_3$ responsible for the growth SDW fluctuations, which scales with $t'_\perp$. As discussed in detail in preceding works [33,34,51], this scaling gives rise to an extended region of quantum critical SDW effects in the phase diagram that goes over the edges of an inverted-triangle-shaped domain usually expected when only the SDW state is present and Cooper pairing is absent. According to Fig. 7, extended quantum criticality for the Seebeck coefficient manifests by a domelike domain of negative $Q_a$, characterized along the $t'_\perp$ axis by a broadened base at low temperature and a top peaking above $t'^*_\perp$ at a sizable $T_c$ [52]. The crossover toward the region of positive Seebeck coefficients is achieved at high enough $t'_\perp$. However, fluctuation effects and deviations from Fermi liquid predictions down to the lowest temperature still persist. It is only at large $t'_\perp$, when $T_c$ is small enough and $g_3$ renormalizes sufficiently weakly, that the Fermi liquid limit is recovered.

## V. COMPARISON WITH EXPERIMENTS IN LOW-DIMENSIONAL ORGANIC CONDUCTORS

We now turn to the comparison of the above results with experiments. In this matter, it is instructive to first examine the Seebeck coefficient for some members of the $(TMTTF)_2X$ series, the so-called Fabre salts, which are known to exhibit a more correlated normal phase than the Bechgaard salts in normal pressure conditions as a result of stronger umklapp scattering [23,53]. The weak-coupling RG can be used to compute the flow of umklapp scattering down to the approach of the Mott strong-coupling region. After this incursion in the physics of the Fabre salts, we then proceed to the discussion of the Seebeck coefficient experiments in the Bechgaard salts in light of the results of the present calculations.

### A. The Fabre salts $(TMTTF)_2X$

The Fabre salts, with $X = PF_6$, $AsF_6$, Br, . . ., form a series of quasi-1D conductors characterized by the same crystallographic structure as the Bechgaard salt $(TMTSF)_2X$ series [54]. The difference between the two series lies in the chemical composition of the TMTTF organic molecule for which the sulfur atoms are substituted in place of selenium in TMTSF. As a consequence, the amplitude of the dimerization of TMTTF stacks turns out to be more pronounced in the solid state, along with band parameters that are typically smaller than those found in $(TMTSF)_2X$ (see Sec. III) [44,55]. In normal pressure conditions, the $(TMTTF)_2X$ are thus more one-dimensional in character and also more correlated than $(TMTSF)_2X$ through essentially a stronger influence of electronic umklapp processes.

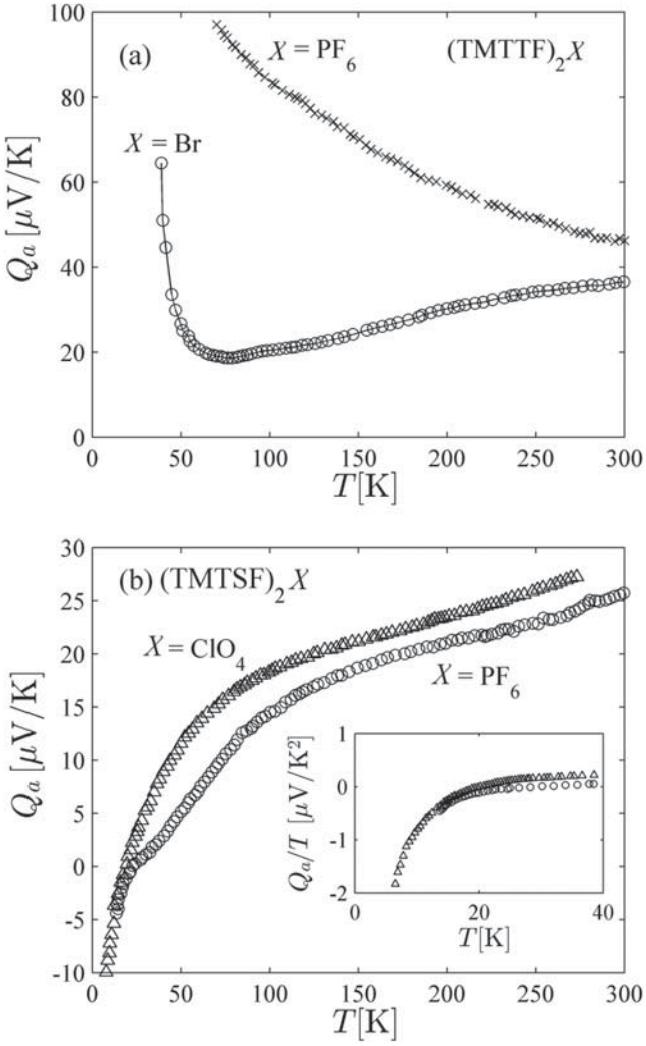


FIG. 8. Temperature dependence of Seebeck coefficients in (a) a few $(TMTTF)_2X$ salts at ambient pressure (after Ref. [37]) and (b) $(TMTSF)_2X$ in the metallic state above $T_{SDW}$, $X = PF_6$, and $T_c$, $X = ClO_4$. The inset shows the sign reversal of the ratio $Q_a/T$ in the low-temperature domain (after Ref. [15]).

This is exemplified by an upturn in electrical resistivity at the intermediate temperature $T_\rho$, indicative of strong umklapp scattering that evolves towards an insulating 1D Mott behavior [53,56–58]. Long-range ordered states can be found at much lower temperature, which can involve charge, spin, and even lattice degrees of freedom [23]. A remarkable property of the series emerges when sufficiently high pressure is applied to $(TMTTF)_2X$, which ultimately maps their physical properties to those of $(TMTSF)_2X$ at low pressure.

$(TMTTF)_2PF_6$ is a prototype compound of the Fabre series characterized by the temperature scale $T_\rho \simeq 220$ K [56,57]. The measurements of the Seebeck coefficient by Mortensen *et al.* [37] for this compound are reproduced in Fig. 8(a). The data show a monotonic increase of the Seebeck coefficient with decreasing temperature. The increase is consistent with nonmetallic behavior shown by resistivity in the same range of temperature [56,57].

The calculated results for a compound like $(TMTTF)_2PF_6$ are displayed in Fig. 3(b); when in accordance with band calculations [44], smaller hopping terms ($t/k_B = 1300$ K, $t_\perp/k_B = 100$ K, $E_F/k_B = 1500$ K, $t'_\perp/k_B = 15$ K) [59] and larger amplitudes for the bare umklapp ($g_3 = 0.15$) are used. With these figures, the instability at $T_{SDW}$ occurs at much higher temperature ($T_{SDW} = T_\rho \sim t_\perp$) and corresponds to the 1D Mott scale $T_\rho$ at the one-loop level of the RG [23,53]. The important reduction of the longitudinal hopping $t$ is responsible for a larger amplitude of the Seebeck coefficient, which is mainly dominated by the band term $Q_a^0$ at high temperature, as shown by the dashed line of Fig. 3(b). Note that this term surpasses the total $Q_a$, indicating that the contribution of $Q_a^c$ coming from collisions is relatively small but negative at very high temperature. The resulting $Q_a$ then shows a smooth decrease with decreasing temperature, contrary to observation in $(TMTTF)_2PF_6$. However, the effect of the collision term quickly becomes positive and gives rise to an upturn of the Seebeck coefficient with lowering temperature, as observed.

The case of $(TMTTF)_2Br$ is also of interest since, along the pressure axis of a generalized phase diagram including both families, this compound is chemically shifted at about half the distance between $(TMTTF)_2PF_6$ and the members of the $(TMTSF)_2X$ series at low pressure [23]. For normal-state properties, for instance, this is illustrated by the intermediate-scale $T_\rho \simeq 100$ K seen in resistivity [56,60], in line with a smaller dimerization of the organic stacks for $(TMTTF)_2Br$. The temperature variation of the Seebeck coefficient for the bromine salt is displayed in Fig. 8 [37]. At room temperature the coefficient is smaller in amplitude compared to that of $(TMTTF)_2PF_6$; it drops as temperature is lowered, consistent with the more pronounced metallic character of this salt in this temperature range. However, the variation is not linear in temperature but reveals an enhancement with respect to the free-carrier situation. A minimum for temperature under $T_\rho$ is reached, followed by an increase that evolves toward a characteristic $1/T$ behavior for $Q_a$ at sufficiently low temperature [37], in agreement with a well-defined insulating (Mott) gap.

By using intermediate figures for the band parameters ($t = 2000$ K, $t_\perp = 100$ K, $E_F = 2200$ K, $t'_\perp/k_B = 15$ K) and bare umklapp amplitude ($g_3 = 0.08$), the amplitude of the calculated Seebeck coefficient at ambient temperature in Fig. 3 is intermediate between $(TMTTF)_2PF_6$ and $(TMTSF)_2X$, as shown in Figs. 8(a) and 8(b). The calculated decrease of $Q_a$, although enhanced compared to $Q_a^0$ due to inelastic scattering, is less rapid than observed. The flow to strong umklapp scattering then results in the upturn in the Seebeck coefficient.

### B. The Bechgaard salts $(TMTSF)_2X$

The Seebeck coefficient measured for the $X = PF_6$ and $ClO_4$ members of the Bechgaard salts is shown in Fig. 8(b). Let us recall that in contrast to the sulfur-based $(TMTTF)_2X$ compounds at low pressure, $T_\rho$ is an irrelevant 1D scale for $(TMTSF)_2X$ since these materials are metallic down to the temperature of onset of long-range order ($T_{SDW,c} \ll t_\perp$). In this range of temperature the system becomes effectively 2D regarding one-particle coherence, although it is strongly anisotropic. In Fig. 8(b) we reproduce the temperature

dependence of $Q_a$ obtained by Chai *et al.* [15] (see also Choi *et al.* [16], Sun *et al.* [17], Chaikin *et al.* [18], and Gubser *et al.* [19]). $(TMTSF)_2PF_6$ shows SDW ordering at $T_{SDW} \simeq 12.5$ K, whereas for $(TMTSF)_2ClO_4$ the anion ($ClO_4$) ordering in slow-cooling conditions pushes the compound on the SC part of the phase diagram of series with $T_c \simeq 1.2$ K [22,61].

Close to ambient temperature, the Seebeck coefficient for both compounds reveals values relatively close to the calculated band limit $Q_a^0$ given in Fig. 3 using the $(TMTSF)_2X$ band parameters of Sec. III. At lower temperature a positive enhancement with respect to a $T$-linear descent is observed for both compounds, in qualitative agreement with the one found in the present calculations in Fig. 3. However, in contrast to predictions, no maximum for $Q_a$ is found experimentally; the data in Fig. 8(b) rather show a shoulderlike structure that precedes the low-temperature descent of the Seebeck coefficient. This suggests that the energy variation of the collision term is less rapid than predicted in this temperature range. We do not exclude, however, that such a maximum would show up if a small pressure was applied to a compound like $(TMTTF)_2Br$ [see Fig. 8(a)], which would suppress $T_\rho$ [60] and shift the compound on the left-hand side of $(TMTSF)_2X$ along the pressure axis [23] (see also [62]).

For both compounds, Fig. 8(b) shows that the drop seen at low temperature for the Seebeck coefficient does not extrapolate toward zero but exhibits negative enhancement from $Q_a^c$ that evolves toward a net sign reversal of the Seebeck coefficient. Because $T_c$ for $(TMTSF)_2ClO_4$ is small, this sign reversal can occur down to a very low temperature of the metallic state, as shown in the inset of Fig. 8(b) for the ratio $Q_a/T$. The sign reversal of the Seebeck coefficient occurs in the metallic state in the absence of a Fermi surface reconstruction that would transform the nature of carriers from hole to electron type. The crossing temperature $T_0 \simeq 18$ K observed for the sign reversal is distinctly larger than calculated in Fig. 7. Although the set of model parameters (hopping integral and interaction strength) could be slightly modified in order to increase $T_0$ and make the comparison with the data in Fig. 8(b) more favorable quantitatively, it must be stressed, however, that as a crossover temperature, $T_0$ is found to be appreciably lower in other experiments [14,16–19]. The origin of this disparity in the observed $T_0$ is not clear, limiting the comparison between theory and experiments to a more qualitative level.

The present calculations can thus provide an avenue of explanation for the sign reversal of the Seebeck coefficient in terms of an anomalous energy dependence of the inelastic umklapp scattering time at the Fermi level which becomes electronlike in character (see Fig. 6). This transformation has its origin in the SDW fluctuations which act as the source of enhancement of umklapp scattering. As we have seen in Sec. III A, the development of these spin fluctuations can be greatly enhanced over sizable intervals of temperature and antinesting in the neighborhood of the quantum critical point $t_\perp'^*$ [see, for example, Fig. 2(b)] [33], in qualitative agreement with the spreading of the sign reversal of the Seebeck coefficient found in Figs. 5 and 7. It is worth stressing that NMR experiments for the temperature variation of the nuclear spin lattice relaxation rate have provided considerable evidence for the presence of spin fluctuations for both compounds in the same temperature range and their smooth decaying amplitude with pressure [25,28,29,41,63,64].

## VI. SUMMARY AND CONCLUDING REMARKS

In the work developed above, a derivation of the Seebeck coefficient in quasi-1D interacting electron systems has been carried out from a numerical solution of the linearized Boltzmann equation using the renormalization-group method for the evaluation of the electron-electron scattering matrix element. From a parametrization of the electron-gas model compatible with the spin-density wave to the superconducting sequence of orderings found in organic superconductors under pressure, the temperature variation of the Seebeck coefficient in the metallic phase was calculated. It was shown to develop marked deviations with respect to the hole-band linear-$T$ prediction. These deviations exhibited striking expression in an extended quantum critical region of the metallic phase linked to the juncture of antiferromagnetic and superconducting orders. It is where the enhancement of the Seebeck coefficient undergoes a sign reversal, attributable to an anomalous low-energy variation of the anisotropic electron-electron scattering time becoming electronlike in character over most of the Fermi surface. Spin fluctuations, which act as a source of inelastic umklapp scattering, appear to be a key determinant for this sign reversal, which occurs in the absence of a Fermi surface reconstruction. It is only when the antinesting parameter, which simulates the role of pressure in real materials, is tuned sufficiently far away from the quantum critical point that a Fermi liquid type of enhancement of the Seebeck coefficient is recovered.

The results were shown to capture many features of existing data in quasi-1D conductors like the Bechgaard salts $(TMTSF)_2X$, in particular the crossover to negative values of the Seebeck coefficient at low temperature in the neighborhood of their quantum critical point along the pressure axis. The size of the enhancement with respect to the band prediction is also fairly well taken into account, suggesting that electron-electron scattering in the presence of electron-hole asymmetry mainly due to nesting alterations is likely to be the most important process governing the temperature dependence of the thermoelectric response of these materials. The results of the calculations are obtained at arbitrary antinesting distance from the quantum critical point of the phase diagram, so they can serve as a stimulus for future experiments of the Seebeck coefficient in Bechgaard salts as a function of applied hydrostatic pressure. Such a systematic study is lacking so far. Following the example of previous electrical transport [27,65] and NMR studies [25,28,29,66], it would be worthwhile to check if the Fermi liquid behavior of the Seebeck coefficient is recovered sufficiently far above the quantum critical pressure.

It is also important to confirm from other experimental probes the anomalous particle-hole asymmetry in the inelastic scattering time in systems like the Bechgaard salts. In this respect, the quasiparticle lifetime extracted from the photoemission cross section may be useful to directly probe the anomalous energy profile of inelastic scattering near the Fermi level. Among other possible probes is the Hall effect. The temperature dependence of the Hall coefficient in the normal state

may reveal asymmetry in the scattering dynamics, especially in the absence of Fermi surface reconstruction that would affect the carrier concentration. In this respect, it is worth mentioning the anomalous temperature dependence of the Hall coefficient reported for a compound like $(TMTSF)_2PF_6$. The coefficient is found to strongly deviate from the band prediction at the approach of $T_{SDW}$ [67].

The present theory of the Seebeck coefficient was also applied to the more correlated Fabre $(TMTTF)_2X$ series, whose members with centrosymmetrical anions $X$ are known to become Mott insulators at relatively high temperature in normal pressure conditions. Stronger umklapp scattering and narrower bands characterize these materials. This precipitates an instability toward an insulating state at much higher temperature and, accordingly, yields a pronounced enhancement of the Seebeck coefficient that is present in experiments.


## ACKNOWLEDGMENTS

The authors would like to thank H. Bakrim and A. Sedeki for their valuable comments on computing aspects of this work. C.B. thanks the National Science and Engineering Research Council of Canada (NSERC) under Grant No. RGPIN-2016-06017, and the Réseau Québécois des Matériaux de Pointe (RQMP) for financial support. Simulations were performed on computers provided by Canadian Foundation for Innovation, the Ministère de l'Éducation des Loisirs et du Sport (Québec), Calcul Québec, and Compute Canada.


## APPENDIX: LINEARIZED BOLTZMANN EQUATION

In the presence of an external longitudinal thermal gradient and induced electric field, the linearized Boltzmann equation for the normalized deviations $\bar{\phi}_{\boldsymbol{k}}$ ($= \bar{\phi}_{\boldsymbol{k}}^{j=\mathcal{E},T}$) can be put in the single form of Eq. (14):

$$\mathcal{L}\bar{\phi}_{\boldsymbol{k}} = \sum_{i=1}^{4}\sum_{\boldsymbol{k}'}\mathcal{L}^{[i]}_{\boldsymbol{k},\boldsymbol{k}'}\bar{\phi}_{\boldsymbol{k}'} = 1. \tag{A1}$$

The collision operator is expressed as the sum of four terms,

$$\sum_{i=1}^{4}\mathcal{L}^{[i]}_{\boldsymbol{k},\boldsymbol{k}'} = \frac{1}{(LN_P)^2}\sum_{\boldsymbol{k}_2,\boldsymbol{k}_3,\boldsymbol{k}_4}\frac{1}{2}|\langle \boldsymbol{k},\boldsymbol{k}_2|g_3|\boldsymbol{k}_3,\boldsymbol{k}_4\rangle - \langle \boldsymbol{k},\boldsymbol{k}_2|g_3|\boldsymbol{k}_4,\boldsymbol{k}_3\rangle|^2\frac{2\pi}{\hbar}\delta_{\boldsymbol{k}+\boldsymbol{k}_2,\boldsymbol{k}_3+\boldsymbol{k}_4+p\boldsymbol{G}}$$
$$\times\,\delta\big(\varepsilon^{p}_{\boldsymbol{k}}+\varepsilon^{p_2}_{\boldsymbol{k}_2}-\varepsilon^{p_3}_{\boldsymbol{k}_3}-\varepsilon^{p_4}_{\boldsymbol{k}_4}\big)\frac{f^0(\boldsymbol{k}_2)[1-f^0(\boldsymbol{k}_3)][1-f^0(\boldsymbol{k}_4)]}{[1-f^0(\boldsymbol{k})]}(\delta_{\boldsymbol{k},\boldsymbol{k}'}+\delta_{\boldsymbol{k}_2,\boldsymbol{k}'}-\delta_{\boldsymbol{k}_3,\boldsymbol{k}'}-\delta_{\boldsymbol{k}_4,\boldsymbol{k}'}). \tag{A2}$$

The amplitude of the umklapp vertex is evaluated by the RG in the framework of the quasi-1D electron-gas model,

$$\langle \boldsymbol{k}_1,\boldsymbol{k}_2|g_3|\boldsymbol{k}_3,\boldsymbol{k}_4\rangle = \pi\hbar v_F g_3\big(\boldsymbol{k}^{p}_{F,1},\boldsymbol{k}^{p}_{F,2};\boldsymbol{k}^{-p}_{F,3},\boldsymbol{k}^{-p}_{F,4}\big)$$
$$= \pi\hbar v_F g_3(k_{\perp 1},k_{\perp 2};k_{\perp 3},k_{\perp 4}), \tag{A3}$$

where the position on the Fermi surface is parametrized by the transverse wave vectors. To solve the equation with the explicit form of matrix elements shown in Eq. (A2), we separate the momentum conservation constraint into longitudinal and transverse components [50],

$$\delta_{\boldsymbol{k}+\boldsymbol{k}_2,\boldsymbol{k}_3+\boldsymbol{k}_4+p\boldsymbol{G}} = \delta_{k_\perp+k_{\perp 2},k_{\perp 3}+k_{\perp 4}}\frac{2\pi}{L}\hbar v_F\delta\big(\varepsilon^{p}_{\boldsymbol{k}}+\varepsilon^{p_2}_{\boldsymbol{k}_2}+\varepsilon^{p_3}_{\boldsymbol{k}_3}+\varepsilon^{p_4}_{\boldsymbol{k}_4}-\Sigma\big), \tag{A4}$$

where $\Sigma = \epsilon_\perp(k_\perp)+\epsilon_\perp(k_{\perp 2})+\epsilon_\perp(k_{\perp 3})+\epsilon_\perp(k_{\perp 4})$. The summation over the momentum vectors can be written as

$$\frac{1}{LN_P}\sum_{\boldsymbol{k}} = \sum_{p}\int\frac{d\varepsilon^{p}_{\boldsymbol{k}}}{2\pi\hbar v_F}\frac{1}{N_P}\sum_{k_\perp}. \tag{A5}$$

Carrying out the integration over $\varepsilon^{p'}_{\boldsymbol{k}'}$ and rearranging the terms, we arrive at the final equation,

$$\frac{\pi}{\beta\hbar}\frac{1}{N_P^2}\sum_{k'_\perp,k_{\perp 3},k_{\perp 4}}\Big\{|g_3(k_\perp,k_{\perp 3}+k_{\perp 4}-k_\perp;k_{\perp 3},k_{\perp 4})-g_3(k_\perp,k_{\perp 3}+k_{\perp 4}-k_\perp;k_{\perp 4},k_{\perp 3})|^2\delta_{k_\perp,k'_\perp}$$
$$\times\frac{\beta\Sigma'/4\cosh(\beta E/2)}{\cosh[\beta(\Sigma'/4-E/2)]\sinh(\beta\Sigma'/4)} + |g_3(k_\perp,k'_\perp;k_{\perp 3},k_{\perp 4})-g_3(k_\perp,k'_\perp;k_{\perp 4},k_{\perp 3})|^2$$
$$\times\frac{\beta\Sigma''/4\cosh(\beta E/2)}{\cosh[\beta(\Sigma''/4-E/2)]\sinh(\beta\Sigma''/4)}\delta_{k_\perp+k'_\perp,k_{\perp 3}+k_{\perp 4}} - 2|g_3(k_\perp,k_{\perp 3};k'_\perp,k_{\perp 4})-g_3(k_\perp,k_{\perp 3};k_{\perp 4},k'_\perp)|^2$$
$$\times\frac{\beta\Sigma''/4\cosh(\beta E/2)}{\cosh[\beta(\Sigma''/4-E/2)]\sinh(\beta\Sigma''/4)}\delta_{k_\perp+k_{\perp 3},k'_\perp+k_{\perp 4}}\Big\}\bar{\phi}_{E,k'_\perp} = 1, \tag{A6}$$

where $\Sigma' = \epsilon_\perp(k_\perp)+\epsilon_\perp(k_{\perp 3}+k_{\perp 4}-k_\perp)+\epsilon_\perp(k_{\perp 3})+\epsilon_\perp(k_{\perp 4})$ and $\Sigma'' = \epsilon_\perp(k_\perp)+\epsilon_\perp(k'_\perp)+\epsilon_\perp(k_{\perp 3})+\epsilon_\perp(k_{\perp 4})$. By inserting the RG results of Sec. III A for the momentum-resolved umklapp scattering, the numerical solution of (A6) for $\bar{\phi}_{E,k_\perp}$ allows the evaluation of the scattering contribution $Q^c_a$ to the Seebeck coefficient (13).

[1] S. Hartmann, N. Oeschler, C. Krellner, C. Geibel, S. Paschen, and F. Steglich, Phys. Rev. Lett. **104**, 096401 (2010).
[2] H. Pfau, R. Daou, M. Brando, and F. Steglich, Phys. Rev. B **85**, 035127 (2012).
[3] Z. Ren, G. W. Scheerer, G. Lapertot, and D. Jaccard, Phys. Rev. B **94**, 024522 (2016).
[4] I. Paul and G. Kotliar, Phys. Rev. B **64**, 184414 (2001).
[5] K.-S. Kim and C. Pépin, Phys. Rev. B **81**, 205108 (2010).
[6] S. Arsenijević, H. Hodovanets, R. Gaál, L. Forró, S. L. Bud'ko, and P. C. Canfield, Phys. Rev. B **87**, 224508 (2013).
[7] F. Laliberté, J. Chang, N. Doiron-Leyraud, E. Hassinger, R. Daou, M. Rondeau, B. J. Ramshaw, R. Liang, D. A. Bonn, W. N. Hardy, S. Pyon, T. Takayama, H. Takagi, I. Sheikin, L. Malone, C. Proust, K. Behnia, and L. Taillefer, Nat. Commun. **2**, 432 (2011).
[8] R. Daou, N. Doiron-Leyraud, D. LeBoeuf, S. Y. Li, F. Laliberté, O. Cyr-Choinière, Y. J. Jo, L. Balicas, J.-Q. Tan, J.-S. Zhou, J. B. Goodenough, and L. Taillefer, Nat. Phys. **5**, 31 (2009).
[9] J. M. Buhmann, M. Ossadnik, T. M. Rice, and M. Sigrist, Phys. Rev. B **87**, 035129 (2013).
[10] L.-F. Arsenault, B. S. Shastry, P. Sémon, and A.-M. S. Tremblay, Phys. Rev. B **87**, 035126 (2013).
[11] P. Li, K. Behnia, and R. L. Greene, Phys. Rev. B **75**, 020506 (2007).
[12] F. Gollnik and M. Naito, Phys. Rev. B **58**, 11734 (1998).
[13] K. Bechgaard, C. Jacobsen, K. Mortensen, H. Pedersen, and N. Thorup, Solid State Commun. **33**, 1119 (1980).
[14] K. Mortensen, Solid State Commun. **44**, 643 (1982).
[15] Y. Chai, H. Yang, J. L. C. Sun, H. Gao, X. Chen, L. Cao, and J.-C. Lasjaunias, J. Phys. Soc. Jpn. **78**, 063602 (2009).
[16] E. S. Choi, H. Y. Kang, Y. J. Jo, J. Yeom, and W. Kang, Synth. Met. **120**, 1069 (2002).
[17] C.-H. Sun, H.-S. Yang, J. Liu, H.-X. Gao, J.-B. Wang, L. Cheng, L.-Z. Cao, and J. C. Lasjaunias, J. Phys. Condens. Matter **20**, 235223 (2008).
[18] P. M. Chaikin, M.-Y. Choi, and R. L. Greene, J. Phys. Colloq. **44**, C3783 (1983).
[19] D. U. Gubser, W. W. Fuller, T. O. Poehler, J. Stokes, D. O. Cowan, M. Lee, and A. N. Bloch, Mol. Cryst. Liq. Cryst. **79**, 225 (1982).
[20] Y. Machida, X. Lin, W. Kang, K. Izawa, and K. Behnia, Phys. Rev. Lett. **116**, 087003 (2016).
[21] K. Behnia, *Fundamentals of Thermoelectricity* (Oxford University Press, Oxford, 2015).
[22] D. Jérome and H. J. Schulz, Adv. Phys. **31**, 299 (1982).
[23] C. Bourbonnais and D. Jérome, in *The Physics of Organic Superconductors and Conductors*, edited by A. Lebed, Springer Series in Materials Science Vol. 110 (Springer, Heidelberg, 2008), p. 357.
[24] L. Taillefer, Annu. Rev. Condens. Matter Phys. **1**, 51 (2010).
[25] S. E. Brown, Physica C (Amsterdam, Neth.) **514**, 279 (2015).
[26] D. Jérome and S. Yonezawa, C. R. Phys. **17**, 357 (2016).
[27] N. Doiron-Leyraud, P. Auban-Senzier, S. René de Cotret, C. Bourbonnais, D. Jérome, K. Bechgaard, and L. Taillefer, Phys. Rev. B **80**, 214531 (2009).
[28] S. E. Brown, P. M. Chaikin, and M. J. Naughton, in *The Physics of Organic Superconductors and Conductors*, edited by A. Lebed, Springer Series in Materials Science Vol. 110 (Springer, Heidelberg, 2008), p. 49.
[29] F. Creuzet, C. Bourbonnais, L. G. Caron, D. Jérome, and A. Moradpour, Synth. Met. **19**, 277 (1987).
[30] Y. Kimura, M. Misawa, and A. Kawamoto, Phys. Rev. B **84**, 045123 (2011).
[31] R. Duprat and C. Bourbonnais, Eur. Phys. J. B **21**, 219 (2001).
[32] J. C. Nickel, R. Duprat, C. Bourbonnais, and N. Dupuis, Phys. Rev. B **73**, 165126 (2006).
[33] C. Bourbonnais and A. Sedeki, Phys. Rev. B **80**, 085105 (2009).
[34] A. Sedeki, D. Bergeron, and C. Bourbonnais, Phys. Rev. B **85**, 165129 (2012).
[35] Y. Fuseya, C. Bourbonnais, and K. Miyake, Europhys. Lett. **100**, 5708 (2012).
[36] M. Shahbazi and C. Bourbonnais, Phys. Rev. B **92**, 195141 (2015).
[37] K. Mortensen, E. M. Conwell, and J. M. Fabre, Phys. Rev. B **28**, 5856 (1983).
[38] H. Haug and A. P. Jauho, in *Quantum Kinetics in Transport and Optics of Semiconductors*, edited by M. Cardona and P. Fulde, Springer Series in Solid-State Sciences Vol. 110 (Springer, Heidelberg, 2008), p. 3.
[39] M. Cutler and N. F. Mott, Phys. Rev. **181**, 1336 (1969).
[40] J. M. Ziman, *Principles of the Theory of Solids* (Cambridge University Press, London, 1972).
[41] P. Wzietek, F. Creuzet, C. Bourbonnais, D. Jérome, K. Bechgaard, and P. Batail, J. Phys. I **3**, 171 (1993).
[42] S. Barisic and S. Brazovskii, in *Recent Developments in Condensed Matter Physics*, edited by J. T. Devreese (Plenum, New York, 1981), Vol. 1, p. 327.
[43] K. Penc and F. Mila, Phys. Rev. B **50**, 11429 (1994).
[44] L. Ducasse, A. Abderrabba, J. Hoarau, M. Pesquer, B. Gallois, and J. Gaultier, J. Phys. C **19**, 3805 (1986).
[45] M. T. Béal-Monod, C. Bourbonnais, and V. J. Emery, Phys. Rev. B **34**, 7716 (1986).
[46] L. G. Caron and C. Bourbonnais, Physica B+C (Amsterdam) **143**, 453 (1986).
[47] V. J. Emery, Synth. Met. **13**, 21 (1986).
[48] M. Dressel, A. Schwartz, G. Gruner, and L. Degiorgi, Phys. Rev. Lett. **77**, 398 (1996).
[49] This much longer time scale for scattering processes would be rather compatible with the so-called zero-frequency mode seen in optical conductivity of the Bechgaard salts in their low-temperature metallic state [48].
[50] L. P. Gorkov and M. Mochena, Phys. Rev. B **57**, 6204 (1998).
[51] C. Bourbonnais and A. Sedeki, C. R. Phys. **12**, 532 (2011).
[52] As shown in Fig. 7, the calculations reveal a noticeable nonuniform variation of $Q_a$ with $t'_\perp$ close to $T_c$ that is at the base of the dome of negative values in the interval of $t'_\perp/k_B$ between 33 and 39 K and beyond $t'_\perp/k_B \simeq 43$ K in the positive sector. This nonuniform variation is not the result of additional quantum critical points in the phase diagram, as confirmed by the absence of any anomaly in the RG quantities. It is rather ascribed to critical effects close to a sizable $T_c$ where interactions get relatively strong and weak-coupling RG and the energy derivative of the scattering time become less accurate.
[53] V. J. Emery, R. Bruinsma, and S. Barisic, Phys. Rev. Lett. **48**, 1039 (1982).
[54] P. Delhaes, C. Coulon, J. Amiell, S. Flandrois, E. Toreilles, J. Fabre, and L. Giral, Mol. Cryst. Liq. Cryst. **50**, 43 (1979).
[55] P. M. Grant, J. Phys. Colloq. **44**, C3-847 (1983).

[56] C. Coulon, P. Delhaes, S. Flandrois, R. Lagnier, E. Bonjour, and J. Fabre, J. Phys. (Paris) **43**, 1059 (1982).

[57] R. Laversanne, C. Coulon, B. Gallois, J. P. Pouget, and R. Moret, J. Phys. Lett. **45**, L393 (1984).

[58] T. Giamarchi, Physica B: Condensed Matter (Amsterdam, Neth.) **230–232**, 975 (1997).

[59] We have chosen an effective range of values for $t_\perp$ that is slightly lower than that of band calculations in order to incorporate the effect of the downward renormalization of $t_\perp$ that takes place at the approach of the Mott scale $T_\rho$. This effect is not taken into account by the present RG calculations at the one-loop level [23,34].

[60] B. J. Klemme, S. E. Brown, P. Wzietek, G. Kriza, P. Batail, D. Jérome, and J.-M. Fabre, Phys. Rev. Lett. **75**, 2408 (1995).

[61] K. Bechgaard, M. Carneiro, M. Olsen, F. B. Rasmussen, and C. S. Jacobsen, Phys. Rev. Lett. **46**, 852 (1981).

[62] It should be stressed here that experiments are performed under constant-pressure conditions, whereas the calculations are obtained at constant volume. For relatively soft materials like the organics, constant-volume corrections to the data may modify the actual temperature dependence for a transport quantity like the Seebeck coefficient (see, for example, Ref. [68]).

[63] C. Bourbonnais, F. Creuzet, D. Jérome, K. Bechgaard, and A. Moradpour, J. Phys. Lett. **45**, L755 (1984).

[64] J. Shinagawa, Y. Kurosaki, F. Zhang, C. Parker, S. E. Brown, D. Jérome, K. Bechgaard, and J. B. Christensen, Phys. Rev. Lett. **98**, 147002 (2007).

[65] N. Doiron-Leyraud, P. Auban-Senzier, S. R. de Cotret, C. Bourbonnais, A. Sedeki, D. Jérome, K. Bechgaard, and L. Taillefer, Eur. Phys. J. B **78**, 23 (2010).

[66] F. Creuzet, D. Jerome, C. Bourbonnais, and A. Moradpour, J. Phys. C **18**, L821 (1985).

[67] J. Moser, J. R. Cooper, D. Jérome, B. Alavi, S. E. Brown, and K. Bechgaard, Phys. Rev. Lett. **84**, 2674 (2000).

[68] J. Moser, M. Gabay, P. Auban-Senzier, D. Jérome, K. Bechgaard, and J. M. Fabre, Eur. Phys. J. B **1**, 39 (1998).

Chapter 4

# Complement to the theory of the Seebeck coefficient of chapter 3

## 4.1 Seebeck coefficient at low temperatures

According to the results of chapter 3 on Seebeck coefficient, equation (3.53), at low temperatures there are two sources of electron-hole asymmetry giving non-zero contributions to the Seebeck coefficient. One is contained in the weakly dimerized bare band structure reflecting electron-hole asymmetry in the density of states and in the particle velocities (the first two terms of equation (3.53)). Another contribution is due to the electron-hole asymmetry portrayed in the scattering time. Included in the collision-related third term of equation (3.53), the scattering time in our calculations is expressed as the energy-dependent normalized deviation $\phi$ from equilibrium. The two factors are present, sometimes with opposite signs, and compete with each other.

In the above approach to the anomalous thermoelectric behavior of the Bechgaard salts, we have looked at the impact of antiferromagnetic spin fluctuations on the energy variation of the electron-electron scattering time. We have seen that the negative sign of the Seebeck coefficient as well as its large value, especially emerge as the nesting deviations $t'_\perp$ approaches its critical value at the quantum critical point. This is where the SDW fluctuations are the strongest as a result of constructive interference between the underlying microscopic pairing mechanisms at the onset of superconductivity and the fading SDW state.

Besides asymmetry in the scattering time, we can in principle expect some fluctuation induced asymmetry in the density of states and in the particle velocity due to short-range antiferromagnetic correlations. In the following, we present the results of some calculations on the reduction of the

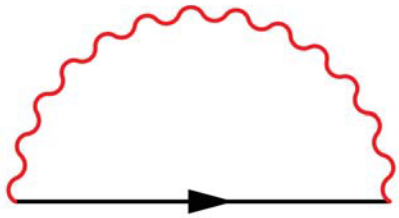

**Figure 4.1** The Lee-Rice-Anderson approximation to the electron self-energy in the absence of vertex corrections.

density of states around the Fermi level, a typical pseudogap-like behavior, in the quantum critical regime of the phase diagram. In the next section, we present our approach to examine this effect on the Seebeck coefficient.

## 4.2 Self-energy in the presence of antiferromagnetic fluctuations

In order to compute the density of states, we calculate the leading term of electron self-energy in the framework of the Lee-Rice-Anderson approximation. The approach starts from the expression of the one-particle Green's function

$$G(\boldsymbol{k}, i\omega_n) = \frac{1}{[G^0]^{-1} - \Sigma(\boldsymbol{k}, i\omega_n)}, \tag{4.1}$$

where $\Sigma$ is the self-energy and the free electron propagator, $G^0(\boldsymbol{k}, i\omega_n) = \dfrac{1}{i\omega_n - \varepsilon_{\boldsymbol{k}}}$. Here $\omega_n = 2\pi(n+1)T$ are the fermionic Matsubara frequencies, $\varepsilon_{\boldsymbol{k}}$ is the tight binding energy spectrum for a weakly dimerized hole band

$$\varepsilon_{\boldsymbol{k}} = \sqrt{2(t^2 + \delta t^2) + 2(t^2 - \delta t^2)\cos ka} + \epsilon_\perp(k_\perp), \tag{4.2}$$

with the transverse part $\epsilon_\perp(k_\perp) = 2t_\perp \cos k_\perp d_\perp + 2t'_\perp \cos 2k_\perp d_\perp$. For simplicity in this chapter, we take the lattice parameters $d_\perp$ and $a$ as unity.

The self-energy term corresponds to the Feynman diagram in figure 4.1, whose mathematical expression is

$$\Sigma(\boldsymbol{k}, i\omega_n) = \frac{T}{LN_P} g_3^2 \sum_{\boldsymbol{q}, \omega_m} G^0(\boldsymbol{k} + \boldsymbol{q} + \boldsymbol{Q}, i\omega_n + i\omega_m)\chi(\boldsymbol{q} + \boldsymbol{Q}, i\omega_m), \tag{4.3}$$

where $\chi$ is the renormalized dynamic SDW susceptibility obtained in reference [10] by the weak coupling renormalization group method and which is given by

$$\chi(q+Q,i\omega_m)=\frac{(\pi v_F\hbar)^{-1}\tilde{\chi}_Q}{1+{\xi_\parallel}^2q^2+{\xi_\perp}^2q_\perp^2-i\Gamma\omega_m}. \tag{4.4}$$

Here $Q=(2k_F,\pi)$ is the SDW wave vector, and ${\xi_i}^2={\xi_i^0}^2\tilde{\chi}_Q$ is the square of SDW correlation lengths parallel and perpendicular to the chains. $\tilde{\chi}_Q$ is the dimensionless static susceptibility at the SDW wave vector; $\xi^0_{\parallel(\perp)}=v_F(t_\perp)/T^0_{\mathrm{SDW}}$ are the parallel and transverse coherence lengths at $T^0_{\mathrm{SDW}}$, the SDW transition temperature for small $t'_\perp$ value. Finally, $\Gamma$ is the relaxation time for SDW fluctuations.

Following a change of variable, equation (4.3) can be rewritten as

$$\Sigma(k,i\omega_n)=\frac{-ig_3^2T}{2\pi LN_P}\sum_q\int d\omega' G^0(k+q+Q,i\omega_n+\omega')\chi(q+Q,\omega'). \tag{4.5}$$

To proceed further, we use the Kamf and Schrieffer [152] approximation assuming the slow antiferromagnetic fluctuations compared to the electronic frequencies at low temperatures. This allows to write

$$\chi(q+Q,\omega')=i2\pi T\chi(q+Q)\delta(\omega'). \tag{4.6}$$

The self-energy then yields as

$$\Sigma(k,i\omega_n)=\frac{g_3^2T}{LN_P}\sum_q G^0(k+q+Q,i\omega_n)\chi(q+Q). \tag{4.7}$$

Now to do the summation over $q$ we apply another approximation to equation (4.4), in its static limit, inspired by the work of Schmalian et al. [153], who have shown that this approximation retains the essential information on spin fluctuation precursors near the pseudogap regime of the magnetic phase diagram of cuprate superconductors. Accordingly, we have

$$\chi(q+Q)=(\pi v_F\hbar)^{-1}\frac{\tilde{\chi}_Q^{1/2}}{1+{\xi_\parallel}^2q^2}\frac{\tilde{\chi}_Q^{1/2}}{1+{\xi_\perp}^2q_\perp^2}. \tag{4.8}$$

In addition, for the momentum transfer $q=(q,q_\perp)$ of the spin fluctuations close to the SDW wave vector $Q=(2k_F,\pi)$ we can expand the energy dispersion as

$$\varepsilon_{k+q+Q}\approx\varepsilon_{k+Q}+v_{k+Q}\cdot q=\varepsilon_{k+Q}+v_{k+Q}q, \tag{4.9}$$

where $v_{k+Q} = \partial\varepsilon_{k+Q}/\partial k$ is the electron velocity along the Fermi surface.

Introducing the above approximations and transforming the summation on $\boldsymbol{q}$ into an integral by $\frac{1}{LN_P} = \frac{1}{2\pi^2}\int dq dq_\perp$, the $q$-integral in (4.7) can be done by the residue method and the remaining $q_\perp$-integral is simple. The self-energy of the system becomes

$$\Sigma(\boldsymbol{k}, i\omega_n) = \frac{\langle|\Delta|^2\rangle}{iv_{k+Q}\xi_{\parallel}^{-1} + (i\omega_n - \varepsilon_{k+Q})}, \tag{4.10}$$

where $\langle|\Delta|^2\rangle = \frac{g_3^2 T\tilde{\chi}_Q(\pi v_F\hbar)^{-1}}{4(\xi_{\parallel}\xi_{\perp})}$ has the unit of square of energy and expresses the amplitude of the fluctuations.

## 4.3 Density of states

Replacing equation (4.10) into the electron propagator in equation (4.1) and after analytic continuation $i\omega_n \to \omega + i\delta$, the expression of the retarded one-particle propagator which contains the principal effects of spin fluctuations, is given

$$G^{\text{ret}}(\boldsymbol{k}, \omega) = \frac{1}{\omega - \varepsilon_k - \dfrac{\langle|\Delta|^2\rangle}{iv_{k+Q}\xi_{\parallel}^{-1} + (\omega - \varepsilon_{k+Q})}}. \tag{4.11}$$

The density of states is related to the imaginary part of the retarded Green function as

$$D(\omega) = \frac{-1}{\pi LN_P}\sum_{\boldsymbol{k}} \text{Im}G^{\text{ret}}(\boldsymbol{k}, \omega), \tag{4.12}$$

which in our case is converted to the following expression

$$D(\omega) = \frac{-1}{2\pi^2 N_P}\sum_{k_\perp} D_0(\omega)\text{Im}\int G^{\text{ret}}(\boldsymbol{k}, \omega)d\varepsilon_k, \tag{4.13}$$

where $D_0(\omega)$ is the bare density of states which for the spectrum (4.2) is given by

$$D_0(\omega) = \frac{1}{2t\sqrt{1 - \dfrac{4\delta t^2}{\left(\omega + \sqrt{2(t^2+\delta t^2)}\right)^2} - \dfrac{1}{4t^2}\left(\omega + \sqrt{2(t^2+\delta t^2)}\right)^2 + \left(\dfrac{\delta t}{t}\right)^2}}. \tag{4.14}$$

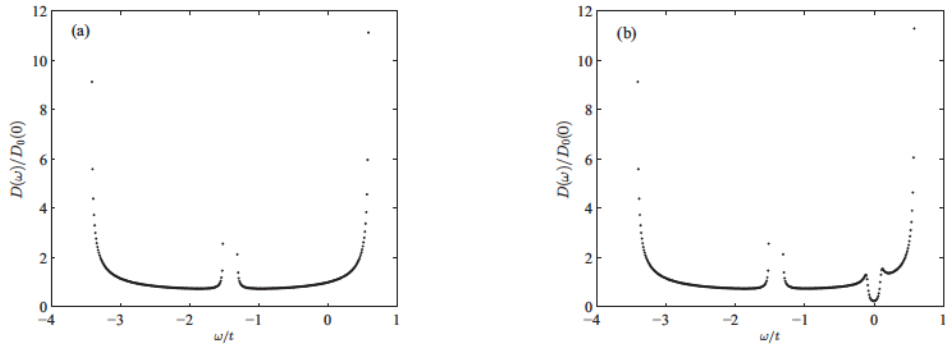


**Figure 4.2** (a) The bare density of states for a slightly dimerized quasi-1D tight-binding band. (b) The density of states as given by equation (4.19) at a given value of temperature showing a reduction of density of states at the Fermi level ($\omega/t = 0$) after the introduction of antiferromagnetic fluctuations.

We linearize the longitudinal part of the energy spectrum (4.2) around the right/left 1D Fermi points $pk_F = \pm k_F$ as $\varepsilon_k^p = v_F\hbar(pk - k_F)$ where $v_F = \partial E_k/\partial k|_{k=k_F} = (t^2 - \delta t^2)a/(\hbar\sqrt{2t^2 + 2\delta t^2})$ is the longitudinal Fermi velocity. Therefore, we distinguish between the right- ($p = +$) and the left-going ($p = -$) fermions. We then perform the calculations for the left-going fermion propagator. The calculation for the right-going fermions is similar. Thus

$$G_-^{\rm ret}(\boldsymbol{k},\omega) = \frac{1}{\omega - \varepsilon_{\boldsymbol{k}}^- - \dfrac{\langle|\Delta|^2\rangle}{iv_{k+Q}\xi_\parallel^{-1} + (\omega - \varepsilon_{k+Q}^+)}}, \tag{4.15}$$

where $\varepsilon_{k+Q}^+ = -\varepsilon_{\boldsymbol{k}}^- - \delta(k_\perp)$ with $\delta(k_\perp) = 4t'_\perp\cos(2k_\perp)$.

For the $\varepsilon$-integral in (4.13) after a change of variable $\omega - \varepsilon = z$ we obtain

$$\begin{aligned}\int_{-\infty}^{\infty} dz G_-^{\rm ret}(\boldsymbol{k},z) &= \int_{-\infty}^{\infty} dz \frac{-2\omega - iv_{k+Q}\xi_\parallel^{-1} - \delta(k_\perp) + z}{(z - z_+)(z - z_-)} \\ &= \int_{-\infty}^{\infty} dz \frac{-2\omega - iv_{k+Q}\xi_\parallel^{-1} - \delta(k_\perp) + 1/2(z_+ + z_-)}{(z - z_+)(z - z_-)},\end{aligned} \tag{4.16}$$

where $z_-$ and $z_+$ are the simple poles of the integrand in the second line of the above equation, which are given by

$$z_\pm = \langle|\Delta|^2\rangle\left(\tilde{\omega} + i\alpha/2 \pm \sqrt{-x + i\alpha\tilde{\omega}}\right), \tag{4.17}$$

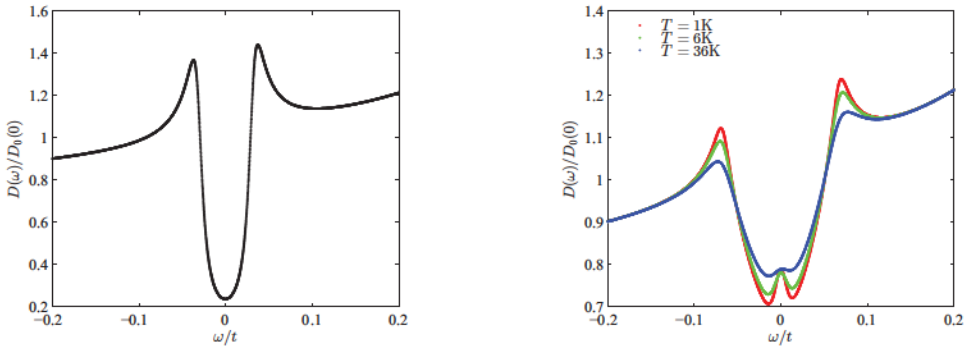


(a) (b)

**Figure 4.3** (a) Density of states around the Fermi level as given by equation (4.19) at $t'_\perp = 0$. (b) Density of states around the Fermi level after switching $t'_\perp$ at several temperatures.

with

$$\tilde{\omega} = \frac{\omega + \delta(k_\perp)/2}{\langle|\Delta|^2\rangle^{1/2}}$$
$$\alpha = \frac{v_{k+Q}\xi_\parallel^{-1}}{\langle|\Delta|^2\rangle^{1/2}}$$
$$x = 1 + 1/4\alpha^2 - \tilde{\omega}^2. \tag{4.18}$$

Solving the integral, the resulting density of states reads

$$D(\omega) = \frac{1}{2\pi N_P}\sum_{k_\perp} D_0(\omega)\frac{\sqrt{x+y}}{2\sqrt{2}y\alpha}\left(\alpha^2 + 2(y-x)\right), \tag{4.19}$$

where $y = \left(x^2 + \alpha^2\tilde{\omega}^2\right)^{1/2}$.

The two factors that tune the spin fluctuations all over the phase diagram are the temperature and the deviations from perfect nesting $t'_\perp$. Here, these two factors enter through the parameters defined in (4.18). From the microscopic point of view $\langle|\Delta|^2\rangle^{1/2}$ is the amplitude of fluctuations of SDW order parameter as $\langle|\Delta|^2\rangle^{1/2} \propto \langle\phi(q+Q)\phi^*(q+Q)\rangle$ around its value at the SDW wave vector. We fix $\langle|\Delta|^2\rangle^{1/2}$ by the mean field BCS relation $\langle|\Delta|^2\rangle^{1/2} = 1.75T^0_{\mathrm{SDW}}$ [68] with $T^0_{\mathrm{SDW}}$ as the SDW transition temperature at $t'_\perp = 0$. For this temperature scale we use the respective value obtained from the RG method when the SDW correlations are at their maximum due to the perfect

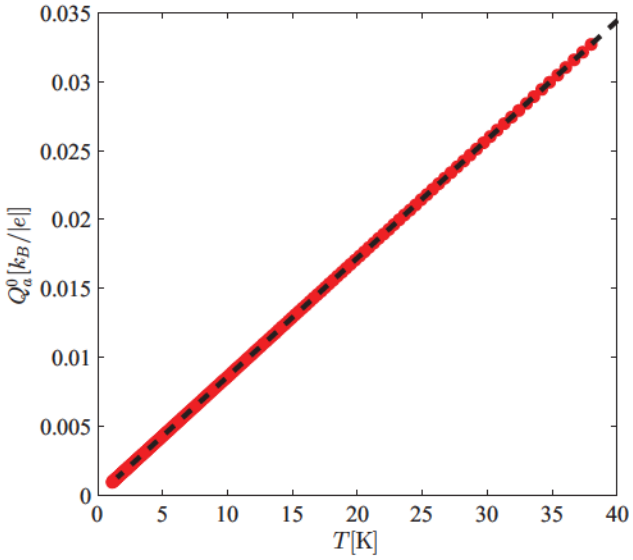


**Figure 4.4** The band part of the Seebeck coefficient versus temperature obtained from the perturbed density of states (red dotted line) and compared with the one from the bare spectrum (dashed balck line)

nesting condition. As for $\alpha$, we have

$$\alpha \sim \frac{v_F \xi_{\parallel}^{-1}}{T_{\mathrm{SDW}}^0} = \xi_{\parallel}^0 / \xi_{\parallel}. \tag{4.20}$$

According to RG calculations of reference [10], in a large part of metallic phase in the phase diagram above the SC phase, the SDW susceptibility shows a Curie-Weiss temperature dependent behavior $\tilde{\chi}_Q(T)^{-1} \propto (T + \Theta)$ with $\Theta$ scaling the intensity of spin fluctuations as a function of $T$ and $t'_{\perp}$. The in-plane antiferromagnetic correlation length $\xi_{\parallel}$ then is expected to be proportional to $(T + \Theta)^{1/2}$ in this Curie-Weiss regime. We take this hint and we write

$$\alpha = \frac{\tilde{\chi}_Q(T_{\mathrm{SDW}}^0)^{1/2}}{\tilde{\chi}_Q(T)^{1/2}}, \tag{4.21}$$

with $\tilde{\chi}_Q(T_{\mathrm{SDW}}^0)^{1/2}$ and $\tilde{\chi}_Q(T)^{1/2}$ values obtained by our RG calculations.

## 4.4 Results and discussion

We now turn into our principal results. According to the results of chapter three, the longitudinal Seebeck coefficient is the summation of the three following terms

$$Q_a = \frac{\pi^3}{3}\frac{k_B^2 T}{|e|}\left\{ \underbrace{\left[ -\frac{d\ln\langle N(E,k_\perp)\rangle_{k_\perp}}{dE} - 2\frac{d\ln\langle v^a_{E,k_\perp}\rangle_{k_\perp}}{dE} \right]}_{\sim Q_a^0} - \frac{\partial \ln\langle \bar{\phi}_{E,k_\perp}\rangle_{k_\perp}}{\partial E} \right\}_{E=0}$$
$$= Q_a^0 + Q_a^c. \tag{4.22}$$

We obtained the third term as the solution of $\boldsymbol{k}$-dependent Boltzmann integral equation which contains the umklapp scattering. As for the first two terms we took their value from the bare conduction band in the absence of any interaction with the spin fluctuations. In this complement we have introduced the influence of interactions to the first term by calculating the fluctuation effects on the density of states using the Lee-Rice-Anderson approximation for the one-particle self-energy.

As illustrated in figure 4.2, introducing the antiferromagnetic fluctuations at a given temperature and a given $t'_\perp$ in the magnetic quantum critical region, a pseudogap at the Fermi level develops in the density of states. A close-up of the density of states around the Fermi level is shown in figure 4.3. In the absence of $t'_\perp$, the pseudogap is uniform with still a non-zero positive slope at the Fermi level (See figure 4.3-a). As shown in figure 4.3-b, switching on the $t'_\perp$, an asymmetry in the form of a quasi-particle peak begins to develop its intensity depending on the strength of spin fluctuations through the $\alpha$ parameter. The peak sharpens approaching the superconducting transition temperature where the SDW fluctuations are enhanced, as a result of the positive feedback of Cooper pairing scattering channel on the Peierls one.

The temperature dependence of the band contribution $Q_a^0$ to the Seebeck coefficient is plotted in figure 3.53, the dotted red line, and compared to the case obtained with the bare density of states, the black dashed line. As we see, despite the obvious asymmetry in the density of states, the band contribution to Seebeck coefficient which contains the slope of the density of states at the Fermi level does not change. Therefore, the introduction of spin fluctuations, at least in the present approximation, does not affect neither the sign nor the amplitude of the $T$-dependence of the Seebeck coefficient. Perhaps, a more systematic treating of spin fluctuations from the microscopic models such as solving the famous Kubo formulas would be more rigorous and changes this result. Calculating elaborated current-current vertex functions could give more precise information on the temperature variation of the Seebeck coefficient from the full band structure contributions. This is beyond our present work and might be itself a separate stimulating project using the renormalization group techniques for calculating vertex corrections.

# Conclusion

In this work we have studied the low temperature instabilities and normal state transport properties of the quasi-1D electron gas model of superconductors like the Bechgaard salts. We employed the renormalization group method, which takes into account the main characteristics of the quasi-1D compounds such as electron band anisotropy, nesting property of Fermi surface, and quantum fluctuation effects resulting from the electron-electron and the electron-hole interfering scattering channels. This has enabled us firstly to investigate possible phase transitions under the application of a Zeeman coupling of spins to a magnetic field and secondly, to use the renormalized umklapp scattering vertex to solve the Boltzmann equation for the transport coefficients.

In the first part of the thesis, we have applied the RG approach to the quasi-1D electron gas model with both inter-chain and intra-chain repulsive interactions. We then study the effect of a magnetic field, exclusively coupled to spins, on the phase diagram as a function of temperature and nesting deviations. By lowering the temperature, the scattering amplitudes and the response functions are renormalized as a result of quantum interference between the electron-electron (Cooper) and electron-hole (Peierls) scattering channels. From the singularities in the scattering amplitudes which give the possible instabilities of the normal state, different sequences of instabilities as a function of the antinesting parameter $t'_\perp$ and of magnetic field could be obtained in the presence or not of inter-chain repulsion between electrons. For purely intra-chain interactions, the field is found to induce a spatially inhomogeneous superconducting (FFLO) state, a result consistent with the previous work of Fuseya et al., [18] in the absence of umklapp scattering. The upper critical field line found for the FFLO state becomes anomalously large at low temperature, which may explain the violation of the Pauli limit in the Bechgaard salts from resistivity measurements. No matter the value of field, at sufficiently high value of inter-chain coupling the CDW emerges instead of SDW and gives rise to the triplet pairing of $f$ symmetry as the antinesting deviation increases. The transition from singlet to triplet SC at low $T$ and high magnetic field, as a suggested scenario explaining the observed survival of superconductivity, is just found at certain intermediate value of inter-chain coupling. The cooper pairs of the triplet phase have a finite momentum and thus the superconducting state is inhomogeneous.

In the second part of the thesis, we have investigated the behavior of electrical resistivity and of the Seebeck coefficient over the whole temperature domain of the normal phase. We have proceeded to the linearization of the semi-classical Boltzmann equation for which the collision integral equation for the scattering has been calculated numerically using the umklapp scattering amplitudes obtained from the RG method. Owing to anomalous enhancement of umklapp scattering near the quantum critical point joining antiferromagnetism and superconductivity, anomalous temperature behavior of resistivity and Seebeck coefficients are found. The strength of the anomalous behaviors is correlated with the amplitude of antinesting or the value of $T_c$.

In the case of longitudinal electrical resistivity, it evolves from a pronounced $T$-linear component at the quantum critical point towards a Fermi-liquid $T^2$ component at large antinesting parameter or very low $T_c$. This defines an extended fan-shape region of quantum criticality, which can be realized as the variation of umklapp scattering with temperature. In addition, the anisotropy of resistivity on the Fermi surface is tied to the strong anisotropy of umklapp scattering.

As for the longitudinal Seebeck coefficient, it exhibits remarkable deviations from the hole band $T$-linear prediction and also an anomalous enhancement that is opposite in sign in an extended region around the quantum critical point. Moving away from the quantum critical point, the Fermi-liquid features of the Seebeck coefficient is recovered. In this quantum critical regime, large spin fluctuations, as a source of inelastic umklapp scattering, near the quantum critical point leads to a change of asymmetry of anisotropic electron-electron scattering time as well as its enhancement with energy.

Both transport results have been shown to qualitatively account for the relevant experimental observations in the phase diagram of Bechgaard salts. Longitudinal resistivity for instance, is linear in $T$ around the quantum critical point on the pressure axis and gradually tends toward the Fermi-liquid behavior sufficiently far from that point along the pressure axis. Moreover, the Seebeck coefficient sign reversal from positive to negative with relatively large values agree qualitatively well with the predictions. The comparison between theory and experiments has also revealed limitations of the present Boltzmann theory. In the case of resistivity, for example, the high temperature Fermi-liquid behavior observed for the Bechgaard salts was found to be inconsistent with the results of the present model. This suggests that additional sources of inelastic scattering mechanism are at play at high temperatures. This certainly deserves in the future further theoretical works on the nature of scattering processes outside the quantum critical domain.

# Bibliography


[1] T. Giamarchi, *Quantum Physics in One Dimension* (Oxford University Press, Oxford, 2004).

[2] D. Jérome, A. Mazaud, M. Ribault, and K. Bechgaard, J. Phys. (Paris) Lett. **41**, L95 (1980).

[3] D. Jérome and H. J. Schulz, Adv. Phys. **31**, 299 (1982).

[4] C. Bourbonnais and D. Jérome, in *Advances in Synthetic Metals, Twenty Years of Progress in Science and Technology*, edited by P. Bernier, S. Lefrant, and G. Bidan, pp. 206–261, Elsevier, New York, 1999, arXiv:cond-mat/9903101.

[5] C. Bourbonnais and D. Jérome, in *The Physics of Organic Superconductors and Conductors*, p. 357, Interscience Publishers, New York, London, 1961, See also arXiv:cond-mat/0904.0617.

[6] S. Brown, Physica C **514**, 279 (2015).

[7] D. Jérome and S. Yonezawa, C. R. Physique **17**, 357 (2016).

[8] R. Duprat and C. Bourbonnais, Eur. Phys. J. B **21**, 219 (2001).

[9] J. C. Nickel, R. Duprat, C. Bourbonnais, and N. Dupuis, Phys. Rev. B **73**, 165126 (2006).

[10] C. Bourbonnais and A. Sedeki, Phys. Rev. B **80**, 085105 (2009).

[11] A. Sedeki, D. Bergeron, and C. Bourbonnais, Phys. Rev. B **85**, 165129 (2012).

[12] D. J. Scalapino, Rev. Mod. Phys **349**, 1383 (2012).

[13] T. Tomita, K. Kuga, Y. Uwatoko, P. Coleman, and S. Nakatsuji, Science **349**, 506 (2015).

[14] L. Taillefer, Annu. Rev. Condens. Matter Phys. **1**, 51 (2010).

[15] N. P. Armitage, P. Fournier, and R. L. Greene, Rev. Mod. Phys. **82**, 2421 (2010).

[16] K. Jin, N. P. Butch, K. Kirshenbaum, J. Paglione, and R. L. Greene, Nature **476**, 73 (2011).

[17] G. R. Stewart, Rev. Mod. Phys **83**, 1589 (2011).

[18] Y. Fuseya, C. Bourbonnais, and K. Miyake, Europhys. Lett **100**, 57008 (2012).

[19] N. Doiron-Leyraud *et al.*, Phys. Rev. B **80**, 214531 (2009).

[20] N. Doiron-Leyraud *et al.*, Eur. Phys. J. B **78**, 23 (2010).

[21] Y. Chai *et al.*, J. Phys. Soc. Japan **78**, 063602 (2009).

[22] J. M. Buhmann, M. Ossadnik, T. M. Rice, and M. Sigrist, Phys. Rev. B **87**, 035129 (2013).

[23] L. B. Coleman *et al.*, Solid State Comm. **12**, 1125 (1973).

[24] D. S. Acker *et al.*, J. Am. Chem. Soc. **82**, 6408 (1960).

[25] F. Wudl, G. M. Smith, and E. J. Hufnagel, J. Chem. Soc., Chem. Comm. **1**, 1453 (1970).

[26] J. Ferraris, D. Cowan, V. Walatka, and J. Perlstein, J. Am. Chem. Soc. **95**, 948 (1973).

[27] G. Thomas, Phys. Rev. B. **13**, 5105 (1978).

[28] R. Peierls, *Quantum Theory of Solids* (Oxford University Press, London, 1955), P.108.

[29] J. Bardeen, L. Cooper, and J. Schrieffer, Phys. Rev. **108**, 1175 (1957).

[30] W. Little, Phys. Rev. **134A**, 1416 (1964).

[31] K. Yamaji, J. Phys. Soc. Jpn. **51**, 2787 (1982).

[32] J. Andersen *et al.*, Acta Cryst. B **34**, 1901 (1978).

[33] C. S. Jacobsen, K. Mortensen, J. R. Andersen, and K. Bechgaard, Phys. Rev. B **18**, 905 (1978).

[34] K. Bechgaard, D. O. Cowan, and A. N. Bloch, Journal of the Chemical Society, Chem. Comm. **22**, 937 (1974).

[35] A. Andrieux, C. Duroure, D. Jérome, and K. Bechgaard, J. Phys. (Paris) Lett. **40**, 381 (1979).

[36] K. Bechgaard, C. Jacobsen, K. Mortensen, H. Pedersen, and N. Thorup, Solid State Comm. **33**, 1119 (1980).

[37] K. Mortensen, Y. Tomkiewiez, T. D. Schultz, and E. M. Engler, Phys. Rev. Lett. **46**, 1234 (1982).

[38] K. Mortensen, Y. Tomkiewiez, and K. Bechgaard, Phys. Rev. B **25**, 3319 (1982).

[39] D. Jérome, Science **252**, 1509 (1991).

[40] D. Jerome, J. Supercond. Nov. Magn **25**, 633 (2012).

[41] C. Coulon *et al.*, J. Phys. (Paris) **43**, 1059 (1982).

[42] K. Bechgaard, M. Carneiro, M. Olsen, and F. Rasmussen, Phys. Rev. Lett. **46**, 852 (1981).

[43] M. Tsuchiizu, H. Yoshioka, and Y. Suzumura, J. Phys. Soc. Jpn. **70**, 1460 (2001).

[44] V. J. Emery, R. Bruinsma, and S. Barisic, Phys. Rev. Lett. **48**, 1039 (1982).

[45] J. P. Pouget and S. Ravy, J. Phys. I (France) **6**, 1501 (1996).

[46] R. Laversanne, C. Coulon, B. Gallois, J. P. Pouget, and R. Moret, J. Phys. (Paris) Lett. **45**, L393 (1984).

[47] T. Giamarchi, Physica **B230-232**, 975 (1997).

[48] F. Nad, P. Monceau, and J.Fabre, J. Phys. IV France **9**, Pr10 (1999).

[49] D. S. Chow *et al.*, Phys. Rev. Lett. **85**, 1698 (2000).

[50] F. Nad and P. Monceau, J. Phys. IV France **12**, Pr9 (2002).

[51] P. Foury-Leylekian *et al.*, Phys. Rev. B **70**, 180405(R) (2004).

[52] D. Chow *et al.*, Phys. Rev. Lett. **81**, 3984 (1998).

[53] J. M. D. , M. Roger, Z.Taffona, A.Moradpour, and K.Bechgaard, J. Phys. France **47**, 839 (1986).

[54] P. Auban, D. Jérome, C. Carcel, and J. Fabre, J. Phys. IV (France) **114**, 41 (2004), and to be published.

[55] P. Auban *et al.*, J. Phys.: Cond. Matt. **23**, 345702 (2011).

[56] N. Thorup, G. Rindorf, H. Soling, and K. Bechgaard, Acta Crystallogr. B **37**, 1236 (1981).

[57] T. Ishiguro and K. Yamaji, *Organic Superconductors*volume 88 of *Springer-Verlag Series in Solid-State Science* (Springer-Verlag, Berlin, Heidelberg, 1990).

[58] A. Lebed, editor, *The Physics of Organic Superconductors and Conductors*volume 110 (Springer Series in Materials Science, Heidelberg, 2008).

[59] V. J. Emery, J. Phys. (Paris) Coll. **44**, 977 (1983).

[60] P. M. Grant, Phys. Rev. B **26**, 6888 (1982).

[61] P. M. Grant, J. Phys. (Paris) Coll. **44**, 847 (1983).

[62] C. Jacobsen, D. Tanner, and K. Bechgaard, Phys. Rev. B **28**, 7019 (1983).

[63] J. B. Torrance, H. J. Pedersen, and K. Bechgaard, Phys. Rev. Lett **49**, 881 (1982).

[64] L. P. Le *et al.*, Phys.Rev.B. **48**, 7284 (1993).

[65] T. Takahashi, Y. Maniwa, H. Kawamura, and G. Saito, Physica **143B**, 417 (1986).

[66] G. Grüner, Rev. Mod. Phys. **66**, 1 (1994).

[67] Y. Machida, X. Lin, W. Kang, K. Izawa, and K. Behnia, Phys. Rev. Lett **116**, 087003 (2016).

[68] S. Tomic, J. R. Cooper, W. Kang, D. Jérome, and K. Maki, J. Phys. I (France) **1**, 1603 (1991).

[69] K. Andres *et al.*, Phys. Rev. Lett. **45**, 1449 (1980).

[70] T. Vuletic *et al.*, Eur. Phys. J. B **25**, 319 (2002).

[71] N. Kang *et al.*, Phys. Rev. B **81**, R100509 (2010).

[72] M. Ribault, G. Benedek, D. Jérome, and K. Bechgaard, J. Phys. Lett. Paris **41**, L (1980).

[73] S. Parkin, J. Voiron, and R. Greene, Mol. Cryst. Liq. Cryst. **33**, 119 (1985).

[74] S. Bouffard, M. Ribault, R. Brusetti, D. Jérome, and K. Bechgaard, J. Phys. C **15**, 295 (1982).

[75] M. Y. Choi *et al.*, Phys. Rev. B **25**, 6208 (1982).

[76] S. Tomić, D. Jérome, D. Mailly, M. Ribault, and K. Bechgaard, J. Physique **44 C3**, 1075 (1983).

[77] N. Joo *et al.*, Eur. Phys. J. B **40**, 43 (2004).

[78] N. Joo, P. Auban-Senzier, C. R. Pasquier, D. Jérome, and K. Bechgaard, Europhys. Lett. **72**, 645 (2005).

[79] M. Takigawa, H. Yasuoka, and G. Saito, J. Phys. Soc. Jpn **56**, 873 (1987).

[80] Y. Hasegawa and H. Fukuyama, J. Phys. Soc. Jpn. **56**, 877 (1987).

[81] S. Belin and K. Behnia, Phys. Rev. Lett. **79**, 2125 (1997).

[82] P. Garoche, R. Brusetti, and K. Bechgaard, Phys. Rev. Lett. **49**, 1346 (1982).

[83] I. J. Lee, M. J. Naughton, G. M. Danner, and P. M. Chaikin, Phys. Rev. Lett. **78**, 3555 (1997).

[84] S. Yonezawa *et al.*, Phys. Rev. Lett. **100**, 117002 (2008).

[85] A. G. Lebed, JETP Lett. **44**, 114 (1986).

[86] A. M. Clogston, Phys. Rev. Lett. **9**, 266 (1962).

[87] L. N. Bulaevskii, Soviet Physics -Solid State **11**, 921 (1969).

[88] I. J. Lee, P. M. Chaikin, and M. J. Naughton, Phys. Rev. B **62**, R14669 (2000).

[89] J. I. Oh and M. J. Naughton, Phys. Rev. Lett. **92**, 067001 (2004).

[90] S. Yonezawa *et al.*, J. Phys. Soc. Jpn. **77**, 054712 (2008).

[91] J. Shinagawa *et al.*, Phys. Rev. Lett. **98**, 147002 (2007).

[92] S. Yonezawa, Y. Maeno, K. Bechgaard, and D. Jerome, Phys. Rev. B **85**, 140502(R) (2012).

[93] N. Joo, P. Auban-Senzier, C. R. Pasquier, D. Jérome, and K. Bechgaard, Europhys. Lett. **72**, 645 (2005).

[94] N. Dupuis, G. Montambaux, and C. A. R. S. de Melo, Phys. Rev. Lett. **70**, 2613 (1992).

[95] N. Dupuis and G. Montambaux, Phys. Rev. B. **49**, 8993 (1993).

[96] A. G. Lebed, Phys. Rev. Lett. **107**, 087004 (2011).

[97] P. Fulde and R. A. Ferrell, Phys. Rev. **135**, A550 (1964).

[98] A. I. Larkin and Y. N. Ovchinikov, Sov. Phys. JETP **20**, 762 (1965).

[99] H. Shimahara, Phys. Rev. B **61**, R14936 (2000).

[100] Y. Fuseya, M. Tsuchiizu, Y. Suzumura, and C. Bourbonnais, J. Phys. Soc. Jpn. **74**, 3159 (2005).

[101] N. Belmechri, G. Abramovici, and M. Heritier, Physica B **405**, S256 (2010).

[102] H. Aizawa, K. Kuroki, and Y. Tanaka, Physica C **470**, 1085 (2010).

[103] L. W. Gruenberg and L. Gunther, Phys. Rev. Lett. **16**, 996 (1966).

[104] D. aint James, G. Sarma, and E. J. Thomas, editors, *Type II Superconductivity* (Pergamon Press, New York, 1969).

[105] B. S. Chandrasekhar, Apply. Phys. Lett. **1**, 7 (1962).

[106] K. Maki and T. Tsuneto, Prog. Theor. Phys. **31**, 945 (1964).

[107] Y. Matsuda and H. Shimahara, J. Phys. Soc. Japan **76**, 051005 (2007).

[108] N. Miyawaki and H. Shimahara, J. Phys. Soc. Japan **83**, 024703 (2014).

[109] L. G. Aslamazov, Sov. Phys. JETP **28**, 773 (1969).

[110] R. Modler *et al.*, Phys. Rev. Lett. **76**, 1292 (1996).

[111] A. Yamashita, K. Ishii, T. Yokoo, and J. Akimitsu, Phys. Rev. Lett. **79**, 3771 (1997).

[112] A. Bianchi, R. Movshovich, C. Capan, P. G. Pagliuso, and J. L. Sarrao, Phys. Rev. Lett. **91**, 187004 (2003).

[113] L. Balicas *et al.*, Phys. Rev. Lett. **87**, 67002 (2001).

[114] M. A. Tanatar, T. Ishiguro, H. Tanaka, , and H. Kobayashi, Phys. Rev. B **66**, 134503 (2002).

[115] S. Uji *et al.*, Phys. Rev. Lett. **97**, 157001 (2006).

[116] R. L. Greene and E. M. Engler, Phys. Rev. Lett. **45**, 1587 (1980).

[117] R. Brusetti, M. Ribault, D. Jerome, and K. Bechgaard, J. Phys. (Paris) **43**, 801 (1982).

[118] S. Tomic, Jérome, P. Monod, and K. Bechgaard, J. de Phys. (Paris) Lett. **43**, L839 (1982).

[119] I. J. Lee, S. E. Brown, W. Yu, M. J. Naughton, and P. M. Chaikin, Phys. Rev. Lett. **94**, 197001 (2005).

[120] A. Narayanan, D. G. A. Kiswandhi, J. Brooks, and P. Chaikin, Phys. Rev. Lett. **112**, 146402 (2014).

[121] F. Creuzet, C. Bourbonnais, L. G. Caron, D. Jérome, and K. Bechgaard, Synthetic Metals **19**, 289 (1987).

[122] S. E. Brown, P. M. Chaikin, and M. J. Naughton, in *The Physics of Organic Superconductors and Conductors*, edited by A. Lebed, volume 110, Springer Series in Materials Science, p. 49, Springer, Heidelberg, 2008.

[123] Y. Kimura, M. Misawa, and A. Kawamoto, Phys. Rev. B **84**, 045123 (2011).

[124] W. Wu *et al.*, Phys. Rev. Lett. **94**, 097004 (2005).

[125] A. J. Millis, H. Monien, and D. Pines, Phys. Rev. B **42**, 167 (1990).

[126] T. Moriya and K. Ueda, Adv. Phys. **49**, 555 (2000).

[127] D. K. C. MacDonald, in *Thermoelectricity: An Introduction to the Principles*, John Wiley and Sons, New York, 1962.

[128] J. M. Ziman, in *Principles of the Theory of Solids*, Cambridge University Press, Cambridge, England, 1964.

[129] K. Behnia, in *Fundamentals of Thermoelectricity*, Oxford University Press, Oxford, 2015.

[130] C. Sun *et al.*, J. Phys.: Condens. Matter **20**, 235223 (2008).

[131] J. W. Negele and H. Orland, *Quantum Many Particle Systems*volume 68 of *Frontiers in Physics series* (Addison-Wesley, New York, 1988).

[132] C. Bourbonnais, B. Guay, and R. Wortis, in *Theoretical methods for strongly correlated electrons*, edited by D. Sénéchal, A. M. Tremblay, and C. Bourbonnais, pp. 77–78, Springer, Heidelberg, 2003, arXiv: cond-mat/0204163.

[133] P. Wzietek *et al.*, J. Phys. I (France) **3**, 171 (1993).

[134] N. Miljak, J. R. Cooper, and K. Bechgaard, J. Phys. Colloq. **44**, C3 (1983).

[135] N. Miljak and J. R. Cooper, Mol. Cryst. Liq. Cryst. **119**, 141 (1985).

[136] S. Barisic and S. Brazovskii, in *Recent Developments in Condensed Matter Physics*, edited by J. T. Devreese, volume 1, p. 327, Plenum, New York, 1981.

[137] G. Xiao, P. Xiong, and M. Z. Cieplak, Phys. Rev. B **46**, 8687(R) (1992).

[138] T. Nishikawa, J. Takeda, and M. Sato, J. Phys. Soc. Japan **63**, 1441 (1994).

[139] J. Takeda, T. Nishikawa, and M. Sato, Physica C **231**, 293 (1994).

[140] P. Fournier, X. Jiang, and W. Jiang, Phys. Rev. B **56**, 14149 (1997).

[141] Y. Sushkoa *et al.*, Synth. Metals **85**, 1541 (1997).

[142] J. Moser *et al.*, Phys. Rev. Lett. **84**, 2674 (2000).

[143] E. S. Choi, H. Y. Kang, Y. J. Jo, J. Yeom, and W. Kang, Synth. Metals **120**, 1069 (2001).

[144] Y. Nakajima *et al.*, J. Phys. Soc. Japan **73**, 5 (2004).

[145] S. Sachdev, Rev. Mod. Phys **75**, 913 (2003).

[146] Y. Dagan, M. M. Qazilbash, C. P. Hill, V. N. Kulkarni, and R. L. Greene, Phys. Rev. Lett **92**, 167001 (2004).

[147] K. Behnia, D. Jaccard, and J. Flouquet, J. Phys.: Condens. Matter **16**, 5187 (2004).

[148] P. Gegenwart, Q. Si, and F. Steglich, Nature Physics **4**, 186 (2008).

[149] M. Dressel, J. Phys.: Condens. Matter **23**, 293201 (2011).

[150] H. Haug and A. P. Jauho, in *Quantum Kinetics in Transport and Optics of Semiconductors*, edited by M. Cardona and P. Fulde, volume 110, Springer Series in Solid-State Sciences, p. 3, Springer, Heidelberg, 2008.

[151] L. P. Gorkov and M. Mochena, Phys. Rev. B **57**, 6204 (1998).

[152] A. Kampf and J. R. Schriffer, Phys. Rev. B **41**, 6399 (1990).

[153] J. Schmalian, Phys. Rev. Lett. **81**, 4232 (1998).